Dissertation
submitted to the
Combined Faculties for the Natural Sciences and for Mathematics
of the Ruperto-Carola University of Heidelberg, Germany
for the degree of
Doctor of Natural Sciences

Put forward by

Neven Tomičić

Born in: Zadar, Republic of Croatia
Oral examination: 15.5.2019

Probing the cold phase of the interstellar medium and star formation in nearby galaxies

Neven Tomičić

Referees:
Prof. Dr. Hans-Walter Rix
Prof. Dr. Simon Glover

Posvečujem ovaj doktorski rad mojim roditeljima, prijateljima, i kolegama znanstvenicima, ali isto tako i široj astronomskoj zajednici.

I dedicate this PhD thesis to my parents, friends, and research colleagues, but also to the broad astronomical society.

Ich widme diese Doktorarbeit meinen Eltern, Freunden und Kollegen, sowie allen in der astronomischen Wissenschaft arbeitenden Personen.

ABSTRACT

Properly measuring the spatial distribution of the star formation rate (SFR) in galaxies helps us to understand the driving forces for the star formation in galaxies, effects on their interstellar media (ISM), and their evolution. However, this is hindered by the uncertainties in estimating SFRs and calibrating the SFR prescriptions. These uncertainties are caused by not properly measuring the attenuation of light, probing large spatial scales, or averaging over large sample of galaxies. Additionally, the physical factors that set the efficiency whith which galaxies convert gas into stars (star formation efficiency; SFE), and their role in galactic evolution, are not yet fully understood. Variations in the SFE are difficult to disentangle from uncertainties of estimated SFRs.

The main goal of this thesis is to use optical integral field unit (IFU) observations of nearby galaxies, in order to probe the cold phase of their ISM at sub-kpc scales. We aim to measure the attenuation, thus to properly estimate the SFRs and calibrate the SFR prescriptions. We also estimate variations of SFE across the disk of an interacting galaxy.

Using IFU observations of the outskirts of the Andromeda galaxy (M31) at sub-kpc scales (from 10 pc to kpc), we derive the Balmer line attenuation. By comparing attenuation with the dust mass surface density, we derive the 3-dimensional spatial distribution of dust and ionized gas in M31. Our results indicate that the vertical dust/gas distribution from the central areas of nearby galaxies differs from the outskirts of M31. From this evidence, we hypothesize that the vertical dust/gas distribution in galactic disks varies as a function of the galactocentric distance. Following that, we use extinction corrected Balmer line emission as a reference SFR tracer in a combination with ultraviolet and near-infrared images, to calibrate hybrid SFR prescriptions. We find that the hybrid SFR prescriptions do not change with spatial scale or with the subtraction of a diffuse component. However, our SFR prescriptions observed in M31 differ from the prescriptions in the literature. This indicates that the SFR prescriptions are not universal and that they may vary with the inclination and the galactocentric radius, due to varying dust/gas distributions.

Our IFU observations of the interacting galaxy NGC 2276 are used to investigate how the early phase of galactic interaction affects the ISM, and SFE across its disk. Although NGC 2276 shows a significant asymmetrically elevated SFR surface density, and asymmetric stellar distribution, it does not show an unusual gas phase metallicity gradient or shock ionization. On the other hand, we probed the SFE at sub-kpc scales (0.5 kpc) across NGC 2276's disk to trace the origin of its elevated and asymmetric SFR and found more than two orders of magnitude variation in SFE. This is significantly larger than what is seen in nearby galaxies. We speculate that this is caused by both tidal forces exerted from a neighboring galaxy and ram pressure affecting NGC 2276.

KURZFASSUNG

Die korrekte Messung der räumlichen Verteilung der Sternentstehungsrate (engl. star formation rate, SFR) in Galaxien erlaubt es uns die treibenden Kräfte für die Sternentstehung in Galaxien, ihre Auswirkungen auf ihre interstellaren Medien (ISM) und ihre Entwicklung zu verstehen. Dies wird jedoch durch die Unsicherheiten bei der Abschätzung der SFRs und der Kalibrierung der SFR-Umwandlung erschwert. Diese Unsersichterheiten resultieren aus einer unkorrekten Bestimmung der Abschwächung des Lichts, der Untersuchung von großen räumlichen Skalen, oder dem Mitteln über große Stichproben von Galaxien. Darüber hinaus sind die physikalischen Faktoren, die die Effizienz bestimmen, mit der Galaxien Gas in Sterne umwandeln (Sternentstehungseffizienz; engl. star formation efficiency, SFE), und ihre Rolle in der galaktischen Evolution noch nicht vollständig verstanden. Abweichungen in der SFE sind schwer von den Unsicherheiten der geschätzten SFRs zu trennen.

Das Hauptziel dieser Arbeit ist die Analyse von Beobachtungsdaten von optischen abbildenden Spektrometern (IFU) von nahegelegenen Galaxien, um die kalte Phase ihrer ISM auf Sub-kpc-Skalen zu untersuchen. Wir messen die Abschwächung des Lichtes, um somit die SFRs richtig abzuschätzen und die SFR-Umwandlungen zu kalibrieren. Zudem schätzen wir die Variationen der SFE innerhalb der Scheibe einer interagierenden Galaxie ab.

Unter Verwendung von IFU-Beobachtungen der äußeren Scheibe der Andromeda-Galaxie (M31) auf sub-kpc-Skalen (von 10 pc bis kpc) leiten wir die Balmer-Liniendämpfung ab. Durch den Vergleich der Dämpfung mit der Staubmassendichte wird die dreidimensionale räumliche Verteilung von Staub und ionisiertem Gas in M31 ermittelt. Unsere Ergebnisse zeigen, dass sich die vertikale Verteilung von Staub / Gas aus den zentralen Bereichen benachbarter Galaxien von den Randbereichen von M31 unterscheidet. Aufgrund dieser Evidenz stellen wir die Hypothese auf, dass die vertikale Staub-/Gasverteilung in galaktischen Scheiben in Abhängigkeit von der galaktozentrischen Entfernung variiert. Anschließend verwenden wir die extinktionskorrigierte Balmer-Linienemission als Referenz-SFR-Tracer in Kombination mit Ultraviolett- und Nahinfrarotbildern, um hybride SFR-Umwandlungen zu kalibrieren. Wir finden, dass sich die hybriden SFR-Umwandlungen nicht mit der räumlichen Skala oder mit der Subtraktion einer diffusen Komponente ändern. Unsere in M31 beobachteten SFR-Umwandlungen unterscheiden sich jedoch von den Umwandlungen in der Literatur. Dies deutet darauf hin, dass die SFR-Umwandlungen nicht universell sind und aufgrund der unterschiedlichen Staub-/Gasverteilungen mit der Neigung und dem galaktozentrischen Radius variieren können.

Unsere IFU-Beobachtungen der interagierenden Galaxie NGC 2276 wurden genutzt, um zu untersuchen, wie sich die frühe Phase einer galaktischen Interaktion auf die Eigenschaften des ISM und der SFE in der gesamten Scheibe auswirkt. Obwohl NGC 2276 eine signifikant asymmetrisch erhöhte SFR-Oberflächendichte und asymmetrische Sternverteilung aufweist, zeigen sich keine ungewöhnlichen Gasphasen-Metallizitätsgradienten oder Anzeichen für Schockionisation. Zudem untersuchten wir die SFE auf sub-kpc-Skalen (0,5 kpc) in der Scheibe von NGC 2276, um den Ursprung ihrer erhöhten und asymmetrischen SFR zu ermitteln, und fanden eine Variation von mehr als zwei in SFE. Dies ist deutlich größer als in nahegelegenen Galaxien. Wir spekulieren, dass dies sowohl durch von einer benachbarten Galaxie ausgeübte Gezeitenkräfte, als auch durch den Staudruck der auf NGC 2276 einwirkt, verursacht wird.

TABLE OF CONTENTS

ABSTRACT i

LIST OF FIGURES ix

LIST OF TABLES xii

1 Introduction 2

1.1 Evolution of galaxies and star formation 2

1.1.1 Formation of stars and galaxies 4

1.1.2 Components of the cold interstellar medium 6

1.1.3 Star formation through cosmic time 9

1.2 The Star Formation law 11

1.2.1 Observations and efficiency of star formation 12

1.2.2 Effects of environments and interaction 14

1.3 Estimation of star formation rates 15

1.3.1 Direct stellar tracers 16

1.3.2 Ionized gas, dust and synchrotron emission 17

1.3.3 Attenuation 19

1.3.4 Hybrid SFR prescriptions 20

1.3.5 Problem of scales and instruments 21

1.4 Integral field spectroscopy 22

1.5 Purpose and outlook of this thesis 25

2 Attenuation and the relative dust/gas distribution as seen in M31 30

2.1 Introduction 30

2.2 Data 32

2.2.1 Optical Integral Field Spectroscopy 32

2.2.2 Far-IR data and dust column densities 37

2.3 Results 38

2.3.1 Attenuation maps 38
2.3.2 A_V vs. Σ_{dust} 45
2.4 Discussion 48
2.4.1 The impact of physical resolution 48
2.4.2 Effects of an additional component to the dust/gas distribution model . . . 50
2.4.3 [SII]($\lambda6717 + \lambda6731$)/H$\alpha$ vs. A_V diagram 54
2.4.4 Modeling the impact of geometry 56
2.4.5 Effects of location on the relative vertical distribution of dust and DIG . . 58
2.5 Wider implications 61
2.6 Summary 62

3 Calibrating the SFR prescriptions at sub-kpc scales in M31 66

3.1 Introduction 66
3.2 Data 68
3.2.1 WISE 22 μm and SPITZER 24 μm images 69
3.2.2 Other IR tracers: WISE 12 μm, PACS 70 μm and PACS 160 μm data . . . 71
3.2.3 GALEX FUV data 71
3.2.4 Optical Hα data 71
3.2.5 Convolution & apertures 73
3.2.6 Maps of SFR tracers 74
3.3 Hα as our reference SFR tracer 81
3.3.1 Conversion from Hα and FUV to SFR 81
3.3.2 Effects of different extinction curves 82
3.3.3 Comparison with SFRs derived from the PHAT survey 83
3.3.4 Comparison by using molecular cloud masses 84
3.4 Calibration of the SFR prescriptions 84
3.4.1 Monochromatic SFRs 86
3.4.2 The hybrid SFR prescriptions at smallest scales 88
3.4.3 Effects of spatial scales and diffuse component subtraction 91
3.5 Effects of inclination and galactocentric distance on the SFR prescriptions 93
3.5.1 Effects of galactocentric distance and inclination 93
3.5.2 Calibration factor as a function of various physical quantities 95
3.6 Discussion 97

3.6.1 Galactocentric distance and inclination 97
3.6.2 Spatial scales, age of the clusters and sampling initial mass function . . . 99
3.6.3 Effects of the diffuse emission components 100
3.6.4 Implications of the results 100
3.7 Summary 100

4 Multi-wavelength view of the interacting galaxy NGC 2276 105
4.1 Introduction 105
4.2 Data 107
4.2.1 Nebular emission line maps 107
4.2.2 Calibration of optical IFU observations 109
4.2.3 IFU spectral analysis 111
4.2.4 UV images 111
4.2.5 IR and stellar distribution 112
4.3 Results 115
4.3.1 SFR and the star formation tracers 115
4.3.2 Gas velocity 115
4.3.3 Inclination 117
4.3.4 BPT diagram 117
4.3.5 The diffuse gas fraction 119
4.3.6 Metallicities 121
4.4 Summary 123

5 Large variation in SFE in interacting galaxy NGC 2276 128
5.1 Introduction 128
5.2 Data 130
5.3 Results 130
5.3.1 The depletion time 130
5.3.2 Tidal forces and ram pressure 133
5.4 Discussion and summary 135

6 Conclusions & Future Perspective 140
6.1 Summary 140
6.1.1 The dust/gas geometry in nearby galaxies 141

6.1.2 SFR prescriptions at small scales 141
6.1.3 Effects of galactic interactions on ISM and galaxy 142
6.1.4 Effects of galactic interactions on the SF efficiency 142
6.2 Concluding remarks 143
6.2.1 Effects of our results on star formation estimation in nearby galaxies . . . 143
6.2.2 Varying star formation and star formation efficiency at sub-galactic scales 143
6.3 Future perspective 145
6.3.1 What affects SFR prescriptions in nearby galaxies? 145
6.3.2 Variations in SFE at different phases of interactions 146
APPENDIX: SFR PRESCRIPTIONS 150
PUBLICATIONS OF N. TOMIČIĆ USED IN THIS THESIS 157
REFERENCES 171
LIST OF ACRONYMS AND ABBREVIATIONS 171
ACKNOWLEDGEMENTS 177

LIST OF FIGURES

1.1 Probing different spatial scales and different astronomical objects 3

1.2 Multi-wavelength images of a grand design galaxy M51 5

1.3 Example of the spectral energy distribution of a galaxy 7

1.4 Star formation rate density, metallicity, and gas/stellar mass ratio through cosmic time 10

1.5 Example of correlation between the ionized star-forming gas and the molecular gas in NGC 628 13

1.6 Kennicutt-Schmidt diagram 14

1.7 M20 seen in multiple SFR tracers (optical and IR) 17

1.8 Light absorption in the Taurus constellation and the extinction curves 19

1.9 Integral field spectroscopy 23

1.10 Integral field unit PPaK 24

2.1 Observed fields in M31 33

2.2 Analysed spectra in M31 36

2.3 Maps of Hα line, A_V, and dust mass distribution of Field 1 in M31 40

2.4 Maps of Hα line, A_V, and dust mass distribution of Field 2 in M31 41

2.5 Maps of Hα line, A_V, and dust mass distribution of Field 3 in M31 42

2.6 Maps of Hα line, A_V, and dust mass distribution of Field 4 in M31 43

2.7 Maps of Hα line, A_V, and dust mass distribution of Field 5 in M31 44

2.8 A_V vs Σ_{dust} diagram 46

2.9 Variation in dust/gas geometry due to correcting the M31's dust mass 48

2.10 A_V vs Σ_{dust} diagram as a function of spatial scales 49

2.11 A_V vs. Σ_{SFR} of M31 and nearby galaxies data 51

2.12 Variation in the dust/gas distribution with additional diffuse ionized gas 53

2.13 SII/Hα vs. A_V diagram 55

2.14 A simple toy model 58

2.15 A complex toy model 59
2.16 Schematic image of the dust/gas geometry as a function of galactocentric distance 60
3.1 Comparison of spectroscopic and photometric Hα, and of MIPS 24μm and WISE 22μm data 72
3.2 The used apertures in M31 75
3.3 Maps of SFR tracers of Field 1 in M31 76
3.4 Maps of SFR tracers of Field 2 in M31 77
3.5 Maps of SFR tracers of Field 3 in M31 78
3.6 Maps of SFR tracers of Field 4 in M31 79
3.7 Maps of SFR tracers of Field 5 in M31 80
3.8 Variation in SFRs due to different extinction curves 83
3.9 Comparing the SFR maps of M31 with those derived from the SF history and color-magnitude diagrams 85
3.10 Comparing SFR values using the giant molecular clouds masses 87
3.11 The monochromatic SFR prescriptions 87
3.12 The SFR prescriptions at longer IR wavelengths 88
3.13 The hybrid SFR prescriptions 90
3.14 Residuals of the hybrid SFR prescriptions 91
3.15 The effects of scales on the hybrid SFR prescriptions 92
3.16 The effects of subtracting diffuse emission on the hybrid SFR prescriptions . . 92
3.17 The effects of inclination, galactocentric distance, and attenuation on the hybrid SFR prescriptions 94
3.18 Variation in the hybrid SFR prescriptions as a function of $\Sigma(\mathrm{SFR})$, $\Sigma(\mathrm{H}\alpha)$, $\Sigma(\mathrm{IR})$, and the dust temperature 96
4.1 Example of the P3D window while calibrating raw NGC 2276 data 110
4.2 The Hα, gas velocity and the $\mathrm{A_V}$ maps of NGC 2276 112
4.3 Star formation tracers maps of NGC 2276 113
4.4 $\Sigma(\mathrm{M_{stellar}})$ and ionized gas of NGC 2276 and NGC 2300 114
4.5 Determining the NGC 2276's inclination 116
4.6 The BPT map and diagram of NGC 2276 118
4.7 Diffuse gas fraction in NGC 2276 120
4.8 The nebular metallicity in NGC 2276 122

5.1 $\Sigma_{\rm SFR}$(Hα,corr), $\Sigma_{\rm H_2}$, and the depletion time $\tau_{\rm depl}$ of NGC 2276 131
5.2 Correction of H_2 map due to metallicity variation in NGC 2276 132
5.3 The Kennicutt-Schmidt diagram of NGC 2276 134
5.4 The stellar clusters age variation across NGC 2276 135

LIST OF TABLES

2.1 Position and the nebular (gas-phase) metallicities of the fields in M31 34

3.1 Instruments, wavelengths and resolutions of the M31 maps used 70

3.2 Aperture distances and pixel sizes used 73

4.1 Global properties of NGC 2276 108

A.1 The hybrid SFR prescriptions 152

A.2 The hybrid SFR prescriptions at longer IR wavelengths 154

Chapter 1

"Recognize that the very molecules that make up your body, the atoms that construct the molecules, are traceable to the crucibles that were once the centers of high mass stars that exploded their chemically rich guts into the galaxy, enriching pristine gas clouds with the chemistry of life. So that we are all connected to each other biologically, to the earth chemically and to the rest of the universe atomically. That's kinda cool! That makes me smile and I actually feel quite large at the end of that. It's not that we are better than the universe, we are part of the universe. We are in the universe and the universe is in us."

by Neil deGrasse Tyson

1. Introduction

Arp 273
c: D. Pestana, NASA, HST, ESA

Since the dawn of human civilization, people have been asking themselves about the beginning and the rules of the world, and the sky above them. Through the last few centuries of the modern science, astronomers and physicists have been investigating, probing, and observing the surrounding world in order to dig deep into the laws that the universe is governed by. The major questions that astronomers have asked themselves for centuries are: how did the stars form, and how did they affect their nests, which we call galaxies? I find it intriguing that the creatures composed of the dead elements of the universe are able to ask themselves those questions, and to build simple machines to help them answer those questions.

1.1 Evolution of galaxies and star formation

Throughout the history of human kind, especially since the birth of modern science (physics, astronomy, biology, chemistry and medicine) a few centuries ago, societies were mostly improving the means to observe and analyse nature, the universe, and the laws that they are governed by. Due to the advancements in detectors, instruments and facilities, each scientific field increased the horizon of humanity's knowledge. This increased the precision of our predictions of behaviour and characteristics of the surrounding world. This is closely complemented by the advancements in theoretical predictions, hypotheses and models. In the history of astronomy and astrophysics, improvements of telescopes, detectors, laboratories, theoretical models, computing power, and observational techniques (Kitchin 2013; Wall 2018) led to observations of astronomical objects with better angular resolution and higher brightness sensitivity.

This enables us to explore various astronomical objects that probe vastly different physical scales (see Fig. 1.1), such as: cosmic scales (e.g. cosmic web and cosmic microwave background radiation), galactic scales (e.g. galaxies, galactic groups and clusters), intermediate scales (e.g. asteroids, planets, and stars), and atomic and sub-mm scales (e.g. cosmic

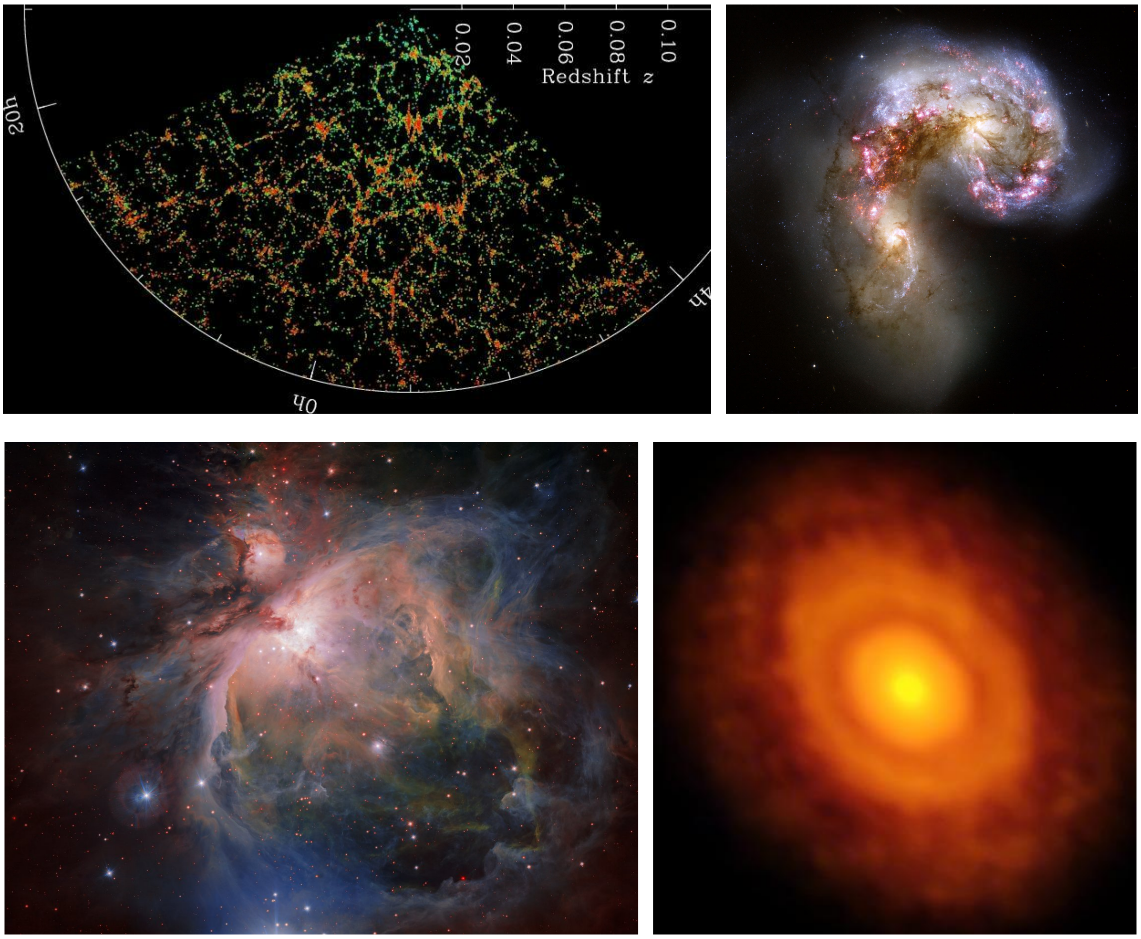

Fig. 1.1 Different astronomical objects and structures throughout different physical scales:
Upper left- An observed filamentary distribution of galaxies through redshift (z) and distance. Presented here is a slice through the Sloan Digital Sky Survey[1] (SDSS) sky map, with the Earth in the center. This slice reaches distances up to 600 Mpc. *Image credit: M. Blanton and the SDSS.*
Upper right- An optical image of the Antennae galaxies (NGC 4038/4039), a merger of two galaxies. Different colors indicate different phases of the ISM (ionized gas with a pink color, and dust with a dark/brown color) and the stellar populations (young stars with a blue color, and older stars with a white color). The length of the image is $\approx$ 16 kpc. *Image credit: B. Whitmore (the Space Telescope Science Institute), and James Long (ESA/Hubble).*
Bottom left- An OmegaCAM optical image (VLT Survey Telescope, ESA) of a spectacular HII region known as the Orion Nebula, and its associated cluster of young stars. The length of the image is $\approx$ 50 pc. *Image credit: G. Beccari (ESO).*
Bottom right- A sub-mm wavelength image of a proto-planetary disk around the young star V883 Orioniz, which is currently in an outburst that has pushed the water snow line (dark ring midway through the disk) further from the star and allowed it to be detected for the first time. *Image credit: L. Cieza (ALMA/ESO/NAOJ/NRAO).*

rays, magnetic fields, atomic and molecular gas, and dust). The astrophysical community revealed the rich chemistry, evolution, and physics of our universe by observing astronomical objects in the full wavelength range of electro-magnetic radiation (see Fig. 1.2 and 1.3), such as: gamma-ray and X-ray (probing the most violent and most energetic events, e.g. black holes, synchrotron radiation, super-novae, and gamma ray bursts), ultraviolet continuum (UV, e.g. probing dust absorption, and young stars), visible (e.g. tracing dust absorption, stellar continuum, and ionized gas emission), infra-red (IR, e.g. emission of the old stellar population and the interstellar dust), (sub-)mm to radio (e.g. probing cosmic microwave background radiation, dust and gas emission, free-free emission, and synchrotron radiation). Scientists started recently to observe extraterrestrial gravitational radiation (Weiss & Block 1965; Sazhin 1978), and for the first time detected gravitational waves that most probably originated from the collision of massive black holes (Abbott et al. 2016; Connaughton et al. 2016). Since Johannes Kepler derived his famous Kepler's law of planetary motion in the 17th century, theoretical and computational astronomy have evolved in synergy with observational astronomy. Its purpose is to understand the underlying physics behind the observed phenomena surrounding the observed astronomical objects.

1.1.1 Formation of stars and galaxies

After many centuries of the scientific investigation of our universe, the following picture of the universe and its evolution emerged. At the beginning of the universe, i.e. the Big Bang, space-time expanded (and the matter with it), first through the inflation phase (Liddle 1999) and then through a slower accelerated expansion (Perlmutter & Schmidt 2003). Through many years of astronomical observations and modeling, the most trusted cosmological model is the standard ΛCDM model (Peebles 1982; Bond et al. 1982; Liddle 1999; Planck Collaboration et al. 2014), which hypothesizes the existence of dark matter (composing 25% of the energy of the universe), dark energy (composing 69% of the energy of the universe), and the visible Baryonic matter (composing 5% of the energy of the universe). In the first seconds of the Big Bang, the process of primordial nucleosynthesis produced the first primordial elements (H, D, $^3\mathrm{He}$, $^4\mathrm{He}$,^{7} Li; Schramm & Turner 1998) in the universe.

Observations of the structures of the cosmic microwave background radiation (Penzias & Wilson 1965, Planck Collaboration et al. 2014 and the references within) invoke the existence of primordial density fluctuation in an early phase of the universe (Liddle 1999; Mo et al. 2010). This resulted in a structured distribution of the matter in the universe (Fig. 1.1), which collapsed due to gravitational attraction of the Baryonic and dark matter (Jeans 1902; Liddle 1999). Unlike the collisionless dark matter, baryonic matter can cool through dissipative processes and condense in the potential well of the assembling halo, eventually reaching densities large enough to form early stars and galaxies (Bond et al. 1982). The early stars (Population III stars), composed of primordial elements, synthesise more heavy atoms (through nucleosyn-

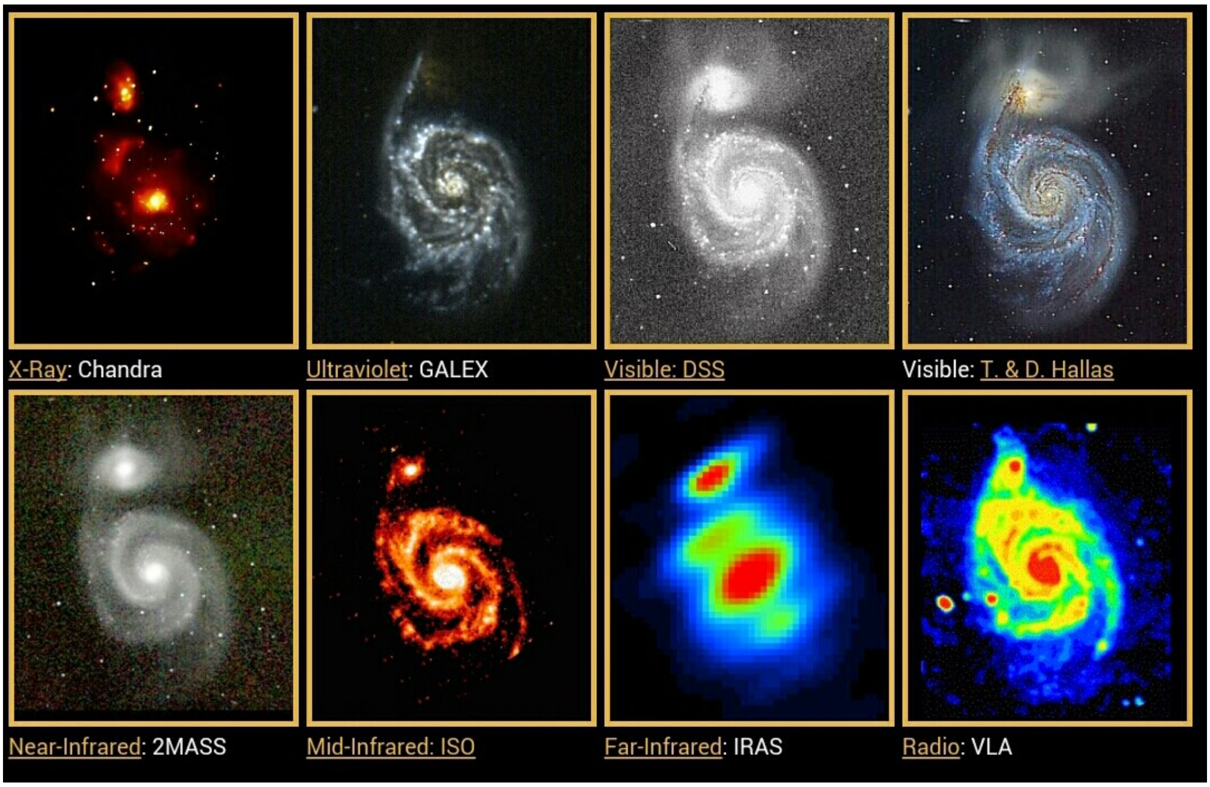

Fig. 1.2 Multi-wavelength images of the interacting galaxy NGC 5194 (M51a, Whirlpool Galaxy), with its interacting companion NGC 5195 (smaller galaxy in the top of the panels), from top left to bottom right:
X-ray (tracing some of the hottest and most violent objects in the universe, e.g. black holes, jets, etc.), ultraviolet (UV, tracing emission from the young massive stars), visible (tracing young stars with a blue color, old stars with a white color, star-forming regions and the ionized gas with a red color, and dust and attenuation with dark patches), near-infrared (near-IR, tracing the old stellar population, and partly the hot dust), mid-infrared (mid-IR, tracing the cold dust, and the hot dust around the star-forming regions), far-infrared (far-IR, tracing the cold dust and the cosmic microwave background radiation), and (sub-)mm to radio partially tracing the cold dust, the neutral gas, the cosmic microwave background radiation, and the ionized gas surrounding the star-forming regions). Each spectral range is observed by different instruments, telescopes and facilities (as labeled below the panels). M51a is also a grand-design spiral galaxy due to its clearly distinguished pair of massive spiral arms. Note that the companion NGC 5195 does not emit in the far-UV and blue part of the visible spectrum, indicating **[a]** low star formation, and that it is mostly composed of an older stellar population. *Image credit: Caltech*[2].

thesis, expulsion of their layers, and supernovae) and more complex molecules (a precursor of interstellar dust). In astronomy, elements heavier than He are referred as ‘metals’, and the chemical abundance as ‘metallicity’. The large-scale structures of the universe exert tidal gravitational forces during the collapse, which cause the collapsing matter to acquire **[an]** angular momentum (White & Rees 1978; Liddle 1999; van den Bosch et al. 2002). This forms the disk type of galaxies, and structures within them (spiral arms, bars, bulge; Liddle 1999; Mo et al. 2010). According to the ΛCDM model, smaller structures like galaxies and the dark matter halos then merge, forming larger galactic groups (Smolčić et al. 2017) and larger objects, such as late type elliptical galaxies (White & Rees 1978; Bond et al. 1982; Fall & Efstathiou 1980; Planck Collaboration et al. 2014; Bull et al. 2016). During galactic evolution, some of the galactic interstellar medium (hereafter the ISM) is expelled or stripped from galaxies (due to ram pressure, feedback from the stars and active galactic nuclei), or is falling back into the galaxies, changing the chemical composition of their interstellar medium.

Galactic structures (the stellar spiral arms and bars) and collision of the dense gas clouds may compress the gas, thus triggering its gravitational collapse (Larson 1981; Liddle 1999; McKee & Ostriker 2007; Meidt et al. 2013). These clouds of gas form more dense, self-gravitating structures in the molecular gas known as giant molecular clouds (GMC; Toomre & Toomre 1972; Scoville & Solomon 1975; Draine 2011c; Hughes et al. 2014a). The molecular H_2 gas is dominantly produced on dust grains (Lequeux 2005), and the GMCs are shielded from the interstellar radiation (hazardous for the H_2 molecules) by the dust clouds. The GMCs eventually fragment into highly dense cores that may form stars (Toomre & Toomre 1972; McKee & Ostriker 2007; Bromm & Yoshida 2011; Kravtsov & Borgani 2012) in the star-forming regions (see Fig. 1.1 and 1.5). When a group of stars within the cloud is formed, they have a wide range of masses (Kroupa 2001), of which the most massive and the most short-lived (< 5 Myr) ones are the stars of the spectral types O and B. These young and massive stars form OB association, ionize the surrounding gas (Strömgren 1939; Murphy et al. 2011), and destroy the surrounding dust (Dreher & Welch 1981; Verley et al. 2010). Stellar feedback phenomena such as high-energy radiation, stellar jets, winds, outflows, planetary nebulae and super-novae, exert an additional force on the surrounding gas (McKee & Ostriker 2007). This enriches the surrounding ISM with heavier elements (metals), disrupts the GMCs, and creates cavities and overdensities within the clouds, thus triggering a new wave of star formation near the young stars. Around stars, circumstellar and proto-planetary disks of gas and dust form (Fig. 1.1), and within proto-planetary disks larger particles (more massive than the interstellar dust grains) and eventually planets form.

1.1.2 Components of the cold interstellar medium

The evolution of the universe formed the ISM with a wide range of characteristics (Ferrière 2001; Draine 2011c), chemical compositions, temperatures, and densities that emit at in differ-

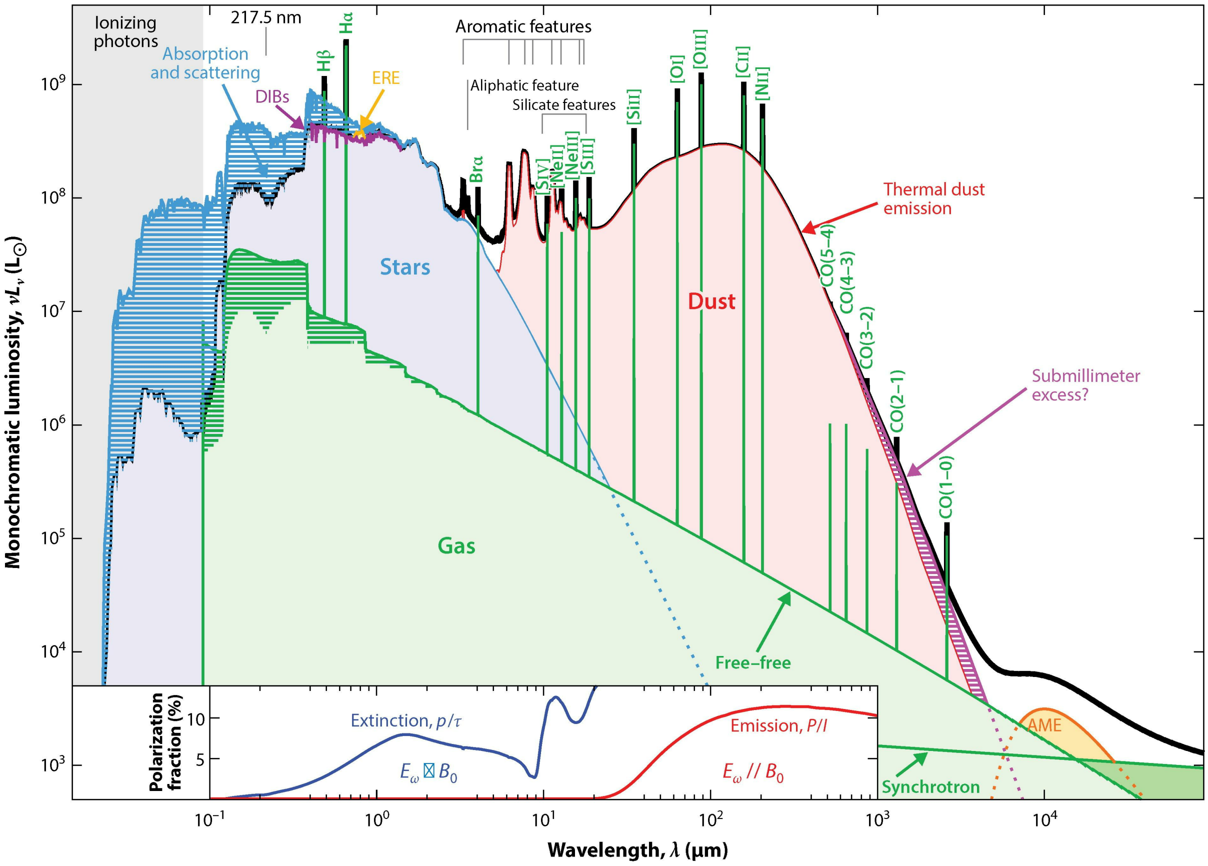

Fig. 1.3 Example of the spectral energy distribution of a galaxy, and the emission from various components of the ISM (atomic and molecular gas, and dust), and stars. *Figure credit: Fig. 1 in Galliano et al. 2018.*

ent wavelength ranges (see Fig. 1.2, 1.3, and 1.7). The importance of the ISM lies in the fact that it directly affects the formation of stars within galaxies, thus affecting their mass distributions, evolution, chemical stellar and gas-phase abundances (stellar and nebular metallicity), and their light emission. The ISM could be regarded as *anything* between the stars, such as interstellar gas and dust, cosmic rays (CR), electromagnetic radiation and interstellar magnetic fields, interstellar gravitational fields, and the dark matter field particles (Tielens 2005; Draine 2011c). In this thesis, our research will concentrate on some of the *baryonic* ISM that does not exceed temperatures greater than 10^4 K. The full list of the ISM constituents is well described in the general literature about the ISM (Ferrière 2001; Tielens 2005; Draine 2011c). The phases of the ISM used in this thesis are:

- **ionized gas in HII regions:** This hot gas (atoms and electrons) is photo-ionized by UV photons from young O/B stars in star-forming regions (HII regions). It reaches temperatures around 10^4 K, densities around $10^4\ \mathrm{n_H\,cm^{-3}}$, and galactic physical scales up to 10-100 pc (which is a size of HII regions and HII associations). It cools via optical emission lines (Lyman-Balmer-Paschen series, and other emission lines), fine-structure lines, and via free-free emission in the sub-mm and radio wavelength range. This cooling emission is used to observe the ionized gas (see Fig. 1.3 and 1.7). Similar to the gas in HII regions, gas ionized by pulsars, white dwarfs and supernovae (SN) is found in planetary nebulae and SN remnants.

- **Warm ionized medium or diffuse ionized gas (WIM or DIG):** This photo-ionized gas is similar to the gas in HII regions, but with lower densities ($0.3\ \mathrm{n_H}\,\mathrm{cm}^{-3}$), higher temperatures, and probing large physical scales of a few kpc (Haffner et al. 2009). It may originate from photo-ionization in HII regions, the older stellar population, CRs or dust (for details see Sec. 2.4.2.1).
- **Dust:** Small solid particles (less than or a few $1\,\mu$m in size) made of complex molecules, primarily based on silicates and carbonaceous material, and compose around 1% of the galactic ISM (Draine & Li 2007; Draine 2011c; Kennicutt & Evans 2012). Dust is heated by the interstellar radiation to temperatures from 10 K (far from HII regions) to a few hundred K (in HII regions). It re-radiates this energy in the infra-red and (sub-)mm (see Fig. 1.3), in the form of black body radiation and emission lines (Draine & Li 2007; Draine 2011c; Draine et al. 2014). It attenuates (combined effects of absorption and scattering) the stellar light, mostly at shorter ($\lambda < 2\,\mu$m) wavelengths (Cardelli et al. 1989; Calzetti et al. 1994; Gordon et al. 2003; Clayton et al. 2015).
- **Diffuse cold molecular gas (bulk of the molecular gas):** The molecular gas is composed of molecules with two or more atoms, of various compositions (H_2, CO, etc.). It is relatively cold (≈ 50 K), and dense ($100\ \mathrm{cm}^{-3}$), and is mostly heated by the photo-ionization from young stars, CRs (Schinnerer et al. 2013), or by photo-electrons from dust. It mostly cools by emitting rotational lines in the infra-red and sub-mm wavelength range (Tielens 2005; Draine 2011c). In the case of H_2 molecules, the dust grains help its chemical formation (on the dust grain surfaces), and shield it from hazardous high-energy radiation. H_2 was directly detected for the first time through UV absorption features in spectra from hot stars (Ferrière 2001). Due to the quantum states of the electrons, direct observations of H_2 rotational lines is difficult, and therefore this molecule is observed by proxy, through emission from the rotational transition of the CO molecule (see Fig. 1.3). For that, a certain H_2-to-CO conversion factor ($\mathrm{X_{CO}}$ or α_{CO}) between emission from CO molecules and H_2 mass is assumed (Bolatto et al. 2013). However, this factor may decrease in the regimes of higher metallicities, higher gas densities (that usually occur in galactic centers) and higher ionization parameters[3], due to a decrease in the dust density (Bolatto et al. 2013; Narayanan et al. 2012). The cold molecular gas is mostly observed by (sub-)mm facilities.
- **Dense molecular gas:** The dense molecular gas is mostly probed by more complex molecules (HCN, HCO^+, HNC, ^{13}CO, C^{18}, etc.). It traces more dense ($10^3 - 10^6\ \mathrm{cm}^{-3}$)

---

[3] The ionization parameter $\mathcal{U} = n_\gamma/n_{\mathrm{H}}$ is the ratio of ionizing photon density to hydrogen density (Yeh & Matzner 2012).

and cooler (10-50 K) regions where star-forming clumps and cores reside, within which new stars are formed.

It is worth noting that there is an elegant connection between star formation (SF) and the ISM components listed above. The collapsing gas, well traced with the molecular gas, acts as fuel that forms stars. The newborn massive stars then ionize the surrounding (atomic) gas, and heat the dust particles. The ionized gas and the heated dust particles then emit in the optical and IR (lines and continuum). This connection is used for the estimation of star formation rates (SFR; see Sec. 1.3).

1.1.3 Star formation through cosmic time

In the last two decades of advancement in astronomical instrumentation and observations, multiple surveys (Carilli & Walter 2013; Madau & Dickinson 2014) probed the sky more deeply (with higher brightness sensitivity), with a wide range of multiwavelength data (from X-ray to radio), and at various redshifts. Examples of these surveys include: the Hubble deep field North (HDF-N; Williams et al. 1996), the Hubble Ultradeep Field (HUDF; Beckwith et al. 2006), the Great Observatories Origins Deep Survey (GOODS; Giavalisco et al. 2004), the Cosmic Evolution Survey (COSMOS; Scoville et al. 2007), etc. The purpose of these surveys was to estimate the parameters of galaxy formation and evolution through cosmic time, including the history of star formation, metal enrichment, and gas fractions.

It was found that the SFR density peaked at z$\approx$ 2 (corresponding to 3.5 Gyr after the Big Bang; Shapley 2011; Madau & Dickinson 2014; Robertson et al. 2015), and declined exponentially since then (see Fig. 1.4). About 25% of the current stellar population was formed before the peak of the cosmic SFR density, and another 25% formed after z=0.7 (Madau & Dickinson 2014). Furthermore, the accretion of the central, super-massive black holes in galaxies was found to follow the growth in SFR, thus offering evidence of co-evolution between galaxies and massive black holes (Madau & Dickinson 2014). Due to the chemical enrichment of the ISM from stellar feedback, the overall solar and gas-phase metallicity of the universe increased with time (Fig. 1.4). The high gas-to-stellar mass ratio (≈ 1) at $z > 1$ indicates that the increase and the peak in the cosmic SFR happened while cold gas was dominant in galaxies. In the early universe ($z > 1$), the increase in metallicity boosted dust production, which led to an increase in molecular gas density. These increases in the total gas and molecular clouds triggered higher SFRs. Later in time, that ratio decreased due to gas depletion through SF (van den Bergh 1957), thus lowering the overall SFR density, gas-to-stellar mass fractions, and the overall molecular gas volume density (as seen in Fig. 1.4). However, there are still large uncertainties in observations of molecular gas at high redshift. This may explain the large discrepancies between observed data from different surveys, as seen in the lower right panel of Fig. 1.4. Due to disagreements between different observations of the molecular gas fraction, it

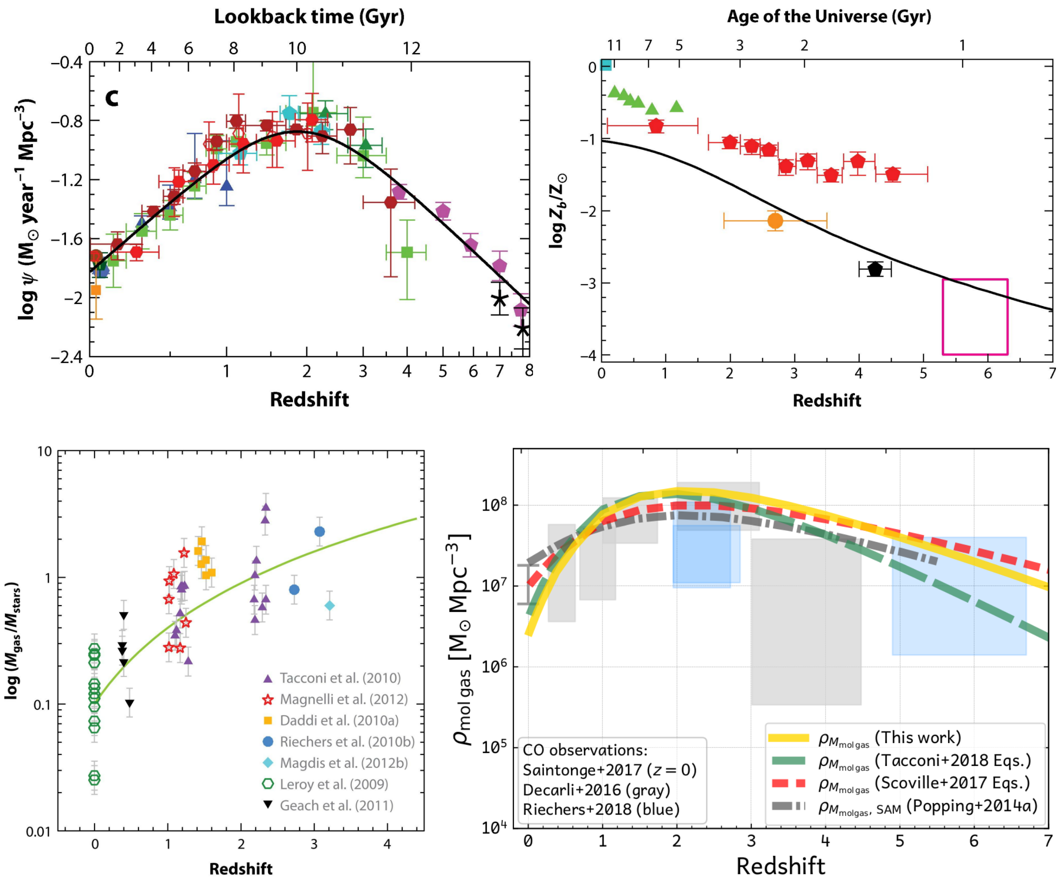

Fig. 1.4 Star formation, metallicity, gas-to-stellar mas ratio and molecular gas density through cosmic time. The data are labeled with symbols, and the theoretical models with lines.

Upper left- The star formation rate density of the universe, using various surveys' data and tracers (UV and IR). *Figure credit: Fig. 9 in Madau & Dickinson (2014).*

Upper right- Stellar metallicity through cosmic time. *Image credit: Fig. 14 in Madau & Dickinson (2014).*

Bottom left- Gas to stellar mass ratio through cosmic time. *Figure credit: Fig. 9 in Carilli & Walter (2013).*

Bottom right- Volume density of the molecular gas in the universe through time. Lines are theoretical fits from observational data by Liu et al. (2019, in prep.), Popping et al. (2014), Scoville et al. (2017), and Tacconi et al. (2018). Variations between observed data are due to the depth (sensitivity) of the CO brightness observations. *Figure credit: Liu et al. (2019, in prep.).*

is not clear if the diminishing gas fraction is the sole cause of the declining SFR through the cosmic time (Genzel et al. (2015)), or if changes in both the gas fraction and the star formation efficiency decreased the SFR (Scoville et al. (2016)).

1.2 The Star Formation law

There is a clear correlation between the gas within the galaxies and the rate of star formation, which consumes and thus depletes that gas reservoir (see Fig. 1.5). Schmidt (1959) proposed a power-law relationship between the gas and SFR volume densities, with a positive power-law index N (Eq. 10 in Schmidt 1959). Translated into observable quantities, this relation (Kennicutt 1998) behaves as:

$$\Sigma_{\rm SFR} = {\rm K} \cdot \Sigma_{\rm gas}^{\rm N} \,, \tag{1.1}$$

where $\Sigma_{\rm SFR}$ and $\Sigma_{\rm gas}$ are SFR and gas surface densities, and K an empirical constant. Both constant K and index N are determined by an interplay between the stars and gas.

The constant K may indicate an efficiency of converting interstellar gas into stars per freefall time of a cloud. On the other hand, variation in the index N may be caused by different regimes of the GMCs, which trigger SF. Previous observations of SF laws probed a wide range of GMCs and SFRs, at different scales (from small clouds to galactic values), and in different galactic environments (galactic centers, spiral arms, etc.), which resulted in various interpretations of their effects on the SF law. It is not clear whether variations in observed SF laws are due to different circumstances (gravitational instabilities, mid-plane pressure, supersonic turbulence, magnetic fields), or are sensitive to large-scale galaxy properties rather than local properties (galactic rotation period), or depend on different high density thresholds (Toomre & Toomre 1972; Leroy et al. 2008; Kennicutt & Evans 2012; Krumholz et al. 2012, and references within).

Kennicutt (1998) noticed that the SF law could be well described with the galactic rotation period ($\Sigma_{\rm SFR} \propto \Sigma_{\rm gas}/\tau_{\rm dyn}$; Eq. 6 in their work). On the other hand, Krumholz & McKee (2005) and Krumholz et al. (2012) postulated $\Sigma_{\rm SFR} \propto \Sigma_{\rm gas}^{\rm N}/\tau_{\rm ff}$ (Eq. 2 in their work), where ${\rm N} \approx 0.7 - 1$ and $\tau_{\rm ff}$ is the freefall time of GMCs, which behaves as $\tau_{\rm ff} \propto \Sigma_{\rm gas}^{-0.5}$. This indicates that gravitationally bound GMCs will convert their gas into stars over the freefall time of individual gas clouds, independently of the galactic rotation period. Krumholz & McKee (2005) found that only 1% of the mass of a virialised GMC would be over-dense enough to form stars, thus indicating a universal star formation efficiency for all clouds (Krumholz et al. 2012). Salim et al. (2015) noted that previous theoretical models take only average densities of the clouds, and neglect density variations within them. Therefore, they prescribe a new SF law with a multi-freefall parameter dependant on the Mach number (Eq. 10 in their work). Another caveat for determining a universal SF law is the difference between using neutral HI, molecular, dense molecular or total cold (HI and molecular) gas. In the case of total gas, then the index N is expected to be N$\approx 1.5 - 2$ (Madore 1977). In the case of low mass galaxies (where the HI dominates), the index N significantly increases (up to a factor of 4).

The importance of empirical observations of the SF law is to precisely estimate which physical processes lead to variation in the K and N parameters mentioned above, and to allow theoretical astronomers to include better initial assumptions in their models of star formation in galaxies (Li et al. 2006; Tasker & Bryan 2006; Wada & Norman 2007; Bush et al. 2010).

1.2.1 Observations and efficiency of star formation

When nearby galaxies are observed, a clear spatial correlation between the gas (especially the molecular gas) and the star-forming regions is seen (see Fig. 1.5), as predicted by the SF law.

A nice representation of the SF behaviour of observed data is presented in the $\Sigma_{\rm SFR}$ vs. $\Sigma_{\rm gas}$ diagram (Kennicutt & Evans 2012), also known as the Kennicutt-Schmidt diagram, shown in Fig. 1.6. When the total cold gas is used for the Kennicutt-Schmidt diagram, there are three main regimes: 1) the HI dominated regime (low total gas density, $\Sigma < 10\,\rm M_{\odot}pc^{-2}$), with a low SF efficiency, and no correlation between the SFR and gas, 2) the H_2 dominated regime (high total gas densities, $\Sigma > 200\,\rm M_{\odot}pc^{-2}$), mostly with star-burst galaxies, and with higher SF efficiency, and 3) the intermediate regime (intermediate total gas densities), with normal spiral galaxies, where nether HI nor H_2 dominate. Schruba et al. (2011) and Leroy et al. (2013) found that the bulk of the molecular gas (H_2), which traces denser gas regions than HI, correlates better with SFR than the HI gas. However, at higher molecular gas mass densities, estimation of the molecular gas becomes more uncertain due to the dependence of $\rm X_{CO}$ on the environment, such as gas phase metallicity, ionization parameter and optical thickness of the gas (Bolatto et al. 2013). Compared to the bulk of the molecular gas, tracers of the dense molecular gas show a better correlation and smaller scatter across the entire range of physical scales, from individual clouds to galactic scales (Bigiel et al. 2016).

Schmidt (1959) observed various objects (HII regions and HI clouds) in the Milky Way and derived index N=2-3 for the SF regions perpendicular to the galactic plane, N=2 by using the white dwarfs, and N>=2 if HI gas is considered. Sanduleak (1969) and Hartwick (1971) conducted the first observations of the SF law in nearby galaxies and obtained N=1.8 (Magellanic clouds) and N=3.5 (the Andromeda galaxy) when molecular gas is used. In the following years, many other observations of SF were conducted in the Milky Way, nearby galaxies, and high redshift galaxies, which resulted in N varying between 0.5 and 3.3, depending on the objects observed and the gas tracers used (Hamajima & Tosa 1975; Kennicutt 1998; Wong & Blitz 2002; Heyer et al. 2004; Misiriotis et al. 2006; Bigiel et al. 2008; Blanc et al. 2009; Fukui & Kawamura 2010; Schruba et al. 2011; Shapley 2011; Leroy et al. 2013; Vutisalchavakul et al. 2016 and references within). Kennicutt (1998) found N to be around ≈2.5 (≈1.4) for a sample of spiral galaxies (composite of spiral and starburst galaxies), in the case of molecular gas. On the other hand, Schruba et al. (2011) and Leroy et al. (2013) estimated N≈1 in the HERACLES

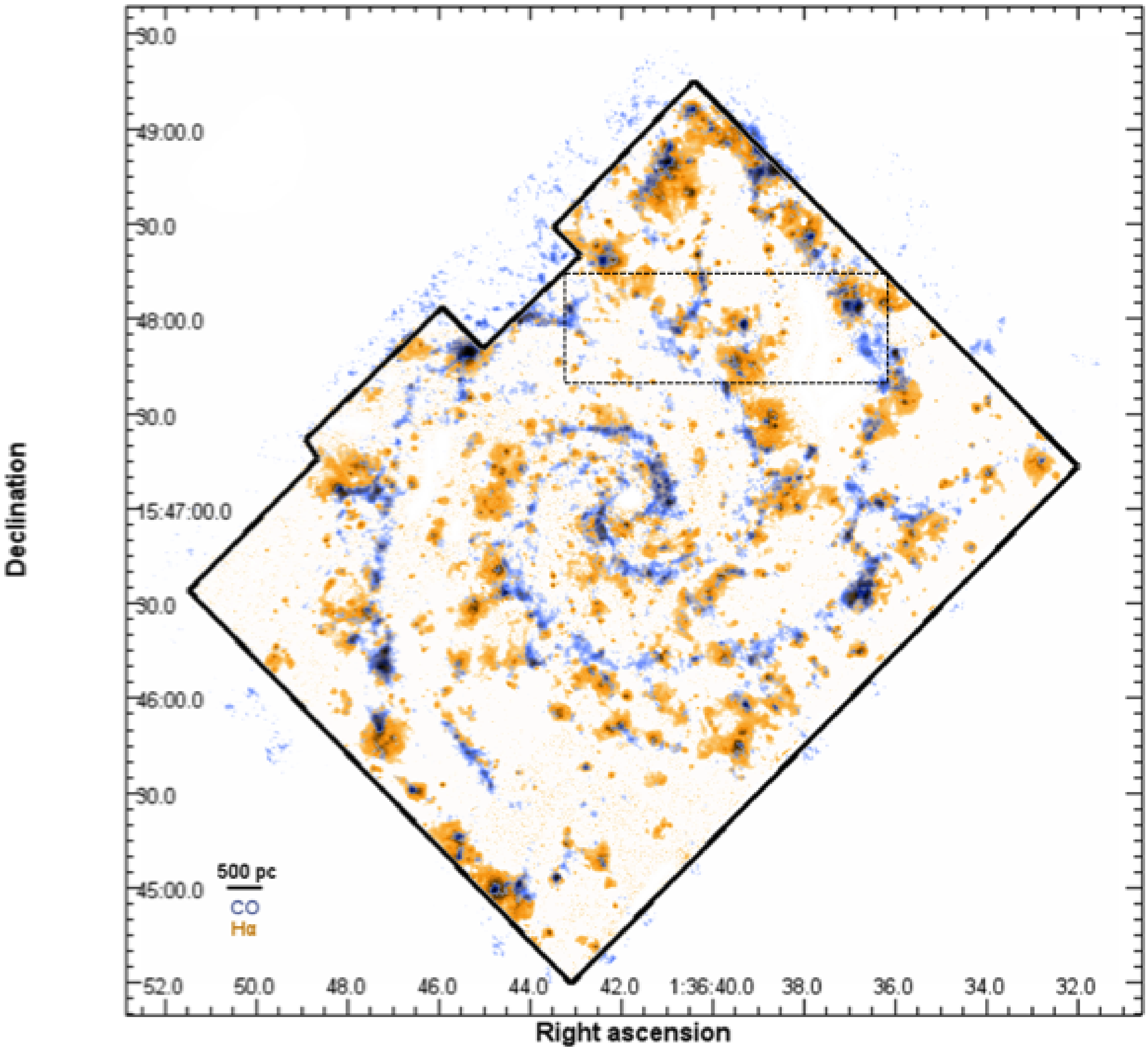
30.0
49:00.0
30.0
48:00.0
30.0
15:47:00.0
30.0
46:00.0
30.0
45:00.0
Declination
52.0
50.0
48.0
46.0
44.0
42.0
1:36:40.0
38.0
36.0
34.0
32.0
Right ascension
500 pc
CO
Hα

Fig. 1.5 The CO(2-1) molecular emission (blue) and Hα (orange) intensity maps cover the central star-forming disk of NGC 628 at 50 pc resolution. Giant molecular clouds (GMCs; represented by the CO line) and star-forming HII regions (evident by their Hα flux) are clearly resolved into discrete structures, which are closely associated. *Figure credit: Fig. 1 in Kreckel et al. (2018)* .

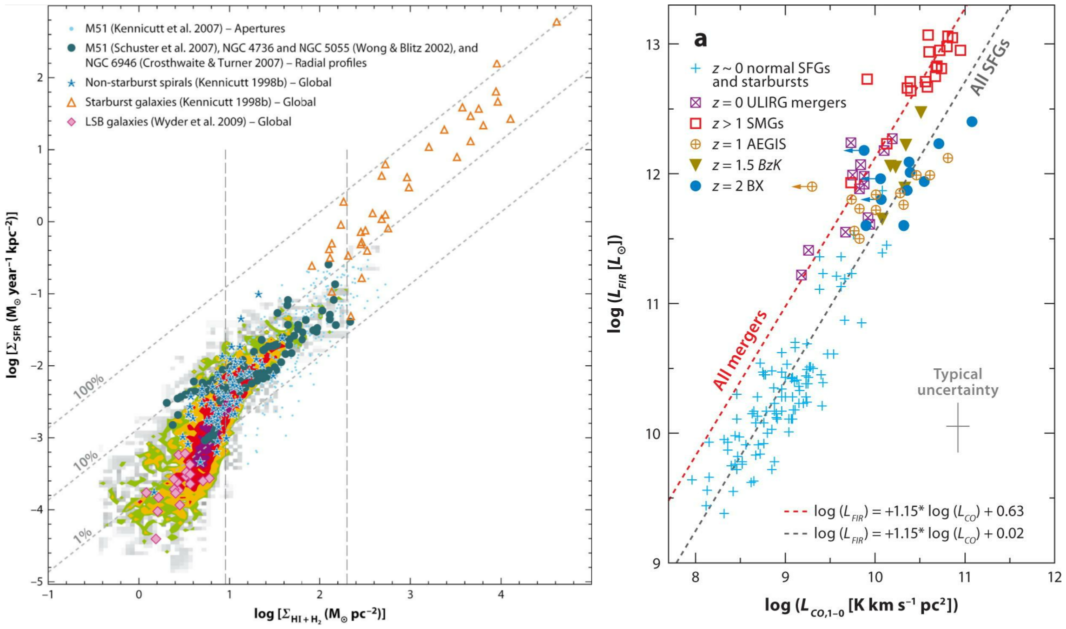

Fig. 1.6 The Σ_{SFR} vs. Σ_{gas} diagram, also known as the Kennicutt-Schmidt diagram, of various surveys of galaxies. *Left-* Here, the gas used is the total (HI+H_2) gas. There are three main regimes (separated by vertical lines) seen on the diagram: 1) the HI dominated regime (low total gas density), 2) the H_2 dominated regime (high total gas densities), and 3) the intermediate regime (intermediate total gas densities). Image credit: Fig. 12 in Kennicutt & Evans (2012). *Right-* The IR (as proxy for SFR) vs. molecular gas of high redshift galaxies. Galaxy mergers show a clear separation from the rest of the galaxies. *Figure credit: Fig. 14 in Shapley (2011).*

and THINGS surveys of normal star-forming, spiral galaxies, also using molecular gas. The N index drastically increases when using HI gas. Similarly, Gao & Solomon (2004) reported N≈1 when they use dense molecular gas traced by HCN instead of CO traced gas.

The ratio between H_2 mass and SFR yields the depletion time of the H_2 gas, i.e. the time needed to deplete the molecular gas reservoir assuming that the current SFR is constant, $\tau_{\mathrm{depl}} = \mathrm{M_{H_2}/SFR}$. Similarly, the ratio of SFR over H_2 mass gives the star formation efficiency ($\mathrm{SFE} = \mathrm{SFR/M_{H_2}}$). As seen on the Kennicutt-Schmidt diagram, a characteristic τ_{depl} of 1-2 Gyr is observed for local normal star-forming disk galaxies on the main-sequence (Saintonge et al. 2011; Leroy et al. 2013). Local interacting starburst galaxies (Klaas et al. 2010; Nehlig et al. 2016; Saito et al. 2016) and ultra-luminous infrared galaxies (LIRGs, ULIRGS; Saintonge et al. 2011; Martinez-Badenes et al. 2012) exhibit a higher SFE, and a lower systematic τ_{depl} of 0.05-0.8 Gyr (see both panels in Fig. 1.6).

1.2.2 Effects of environments and interaction

One of the main goals in the research field of star formation is to investigate what is triggering and controlling the level of star formation, what changes the SFE and τ_{depl} in GMCs and galaxies, and whether there is a combination of tracers of SFR and gas that universally describes astronomical objects across *all* spatial scales.

Theoretical astronomy shows that the gravitational collapse of GMCs and stellar feedback (SNs, stellar winds, etc.) exert additional forces, and may trigger SF and add to the variation in SFE. There is increasing evidence that both internal and external galactic dynamics also affect the SFRs and SFEs (Kennicutt et al. 1987; Meidt et al. 2013; Sivanandam et al. 2014; Renaud et al. 2014; Moreno et al. 2015). An example of internal dynamical processes is gravitational torques caused by galactic stellar structures, which have been observed to modify $\tau_{\rm depl}$ in the spiral arms of M51 (Steinhauser et al. 2012; Meidt et al. 2013). Recently, observations of interacting galaxies in clusters and groups have provided evidence that external dynamical forces, such as tidal forces and ram pressure, also affect the ISM and stellar distribution of host galaxies, thus affecting their evolution and their SFR (Dressler 1980; Kennicutt et al. 1987; Iglesias-Paramo & Vilchez 1997; Cortese et al. 2007; Bekki 2014; Renaud et al. 2014; Bournaud et al. 2015; Poggianti et al. 2017). For example, SF can be enhanced by galactic collisions and tidal gravitational forces (Toomre & Toomre 1972; Kennicutt et al. 1987; Shapley 2011; Sivanandam et al. 2014; Renaud et al. 2014; Rodríguez-Baras et al. 2014; Renaud et al. 2015; Saito et al. 2015), as seen in both observations and simulations of interacting galaxies in groups. This is easily seen in Fig. 1.6, where galactic mergers and starburst galaxies (supposedly evolved from those mergers) show higher SFE than normal disk galaxies.

1.3 Estimation of star formation rates

To test and derive the proper star formation law and its dependence on physical processes acting on the ISM, good observations and estimates of SFR and gas surface densities are needed. The correct estimation of gas density, and the usage of proper gas tracers, have their own caveats and uncertainties, but this topic is beyond the scope of this work. Rather, here we will concentrate on properly estimating SFR values in nearby galaxies.

In recent decades, there have been large improvements in the diagnostic methods and calibrations for measuring the SFRs in nearby galaxies. These improvements include: higher brightness sensitivity of new instruments and facilities, reduction of the uncertainties on fluxes of the SFR tracers, improved estimation of the attenuation of light, better methodologies of measuring the SFRs, better assumptions of the stellar initial mass function (IMF), probing higher angular resolutions, etc. (see Kennicutt & Evans 2012). Here, we describe in detail the existing uncertainties and biases in estimating SFRs.

To estimate the proper rate of star formation, astronomers exploited the connection between the newly born stars and the effects that these stars have on their surrounding ISM. Young, massive stars ionize the surrounding gas and heat the surrounding dust, and non-attenuated light from these stars directly reaches the observers. The following methods are routinely used to estimate the SFRs.

1.3.1 Direct stellar tracers

There are multiple ways to determine the SFRs from direct stellar light. Each method has its own benefits and drawbacks.

The first method is to directly count young, massive stars (young stellar objects, YSO; Lada et al. 2010) that reside in young stellar clusters, and are observed by optical and IR ground-based and space-based facilities (Lada et al. 2010). Assuming the mean age of those objects, it is possible to estimate the SFR at recent times (a few Myrs). There are a few drawbacks to this method. It is only possible to apply this method for nearby star-forming clouds (within the Milky Way), but not for nearby galaxies, given constraints by the spatial resolution (making it impossible to distinguish individual stars) and brightness sensitivity (stellar flux depends on distance). Moreover, this counting method does not account for all of the stars, because lower mass stars have lower flux, which may not be observed due to the sensitivity of the instruments. This problem could be solved if the initial mass function (IMF) of the entire cluster is taken into account, assuming that the entire cluster is formed at the same time (Kroupa 2001). Lastly, this method does not provide the full picture of the SF history (SFH), due to YSOs being short-lived (only a few Myrs).

Another direct method of estimating the SFRs is measuring UV-optical-IR emission from multiple stellar clusters or multiple stars within a single cluster, and fitting isochrones to a color-magnitude diagram, thus deriving the masses and ages of stars and the SFH of the region. This method is used by Lewis et al. (2015) and Fouesneau et al. (2014) to derive the SFH of regions in the Andromeda galaxy (M31), using Hubble space telescope (HST) images. A drawback of this method is the uncertainty in the fitting of the isochrones, which needs to account for both the stellar cluster age and the unknown extinction of the stellar light. The extinction of the stellar light has a similar effect on the color-magnitude diagram as the cluster having a higher age.

The third method is measuring direct UV emission, which comes from young massive stars with ages up to few hundred Myrs (Calzetti et al. 1994; Kong et al. 2004; Leroy et al. 2008; Hao et al. 2011; Thilker et al. 2005; Kennicutt & Evans 2012). Assuming a general IMF for the stars and an attenuation of the UV light, it is possible to derive how many stars were produced recently. If the far-UV (FUV) emission is observed, the SFH could be traced up to the last 100 Myrs, which is the age of stars that emit in the FUV. If near-UV (NUV) emission is used, the SFH within up to a few hundreds of Myrs could be deduced. However, the main caveat of this method is that the estimated attenuation needs to be accurate because the UV is very sensitive to extinction. Unfortunately, the extinction and its systematic uncertainty is highest at these short wavelengths (see Sec. 1.3.3). Furthermore, estimating attenuation from the FUV-NUV ratio has an intrinsic high uncertainty (Calzetti et al. 1994; Kong et al. 2004; Salim et al. 2007; Hao et al. 2011; Kennicutt & Evans 2012). The assumption of a specific spatial geometry and distribution of the dust and stars along the line of sight may be incorrect, which can highly af-

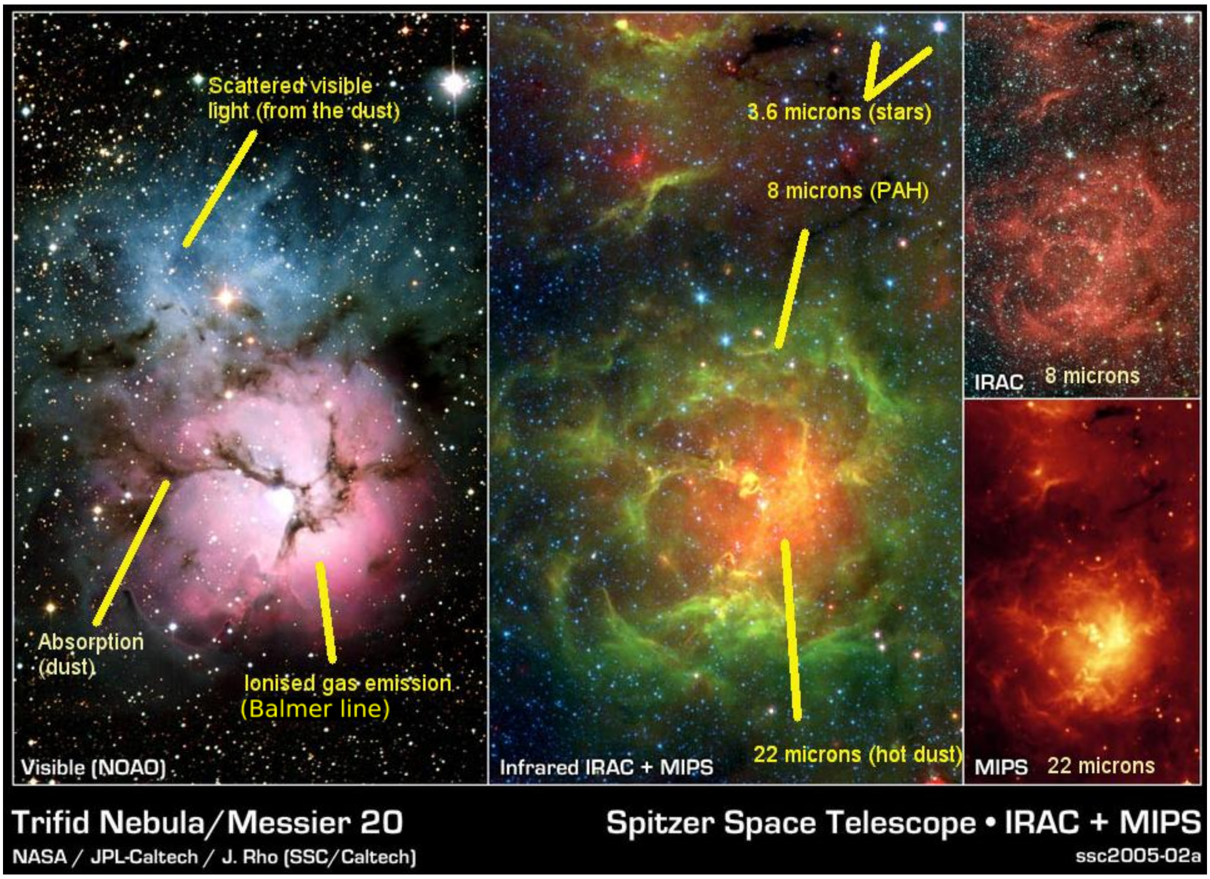
Scattered visible light (from the dust)
Absorption (dust)
Ionised gas emission (Balmer line)
Visible (NOAO)
3.6 microns (stars)
8 microns (PAH)
22 microns (hot dust)
Infrared IRAC + MIPS
IRAC 8 microns
MIPS 22 microns
Trifid Nebula/Messier 20
NASA / JPL-Caltech / J. Rho (SSC/Caltech)
Spitzer Space Telescope • IRAC + MIPS
ssc2005-02a

Fig. 1.7 The Trifid nebula (M20) seen in various SFR tracers: optical (with prominent Hα emission in red), 8 μm (tracing the PAH dust molecules), and 22 μm (tracing hot dust). The image also shows dust features in the forms of the scattered visible light and absorbed features. *Image credit: NOAO (visible), Spitzer (IR), IRAC (IR), and MIPS (IR) by J. Rho (Caltech), JPL-Caltech, and NASA.*

fect the implied attenuation value (see Chap. 2, and Calzetti et al. 1994). The second caveat is the fact that the older stellar population (spectral types B and A) partly contributes to the FUV continuum. The extinction of UV spectra also has a similar effect as probing the older stellar populations, which may affect the estimation of SFRs and attenuation. Lastly, the uncertainty in the IMF distribution may also affect the conversion from UV emission to the SFRs (see Eq. 3.2), even if the attenuation and the age of the massive stars are correct.

1.3.2 Ionized gas, dust and synchrotron emission

The main benefit of using the optical and IR emission from ionized gas and dust is that they are less sensitive to attenuation than UV emission, and lie spatially close to the young stars (Fig. 1.7). In the case of the IR emission, extinction is negligible.

Most of the ionized gas emission (continuum and emission lines) is spatially correlated with the massive young stars in the OB associations in HII regions (see Fig. 1.7), which live up to 5-10 Myrs (Kroupa 2001; Leroy et al. 2008). While its optical continuum is relatively weak compared to the background stellar continuum in the galaxies, its emission lines are noticeably strong (see the example of M31's spectra in Fig. 2.2). These emission lines from various elements and their ratios are governed by the laws of quantum physics, and are set by the gas temperatures, densities, chemical abundances, and attenuation (Tielens 2005; Draine 2011c; Dopita et al. 2016). Due to reddening and attenuation (effect of scattering and absorption, see Sec. 1.3.3) of those lines, the observed ratios differ from the intrinsic ratios expected from quantum physics. Using the ratios of the *observed* emission lines from the same elements, such as the hydrogen emission lines (Lyman, Balmer, Paschen, or Brackett series), and assuming a certain extinction curve plus the dust and gas distribution along the line of sight, enables the determination of the non-attenuated line emission from the HII regions. This could be applied only if we know the exact intrinsic line ratios, which for HII regions is well constrained **[to] for** the typical temperatures (at 10^4 K) and densities of gas of $10^4\ \mathrm{n_H\,cm^{-3}}$.

Once the non-attenuated line emission from HII regions is deduced, the SFRs could be estimated assuming a typical IMF of the stellar clusters and assuming a fraction of ionization of the hydrogen atoms (see Sec. 3.3). Mostly emission lines from the ionized hydrogen (HII) are used, as they are usually brighter than the lines from other elements. The main caveat of this method is the biases from assuming the dust/gas distribution and extinction curves. The second largest drawback of using ionized gas emission is the contribution of a high fraction (30%-60%) of the diffuse gas emission (DIG) observed in nearby galaxies (Leroy et al. 2008; Haffner et al. 2009). It is not yet clear if the DIG emission originates from ionizing photons from the HII regions or from the older stellar population (see Sec. 2.4.2.1), and therefore it is not clear if this emission should be subtracted from or included in the SFR calculation (Rand 1996; Haffner et al. 2009; Blanc et al. 2009; Leroy et al. 2012). Last but not least, emission lines are accompanied by corresponding stellar absorption lines. In the case of photometric measurements of these lines, this is not accounted for, while in the case of spectroscopy this can hinder precise line flux fitting.

The ionized gas continuum emission could be also traced by free-free[4] emission with the mm-to-radio facilities (see Fig. 1.3, and Murphy et al. 2011). Caveats of this method are that it is dependent on the gas temperature, assumed IMF, and partly absorbed by the dust (Condon 1992; Schmitt et al. 2006; Murphy et al. 2011). Most importantly, the emission observed could contain contributions from either synchrotron or hot dust in addition to free-free.

Non-thermal synchrotron radiation comes from CR electrons mostly from SNs, accelerated in the magnetic fields of galaxies. If we assume a certain rate of CRs from SNs, and assume a certain number of SNs from the stellar population and IMF, we can estimate a correlation between the SFRs and the synchrotron radiation. Additionally, we can combine both the free-free and synchrotron radiation in order to estimate SFRs (Condon 1992; Murphy et al. 2011).

IR emission from the heated dust around HII regions (see Fig. 1.7) can be used as a tracer of

---

[4] Also known as thermal bremsstrahlung. It is produced by free electrons scattering off of ions without being captured.

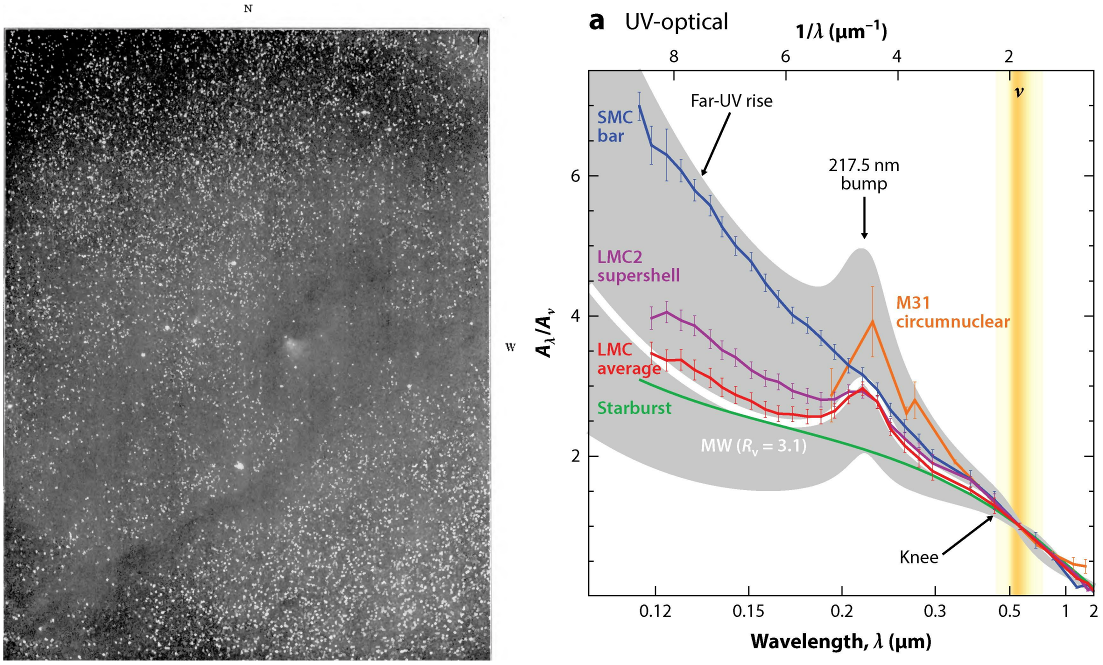

Fig. 1.8 *Left-* A visible image from the Taurus constellation, with noticeable absorption features. *Image credit: Fig. 1 in Barnard (1907). Right-* Extinction curves of the Magellanic clouds (Gordon et al. 2003), compared to the Milky Way (the grey area spans $\mathrm{R_V}$ between 2 and 5 (with the white line at $\mathrm{R_V}$=3.1; Fitzpatrick 1999), attenuation curve of starburst galaxies (Calzetti et al. 2000) and of the circumnuclear region of M31 (Dong et al. 2014). *Figure credit: Fig. 6 in Galliano et al. (2018).*

SF (Calzetti et al. 2000, 2005; Kennicutt et al. 2007; Calzetti et al. 2010; Leroy et al. 2008; Murphy et al. 2011). It is especially useful in the case where the UV-optical light from the young star-forming cluster is highly attenuated due to it being embedded in a dusty cloud (Whitmore et al. 2011; Calzetti et al. 2010; Kreckel et al. 2013). Further emission from polycyclic aromatic hydrocarbon (PAH) can be used as a tracer of the SFRs (Calzetti et al. 2010; Kennicutt et al. 2011; Jarrett et al. 2013). However, the IR emission alone does not account for the entire SFR, as not all of the light from young stars is absorbed by dust. In addition, it can be contaminated by diffuse IR emission coming from dust that is heated by the older stellar population, also known as 'IR cirrus' (Tielens 2008; Haffner et al. 2009; Leroy et al. 2012; Steinacker et al. 2013). The dust emission is also sensitive to the dust grain sizes and temperatures (Draine & Li 2007; Draine 2011c; Galliano et al. 2018), which change the black body radiation curves in the NIR, MIR, and FIR, and their flux ratios.

1.3.3 Attenuation

The absorption of stellar light in the Taurus constellation (see Fig. 1.8) was the first indication for the existence of the ISM in our galaxy (Barnard 1907). The explanation for the absorption, and also for the scattered light, was found in the dust particles.

The effect of absorption and scattering of the light by dust (example in Fig. 1.7) along a single line of sight is labeled as “extinction” (A_λ). For an initial flux of light F^0_λ, the observed and extincted light (F_λ) behaves as (Eq. 1 and 8 in Calzetti et al. 1994):

$$A_\lambda\,[mag] = 2.5 \cdot \log_{10}\left(\frac{F^0_\lambda}{F_\lambda}\right) \tag{1.2}$$

$$F_\lambda = F^0_\lambda \cdot e^{-\tau_\lambda} = F^0_\lambda \cdot e^{-A_\lambda/(2.5\log_{10}e)} = F^0_\lambda \cdot e^{-(0.921 \cdot A_\lambda)} \tag{1.3}$$

Due to the small sizes of the dust grains ($< 2\,\mu$m) and their chemistry, the effect on the light is more pronounced at shorter wavelengths, resulting in an overall reddening of the light. At longer wavelengths, extinction diminishes ($A_{\lambda\to\infty} \to 0$ mag). The reddening of light in astronomy is usually denoted by the selective extinction E_{B-V} that is equal to $A_B - A_V$. Standard extinction curves are normalised in terms of E_{B-V} as:

$$k_\lambda = \frac{A_\lambda}{A_B - A_V} = \frac{A_\lambda}{E_{B-V}}. \tag{1.4}$$

Conventionally, the ratio of total (A_V) to selective extinction is $R_V \equiv A_V/E_{B-V}$. The shape of the extinction curve and R_V depend on the characteristics (e.g. size, chemical composition) of the dust grains. Fig. 1.8 shows examples of measured extinction curves (Cardelli et al. 1989; Fitzpatrick 1999; Calzetti et al. 2000; Gordon et al. 2003; Draine 2011c), where different galaxies were used, and variations in the curves when R_V varies between 2 and 5 (the typical Milky Way value is 3.1). The extinction curves increase toward shorter wavelengths, and have a strong feature at 2175 Å that corresponds to PAH absorption feature. For example, if two Hydrogen lines for which the intrinsic ratio is known are observed, it is possible to measure the extinction using Eq. 2.2.

Different relative geometrical distributions of the dust and light emitters (ionized gas and stars), affects the observed light differently. Caplan & Deharveng (1986), Witt et al. (1992), Calzetti et al. (1994), Gordon et al. (2003) and Draine (2011a) derived various models for the relative dust/gas distributions and the corresponding effects on the stellar light and observed attenuation.

1.3.4 Hybrid SFR prescriptions

As shown above, various SFR tracers target direct or reprocessed light from short-lived massive, young and luminous stars, such as UV, nebular hydrogen emission lines, IR, and free-free emission (Gao & Solomon 2004; Thilker et al. 2007; Calzetti et al. 2007; Kennicutt et al. 2007; Rieke et al. 2009; Murphy et al. 2011; Herrera-Camus et al. 2015). However, each of these tracers *alone* underestimates the SFR.

If we assume that the entire absorbed light of the SFR tracers is re-radiated through IR emission, combining the obscured (UV and optical) and un-obscured (IR) tracers results in measuring the total SFR (Kennicutt et al. 2003; Calzetti et al. 2005; Wu et al. 2005; Calzetti et al. 2007; Thilker et al. 2007; Tabatabaei & Berkhuijsen 2010; Leroy et al. 2012; Davis et al. 2014; Catalán-Torrecilla et al. 2015). This combination of tracers is often referred to as ”hybrid” SFR prescription, while single tracers are ”monochromatic” prescription.

A key assumption here is that the dust acts as a proxy of local attenuation, and that all absorbed light from the tracers needs to be re-radiated in the IR. Following that, we can connect the IR emission ($\mathrm{S_{IR}}$) with the obscured and un-obscured SFR tracer ($\mathrm{S_\lambda^{obscured}}$, and $\mathrm{S_\lambda^{un-obscured}}$) as an SFR prescription in the following way:

$$\mathrm{SFR} = \mathrm{K} \cdot \left(\mathrm{S_\lambda^{un-obscured}} + \mathrm{S_\lambda^{obscured}}\right) = \mathrm{K} \cdot \left(\mathrm{S_\lambda^{un-obscured}} + \mathrm{a_{IR}} \cdot \mathrm{S_{IR}}\right), \tag{1.5}$$

where K is the conversion factor between the SFR tracer (UV or optical) and the SFR value, and the factor $\mathrm{a_{IR}}$ the SFR calibration factor. One of the major tasks of modern observational astronomy is to empirically estimate the value of $\mathrm{a_{IR}}$ factors for different tracers and at different scales (Calzetti et al. 1994; Kong et al. 2004; Salim et al. 2007; Leroy et al. 2008; Hao et al. 2011; Kennicutt & Evans 2012).

1.3.5 Problem of scales and instruments

In the past, the SFRs in galaxies were estimated using SFR prescriptions that were calibrated for a given population synthesis model, at large spatial scales, and averaged over many galaxies (Kennicutt & Evans 2012). This is problematic due to not being able to distinguish between emission that originates from SF regions and diffuse emission. Moreover, averaging over large scales diminishes our ability to disentangle different physical processes that may affect the SF law. Recently, new surveys have emerged that probe the ISM and the SF at smaller, sub-galactic and sub-kpc scales (Calzetti et al. 2007; Leroy et al. 2008; Blanc et al. 2009; Schruba et al. 2011; Kreckel et al. 2018).

Calibration of the SFR prescriptions in the past was done using images from filters (narrowband and broadband; Kennicutt 1998; Calzetti et al. 1994) on the emission lines and the stellar continuum. However, estimation of the SFRs using this method is hindered by not accounting for underlying absorption lines in stellar spectra. This is improved by the advancement in integral field spectroscopy (IFS; see next section).

1.4 Integral field spectroscopy

Imaging instruments give only 2D spatial information on the sky, while the standard spectroscopic instruments give 1D (single-fiber), 2D (slit) or 3D (slit-less) information from spectra. These techniques require a long time of observation (if images of the specific emission lines are needed), do not provide sufficient information in other dimensions (spatial in the case of slits, or wavelength and velocities in the case of imaging), or give overlapping, low-resolution spectra of multiple objects (in the case of slit-less spectroscopy).

Integral field spectroscopy (IFS; Bacon et al. 1995; Weitzel et al. 1996) uses a combination of a spectrometer and the integral field unit (IFU), which samples individual spatial elements of the astronomical scene. In this configuration, the spectrometer provides the spectral (wavelength) dimension, while the IFU provide the spatial information by bringing the light from different positions on sky through fibers toward the spectrometer. This results in detectors being illuminated by multiple and separate spectra at the same time, where each spectrum comes from a different fiber and thus different sky positions (Bacon et al. 1995; Allington-Smith & Content 1998; Weitzel et al. 1996; Walcher et al. 2014).

There are many types of IFU that use different techniques for splitting the spatial information (see Fig. 1.9; Barden & Wade 1988; Bacon et al. 1995; Weitzel et al. 1996; Allington-Smith et al. 1997; Content 1997; Kenworthy et al. 1998). For example there is **[an] a** fiber bundle (using optical fibers to redirect light from different parts of an observed object), image slicer (using slicing mirrors to redirect the light from different parts of an observed object), and lenslets (using a close packed array of micro-lenses in front of the fibre array). The most commonly used IFUs are: FIFI-LS on SOFIA (Looney et al. 1999), KMOS (Sharples et al. 2006; Davies et al. 2013) , the IFU for the MANGA survey (Bundy et al. 2015), MUSE (Laurent et al. 2006), the PPaK/PMAS (Roth et al. 2005), SAMI (Croom et al. 2012), SINFONI (Eisenhauer et al. 2003), VIRUS-P (Visible Integral field Replicable Unit Spectrograph Prototype; Blanc et al. 2009), ect. This results in various surveys of astronomical objects (e.g. planets, stellar clusters, galaxies, AGNs, etc.).

There are many famous surveys of nearby galaxies that provide scientists with beautiful images of the stellar continuum and nebular line fluxes, and dynamical (velocities, velocity dispersion) information of nearby galaxies. Some of these surveys are the CALIFA survey (Calar Alto Legacy Integral Field Area Survey; Walcher et al. 2014), the PHANGS (Physics at High Angular Resolution in Nearby Galaxies Survey; Kreckel et al. 2018), the PINGS (PPAK IFS Nearby Galaxies Survey;Rosales-Ortega et al. 2010), The SAMI Galaxy Survey (Croom et al. 2012), the SDSS-IV survey with MANGA (Mapping Nearby Galaxies at Apache Point Observatory; Bundy et al. 2015), the VENGA survey (VIRUS-P Exploration of Nearby Galaxies; Blanc et al. 2013), etc. Regardless of the technique used to obtain the data, the final product is a 3D data cube, with two spatial axes and wavelength axis.

In this work, we will primarily use data from the Potsdam Multi-Aperture Spectrophotome-

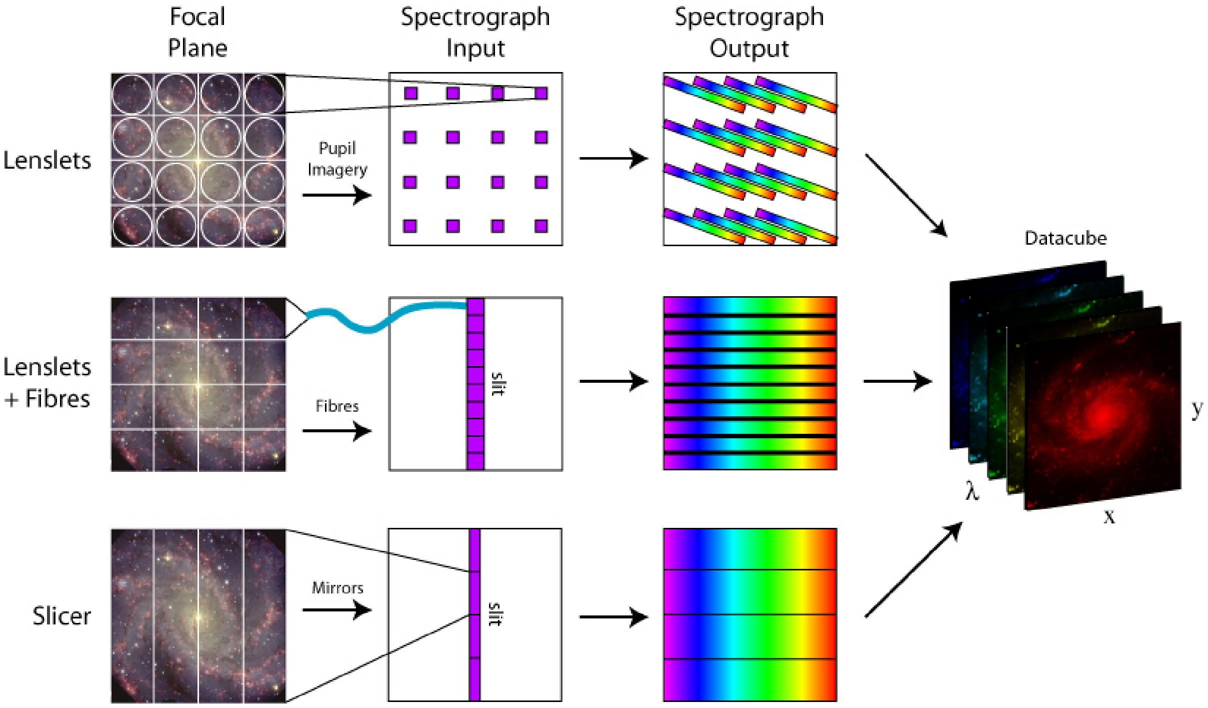
Focal Plane
Spectrograph Input
Spectrograph Output
Lenslets
Pupil Imagery
Datacube
Lenslets + Fibres
Fibres
slit
y
λ
x
Slicer
Mirrors
slit

Fig. 1.9 Examples of ways of splitting the spatial information with an integral field spectrograph (IFS). *Image credit: M. Westmoquette, adapted from Fig. 1 in Allington-Smith & Content (1998).*

ter (PMAS; Roth et al. 2005) and the PPaK fiber bundle at the Calar Alto observatory in Spain. We provide further information about the observations and the data calibration later on (Sec. 2.2.1).

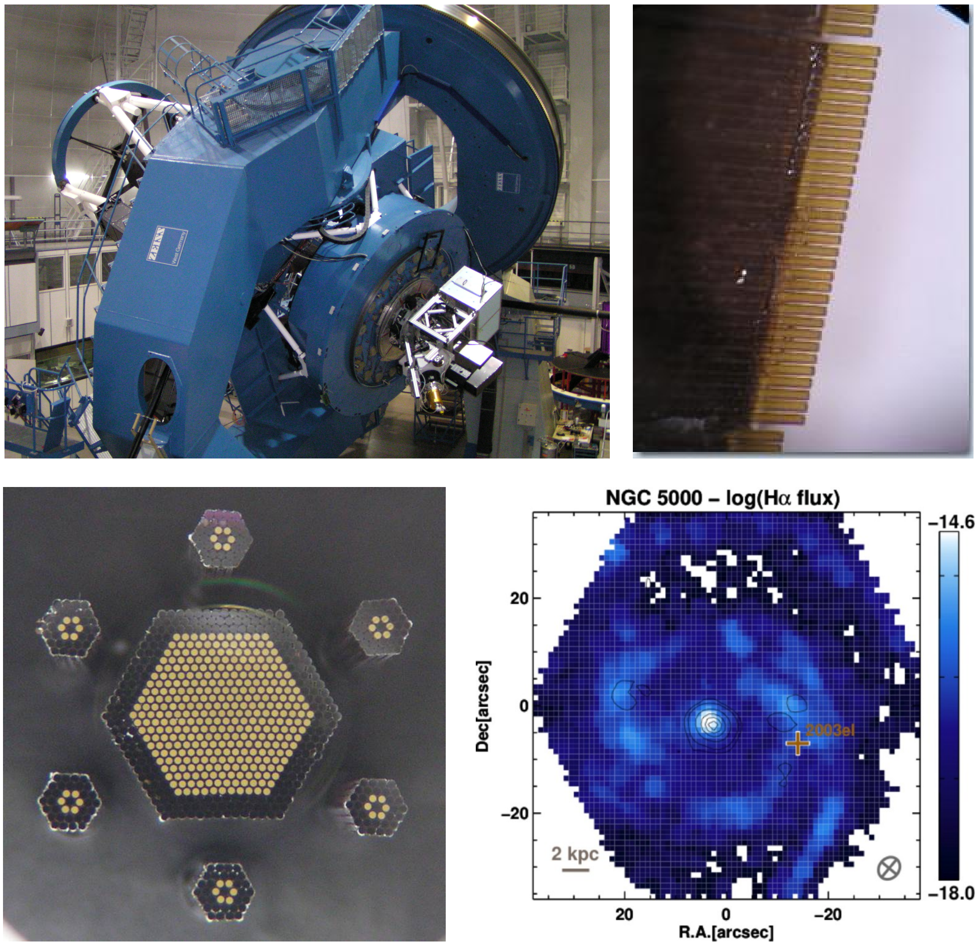

Fig. 1.10 *Upper left-* The 3.5 m telescope at Calar Alto (Spain). *Image credit: Leibniz Institute for Astrophysics Potsdam (AIP).*
Upper right- The fibers of 2.7” are re-arranged from the 2-dimensional configuration in the focal plane, illuminating a spectrograph. *Image credit: Leibniz Institute for Astrophysics Potsdam (AIP).*
Bottom left- Close view on the PPAK integral field unit (IFU) at Calar Alto telescope (Spain), in the 2-dimensional configuration in the focal plane. The central hexagon of fibers are science fibers (for objects of observation), and the surrounding fibers are sky and calibration fibers. *Image credit: Leibniz Institute for Astrophysics Potsdam (AIP).*
Bottom right- Example of a Balmer Hα line flux image of the galaxy NGC 5000, taken by the PPaK IFU. *Image credit: Galbany et al. (2017).*

1.5 Purpose and outlook of this thesis

In order to investigate the behaviour of star formation, and how physical processes such as a galaxy interaction affect the ISM and star formation in galaxies, we need precise measurements of the star formation rates in nearby galaxies. However, there are certain biases, uncertainties, and effects that hamper the estimation of SFR. These are estimations of a correct attenuation, proper assumptions about the relative 3-dimensional (3D) distribution of the dust and gas/stars along the line of sight, biases due to contribution of diffuse emission to the SFR tracers that do not come from star-forming regions, and probing too large spatial scales of the ISM.

To address these issues, in this work we are probing the cold phase of the ISM (ionized gas, dust, and molecular gas) in two nearby galaxies, the Andromeda galaxy (M31) and the interacting galaxy NGC 2276. Their distances enable us to probe the ISM at 10 pc-1 kpc scales, and to test what role spatial scales have when measuring attenuation and estimating SFRs. We are using optical IFU observations of emission lines (specifically the hydrogen Balmer lines) in order to account for underlying absorption features in the stellar spectra, thus obtaining a proper determination of Balmer line attenuation. This will enable us to properly estimate the SFR in nearby galaxies. It also opens the possibility to answer a few questions that may interest both the astronomical and wider scientific communities:

- **What is the dust/gas geometry in nearby galaxies?**
  When SFRs are estimated, usually a certain relative 3D distribution of dust and gas/stars is assumed. However, Kreckel et al. (2013) found by probing nearby galaxies that the dust/gas geometry lies somewhat in between the screen model (previously assumed) and the mixed model. The screen model is the case when the dust screen is between an observer and gas (separated from dust), while the mixed model is the case when the dust and gas are mixed. In Chap 2, we will combine the attenuation derived from the Balmer lines (observed by the IFU) and the dust mass surface distribution in M31, in order to derive the relative 3D dust/gas geometry at small spatial scales (100 pc). This will show if the assumptions about our dust/gas geometry are correct and enable the estimation of SFRs in M31. We will also test how this geometry might change when probing different spatial resolutions.
- **What are SFR prescriptions at small scales?**
  Previous calibrations of the SFR prescriptions in the literature were done at various scales and in different regimes. However, the M31 data offer an opportunity to test these calibrations at even smaller scales (at $\approx$50 pc scales), enabling us to easily distinguish between emission coming from star-forming regions and locations where diffuse emission is. Following our calculation of Balmer line attenuation, in Chap. 3, we use this attenuation to estimate the non-attenuated Hα flux, which is used as our reference SFR tracer. We calibrate our own SFR prescriptions using that SFR tracer, and test how they change with

spatial scales, with subtracting diffuse emission, galactocentric distance and inclination.

- **Are ISM characteristics changed via galactic interactions?**
  Recent and ongoing surveys of interacting galaxies investigate how external forces, such as the tidal force and ram pressure, affect the ISM and galaxies during their interactions. In Chap. 4, we observe the interacting galaxy NGC 2276 at an early phase of interaction, in order to investigate its SFR, stellar distribution, the source of ionization of its gas, diffuse gas fractions, and gas-phase metallicity.
- **Does the Star Formation Efficiency of the gas change in interacting galaxies?**
  Multiple observations and simulations give various answers to the question of whether galactic interactions affect the star formation efficiency of the host galaxy's ISM, and at what phase of interaction. NGC 2276 shows both an elevated and asymmetric SFR. This offers an opportunity to investigate if this is caused by accumulation of molecular gas, or by changes in the SFE of the gas. In Chap. 5, we observe for the first time the bulk of the molecular gas, and combine it with the SFR estimated from IFU data (in Chap. 4).

Each chapter of this thesis will offer answers on these questions. Through this work, I am extensively using figures and work done in multiple peer-reviewed articles, in which I am the first author. These articles are Tomičić et al. (2017), Tomičić et al. (2018), Tomičić et al. (2019), and Tomičić (2019, in prep.).

Chapter 2

“There is a way out of every box, a solution to every puzzle; it’s just a matter of finding it.”

Jean-Luc Picard, captain of USS Enterprise NCC-1701-D
“Attached” by Nick Sagan; Star Trek: The Next Generation

2. Attenuation and the relative dust/gas distribution as seen in M31

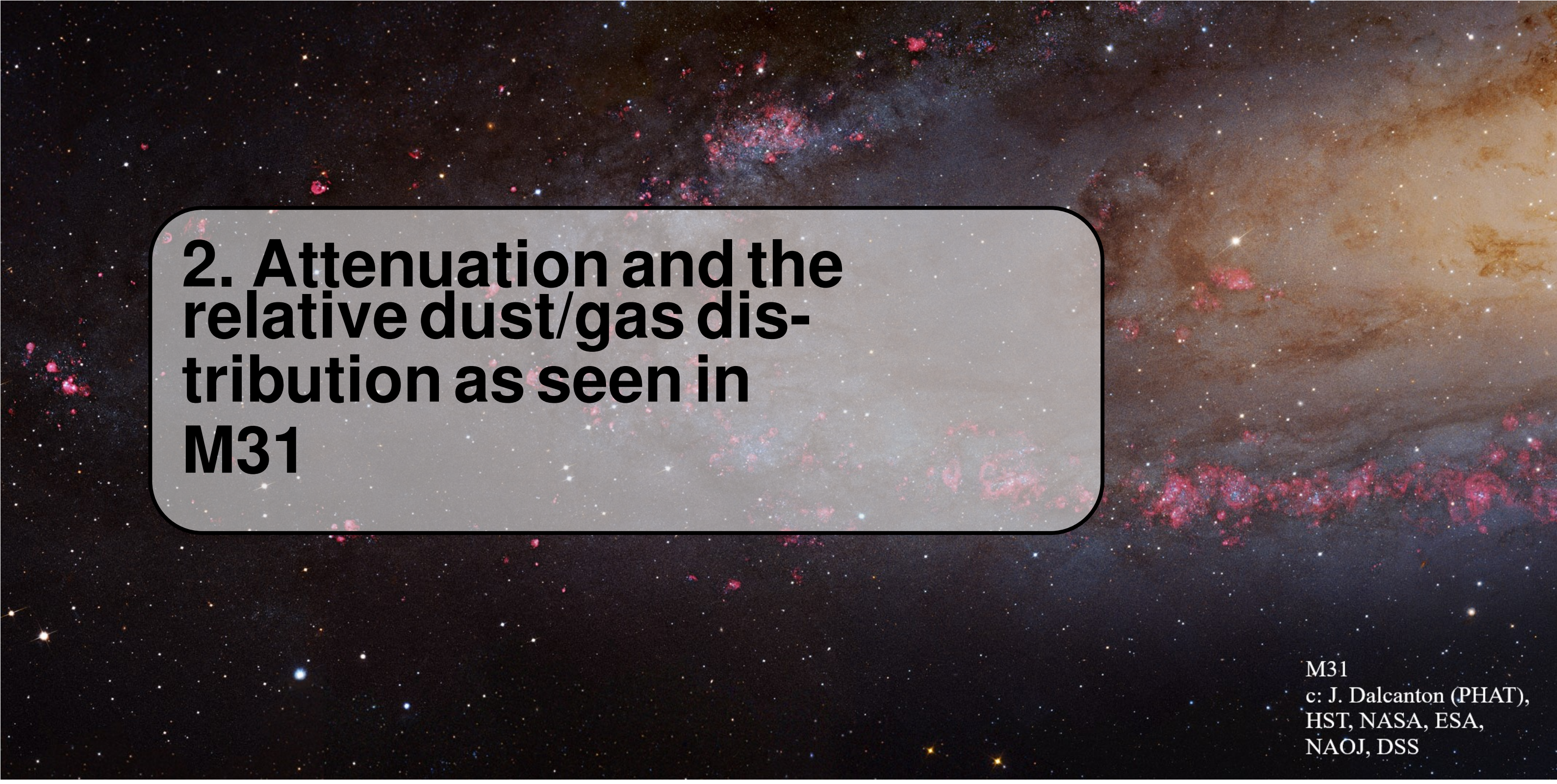

M31
c: J. Dalcanton (PHAT),
HST, NASA, ESA,
NAOJ, DSS

This chapter was published in a refereed article "Attenuation modified by DIG and dust as seen in M31", Tomičić et al. (2017), for which I am the lead author and which has been adapted for this thesis.

Overview: In this chapter, we used optical integral field spectroscopy observations of five ≈ 1 kpc fields in the Andromeda galaxy (Sec. 2.2), to extract the gas-phase emission lines maps, and the Balmer lines attenuation (A_V). We derived the relative dust and ionized gas distribution in M31 at $\approx$100 pc spatial scales (Sec. 2.3), by comparing the attenuation of the light with the dust mass surface density map. We also speculate the effects of diffuse ionized gas emission on the inferred dust/gas geometry (2.4).

2.1 Introduction

The attenuation and reddening by dust can severely impair our understanding of galaxies and the interstellar medium (ISM) environment (see Sec. 1.3.3). Dust preferentially absorbs ultraviolet (UV) and optical photons and re-emits this radiation in the infra-red (IR). The final impact of this reprocessing on the spectral energy distribution of a galaxy is dependent upon the properties of the dust and its spatial distribution relative to the stars and gas (Witt et al. 1992; Gordon et al. 2003; Draine 2011b). To understand the observed light from the galaxies, correct models of dust properties, distribution and the resulting effect on the spectra are needed.

As explained in Chap. 1, extinction is the result of absorption and scattering of the light by dust along a single line of sight. The effect is more pronounced for light at shorter wavelengths, resulting in an overall reddening of the light (usually denoted by the selective extinction E_{B-V}). With different dust/gas geometrical distribution, the effects on observed light would be different. The combined effects of extinction and geometry is usually called "attenuation". Caplan

& Deharveng (1986), Witt et al. (1992), Calzetti et al. (1994), Gordon et al. (2003) and Draine (2011a) derived various models for the relative dust/gas distributions and the corresponding effects on the stellar light and observed attenuation. Among these models, two show extreme scenarios, where in one the dust and gas are not mixed and another where they are.

The 'foreground screen' model assumes that the dust is distributed as a thin screen between the stars and the observer (Calzetti et al. 1994). This model represents the 'Extinction' case where all light is either absorbed or scattered out of the line of sight, and A_V correlates linearly with dust mass surface density. However, if the dust screen is on the far side behind the stars compared to the observer, that will result in no extinction.

The 'mixed media' model assumes the stars and dust are uniformly distributed and mixed (Calzetti et al. 1994). In this distribution some stars suffer relatively less extinction than others (i.e. closer to the observer) altering the attenuation. Also in this distribution light from stars can be scattered into the line of sight of the observer, also altering the attenuation.

van der Hulst et al. (1988) and Calzetti et al. (1996) observed ratios of various hydrogen lines in 14 nearby galaxies. They found that integrated $\sim$kpc regions in these galaxies typically had attenuations suggesting a dust distribution between the screen and mixed models.

Liu et al. (2013) investigated the dust attenuation of HII regions in M83 using the ratio of the Balmer and Paschen lines from *Hubble Space Telescope*/WFC3 narrowband imaging at ~ 6 pc spatial resolution. They found a diverse range of geometries, where the center of M83 has a dust distribution closer to the mixed model while the outer radii have HII regions with attenuation closer to the screen model. When averaged to $\geq$100-200 pc spatial resolution, their data follow a foreground screen model.

Using optically thin tracers, one simple way of deducing the spatial distribution of dust is to observe the effect of extinction on the known ratio of optical Balmer lines (Hα, Hβ, Hγ, Hδ) and then compare it with the extinction expected from the dust mass distribution.

While previous works of van der Hulst et al. (1988), Calzetti et al. (1996) and Liu et al. (2013) used only attenuation based on optical and near-infrared (NIR) lines to determine the dust distribution, Kreckel et al. (2013) (hereafter K13) used two independent measures of dust - optical attenuation and IR emission to measure the distribution. In K13, eight nearby galaxies were observed as a part of the KINGFISH[1] project (Kennicutt et al. 2011) with optical integral field spectroscopy (IFS) and far-IR observations (done with *Herschel Space Observatory*; Griffin et al. 2010; Pilbratt et al. 2010). They distinguish features at physical scales of $\sim$1 kpc within the galaxy disks. K13 conclude that the distribution of dust and gas in these galaxies lies somewhere between the screen and mixed models.

Following the methodology of K13, we observed five fields in the Andromeda galaxy (M31) to determine the spatial distribution of dust as compared to the ionized gas at high spatial resolution ($\approx$100 pc or 24.9$''$). Compared to K13, our higher resolution gives us the opportunity to resolve star-forming complexes at $\approx$100 pc resolution and HII regions at the $\approx$10 pc resolution. With this resolution, we are able to trace different environments of dust and ionizing gas. We analyze the dust distribution using two extreme dust models (foreground screen and mixed model) and compare our results with those from K13.

---

[1] **K**ey **I**nsight on **N**earby **G**alaxies: A **F**ar-**I**nfrared **S**urvey with **H**erschel

2.2 Data

The Andromeda Galaxy (M31) provides the best compromise between spatial resolution and a global view in the study of galaxy structure. The proximity of M31 to the Milky Way enables observation of its ISM with high resolution ($\sim$10.2 pc in the optical and $\sim$100 pc at 350 μm). M31 is a massive ($\sim 10^{10.5}$ $M_\odot$) SA(s)b galaxy with ring-like structures. Its distance from the Milky Way is $\sim$780 kpc (Stanek & Garnavich, 1998) and it is highly inclined ($\sim$70°, Dalcanton et al. 2012). R_{25} of M31 is $\approx$20.5 kpc (Zurita & Bresolin, 2012). The total star-formation rate (SFR) for the entire disk of M31 is ~ 1 $M_\odot yr^{-1}$ (Williams 2003; Lewis et al. 2015).

To study the relationship between attenuation and dust in M31, we have combined optical integral field unit (IFU) spectroscopy with far-infrared imaging. The attenuation is traced using optical spectroscopy, and the dust mass surface density was independently derived from far-IR Spectral Energy Distribution (SED) fitting using *Herschel* and *Spitzer* (Spitzer Space Telescope) photometry.

We targeted five fields in M31, chosen to have a large suite of ancillary multiwavelength data (Hα, 24 μm and FUV) and to cover a range of star formation rates and environments. The fields and data are also used by Kapala et al. (2015) to trace the origin of [CII] line emission, as part of the Survey of Lines in M31 (SLIM, PI Sandstrom K.). The positions of the five fields are shown in Fig. 2.1 and Tab. 2.1.

In the following subsections we describe the data reduction, flux calibration, and analysis of the spectra that are performed following the procedures outlined in K13 and Kapala et al. (2015).

2.2.1 Optical Integral Field Spectroscopy

We observed all fields using the Potsdam Multi-Aperture Spectrophotometer (PMAS, Roth et al. 2005) at the 3.5 m telescope at the Calar Alto Observatory on September 16-24, 2011. To split the spatial image, the telescope uses a specialized fiber-bundle, PPaK, which consists of 331 bare science fibers (with an additional 36 sky and 15 calibration fibers) in a hexagonal grid. The grid has a diameter of $75''$ (Verheijen et al., 2004) and spatial sampling of $2.7''$ per fiber. We used the $4k \times 4k$ CCD detector with the V300 grating to achieve a wavelength coverage of 3500-9000 Å (centred at 5400 Å) and resolution of R$= 1000$.

Each of the five observed fields combines 10 pointings in a mosaic, resulting in an area of $3' \times 4'$ (680 pc $\times$ 900 pc) for each field. Resulting mosaics have an effective PPaK resolution of $2.7''$. Each pointing was observed with a dither pattern (three dither positions shifted by

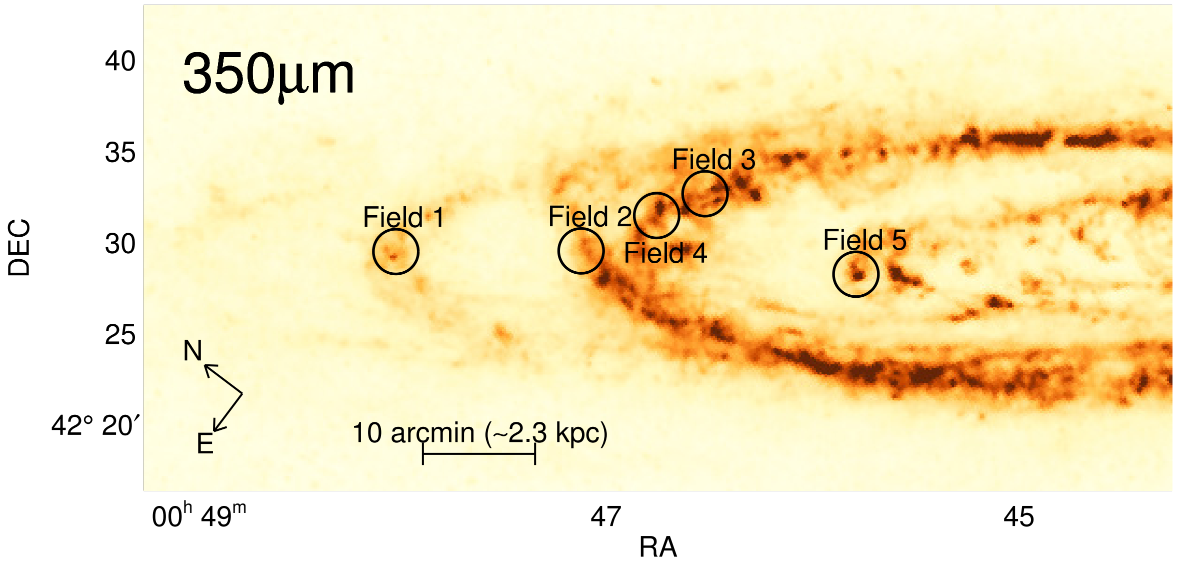

Fig. 2.1 Positions of the five fields in M31 used in this work, overlaid on a *Herschel* SPIRE 350 μm intensity map in 24.9″ resolution.

$\Delta\mathrm{Dec} = +1.''56$, $\Delta\mathrm{Dec} = +0.''78$ and $\Delta\mathrm{RA} = +1.''56$, $\Delta\mathrm{RA} = -0.''78$) with 2×600 s exposures in order to fill in gaps between the fibers, thus covering the entire field of view. Dedicated sky observations (with 120 s exposures) were taken in the same manner between each science observation in order to be subtracted later during calibration.

Astrometry for each mosaic position was applied by eye through comparison of compact HII regions with Hα images from the Local Group Galaxies Survey[2] (Massey et al. 2007; Azimlu et al. 2011). Additionally we compared *r*- and *g*- band SDSS images with our data by applying the SDSS response functions for the corresponding bands to our observed spectra. Maximum deviation in astrometry is 1″. Astrometric inaccuracies at this level do not affect our data analysis as we compare the $\mathrm{A_V}$ and dust maps at 25″ resolution.

To translate the electron count values into fluxes, we observed the standard stars BD +33d2642 and BD +25d4655 (Oke, 1990). The positions of lines and spectra on the detector, the optical path and the transmission are all affected by fiber flexure of the IFU instrument (Sánchez, 2006). To correct for these effects, we obtained calibration continuum lamp images (used for positioning of the spectra), He+HgCd arc lamp images (used for wavelengths calibration) and twilight flats (used for accurate flat fielding).

The atmospheric conditions were mostly clear, resulting in approximately uniform imaging of our fields. The observations of some pointings were repeated on 24th of September due to bad weather (clouds) or moonlight contamination. Seeing was subfiber (less than 2.7″) for all observations.

---

[2] Maps are publicly available on http://www2.lowell.edu/users/massey/lgsurvey.html and https://ned.ipac.caltech.edu/

Table 2.1 Coordinates, approximate distances from the galaxy center (in kpc) and metallicities (using equation 5 in Zurita & Bresolin 2012) for our fields. R_{25} of M31 is ≈20.5 kpc (Zurita & Bresolin, 2012).

Field	R.A. (J2000)	Dec. (J2000)	R kpc	Z 12+log(O/H)
1	$00^h46^m28.88^s$	$+42°11'38.16''$	16	8.3
2	$00^h45^m34.04^s$	$+41°58'33.53''$	12.2	8.4
3	$00^h44^m36.04^s$	$+41°52'53.58''$	11.7	8.4
4	$00^h44^m58.54^s$	$+41°55'09.14''$	11.8	8.4
5	$00^h44^m25.58^s$	$+41°37'37.20''$	6.8	8.6

2.2.1.1 Calibration

The data were reduced and calibrated by Kapala et al. (2015) by using the P3D software package[3], version 2.2.6. (Sandin et al., 2010). Here I describe the calibration steps described in detail in Kapala et al. (2015), and which follow the established IFU data calibration procedures[4] (Zanichelli et al. 2005; Blanc et al. 2009; Sandin et al. 2010; Mármol-Queraltó et al. 2011). For the first step a bias correction is performed using the median image of all bias frames as a master bias. Next, a master flat field is obtained from all twilight flat images. Observations are cleaned of cosmic rays following the L.A. Cosmic technique (van Dokkum, 2001) as adapted within P3D. I verified that the cosmic ray removal algorithm implemented in P3D robustly cleans up the images and the corresponding noise maps. The master trace mask is created to determine the position of all spectra on the CCD. The trace mask is constructed by stacking multiple calibration continuum lamp images, and fitting the peaks of emission lines with Gaussian functions along the cross-dispersion axis (Sandin et al., 2010). To remove the possibility of overlapping Gaussians, a modified optimal extraction method is applied (Horne, 1986) that simultaneously fits all the line profiles. The He+HgCd arc lamp images are used for construction of the dispersion mask, which calculates positions for all wavelength bins along the dispersion axis (Sandin et al., 2010). Furthermore, to remove instrumental scattered light from the CCD detector, the spectra is removed, the flux of the remaining background is interpolated and removed from the raw spectra. All the data is absolute flux calibrated using a spectral response function calculated by comparing the observed stellar spectrum of the standard star and the spectrum from the (Oke, 1990) catalog of the corresponding star. The sky-subtracted stellar spectra is derived from the sum of fibers containing flux from the standard star BD +33d2642.

---

[3] http://p3d.sourceforge.net/

[4] http://ifs.wikidot.com/reducing-fibreoutline

2.2.1.2 Sky subtraction, relative flux calibration and data cubes

The P3D package reduces the PPaK observations into calibrated row-stacked spectrum (RSS) images, from which we then subtract the sky contamination and flux-calibrate them.

Due to the large spatial extent of M31 on the sky, none of the sky fibers, observed simultaneously with the field of view, could be used for sky subtraction. Dedicated sky fields were observed before and after every science field with 120 s exposure times. The sky fields are processed following the same procedure as our science fields. We extract one median sky spectrum for each pointing of sky field observation and we linearly interpolate between sky exposures made before and after each science observations. Such a simple interpolation is possible as the majority of sky emission features change slowly with time. Because not all observing conditions were photometric and some observations ended during twilight, this interpolation technique failed for 23 of the pointings (out of a total of 50 pointings). In these cases, we assume that the median science spectrum across the field does not change significantly between dither positions. We measured a sky subtracted median of the science observation closest to the sky observation that appears least contaminated by clouds or twilight. This median science spectrum is subtracted from the median observed spectrum in the remaining dither positions to recover a single sky spectrum. Finally, these sky spectrum were subtracted from each individual fiber spectrum in that dither position.

To relative flux calibrate the RSS spectra we compare them with Sloan Digital Sky Survey (SDSS, York et al. 2000) images of the same area (Tempel et al. 2011). We use the positions and sizes of all fibers, apply the SDSS response functions to the spectra, and compare resulting photometric fluxes with SDSS g and r band images. Then we scale each dither and combine them into pointings.

The final step was to combine the now flux-calibrated and sky subtracted RSS spectra for all pointings into a single 3D spectral data cube. To do this I combine each of the spectra onto a grid of 1 arcsec^2 spatial pixels (spaxels) using a Delaunay linear triangulation (Delaunay, 1934) individually for each wavelength. Errors from the data and sky contribution (calculated by P3D) are propagated through the entire calibration process.

2.2.1.3 Line maps

The optical galaxy spectrum contains both stellar spectra (with continuum, emission and absorption lines) and emission lines from the ionized gas. We separate the nebular (gas-phase) emission from the stellar spectra using the GANDALF[5] software package[6] version 1.5 (Sarzi et al., 2006). GANDALF simultaneously fits both the emission lines and stellar continuum in an iterative approach.

It fits the emission lines using the penalized pixel-fitting method (pPXF; Cappellari & Em-

---

[5] **G**as **And** **A**bsorption **L**ine **F**itting

[6] http://www-astro.physics.ox.ac.uk/ mxc/software/

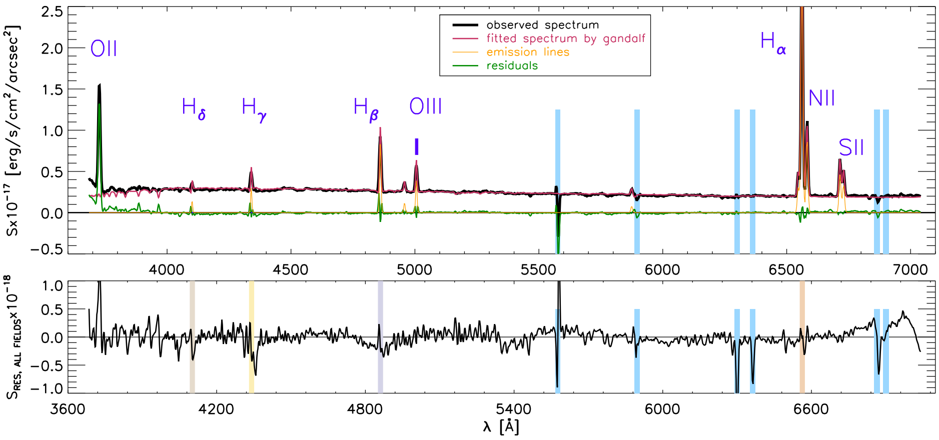

Fig. 2.2 *Upper panel*- Example GANDALF spectrum fit for one spaxel in Field 1. The black line is the original scientific spectrum, the red line is the fitted spectrum (including continuum and emission lines), the yellow lines show just the emission lines and the green line shows the fit residuals. Bright emission lines are labelled, while bright omitted sky lines are shaded in blue. Note that the [OII]λ 3727 emission line doublet is not fit with the other lines (see text for details). *Lower panel*- Stacked residuals of all fields. Filled, coloured areas indicate the positions of Balmer lines, while the bright sky lines are shaded in blue.

sellem 2004). Each prominent emission line is fit by a Gaussian profile with the kinematics tied together (i.e. v and σ) but fluxes left free. To fit the stellar continuum we use template spectra taken from the Tremonti et al. (2004) library of Bruzual & Charlot (2003) simple stellar population (SSP) templates for a range of stellar ages (100 Myr to 12 Gyr) and metallicities ($Z = 0.004$ and 0.05). While SSP spectra may not represent the resolved stellar populations in our fields in M31, we chose to use the same templates as K13 for consistency. All templates are convolved to match the spectral resolution of our spectra.

We checked if using other SSP templates or stellar spectra (with higher spectral resolution and different stellar population) could change the results of our fitting and alter the underlying stellar absorption features. We used the MILES SSP and stellar spectra library templates (Sánchez-Blázquez et al. 2006; Falcón-Barroso et al. 2011) in fitting our spectra and found that the results do not show any significant difference compared to using the Tremonti et al. (2004) library.

In fitting the continuum we also allow for a multiplicative third-order Legendre polynomial correction. This correction is necessary due to the poor flat-field correction in the blue part of the spectra caused by low CCD sensitivity, and to allow for stellar continuum attenuation by dust intrinsic to the fields of M31.

Foreground extinction from the Milky Way is also accounted for in the spectral fitting. However this is considered to be uniform across the disk of M31 with an $A_{\rm V} = 0.1705$ mag in all fields (based on Schlegel et al. 1998; Schlafly & Finkbeiner 2011).

The final data products from our fitting for each spaxel in our data cubes are: pure stellar continuum spectrum and fractional contribution of various SSP templates; multiplicative polynomial indicative of the intrinsic dust attenuation (and flat fielding corrections); gas velocity and gas velocity dispersion; and finally individual line amplitudes and fluxes for the most prominent emission lines. Identified emission lines are: Hδ, Hγ, Hβ, [OIII]λ4959Å, [OIII]λ5007Å, [NII]λ6548Å, Hα, [NII]λ6583Å, [SII]λ6717Å, [SII]λ6731Å.

Atmospheric optical emission lines (dominant around 5500 Å) can cause problems with the sky subtraction. There is a weak Hg I 4358.34 Å sky line (Osterbrock & Martel 1992, Slanger et al. 2000) near the Hγ line, which can also affect sky subtraction and fitting of the Balmer emission line. This effect is visible in the residuals near Hγ (Fig. 2.2, seen as an absorption feature). Additional contaminants like Earthshine and zodiacal light are removed from the spectra during sky subtraction as they exist as faint, extended features on the sky and in the sky spectrum (Reach 1997). Geocoronal emission lines, spatially extended and slowly changing with time, are removed by sky subtraction and do not have a significant effect on our Balmer line fluxes due to their narrowness (Nossal et al. 2001; Bishop et al. 2004; Haffner et al. 2003).

While the [OII] λ3727 Å line doublet is detected in many of our spectra, the line is strongly affected by the poor sensitivity and subsequent calibration in the blue part of the spectrum, and hence it was not used in our analysis. Foreground stars (approximately 2-5 spaxels per field) were not removed from our data cubes, but spaxels affected by the stars are masked during our GANDALF spectral analysis.

The median 3σ sensitivities of Hα and Hβ in all fields are 7.6×10^{-18} and 4.9×10^{-18} erg s^{-1}cm^{-2}arcsec^{-2}, respectively. However, averaged or median 3σ sensitivities of Balmer lines do not determine whether the data from spaxels will be shown or be excluded from the following diagrams and measurements. Data are included only if a line's amplitude is above the 3σ noise on the continuum. GANDALF calculates the noise on the continuum as the standard deviation of the residuals for the entire wavelength range, while uncertainties in the line fits as the amplitude over noise values (AoNs; Sarzi et al. 2006). Fig. 2.2 presents an example of the spectrum fitting for one spaxel in Field 1.

2.2.2 Far-IR data and dust column densities

Far-IR (FIR) emission is a good tracer of the amount of the dust in the line of sight (Wynn-Williams 1982; Neugebauer et al. 1984). Therefore we use the far-IR data observed by the PACS and SPIRE camera on the ESA *Herschel Space Observatory* (Griffin et al. 2010; Pilbratt et al. 2010). The dust mass surface density map of M31 presented by Draine et al. (2014), used for the comparison with attenuation maps, was determined by fitting the spectral energy distribution (SED) of the near and far IR emission (Groves et al. 2012a) with the Draine & Li (2007) dust model. The Draine & Li (2007) model specifies the dust characteristics like distribution of grain sizes, frequency-dependent opacity, fraction of dust in polycyclic aromatic hydrocarbons (PAHs) and dust column densities. The models were determined by calculating emission spectra (in near-IR, FIR and sub-millimeter) and reproducing extinction curves for different abundances of small PAHs and various dust mixtures heated by different starlight intensities.

The resulting dust mass surface density map ($\Sigma_{\rm dust}$) has an effective 24.9″ Gaussian PSF (matched to SPIRE 350 μm resolution). In order to compare our final attenuation maps with the dust mass surface density maps, we convolved our cubes from the effective PPaK resolution of 2.7″ into the SPIRE 24.9″ resolution. To convolve the data we use the kernels and the routine described in Aniano et al. (2011).

We convolve the data cubes by splitting them into images for each wavelength bin, and convolving each image separately. Before the convolution process, we add extrapolated values to the area outside the edges of the image, convolve the image, and then replaces those areas with blanks after the process. Then we reassemble the cubes to the SPIRE 350 μm image grid in order to compare the maps. After the convolution, we perform the same fitting routine and spectral analysis on the convolved images as described in Section 2.1.3.

This convolution technique changes the Balmer lines intensities (up to 30%) on the edges of the data cubes, depending on the position of bright HII regions. It affects both Balmer lines simultaneously, which results in only small changes in $\rm A_V$. If we compare $\rm A_V$ maps derived from the convolved data cubes and smoothed (but not convolved) cube, changes in $\rm A_V$ can be up to 0.3 mag for the bright regions. The effects of foreground stars are minimized due to the convolution process. Fig. 2.3, 2.4, 2.5, 2.6, and 2.7 show our un-convolved and convolved maps of Hα emission within M31's Fields.

2.3 Results

With the resulting data cubes and analyzed spectra, we measure the optical attenuation ($\rm A_V$) and compare it with the dust mass surface density ($\Sigma_{\rm dust}$). In the following subsections we describe the calculation of $\rm A_V$, show the resulting maps and compare the $\rm A_V$ and $\Sigma_{\rm dust}$ maps.

2.3.1 Attenuation maps

Due to reddening by dust (correlated with the extinction) the Balmer line ratios (known as Balmer decrements) are altered from their intrinsic ratios. The total V-band extinction ($\rm A_V$) is related to nebular reddening $\rm E_{B-V}$ by:

$$A_{\rm V} \equiv R_{\rm V} E_{\rm B-V}, \tag{2.1}$$

where $R_{\rm V}$ is the selective extinction. $\rm R_V$ depends on the physical characteristics of the extinguishing dust grains. In the diffuse ISM of the Milky Way, $R_{\rm V}$ has an average value of 3.1, which is the value typically assumed for massive star-forming galaxies (Schultz & Wiemer 1975; Cardelli et al. 1989; Calzetti et al. 2000). We assume the same $\rm R_V$ value for M31 as our fields are at similar galactic radii as the Sun (at 0.3-0.6 $\rm R_{25}$; Bigiel & Blitz 2012) and with similar metallicities (Zurita & Bresolin 2012, Draine et al. 2014). The reddening between two lines (F_1 and F_2) is calculated as (Calzetti et al., 1994):

$$E_{\mathrm{B-V}} = \frac{2.5}{k_2 - k_1} \log_{10} \left(\frac{F_1/F_2}{R_{int}} \right), \tag{2.2}$$

where k is the extinction as a function of wavelength for the corresponding lines. Here we use the extinction curve from Cardelli et al. (1989). By using the Calzetti et al. (2000) attenuation curve instead, the resulting inferred A_V would decrease by 9%. That systematic shift should be kept in mind when comparing our results with those found by K13, where they used the Calzetti et al. (2000) curve. The difference between those two curves is because the Cardelli et al. (1989) curve solely accounts for foreground extinction while the Calzetti et al. (2000) curve takes into account geometrical effects on attenuation. We assume an intrinsic flux ratio of $R_{\mathrm{int}} = \mathrm{H}\alpha/\mathrm{H}\beta = 2.86$, corresponding to an ionized gas temperature of T$\approx 10^4$ (assuming case B recombination; Miller 1974; Osterbrock 1974; Osterbrock & Martel 1992).

We show attenuation (A_V) maps and the dust mass surface density maps (Σ_{dust}) in Fig. 2.3, 2.4, 2.5, 2.6, and 2.7. For all our fields contours show the Hα intensities, tracing the position of the HII regions. All maps are at the same scales, which offers a direct comparison between the fields. A_V spans values between 1.5-4.5 mag in our fields. Similar results are observed by Sanders et al. (2012), where observed HII regions in M31 show values between 1 and 5 mag. The fact that there are no M31 data points with attenuation lower than $A_V = 1$ is an effect of targeting dense spiral arm regions in M31, which biases us to regions of high Σ_{dust}. Were our fields larger and included less dusty regions we would expect our maps to have more data points with $A_V < 1$.

In general, we find that the HII regions are situated near or in the regions of higher dust mass surface densities. This is expected if the dust traces the regions of high gas density where new stars are formed. Contrary to other fields, in Field 1 the HII regions are situated in less attenuated and less dusty areas. We explain this as an effect of stellar feedback from more evolved HII regions that have already destroyed dusty birth cloud.

We exclude from the following analysis and maps regions where the Balmer lines do not exceed a threshold of AoN $\gtrsim 3$ (corresponding to S/N $\gtrsim 3$). Due to the low flux and hence S/N of the emission in Field 5, there are few spaxels that exceed this threshold. This causes some statistical difficulties in the analysis of this field. There is also a possibility that a young HII region is buried in the dense cloud, seen in the center of Field 5 (Fig. 2.7).

Our calculated attenuation depends on the physical condition of the ionized gas (which can cause different intrinsic line ratios) and on the dust composition (resulting in different values of R_V), both of which affect the extinction curve. Therefore, the attenuation values of some data points can be different due to intrinsically different physical condition in those regions. However, these effects are presumed to be small relative to the real variation in A_V due to the dust distribution.

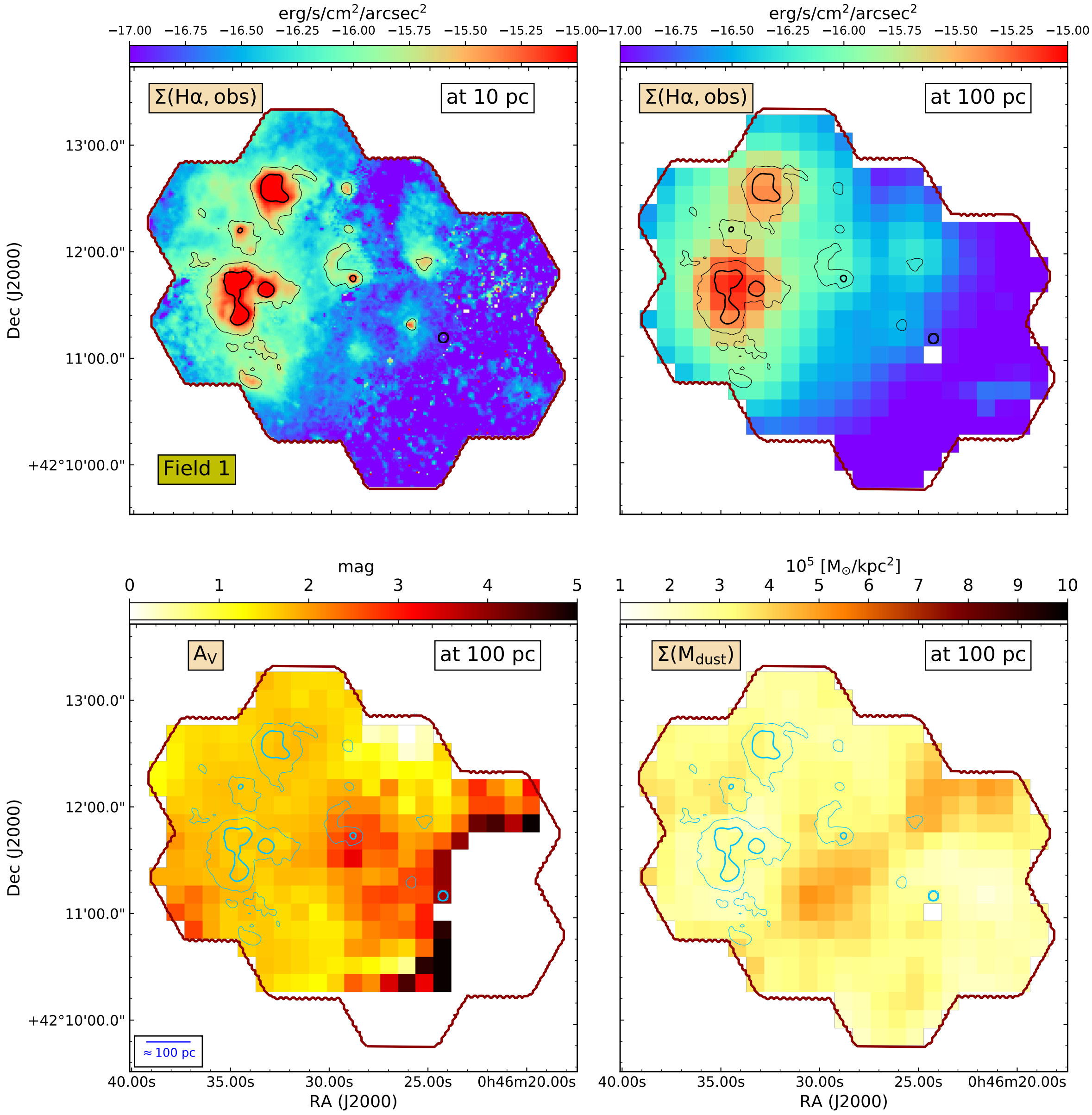
erg/s/cm²/arcsec²
−17.00 −16.75 −16.50 −16.25 −16.00 −15.75 −15.50 −15.25 −15.00
Σ(Hα, obs)
at 10 pc
at 100 pc
Field 1
Dec (J2000)
13'00.0"
12'00.0"
11'00.0"
+42°10'00.0"
mag
0 1 2 3 4 5
10⁵ [M⊙/kpc²]
1 2 3 4 5 6 7 8 9 10
A_V
Σ(M_dust)
≈ 100 pc
40.00s 35.00s 30.00s 25.00s 0h46m20.00s
RA (J2000)

Fig. 2.3 *Upper panels*- Maps of Hα intensity images of Field 1 in M31. On the upper left is the un-convolved image at the native PPaK resolution of 2.7$''$, while on the upper right is the convolved image at the SPIRE 350 μm, 25$''$ resolution. We label the resolution of the maps in the upper right corner of the panels. Contours show the extinction corrected Hα intensities of 5×10^{-16} (thin) and 3×10^{-15}(thick) erg s^{-1}cm^{-2}arcsec^{-2}. *Bottom panels*- The attenuation (A$_\mathrm{V}$, left) and dust mass surface density maps (Σ_dust, right) for Field 1. The contours are the same as on the upper panels. For attenuation, only pixels with AoN of the Balmer lines greater than 3 are shown. All maps are at the same scale, allowing for direct comparison between the fields.

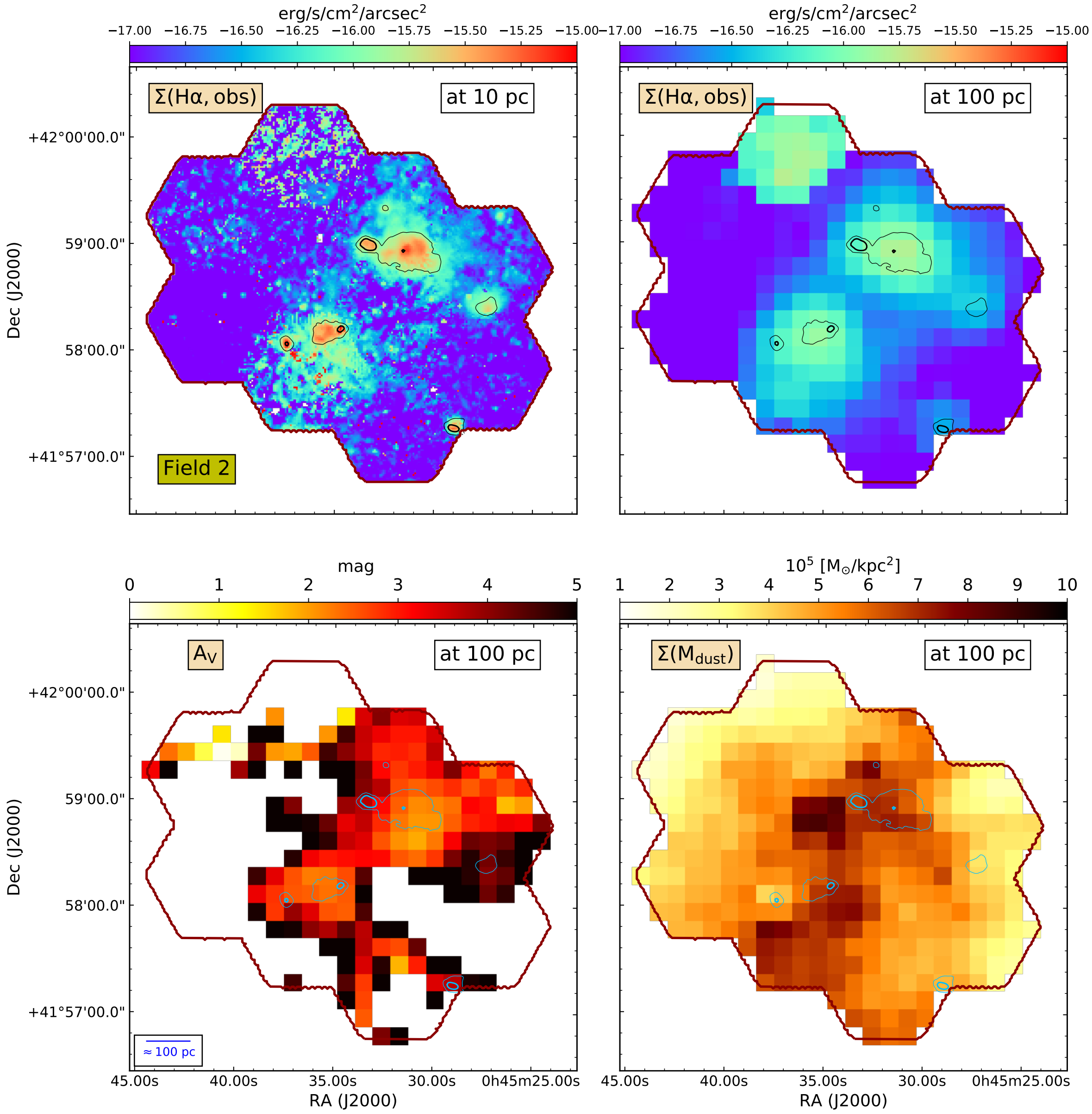
erg/s/cm^2/arcsec^2
−17.00 −16.75 −16.50 −16.25 −16.00 −15.75 −15.50 −15.25 −15.00
Σ(Hα, obs)
at 10 pc
Field 2
Σ(Hα, obs)
at 100 pc
+42°00'00.0"
59'00.0"
58'00.0"
+41°57'00.0"
Dec (J2000)
mag
0 1 2 3 4 5
A$_V$
at 100 pc
10^5 [M$_\odot$/kpc^2]
1 2 3 4 5 6 7 8 9 10
Σ(M$_{dust}$)
at 100 pc
≈ 100 pc
45.00s 40.00s 35.00s 30.00s 0h45m25.00s
RA (J2000)

Fig. 2.4 Same as Fig. 2.3, but for Field 2.

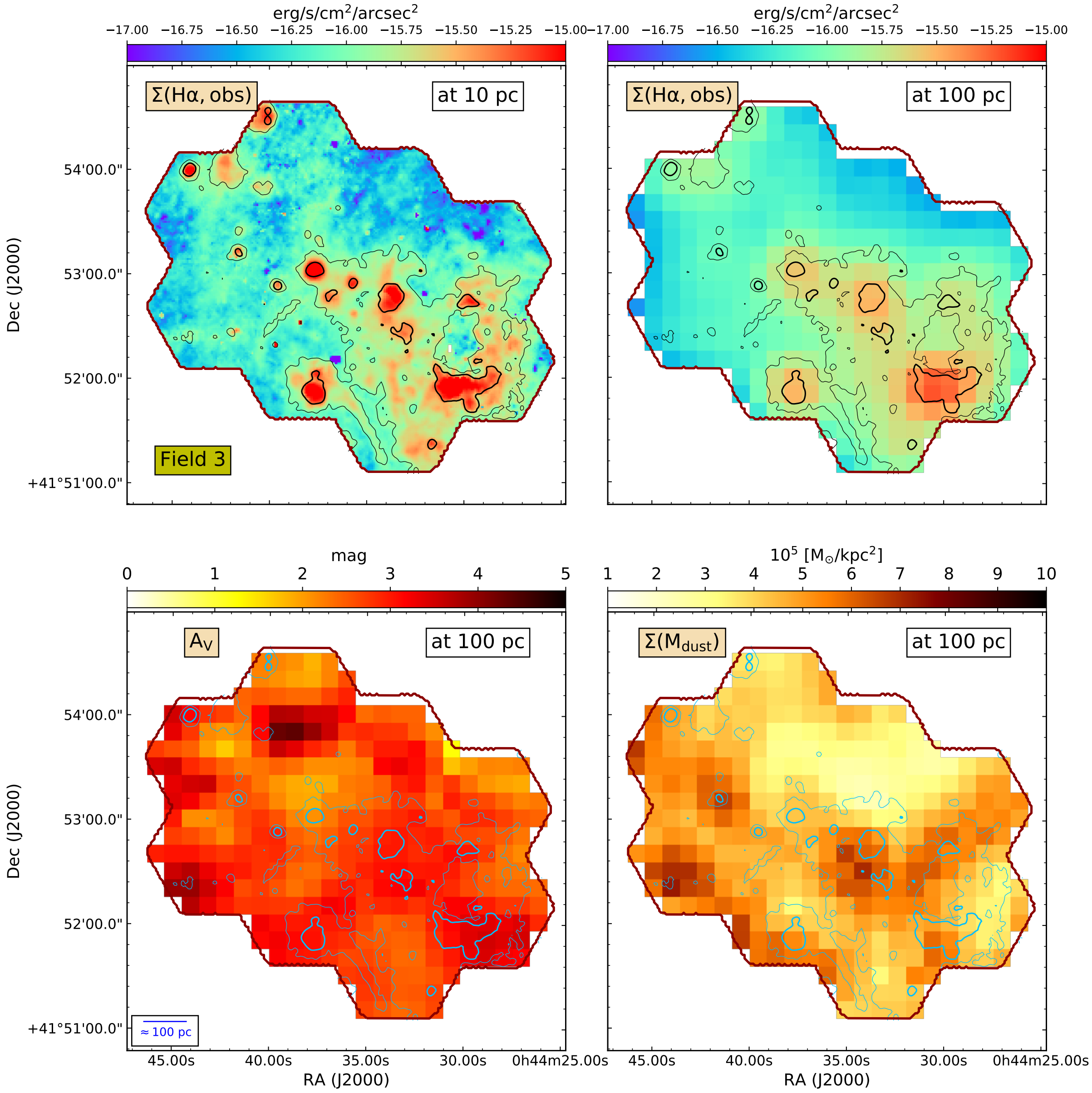
erg/s/cm^2/arcsec^2
−17.00 −16.75 −16.50 −16.25 −16.00 −15.75 −15.50 −15.25 −15.00
Σ(Hα, obs)
at 10 pc
Field 3
at 100 pc
mag
0 1 2 3 4 5
10^5 [M$_\odot$/kpc^2]
1 2 3 4 5 6 7 8 9 10
A$_V$
Σ(M$_{dust}$)
≈ 100 pc
Dec (J2000)
54'00.0"
53'00.0"
52'00.0"
+41°51'00.0"
45.00s 40.00s 35.00s 30.00s 0h44m25.00s
RA (J2000)

Fig. 2.5 Same as Fig. 2.3, but for Field 3.

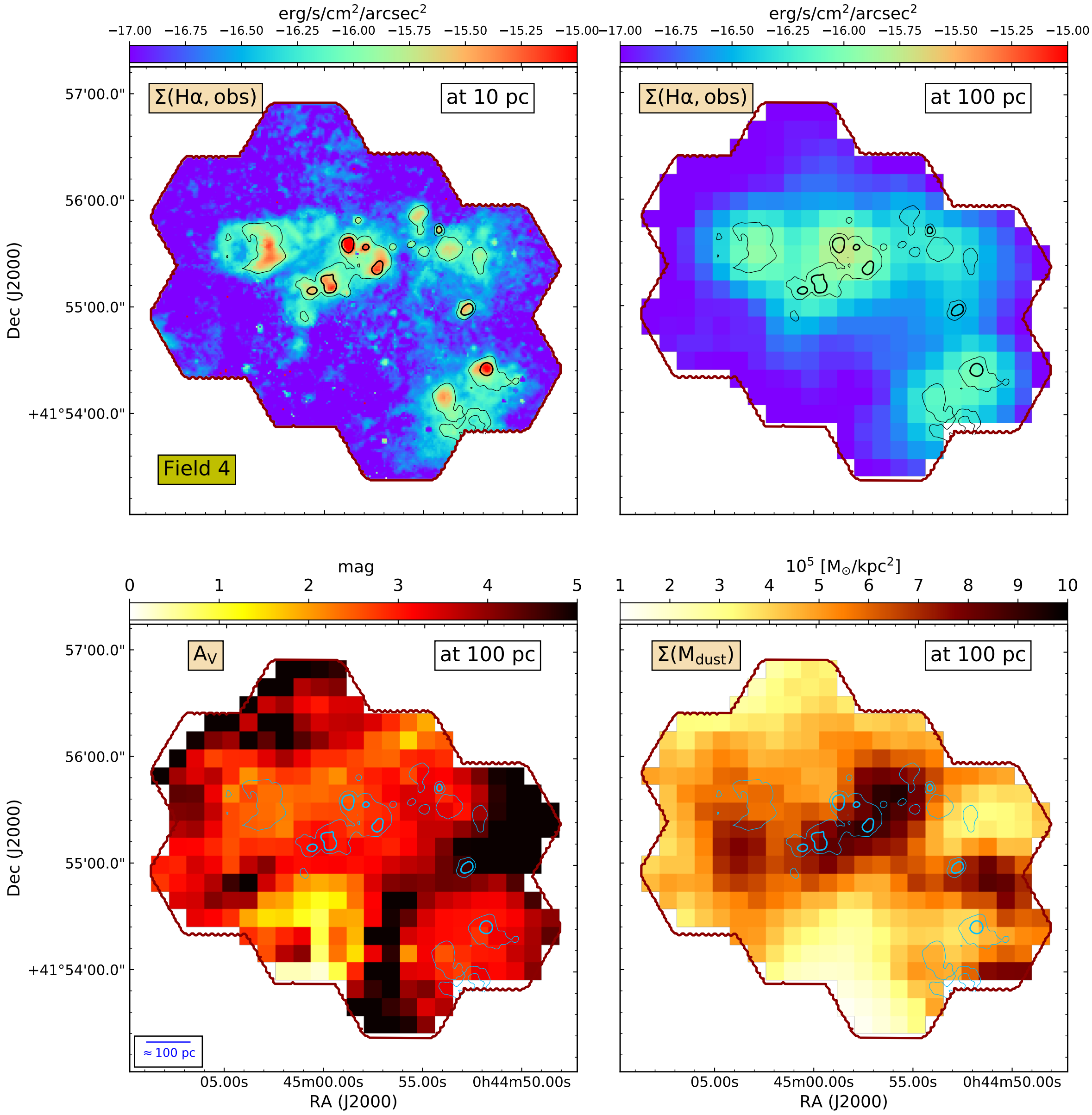
erg/s/cm^2/arcsec^2
−17.00 −16.75 −16.50 −16.25 −16.00 −15.75 −15.50 −15.25 −15.00
Σ(Hα, obs)
at 10 pc
Field 4
at 100 pc
57'00.0"
56'00.0"
55'00.0"
+41°54'00.0"
Dec (J2000)
mag
0 1 2 3 4 5
A$_V$
10^5 [M$_⊙$/kpc^2]
1 2 3 4 5 6 7 8 9 10
Σ(M$_{dust}$)
≈ 100 pc
05.00s
45m00.00s
55.00s
0h44m50.00s
RA (J2000)

Fig. 2.6 Same as Fig. 2.3, but for Field 4.

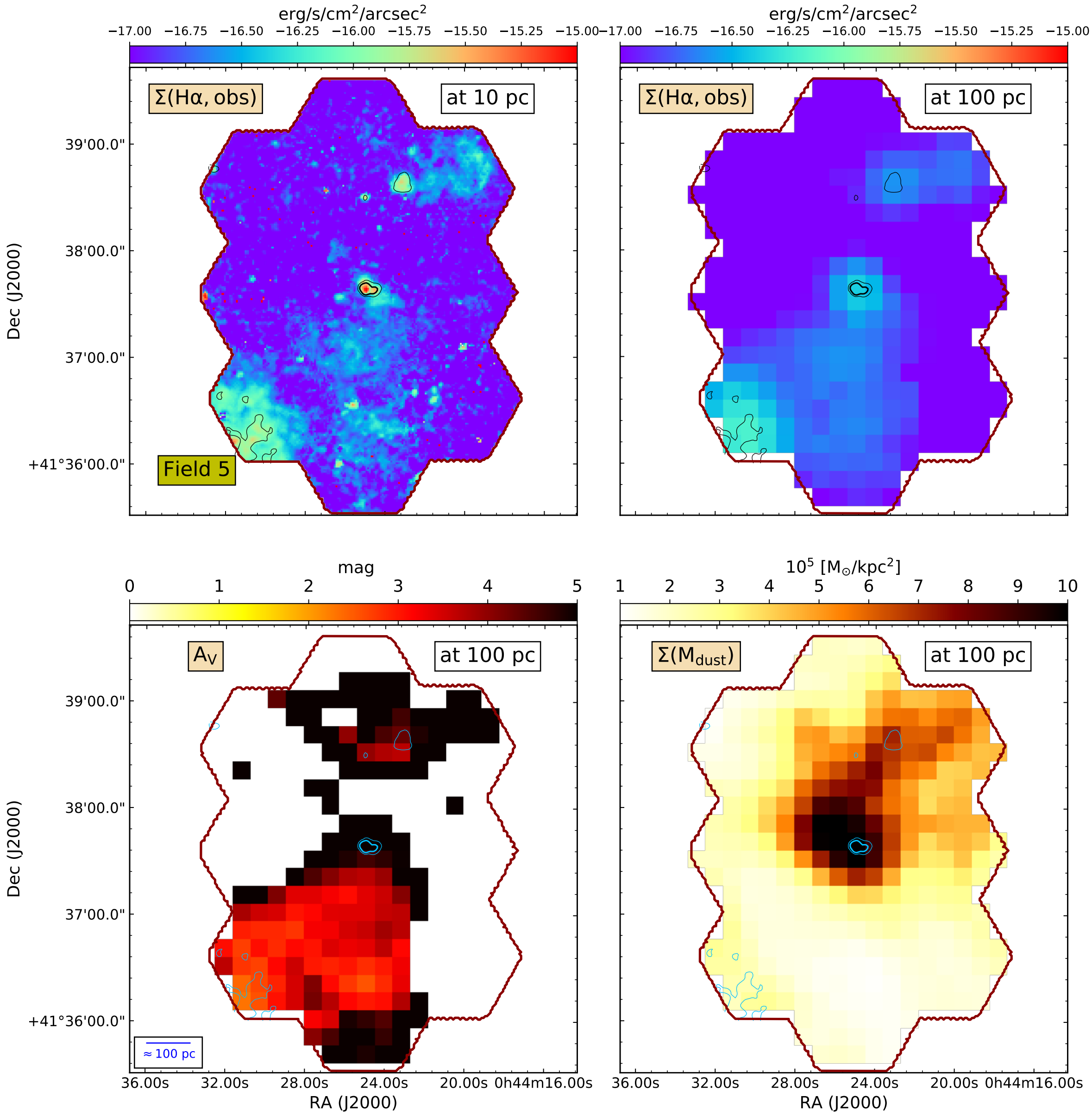
erg/s/cm²/arcsec²
−17.00 −16.75 −16.50 −16.25 −16.00 −15.75 −15.50 −15.25 −15.00
Σ(Hα, obs)
at 10 pc
Field 5
at 100 pc
mag
0 1 2 3 4 5
A_V
10⁵ [M⊙/kpc²]
1 2 3 4 5 6 7 8 9 10
$\Sigma(M_{dust})$
≈ 100 pc
Dec (J2000)
39'00.0"
38'00.0"
37'00.0"
+41°36'00.0"
RA (J2000)
36.00s 32.00s 28.00s 24.00s 20.00s 0h44m16.00s

Fig. 2.7 Same as Fig. 2.3, but for Field 5.

2.3.2 $\mathbf{A_V}$ vs. $\Sigma_{\rm dust}$

The main goal of this paper is to compare the dust in M31 as determined via two independent methods; the attenuation derived from the Balmer decrement, and the dust mass surface density derived from IR photometry. This follows on from the work of K13 who found a relation between these measures within eight nearby galaxies, but with large scatter between galaxies.

The dust attenuation and dust mass surface density are connected via the distribution of dust. We consider here two simplistic models of the dust distribution, derived from Caplan & Deharveng (1986) and Calzetti et al. (1994). The Calzetti models predict the correlation between attenuation and the dust mass surface density for five different spatial distributions of the dust. The two major models that are used for this work are the ‘foreground screen’ model and the ‘mixed’ model (in Calzetti et al. 1994 these are referred to as the “Uniform dust screen” and the “Internal dust” models). The remaining models are variation on those two extremes.

The ‘foreground screen’ model describes a situation where all the dust sits in a smooth, uniform screen between the emitter and the observer (the dust is not mixed with the sources of radiation). Assuming the dust model from Draine & Li (2007) and the dust-to-gas ratio (DGR) from Draine et al. (2014), the attenuation is linearly related to $\Sigma_{\rm dust}$ via:

$$A_{\rm V}^{\rm screen} = 0.74 \cdot \frac{\Sigma_{\rm dust}}{10^5 {\rm M_\odot kpc^{-2}}}[mag]. \tag{2.3}$$

Given our assumptions, this equation provides a theoretical upper limit on the attenuation possible at a given dust mass surface density.

The ‘mixed’ model assumes the dust is uniformly distributed with the sources of radiation. Therefore the attenuation in the mixed model is much lower than in the foreground screen model. The resulting mixed model attenuation, assuming isotropic scattering and the same connection with dust mass as in equation 2.3, is (based on Calzetti et al. 1994):

$$A_{\rm V}^{\rm mixed} = -2.5\log_{10}(\gamma_{\rm V})\ [{\rm mag}], \tag{2.4}$$

where

$$\gamma_{\rm V} = \frac{1 - e^{0.57 A_{\rm V}^{\rm screen}}}{0.57 A_{\rm V}^{\rm screen}}. \tag{2.5}$$

γ functionally limits the value of the optical depth in the optically thick medium (Calzetti et al., 1994). The screen model correlates linearly with the dust column, while the mixed model saturates and for high dust mass surface densities yields a moderate expected attenuation (Fig. 2.8).

Fig. 2.8 shows a comparison of the dust mass surface densities and the attenuation for M31 and for the nearby galaxies observed by K13, together with the two Calzetti models. While the data from K13 span the area between the foreground screen and mixed models, the more resolved M31 data follows more closely a foreground screen model. No clear trends are seen

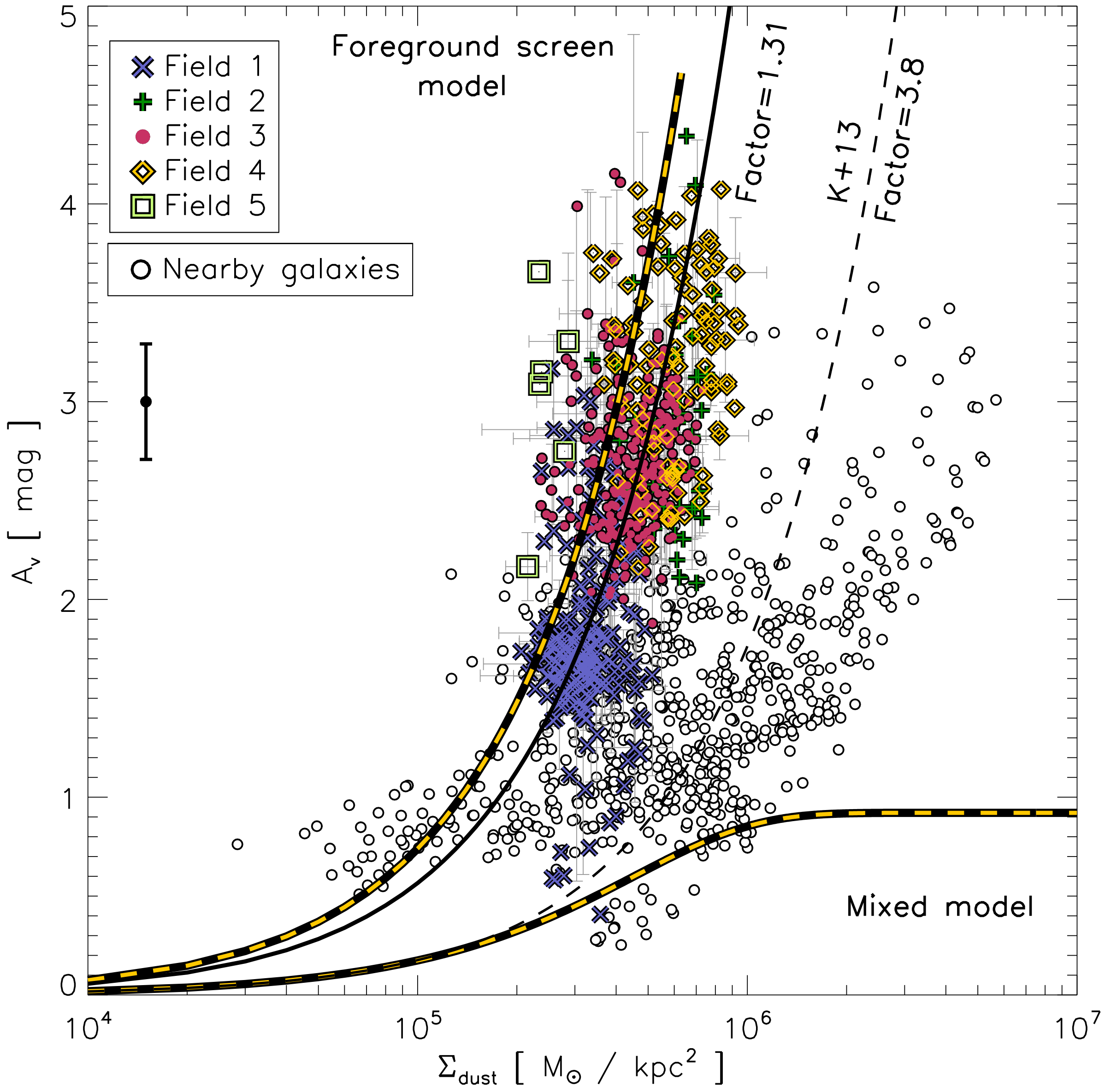

Fig. 2.8 Attenuation (derived from the Hα/Hβ ratio) compared to the dust mass surface density. Foreground screen and mixed models (Calzetti et al., 1994) are represented by thick, black/yellow lines. Various symbols represent data points from our five fields in M31. Data from K13 for nearby galaxies are shown in the background as empty circles. A foreground screen model decreased by a factor of 3.8 (from K13) and 1.35 (best fit for M31) are also shown. The median value of the M31 uncertainties of attenuation values are shown on the left side of the diagram.

within each Field of M31, but when the fields are considered together the data fits very well the foreground screen model. We find the correlation between A_V and Σ_{dust} well fit by scaling down the foreground screen model by a factor of 3.8 for the nearby galaxies (K13) and 1.35 for M31.

We see some regions in M31 that have larger attenuation than is expected from our foreground screen model (Eq. 2.3). Approximately 25% of the data points are above the foreground screen model, or 3% of the data if we take into account their corresponding 1σ errors. These high A_V regions can be explained by: (1) 'clumpiness' in the dust below our resolution that is affecting our measured $\Sigma_{\rm dust}$, (2) an underestimation of the dust mass surface density, (3) poor calibration of the optical spectra, (4) values of $\rm A_V/\Sigma_{dust}$ different from what we have assumed, (5) variation in the extinction curve $\rm k(\lambda)$ that affect $\rm R_V$ and thus $\rm A_V$.

If an area with low $\Sigma_{\rm dust}$ has locally a high density clump of dust covering the HII region, averaging the dust surface density due to the low spatial resolution of our observations could misleadingly show a low $\Sigma_{\rm dust}$ and a high $\rm A_V$. However, when comparing the value of $\rm A_V$ around HII regions at PPaK 2.7$''$ resolution ($\sim$ 10 pc) , we find that $\rm A_V$ does not change rapidly with different aperture sizes.

Previous work has tested the accuracy of estimating dust masses using the Draine & Li (2007) model (Alton et al. 2004; Dasyra et al. 2005; Galametz et al. 2012; Aniano et al. 2012; Dalcanton et al. 2015; Planck Collaboration et al. 2016). Most recently,Dalcanton et al. (2015) and Planck Collaboration et al. (2016) measured dust column density within the Milky Way and M31 by measuring the extinction of the light from background sources. Both studies concluded that the Draine & Li (2007) dust model may overestimate the mass of the dust by a factor of $\sim$2.5. Comparison with independent far-IR observations have shown that this offset is not due to uncertainties in the Herschel photometry (Verstappen et al., 2013; Planck Collaboration et al., 2016).

Planck Collaboration et al. (2016) suggest that this offset is dependent upon the heating radiation field intensity. They propose an empirical renormalization of the dust mass derived from DL07 as a function of the DL07 ionization parameter $\rm U_{min}$ (see Formula 9 in Planck Collaboration et al. 2016). Fig. 2.9 shows the $\rm A_V$ vs. $\Sigma_{\rm dust}$ diagram for M31 and the nearby galaxies from K13, before and after using renormalization proposed by Planck Collaboration et al. (2016). The renormalized $\Sigma_{\rm dust}$ values for M31 are lower than before, pushing the values above the foreground screen limit lines. We do not include here any renormalization of the K13 regions, which have $\rm U_{min} > 1$. As the renormalization is not calibrated for high $\rm U_{min}$ regime, extrapolating the renormalization for K13 data would make widen the relative disagreement between M31 and K13 results.

An additional effect that can play a role in our derived attenuation is the 'mid-plane' effect, as we expect half of the dust to be situated behind the ionizing sources. That can partly explain the offset of M31 data from the 'foreground screen' model line. This effect should be strongest in the case where the scale height of the ionized gas is much smaller than the scale height of the dust. However, in the case of similar scale heights, this effect should play a much smaller role.

Given our confidence in our spectrophotometric calibration, we explain higher attenuation values of some regions as a result of possible variations in the extinction law tied to variations in the dust properties, which we expect are related to variations in our assumed DGR and $\rm R_V$.

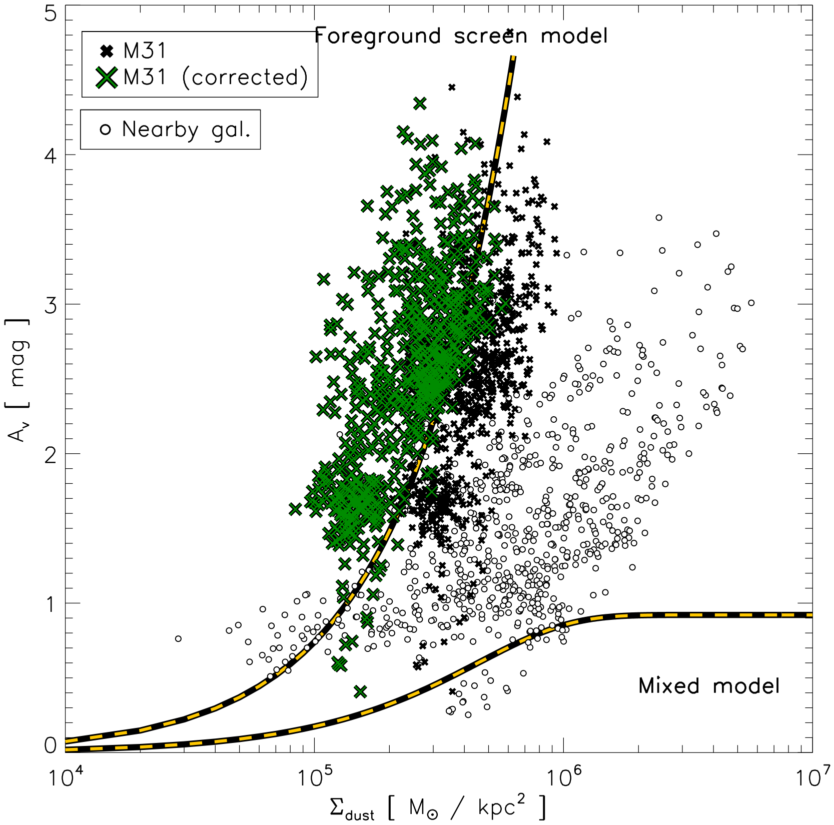

Fig. 2.9 A_V vs. Σ_{dust} before and after correcting dust mass values using the empirically derived renormalization formula 9 in Planck Collaboration et al. (2016). Crosses indicate the data for M31 and circles the data for the nearby galaxies.

2.4 Discussion

Our main result (Fig. 2.8) shows that M31 more closely follows a foreground screen model than a mixed model. This is different from what K13 found in nearby galaxies. In this section, we consider various factors that potentially explain the differences between these results. We examine the effect of physical resolution on attenuation (Sec. 2.4.1). We test the effects of a spatially extended ionized gas component on attenuation (Sec. 2.4.2). We associate this additional gas with diffuse ionized gas (DIG) and discuss the effects of different scale heights of dust, HII regions and DIG on A_V (Sec. 2.4.2, 2.4.3 and 2.4.4). Finally, we explain the varying vertical distribution of dust and gas in M31 and the K13 galaxies by observations at different galactic radii (Sec. 2.4.5).

2.4.1 The impact of physical resolution

While K13 probed spatial scales between $\sim 0.3\,$kpc to $\sim 2\,$kpc, the proximity of M31 means that the SPIRE 350$\,\mu m$ physical resolution is $\sim 100\,$pc. The fields in M31 are located within the most dense and dusty spiral arms and cover only a small fraction of the galaxy. Therefore it is possible that our M31 results are biased by dusty, star-forming regions where a foreground

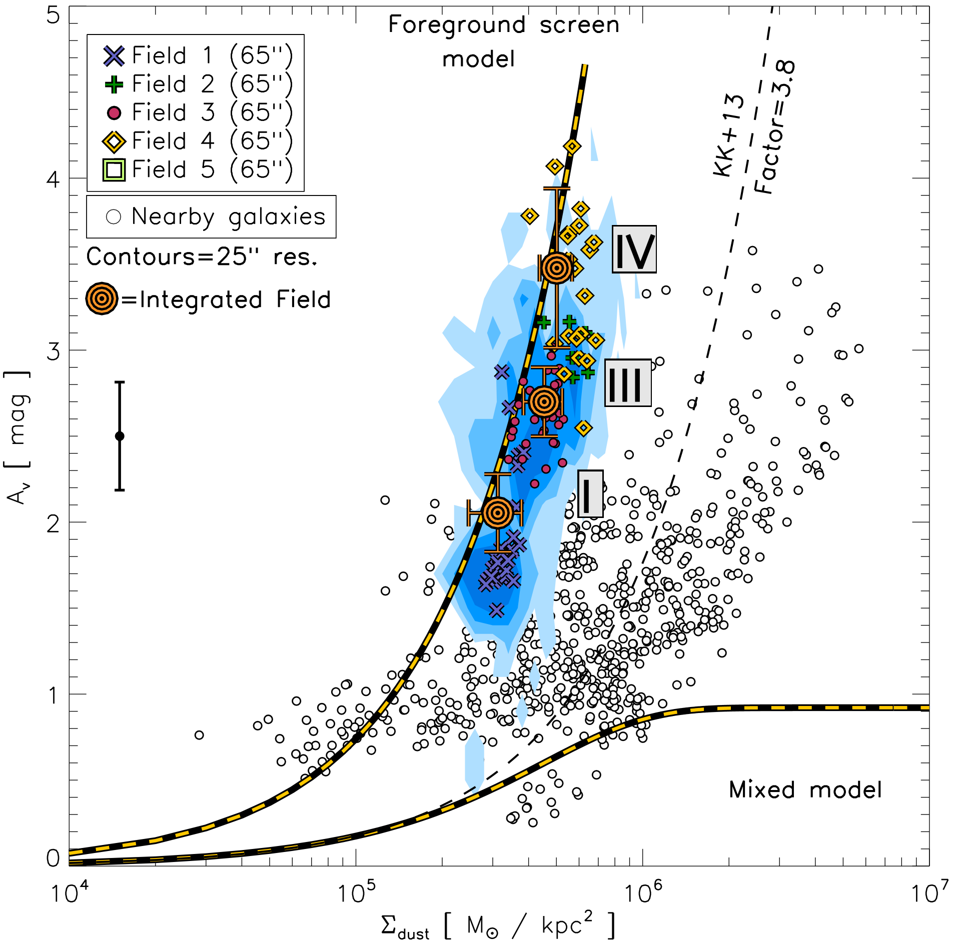

Fig. 2.10 A_V vs. Σ_{dust} for our M31 fields convolved to different spatial scales. Contours show the data from Fig. 2.8 at 24.9″ scales(∼100 pc), the various symbols represent the data at 65″ scales (≈260 pc), while the big circles indicate results from integrating each Field (as labelled) spanning spatial scales of 0.6 kpc×0.9 kpc. Due to the low AoN of Hβ, only three fields can be shown. No obvious change in the A_V versus Σ_{dust} relation is apparent between the different resolutions. 1σ uncertainty error bars for the integrated fields and the median uncertainty of the convolved data (shown in the left corner) are presented. Systematic uncertainties in the spectral fitting dominate over the random instrumental uncertainties.

screen model more closely represents the dust distribution. The larger physical sizes of the regions sampled in K13 can probe both regions where a foreground screen model is more representative and regions where a mixed model more closely matches reality. This yields a result where together all regions show a mixture between the two models. K13 searched for a correlation between A_V - Σ_{dust} slope and different spatial scales, but the changes in slope were not significant.

To directly compare our result with K13 (whose best spatial resolution is ≈300 pc), we smoothed our data (Fig. 2.10) to 65″ resolution (corresponding to spatial scales of ≈260 pc) and find no difference in the slope of the correlation. Moreover, we also integrate all spectra from each field into a single data point and re-extract the line fluxes to determine the average attenuation for each field. Resulting integrated field data points span spatial scales of around $0.6\,\mathrm{kpc}\times 0.9\,\mathrm{kpc}$. We then compare this value to the average dust mass surface density for the field. Integrated field data points are shown as circles in Fig. 2.10, and it is clear that even at these scales we see the same relation between attenuation and dust mass surface density. Some fields are not presented, due to the low number and brightness of HII regions. As Hβ line is faint, this results in low AoN values for those fields.

The regions in K13 target wide areas (covering both spiral arms and inter-arm regions) and can consist of regions with or without low-brightness HII regions. It is possible that the dust probed in some of those regions is heated by an old stellar population and not solely by HII regions. However, as the Draine & Li (2007) model explicitly takes into account starlight heating, the modeled dust mass should not suffer from any bias in either K13 or our results on any of the scales considered. Using the close alignment of disk galaxies in front of early-types, Holwerda & Keel (2013) found that inter-arm regions contain less dust relative to spiral arms. While K13 included regions with a broad range of dust mass surface densities, the regions with weak Hα flux (where dust may be predominantly heated by the old stellar population) are generally removed by the S/N criteria in their work. Therefore we conclude that the difference between our results and their is not related to the treatment of the inter-arm regions. However, the integrated fields of M31, which have a similar spatial resolution to K13 ones, have star-formation rate surface densities (Σ_{SFR}) that are a factor of 10 lower. This makes a direct comparison between fields at fixed Σ_{SFR} impossible. The mean Σ_{SFR} in M31 is around ~ 0.01 $\mathrm{M}_{\odot}\,\mathrm{yr}^{-1}\,\mathrm{kpc}^{-2}$, while for the K13 galaxies Σ_{SFR} spans a $0.03-10$ $\mathrm{M}_{\odot}\,\mathrm{yr}^{-1}\,\mathrm{kpc}^{-2}$ range (see Fig. 2.11).

2.4.2 Effects of an additional component to the dust/gas distribution model

Another possibility to explain the difference in the $\mathrm{A_V}$ - Σ_{dust} relation between M31 and the K13 galaxies is that, in the K13 galaxies, some fraction of the ionized gas resides outside the dust disk. As this emission would not be extinguished, therefore lowering the observed $\mathrm{A_V}$. In this section, we propose the diffuse ionized gas (DIG) as a candidate for this gas outside the dust disk. We also explain why the previously used Calzetti et al. (1994) model of dust/gas distribution (combining only HII regions, stars and dust) need an additional diffuse and spatially extended component.

2.4.2.1 Additional flux from non-attenuated gas

The Calzetti et al. (1994) model for the dust/gas distribution combine only dust and stars (that ionize the gas within the HII regions). That model neglects the possibility of additional flux from ionized gas spatially even more extended than the dust. In the scenario where additional gas presides outside the dust disk, the observed attenuation would be lower than in the case of the Calzetti et al. (1994) model, even for the same observed amount of dust. If we assume that

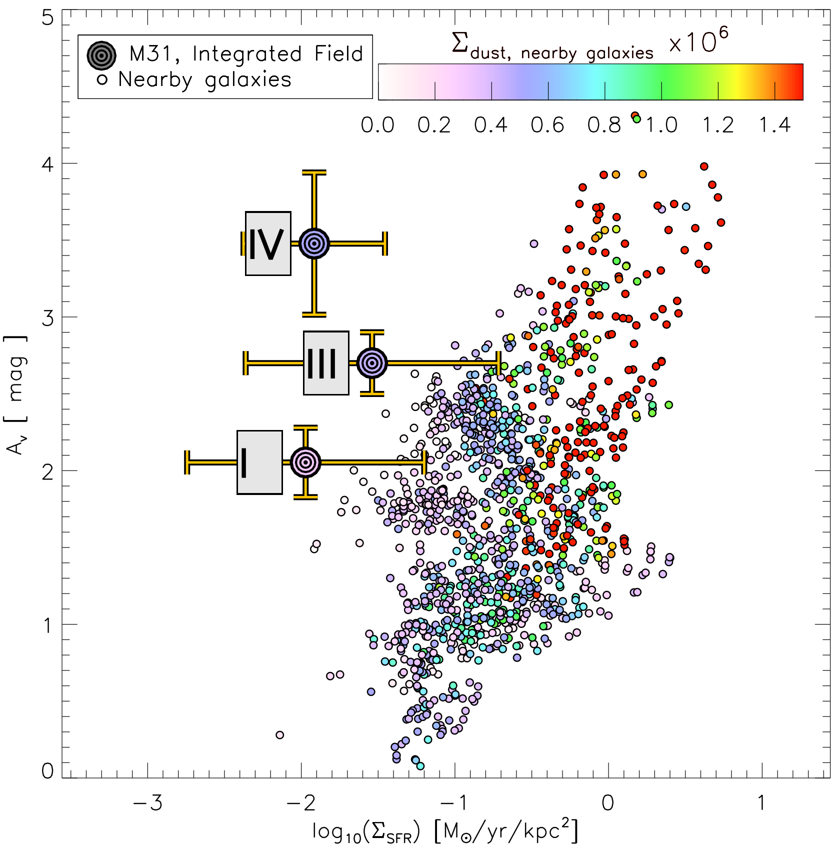

Fig. 2.11 A_V vs. Σ_{SFR} (from extinction corrected Hα) of M31 (big circles) and K13 galaxies (small circles). Colors corresponds to Σ_{dust} of the data. M31 data are at 0.6 kpc×0.9 kpc resolution, while the K13 are at 0.3 kpc-2 kpc resolution.

the M31 regions have all of the ionized gas embedded in the dust disk, we explore how flux from a non-attenuated ionized gas, which may lie outside the dust disk, would effect the A_V - Σ_{dust} relation.

In Fig. 2.12 we investigate how large the contribution from a non-attenuated ionized gas component above the dust disk would need to be in order for the M31 data to follow the trend of K13. Hα flux from that non-attenuated ionized gas, $F^{non-ext}$, is presented as a percentage of the total observed flux, F^{tot}. For M31, we assume that no ionized gas is outside the dust disk. The left panel in Fig. 2.12 shows the impact on our integrated fields in M31 when we add flux from such an additional ionized gas outside the dust disk. Similarly, the right panel shows the impact of that additional ionized gas on the foreground screen model. Even a small amount of flux from the added ionized gas lowers the attenuation enough that we observe values similar to those found by K13.

If 30%-60% of the observed total Hα flux arises from gas which sits outside the dust disk, we can recover the relation observed by K13 within nearby galaxies. This provides a better qualitative fit than simply scaling the foreground screen model by a factor of 3.8, as suggested by K13 (Fig. 2.12, right panel). When the contribution from the additional ionized gas component to the emission is large, our model drops even below the 'mixed' model curve. This is because, unlike the Calzetti model, we are including a component with no attenuation at all in the model. At extreme contributions we would only see the non-attenuated component and measure little to no total attenuation.

It is not expected that the ionzied gas directly associated with HII regions will span large spatial scales, as typical HII region sizes are less than 100 pc (Azimlu et al., 2011). However, a good candidate for the extended ionized gas component we propose here is the diffuse ionized gas.

2.4.2.2 Diffuse ionized gas (DIG) as an additional component

Diffuse ionized gas (DIG, also known as the Warm Ionized Medium or WIM; Reynolds 1971; Walterbos & Braun 1994; Greenawalt et al. 1998; Wang et al. 1999; Oey et al. 2007; Haffner et al. 2009) extends within and outside the galactic disk. Unlike HII regions and most of the dust, which reside within a thin disk and span scale heights of only $\approx$100 pc, the DIG can extend above and below the disk out to kpc scales, similar to the thick disk component (Reynolds 1984; Haffner et al. 2009; Bocchio et al. 2016). Previous studies have shown that the scale height, location and brightness of the DIG follows the brightness and location of star-forming regions (Dettmar 1990; Dettmar & Schulz 1992; Ferguson et al. 1996, 1998; Rand 1998; Wang et al. 1999; Collins et al. 2000; Rand 2005; Heald et al. 2006; Oey et al. 2007). The DIG can be a good candidate for the extended ionized gas, which may lie outside the dust disk and may affect the attenuation. Due to the $\sim$kpc physical resolution observed by K13, they were unable to distinguish the emission arising from HII regions and the DIG.

Physically, the DIG is warmer and less dense than gas in HII regions. In the DIG regions, the [SII]($\lambda6717 + \lambda6731$)/H$\alpha$ ratio is higher (> 0.4, while for the HII regions it is usually < 0.2; Minter & Balser 1998; Haffner et al. 2009). The origin of ionization in the DIG is speculative, but is likely due to a combination of supernova shocks, turbulent dissipation, leaked radiation from nearby OB stars, additional photons provided along channels in the neutral gas, and heating by cosmic rays or dust grains (Reynolds 1990; Reynolds & Cox 1992; Minter & Balser 1998; Madsen et al. 2006; Haffner et al. 2009; Barnes et al. 2014, 2015; Ascasibar et al. 2016).

In M31, Walterbos & Braun (1994) found that after masking all HII regions the DIG flux contributes on average around 40 % of the total Hα flux (or 20 % after extinction corrections). This percentage varies between the observed fields in M31 (Walterbos & Braun 1994) and is observed to vary greatly between galaxies (Haffner et al., 2009).

The DIG fraction we detect in our fields in M31 agrees with the results of Walterbos & Braun (1994); after masking HII regions using an intensity threshold of 2×10^{-16}erg s^{-1}cm^{-2}arcsec^{-2} (as used in Walterbos & Braun 1994), the contribution of DIG flux to the total flux of the fields varies between 40% (Fields 1 and 3) and 70% (Fields 2 and 4). Most of the emission in Field

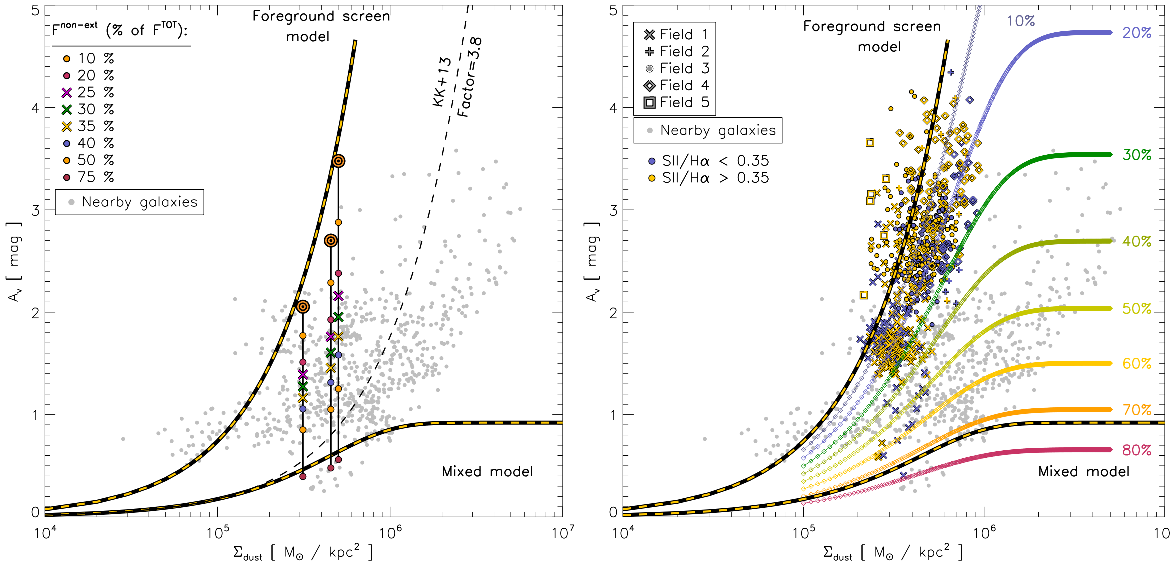

Fig. 2.12 The impact on attenuation when flux from non-attenuated ionized gas ($F^{non-ext}$) is added outside the dust disk. $F^{non-ext}$ is shown as a percentage of the total flux F^{tot}. The left panel shows the impact on A_V for integrated fields in M31 when we add non-attenuated flux. The right panel shows the impact of unattenuated emission on the foreground screen model. The lines on the right panel better reproduce the trend and slope of the K13 data than the scaling factor of 3.8 for the foreground screen model proposed by K13. Some lines are situated below the mixed model limit predicted by Calzetti et al. (1994) as the Calzetti models does not include a contribution from spatially extended, non-attenuated ionized gas. The M31 data on right panel are color-coded according to their [SII]/Hα ratio (yellow for DIG and blue for HII region dominated) .

5 is composed of DIG flux (based on this threshold value). The line ratio of [SII]/Hα is ≈0.5 throughout our fields and the fields observed in Walterbos & Braun (1994) (which are almost 5 times larger).

The intrinsic Hα/Hβ ratio of the DIG is likely to be higher given the higher temperature, but we assume it to be 2.86 for simplicity. Using ITERA[7] (Groves & Allen, 2010), we conclude that the intrinsic Balmer lines ratio of DIG can have values between 2.75 and 3.1, depending on the exact temperature, ionization parameter, magnetic field strength and density. Even if the intrinsic ratio is an extreme value of 3.1, the attenuation values would be lower by only approximately 0.3-0.5 mag from those currently shown in Fig. 2.8, which would not dramatically change our results. Therefore, in the following we assume the same intrinsic ratio while calculating the A_V of the DIG.

2.4.2.3 Effects of different dust-HII-DIG distributions on A_V

The relative distribution and differences in scale heights between HII, DIG, and dust can change our derived attenuation even if the relative amounts stay the same. For example, if both components of ionized gas (DIG and HII regions) have smaller scale heights compared to the dust, the derived $\mathrm{A_V}$ of both components would only correlate with $\Sigma_{\rm dust}$. If the DIG presides outside the dust (i.e. has a larger scale height), the average A_V of the ionized gas (combining both HII region and DIG emission) will be lower for the same $\Sigma_{\rm dust}$. That scenario is equivalent to the one tested in Fig. 2.12 (Sec. 2.4.2.1).

---

[7] **I**DL **T**ool for **E**mission-line **R**atio **A**nalysis

Multiple results indicate the need for more complex dust distribution models within galaxies in order to match simulations and observations (Wong & Blitz 2002; Popescu et al. 2011; Viaene et al. 2017). Wong & Blitz (2002) proposed a "hybrid" model where dust behaves differently in region located in the center/inner and outer disk of galaxies. In the central regions of galaxies, where molecular gas dominates, the dust is more dense and has a smaller scale-height. In the outer regions of galaxies, where the HI gas dominates, the dust is more diffuse and vertically more extended. This complexity in the dust scale height may explain the difference between M31 and the galaxies studied by K13.

If we assume that in M31 the ionized gas (HII and DIG regions) presides within the dust layer (partly mixed with the dust and partly obscured by a dust screen), then the attenuation would follow the slope of the foreground screen model. For the nearby galaxies in K13, we propose that the DIG presides outside the dust and that dust and gas are not mixed. In that case, the non-attenuated flux from the DIG contributes to the already attenuated flux from HII regions (which lie within the dust), and lowers the overall attenuation. It is unlikely that there is no attenuation at all of the DIG component as it is probably mixed with the diffuse dust component in the thick disk (Bocchio et al. 2016, Howk 2012). However, for simplicity we assume that most of the DIG in nearby galaxies do not mix is external to the dust.

In conclusion, unlike the previously used Calzetti models of dust/gas distribution (combining HII regions, stars and dust), our results indicate that by adding a weakly- or unattenuated DIG component to those models, the attenuation can change significantly. The contribution of a DIG component also yields higher [SII]/Hα ratios than in HII regions, which can not be explained by the Calzetti models alone (see Section 4.3). Therefore the contribution of the DIG component and its relative vertical distribution (i.e. scale-height) compared to the dust disk can explain the diskrepancy between the nearby galaxies analyzed by K13 and our result in M31.

2.4.3 [SII]($\lambda6717 + \lambda6731$)/H$\alpha$ vs. $\mathrm{A_V}$ diagram

In the case where the DIG presides outside the dust disk and does affect our observations, we expect areas with higher [SII]/Hα and the same $\Sigma_{\rm dust}$ to have a lower $A_{\rm V}$. There would be no trend between $\mathrm{A_V}$ and [SII]/Hα (at the same $\Sigma_{\rm dust}$) if both components lie within the dust disk.

In Fig. 2.12 our M31 data are color-coded according to their [SII]/Hα ratio (with 0.35 as a threshold). Data points with lower ratio indicate areas with HII regions, while those with higher ratios mark DIG-dominated areas. Our M31 fields do not show a clear trend between the [SII]/Hα ratio and $A_{\rm V}$, with Field 4 even exhibiting lower line ratios for regions lying further

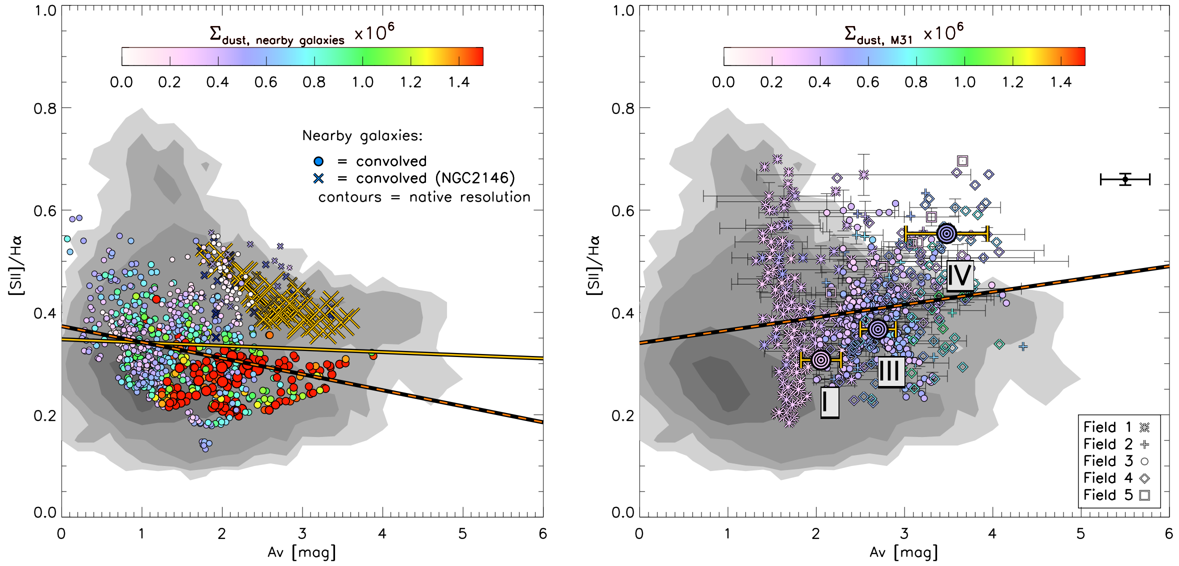

Fig. 2.13 [SII](λ6716+λ6730)/Hα vs. A_V diagrams of nearby galaxies (*left*) and M31 (*right*). Contours on both diagrams represent the K13 data points at native PPaK (24.9″) resolution. *Left*- Convolved (18″ resolution) data points for the K13 nearby galaxies, coloured and in sizes according to $\Sigma_{\rm dust}$. Yellow line shows trend of convolved data of all galaxies while orange dashed line shows the trend of the sample without NGC 2146. *Right*- Convolved (24.9″ resolution) and integrated field data points for M31, also coloured by $\Sigma_{\rm dust}$ values. Orange dashed line shows trends of the convolved data. Error bars are shown for a representative sample of the data, and the median value of all uncertainties (right corner) is also shown.

away from the foreground screen model. Due to possible changes of the intrinsic Balmer lines ratio in DIG dominated spaxels, A_V values of those spaxels could drop by down to 0.3-0.5 mag from those currently shown in Fig. 2.12. K13 showed that there is a trend for a higher [SII]/Hα ratio at lower attenuation in all their galaxies, which they attribute to the fact that HII regions are located within dusty birth clouds (Fig. 4 in K13). As the two lines are very close in wavelength, extinction alone can not account for the change in the [SII]/ Hα line ratio (at A_V=3 mag the change is only 0.02 in the ratio).

Fig. 2.13 shows [SII]/Hα as a function of A_V for regions within nearby galaxies (left panel) and M31 (right panel), color-coded by the dust column density. On both panels, the contours indicate the distribution of the data for nearby galaxies at 2.7″ resolution. On the left panel of Fig. 2.13, the regions within nearby galaxies are convolved to 18″ resolution (spanning physical scales between ≈300 and ≈2000 pc). NGC 2146 (X symbols) is an outlier in this diagram as it has a high inclination, high dust column galaxy, with clear shock driven outflows (Kreckel et al. 2014). On the right panel of Fig. 2.13, our M31 data are shown at 24.9″ resolution (≈100 pc) and the integrated fields.

In general, the change in spatial scales affects our line ratios by diluting the flux from compact, resolved objects like HII regions. HII regions within M31 (with [SII]/Hα < 0.3 at 10pc scales) exhibit higher [SII]/Hα ratios when convolved to 100pc scales. The same diluting effect causes a decrease in the [SII]/Hα ratio for regions dominated by extended DIG emission.

Some areas (20% of all regions and almost half of Fields 2, 4 and 5) are consistent with shock excitation ([SII]/H$\alpha > 0.5$, Kewley et al. 2006), however they also show large uncertainties (due to low S/N as they have low surface brightness).

The left panel in Fig. 2.13 does not show a clear trend for lower attenuation at higher [SII]/Hα ratios. However some of the individual galaxies in the K13 sample (like NGC 3627, NGC 6946 and NGC 3077) do show a weak trend for increased [SII]/Hα towards lower $\mathrm{A_V}$. Shown in the right panel of Fig. 2.13, the M31 data actually suggests an increase of the [SII]/Hα ratio with $\mathrm{A_V}$. However there is a large scatter, and this trend is predominantly driven by variation between the fields, suggesting some dependence on location and physical characteristics of ISM (see section 4.4).

We could miss certain spaxels with both higher [SII]/Hα ratio and $\mathrm{A_V}$ due to faintness of the lines (caused by both low surface brightness and high attenuation). Such spaxels could possibly change the trends seen in Fig. 2.13.

There is a possibility that the gas-phase metallicity has an effect on the global trend in line ratios. Like most galaxies, there exists a radial metallicity gradient in M31 meaning the metallicity increases from Fields 1 to 5 (Table 3 in Kapala et al. 2015; Zurita & Bresolin 2012; Draine et al. 2014). This higher metallicity is associated with the higher DGR and the higher [SII]/Ha ratio. However, this ratio is affected not only by metallicity, but also by ionization parameter and temperature of the gas, and this degeneracy causes issues in the analysis of the ratio and $\mathrm{A_V}$.

Besides the difference in trends, thresholds and biases on $\mathrm{A_V}$, M31 shows higher attenuation at fixed dust mass surface density, and higher [SII]/Hα ratio at fixed $\mathrm{A_V}$ (especially at higher $\mathrm{A_V}$) compared to the other nearby galaxies (as seen on Fig. 2.8 & 2.13). More complicated models are required to better understand the affects of the different relative scale heights of dust, HII regions and DIG on the line ratios and on $\mathrm{A_V}$.

2.4.4 Modeling the impact of geometry

In this sub-section we investigate two simple models that examine how the vertical distribution (scale heights) and intensity of the HII and DIG phases compared to the dust layer can change the observed values and relations between Σ_{dust}, $\mathrm{A_V}$, and the [SII]/Hα ratio.

The first simple model (Fig. 2.14) represents a face-on galactic disk composed of only a thin layer of HII regions (with [SII]/H$\alpha = 0.15$), a uniform dust screen, and a DIG component in front (with [SII]/H$\alpha = 0.75$), all along one line of sight. We took those specific SII/Hα ratio for simplicity, but in a real ISM those values could change. In this model, one resolution element includes emission from an HII region, that suffers an attenuation $\mathrm{A_V}^{real}$ from the dust screen. The emission from the DIG is assumed to be unattenuated. The variables that are changed in the model are: 1) the intrinsic attenuation $\mathrm{A_V}^{real}$ (directly proportional to Σ_{dust}) and

2) the ratio of intrinsic intensities from the DIG and the HII region (parameter X=I^{DIG}/I^{HII}). We emphasize that I^{HII} is not attenuated and can not be associated with the value F^{ext} described in the previous section. By varying these parameters, we can then explore the changes in the observed [SII]/Hα ratio (hereafter labelled S2) and $A_{\mathrm{V}}^{\mathrm{obs}}$. This toy model is insensitive to spatial scales and to the amount of flux, as all variables are relative to each other.

On the left panel of Fig. 2.14, we show the correlation between S2, the intrinsic and observed attenuation, and the ratio of intrinsic intensities from the DIG compared to from HII regions (parameter X). Our model indicates that different combinations of emission from DIG and HII regions can generate the same observed S2 and A_{V} values for a range of dust masses (i.e. $\sim A_{\mathrm{V}}^{\mathrm{real}}$). This is because of the large impact the DIG emission has on the S2 and A_{V} values when the flux from the HII region is highly attenuated. Combining that effect with the dependence of S2 on the dust and the DIG, our model resembles the behavior observed for nearby galaxies (Fig. 2.13). However this model can not explain the data for M31, where we observe high values of [SII]/Hα and A_{V}, nor explain the offset in attenuation between regions at fixed dust mass surface density in M31 and the other nearby galaxies.

The second model (Fig. 2.15) has a more realistic ISM distribution where the layers of DIG and diffuse dust lie on both sides of the HII region and are mixed, as observed by Howk (2012). The left panel shows [SII]/Hα vs. A_{V}^{obs}, while the right panel shows A_{V}^{obs} vs. $\Sigma_{\mathrm{dust}}^{\mathrm{tot}}$. In this model we assume that a certain amount of diffuse dust is mixed with the DIG. The mass of mixed dust is given by the ratio of mixed to total dust mass (parameter Y=$\Sigma_{\mathrm{dust}}^{\mathrm{DIG}}$/$\Sigma_{\mathrm{dust}}^{tot}$). $\Sigma_{\mathrm{dust}}^{tot}$ is equivalent to the total observed dust and it is a sum of the dust layer around HII region which acts as a screen (labeled as $\mathrm{Dust}^{\mathrm{FSC}}$ in Fig. 2.15) and the dust layer mixed with DIG (labeled as $\mathrm{Dust}^{\mathrm{MM}}$ in Fig. 2.15).

On the second model, shown in Fig. 2.15, a case of Y=0 represents the case where the dust is not mixed with DIG and there is no $\mathrm{Dust}^{\mathrm{MM}}$. That is the case similar to the first model shown in Fig. 2.14. When we redistribute the total dust so that some part of it is mixed with the DIG (thus rising value Y), the dust dims the DIG emission and increases the measured attenuation. We present an extra scenario in Fig. 2.15 where there is only DIG and dust and the scale height of the DIG is smaller than the scale height of the dust layer. That scenario shows higher A_{V}^{obs} and higher SII/Hα ratios compared to previous cases. With that scenario, we can reproduce the regions with higher attenuation and higher [SII]/Hα ratio noticed in Fig. 2.12 and 2.13.

Comparing the K13 and M31 data seen in Fig. 2.8 and 2.13 with the models in Fig. 2.14 and 2.15, we notice a complex behaviors and the strong effect the DIG vertical distribution has on the observed A_{V}^{obs} and SII/Hα ratios.

In the nearby galaxies studied by K13, the DIG components could be more extended and not so well mixed with the dust. We draw this conclusion by comparing the observed ratios in Fig. 2.13 with the simple models on Fig. 2.14 and 2.15. The likely difference between those galaxies and M31 is the intensity and relative vertical distribution of dust and DIG.

Unlike K13, the higher spatial resolution data in M31 enables us to clearly distinguish

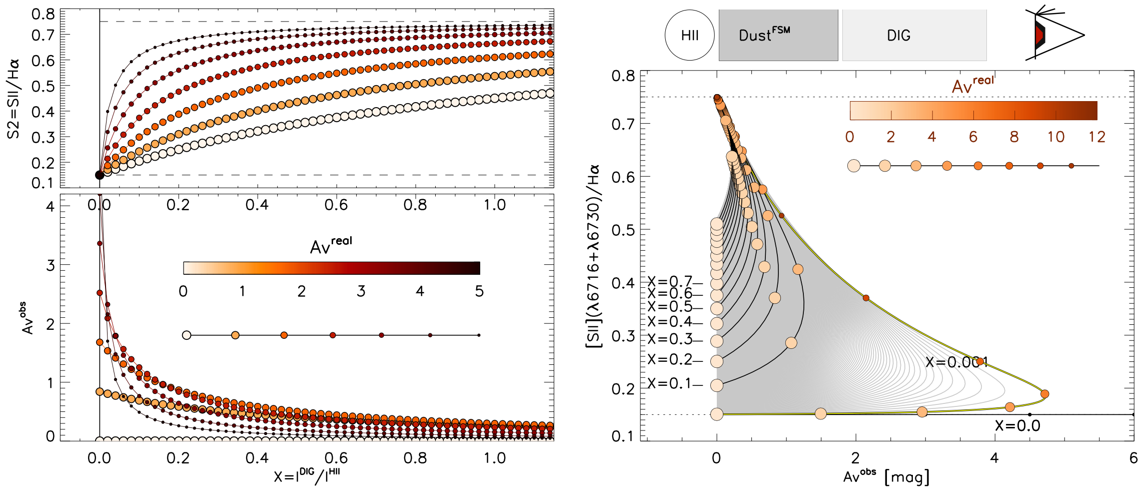

Fig. 2.14 A simplified model (diagram presented above the right panel) that explores the relationship between the observed line ratios and the spatial geometry of dust, HII and DIG regions in LOS of a face-on disk. In this model, between the observer and the HII region (with an intrinsic brightness I^{HII} and S2=[SII]/Hα ratio of 0.15) is a layer of dust screen (labeled as $\mathrm{Dust}^{\mathrm{FSC}}$ and proportional to $\mathrm{A}_{\mathrm{V}}^{\mathrm{real}}$) and DIG (with an intrinsic brightness $\mathrm{I}^{DIG} = X{\cdot}\mathrm{I}^{HII}$ and S2=0.75). *Left-* As an input to the model, we have the amount of dust ($\mathrm{A}_{\mathrm{V}}^{real}$), upper and lower limits of S2 (0.15 and 0.75) and ratio between HII and DIG intensity (or X). The correlation between those parameters (upper left panel) and the resulting observed attenuation $\mathrm{A}_{\mathrm{V}}^{obs}$ can be seen in the lower left panel. Notice that the observed attenuation does not follow the real attenuation and that there are overlaps where one value of $\mathrm{A}_{\mathrm{V}}^{obs}$ can have multiple values of Σ_{dust} (depending on X). *Right-* The correlation between the observed S2=[SII]/Hα ratio and the observed attenuation $\mathrm{A}_{\mathrm{V}}^{obs}$ with different ratios of DIG and HII intensities (shown as X) and different values of Σ_{dust} (shown through $\mathrm{A}_{\mathrm{V}}^{real}$). Notice the resemblance between this image and those on the left panel of Fig. 2.13. See text for more details.

between compact HII regions and those regions with dust and DIG only. Our results indicate that the DIG component in M31 could be smaller in intensity and scale height, and be well mixed with the dust layers in the disk. An additional layer of diffuse dust, extending to even larger scale heights than the DIG, would increase the attenuation even more.

The high inclination of M31 likely plays an additional role in increasing the attenuation. Nevertheless, K13 did not report any significant correlation or change in their relation with inclination. For example, the highly inclined galaxy NGC 3627 (similar to M31) shows lower Av than M31, while NGC 4321 has higher Av values despite its lower inclination (30°) and similar Σ_{dust} as NGC 3627. NGC 2146 and NGC 7331 are both highly inclined (60° and 70° as M31) but have slightly lower A_{V} value than those seen in M31.

2.4.5 Effects of location on the relative vertical distribution of dust and DIG

Given these findings, the question that arises is: why in M31 do we observe a different mixture and scale heights between all three components (DIG, HII regions and the dust) compared to other galaxies? To explain this, we consider the effects of probing different locations within

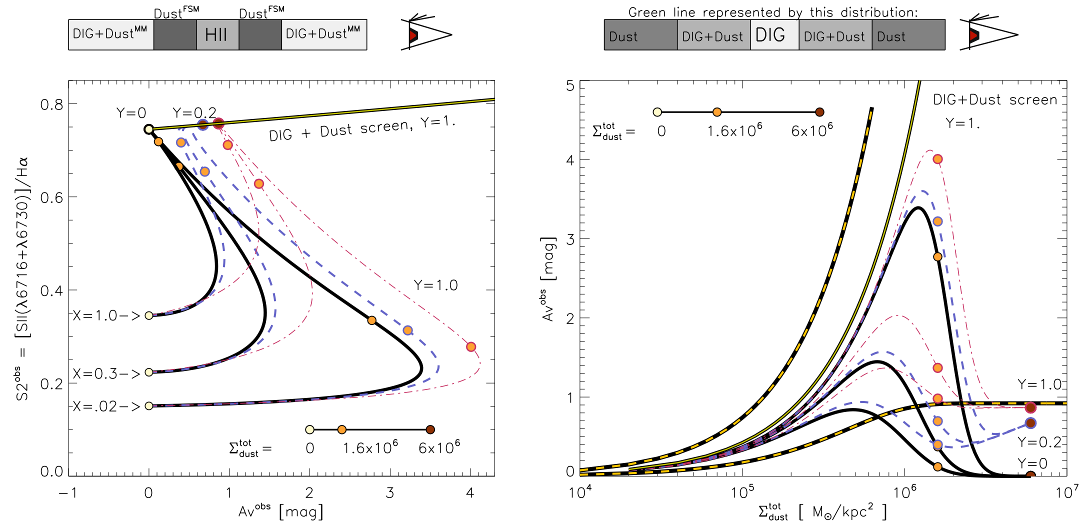

Fig. 2.15 A second model (left panel on top), similar to the previous model (Fig. 2.13), but with a more realistic ISM distribution: DIG (mixed with the diffuse dust layer) and the dust screens lie on both sides of the HII region. The left panel shows [SII]/Hα vs. A_V^{obs}, while the right panel shows A_V^{obs} vs. Σ^{tot}_{dust}. The diagrams show the relationship between the observed attenuation (A_V^{obs}), the [SII]/Hα ratio (S2) with the model variables: the observed total dust column density (Σ^{tot}_{dust}), the relative intensities of the DIG and HII regions (X=I_{DIG}/I_{HII}), and the ratio of the dust mixed with DIG to the total dust column (Y=$\Sigma^{DIG}_{dust}/\Sigma^{tot}_{dust}$). We assumed the same specific intrinsic S2 values for the gas in HII and DIG as in Fig. 2.14. Values of Y=0, 0.2 and 1.0 are shown in black (full), blue (dashed) and red (dot-dashed) lines. We also include the green, full line that represents a scenario (shown above the right panel) where the 90% of DIG is mixed with dust (while 10% lie in the center and is not mixed with dust). This scenario also assumes length of the dust layer twice as large as the length of the ionized gas layer, thus representing our assumption about dust/gas distribution of M31. With this scenario we can reproduce the regions with higher A_V^{obs} and SII/Hα ratios seen in Fig. 2.13.

the galactic disk.

We note that the locations and radii of the fields observed in M31 and in K13 are different. In M31, we observe five small fields within the spiral arms of M31, where the most central field is still ∼6 kpc from the galaxy center (equal to 0.28 R_{25}; Tab. 2.1, Zurita & Bresolin 2012; de Vaucouleurs et al. 1991). The regions observed by K13 are more central (< 0.2 R_{25}, except for one galaxy with < 0.4 R_{25}), and composed of bulges, spiral arms and inter-arm regions. The global SFR and Σ_{SFR} for the nearby galaxies studied by K13 are much higher than that of M31 (SFR ~ 1 $M_\odot$ yr^{-1}; Williams 2003) and the observed fields ($\Sigma_{SFR} \sim 0.01$ $M_\odot$ yr^{-1} kpc^{-2}; see Fig. **??** in Appendix B).

If we assume that the dust follows the gas, as seen in Hughes et al. (2014b) and Holwerda et al. (2012) with some dependence on dust temperature, then we can argue that the scale height of the dust is equal to the gas scale height and follows it. In several observations the scale heights of the gas has been found to increase with galactic radius (Sancisi & Allen 1979; Braun 1991; Rupen 1991; Scoville et al. 1993; Olling 1996; García-Burillo et al. 1999; Wong & Blitz 2002; Matthews & Wood 2003; O'Brien et al. 2010; Velusamy & Langer 2014; Yim et al.

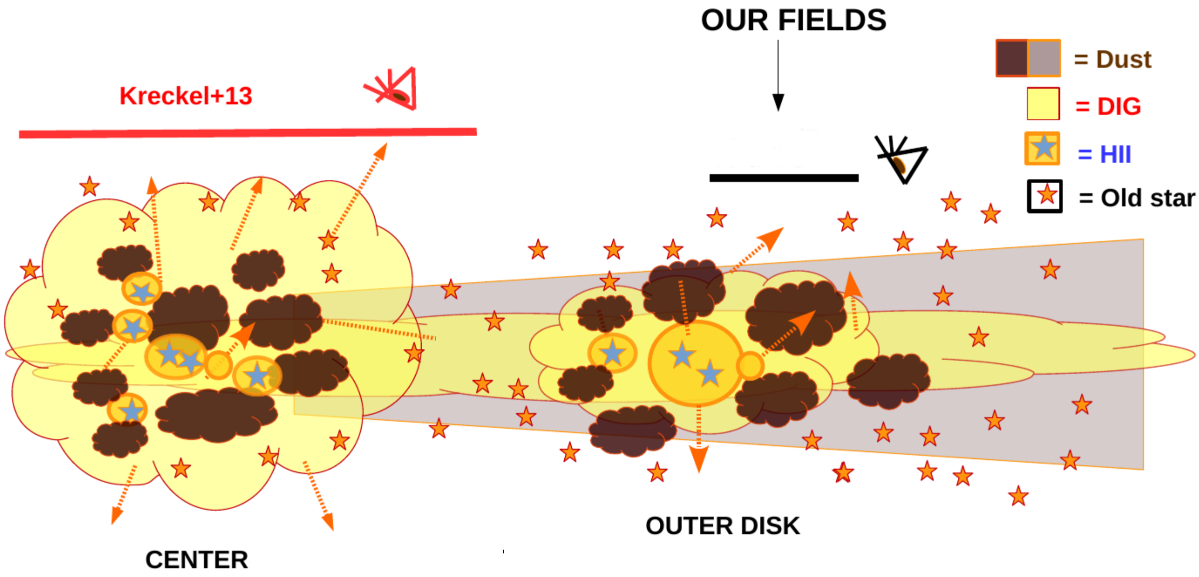

Fig. 2.16 A schematic image of the relative distribution of dust (dark brown clouds and light brown layer), HII (dark yellow circles around young blue stars) and DIG (light yellow layer) regions in a galactic disk. We show the old stars (orange stars), and label the galactic center and the outskirts of the disk. We also indicate a position of the fields and inclinations at which the nearby galaxies (red line; Kreckel et al. 2013) and M31 (this work) were observed.

2014; Zschaechner & Rand 2015). The increase of the gas scale height can be understood via the gravitational and hydrodynamical equilibrium of the gas, and its dependence on gas vertical velocity dispersion, stellar volume density and gas surface density (Koyama & Ostriker 2009; Pety et al. 2013). If the dust and molecular gas are correlated, then this mean that the dust scale height is rising with galactic radius.

On the other hand, the DIG scale height and intensity are correlated with the number and brightness of HII regions and star formation activity (Dettmar 1990; Rand 1996; Wang et al. 1999; Collins et al. 2000; Oey et al. 2007). Numerous, brighter star-forming regions that are more energetically active (Tyler et al. 2004; Yasui et al. 2015) can affect the production, destruction and distribution of dust and also the ionization of the DIG. This can result in a more prominent and extended DIG component. Moreover, Dettmar (1990) noticed a decrease of the Hα scale height with galactic radius (with the highest scale height seen in the starburst regions in the center). We argue that if the scale height of the DIG is proportional to the star formation intensity, then the decrease of star formation with radius would indicate a decrease of the scale height of DIG component. Schruba et al. (2011), Regan et al. (2006) and Bigiel et al. (2010) found the Hα, FUV and 8 μm emission (both correlated to star formation) are decreasing with galactic radius and have their highest values in the centers of galaxies. Furthermore, García-Burillo et al. (1999) noticed the existence of Hα chimneys spanning the extra-planar area from the galactic center with scale height larger than that of the CO.

Since the dust scale height is likely to increase with galactic radius while the DIG scale height should decrease with galactic radius, differences in the relative DIG/dust geometry and scale heights of galaxy centers (as in K13 galaxies) and galactic outskirts (as in M31) may explain the differences in our derived attenuation. We depict this variation in the vertical distribution of three components of the ISM (dust, HII regions, and DIG) at different galactocentric distances in Fig. 2.16. We also indicate the position of observed fields, and inclination at which M31 and other nearby galaxies were observed.

2.5 Wider implications

In order to determine the spatial distribution of dust compared to the ionized gas, we use the models derived by Caplan & Deharveng (1986). The only components of that model are the dust and ionizing stars and their spatial configuration that affects the observed attenuation (Caplan & Deharveng 1986; Calzetti et al. 1994). Our results (Fig. 2.8) show that the regions we observe in M31 follow closely a foreground screen model, while K13 showed that most of the regions they selected in a sample of nearby galaxies fall between the mixed and screen models. Furthermore, Liu et al. (2013) in M83 find that the data points of the central region follow more a mixed model, while the outer regions are in agreement with a foreground screen model. Tests show that neither inclination (K13) nor changes in spatial scales (Fig. 2.10) can explain the differences between those results. However, by degrading the spatial resolution of the data (toward $\geq$100-200 pc scales) in the central region of M83, Liu et al. (2013) showed that their data begin to follow more closely a foreground screen model. While such results are suggestive, their interpretation should be done in caution, given the large uncertainties, large scatter in the data and the small separation of the models in the diagrams.

Our observation of varying [SII]/Hα line ratios and modeling of the impact of the relative vertical distribution of dust and DIG shows that the DIG component needs to be accounted for in the models of Caplan & Deharveng (1986), Calzetti et al. (1994) and Wong & Blitz (2002). From our observations (Fig. 2.8, 2.12 and 2.13) and simple models (Fig. 2.14 and 2.15), we conclude that the differing scale heights of dust and gas in galaxies plays a large role in the measured extinction.

In general, we argue that the star-forming regions are born in a cocoon of dust, with the formed massive stars clearing the dust over time (Dreher & Welch 1981; Verley et al. 2010). The varying scale heights of dust and ionized gas (HII regions and DIG) with radius in galaxies can change the measured attenuation. At large galactocentric distances, especially in M31 with its low star formation rate, the HII regions remain embedded in their dusty cocoons that act as foreground screens. The DIG component is not as prominent in intensity or scale height. The DIG in M31 is well mixed with the thin dusty disk and additionally attenuated by the diffuse dust layer that acts as a screen. The high inclination of M31 also contributes to the higher attenuation.

On the other hand, in the more central and more active regions of galaxies (as in K13), the dust may be blown away by the numerous bright star-forming regions. The DIG will also be more prominent and extended, with a scale height larger than the scale height of dust. This leads to the DIG being less attenuated by dust and causing it to have a larger effect on observations of attenuation.

2.6 Summary

Using IFS and IR photometry in five 680 pc × 900 pc fields in M31, we explore the relative spatial distribution of dust and ionized gas. This is done at $\sim$100 pc scale resolution by comparing the attenuation ($\mathrm{A_V}$) determined from the Balmer decrement and the dust mass surface density determined from fitting to the IR SED photometry (Σ_{dust}). We compare the results with two widely used theoretical models of the dust distribution (mixed and screen models, Calzetti et al. (1994)) and with previous results from the literature for eight nearby galaxies (Kreckel et al. (2013), K13).

Our results show that the dust is approximately distributed as an uniform screen around the ionized gas in M31 (Fig. 2.8). This is distinct from the galaxies observed by K13, which show attenuations between those predicted by the mixture of the foreground screen model and the mixed model (where the dust is uniformly mixed with the gas).

Variations in the spatial resolution do not appear to explain the differences in the measured attenuations (Fig. 2.10).

The contribution from a small amount of non-attenuated gas emission in front of the dust disk can significantly lower the observed attenuation (Fig. 2.12). This can lead to biases in observations of nearby galaxies. This additional gas can be associated to the diffuse ionized gas (DIG).

We also analyze the observed [SII]/Hα ratio and its correlation with $\mathrm{A_V}$ (Fig. 2.13). Although our data do not show a clear trend, we found a difference in behavior between M31 and the nearby galaxies in K13. The M31 data show a slight increase of the ratio with $\mathrm{A_V}$, while the K13 galaxies show the opposite trend.

Using two simple models, we explore the relationship between the observed line ratios and the relative spatial geometry of the dust, HII regions and DIG gas (Fig. 2.14 and 2.15). These models indicate that the relative vertical distribution and contribution of the DIG and the dust play a crucial role in changing the observed [SII]/Hα and $\mathrm{A_V}$ values at given values of the total dust column.

The difference in the results of M31 and K13 can be explained by the fact that the M31 fields lie at large galactocentric distances, whereas the K13 span fields which are in the centers of the galaxies. These differences in distances are associated with differences in the scale heights of the dust, DIG and HII regions which impact the measured attenuation.

Chapter 3

"You need a name. I heard some interesting ones today; perhaps you'll like one."
He mentally ran through the list Brom had given him until he found the names that stuck him as heroic, noble and pleasing to the ear.
"What do you think of Vanilor or his successor, Eridor? Both were great dragons."
"No", said the dragon. It sounded amused with his efforts. *"Eragon"*.
"That's my name; you can't have it," he said, rubbing his chin.
"Well, if you don't like those, there are others."
He continued through the list, but the dragon rejected every one he proposed. It seemed to be laughing at something Eragon did not understand, but he ignored and kept suggesting names.
"There was Ingothold, he slew the..." A revelation stopped him.
"That's the problem! I've been choosing male names. You are a she!"
"Yes". The dragon folded her wings smugly.

Eragon and dragon Saphyra
"Eragon" by Christopher Paolini

3. Calibrating the SFR prescriptions at sub-kpc scales in M31

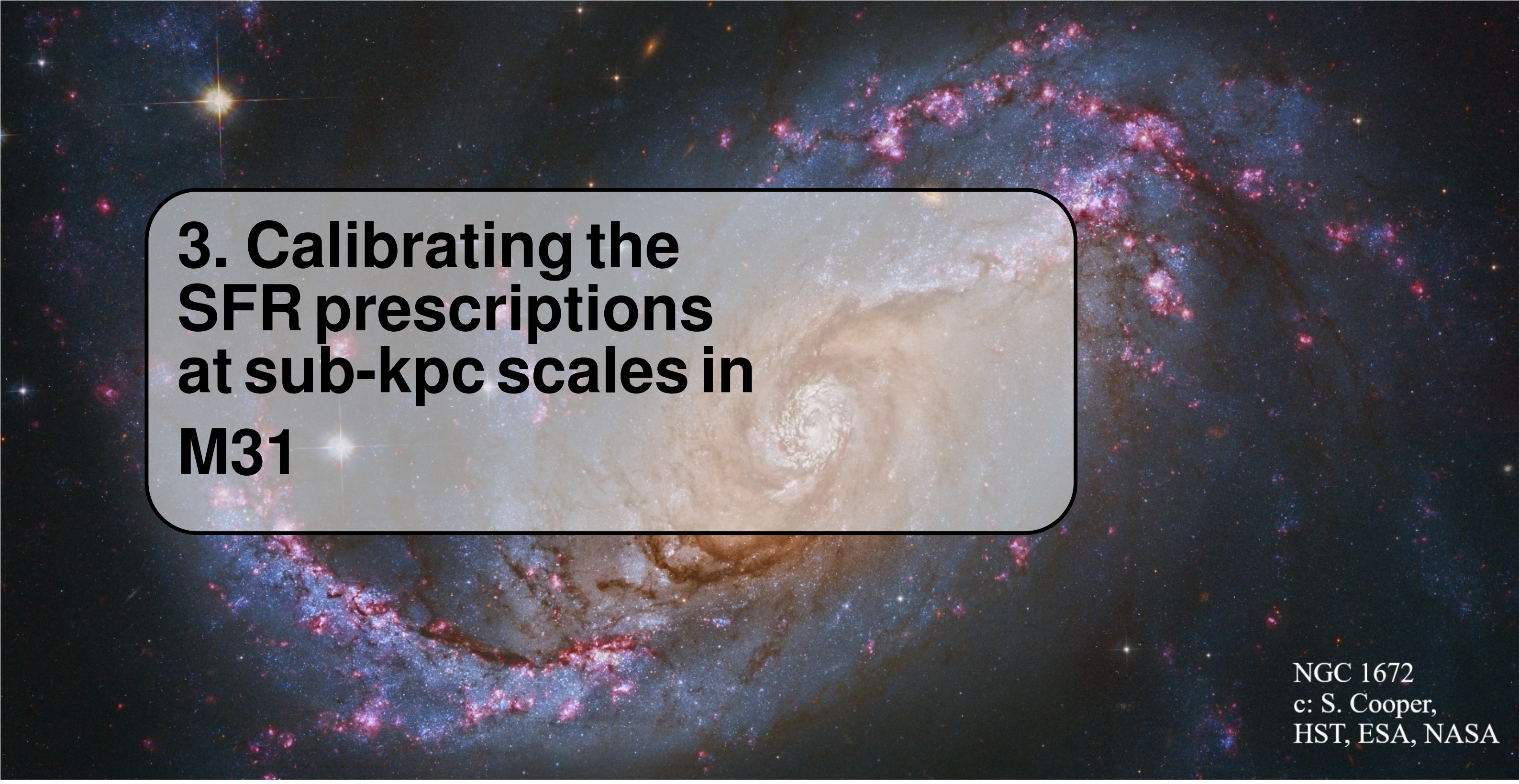

NGC 1672
c: S. Cooper,
HST, ESA, NASA

This chapter is published in a refereed article "Calibrating star-formation rate prescriptions at different scales (10 pc to 1 kpc) in M31", Tomičić et al. (2019), for which I am the lead author and which has been adapted for this thesis.

Overview: Following the last chapter, where the Balmer line attenuation of M31's fields was measured, in this chapter we will use this attenuation to estimate the extinction corrected Hα flux (3.2.4) and use it as a reference star formation rate tracer. In section 3.2, we describe how the data were calibrated and present maps of different star formation tracers. With this tracer, we calibrate the star formation rate prescriptions (3.4) at various spatial scales in M31 by combining it with infrared and far-ultraviolet images of M31. In the same section, we also test the effects of varying spatial scales and subtracting the diffuse emission. In section 3.5, we demonstrate a possible connection between the dust temperature, inclination, and galactocentric distance and the SFR prescriptions. discussion and summary are in Sections 3.6 and 3.7.

3.1 Introduction

As discussed in Chap. 1, understanding the rate and location of star formation (SF) is crucial to constrain the SF laws and to understand what physical processes are driving SF (Schmidt 1959, Robert C. Kennicutt 1998, Kennicutt et al. 2003, Murphy et al. 2011). Reliable star formation rate (SFR) tracers are needed to properly quantify the SF activity. The single SFR tracers, such as the far-ultraviolet (FUV) emission, optical emission lines from the ionized gas (Balmer lines) and infrared (IR) emission, alone underestimate SFR values due to being obscured by the dust, or not tracing directly the young stars or the ionized gas (see Sec. 1.3). Therefore, combining the obscured (UV and optical) and un-obscured (IR) tracers results in the total SFR (Kennicutt et al. 2003; Calzetti et al. 2005; Wu et al. 2005; Calzetti et al. 2007; Thilker et al.

2007; Tabatabaei & Berkhuijsen 2010; Leroy et al. 2012; Davis et al. 2014; Catalán-Torrecilla et al. 2015). The combination of tracers are often referred to as “hybrid” SFR prescriptions, while single tracers are “monochromatic” prescriptions.

Much of the work done in determining the calibration of monochromatic or hybrid SFR prescriptions, which use emission lines from the ionized gas, has two major caveats. The first caveat is that the imaging of emission lines based on broadband and narrowband filters does not account for underlying stellar absorption lines, or for contamination from neighboring emission lines (see Sec. 1.3.5). However, recent progress in integral field unit (IFU; Barden & Wade 1988) spectroscopy resolves individual spectral lines and the underlying stellar continuum, enabling accurate mapping of Balmer emission lines (Kapala et al. 2015; Catalán-Torrecilla et al. 2015; Davies et al. 2016).

The second caveat comes from the low spatial resolution of existing studies, which mostly probe the ISM at 0.5-1 kpc scales or at galactic scales (Robert C. Kennicutt 1998,Calzetti et al. 2005,Salim et al. 2007,Thilker et al. 2007,Jarrett et al. 2012,Leroy et al. 2012,Catalán-Torrecilla et al. 2015,Jarrett et al. 2017). For comparison, active star-forming regions (i.e. HII regions) typically have sizes between 30 pc and 200 pc (Issa 1981; Azimlu et al. 2011). Hence, extragalactic studies of the SFR rate have been unable to resolve HII regions, mixing HII regions and regions without star formation, e.g., diffuse ionized gas (DIG; Haffner et al. 2009) and ”IR-cirrus”[1]. A contribution from the DIG and mid-IR cirrus, and additional ultra-violet emission from older stars may change the SFR prescriptions. Moreover, different regions within the kpc-sized beam may differ in their physical (temperatures, stellar and ISM densities), chemical (metallicities) and morphological (distribution) conditions. For example, Eufrasio et al. (2014) observed the interacting galaxy NGC 6872 with 10 kpc size apertures and found variations in the FUV-IR conversion factor that are correlated with regional differences in stellar populations. Similarly, Boquien et al. (2016) studied eight nearby galaxies at kpc scales and found that the SFR prescription changes with stellar surface density, rather than with the dust attenuation or SFRs. The best spatial resolution (at 30 pc) achieved by extragalactic studies of SFR are from observing galaxies in the local group (Hony et al. 2015; Boquien et al. 2015).

In this chapter, we will calibrate the SFR prescription by using maps of different SFR tracers (FUV, Hα, and IR) in 5 fields of the Andromeda galaxy (M31). Due to its proximity (≈ 0.78 Mpc), we can achieve good spatial resolution (10 pc). Our fields are 0.6 kpc$\times$0.9 kpc in projected size, which enables us to test the SFR prescriptions at various spatial scales and to spatially resolve the HII regions. In addition, we will use IFU spectral data in order to map multiple Balmer lines and measure the extinction corrected Hα emission to use as our baseline SFR tracer.

There are a few main goals of this paper. First, we will test the reliability of extinction corrected Hα (labeled as Hα,corr) as a SFR tracer. Secondly, we will study the behavior of different monochromatic and hybrid SFR tracers (22 μm, 24 μm, Hα+22 μm, Hα+24 μm, FUV+22 μm, FUV+24 μm, 12 μm, 70 μm, 160 μm and total infrared) at different spatial scales (from 10 pc to 750 pc). We will also test how the diffuse components affect SFR prescriptions. Finally, we will test if a (3-dimensional) dust/gas distribution play a role in changing the SFR prescriptions in M31 by looking how it changes as a function of galactocentric distance, inclination, and the dust temperature.

---

[1] IR-cirrus refers to the diffuse component in mid-IR images, which corresponds to emission re-radiated by dust heated by older stellar populations (Leroy et al. 2012).

3.2 Data

M31 is a nearby ($\sim$780 kpc; Stanek & Garnavich 1998) and massive (stellar mass of $\approx 10^{11}$ $M_\odot$; Geehan et al. 2006) SA(s)b galaxy (Corwin et al. 1994), which makes observing the interstellar medium (ISM) at high spatial resolution possible. The inclination of the galaxy is $\sim$70° (Henderson 1979, Courteau et al. 2011 , Dalcanton et al. 2012) and R_{25} $\approx$20.5 kpc [2] (Zurita & Bresolin, 2012). The galaxy also shows ring-like structures at galactocentric distances of 6, 10 and 15 kpc (Gordon et al. 2006).

We use integral field unit (IFU) data from 5 fields (each with a projected size of $\approx$600 pc $\times$ 900 pc; see Fig. 2.1 and 3.3), chosen to cover a range of star formation rates and environments. Positions, radial distances, and metallicities of the 5 fields are tabulated in Table 2.1 and shown in Figure 2.1.

The IFU spectroscopic data provide Hα line maps that are combined with 22 μm, 24 μm and FUV images. We use FUV emission for our SFR calibration instead of NUV because FUV traces younger stars (<30 Myr old), while NUV can also be emitted by older stars. We adopt WISE maps for the 22 μm (Wright et al., 2010), MIPS maps for the 24 μm data (Spitzer; Rieke et al. 2004, Engelbracht et al. 2007), and GALEX (Martin et al. 2005) for the FUV data. A benefit of using the GALEX and WISE observations for FUV and 22 μm is that thay are from all-sky surveys so the derived calibrations can be applied, taking into account the caveats discussed in this paper, to other extragalactic objects in the sky. Additionally, we will also calibrate other tracers, including 12 μm (near-IR tracer of PAH[3]), 70 μm, 160 μm (tracing cold dust) and total IR (TIR). All images are Nyquist-sampled with $\approx$3 pixels across the instrumental point spread function (PSF). We refer to the full width at half maximum (FWHM) of the PSF as the native angular resolution for each tracer. The observed wavelength, (best achieved) angular resolution, and pixel size for each instrument are listed in Table 3.1. The units of the FUV and mid-IR images are flux densities per pixel (F_λ for FUV and F_ν for IR). The final intensity maps (in units of erg s^{-1} cm^{-2} arcsec^{-2}), used in this chapter, are defined as F_λ (F_ν) maps that are devided by their pixel sizes (in arcsec^2) and multiplied by their effective wavelengths (frequencies). For the calibration of the SFR prescriptions, we will consistently use and show de-projected surface brightness values of the tracers throughout this chapter, assuming M31's inclination[4].

---

[2] R_{25} is the radius at which the observed optical intensity is equal to 25 mag in the B band.

[3] Polycyclic aromatic hydrocarbon molecules.

3.2.1 WISE 22 μm and SPITZER 24 μm images

For the 22 μm images, we use maps from the *Wide Field Infrared Survey Explorer* (WISE; Wright et al. 2010). The six-degree-wide maps were constructed to preserve the native resolution of WISE W4 images using a drizzle technique (Jarrett et al. 2012). As described in Chauke (2014) and Jarrett et al. (2017), foreground Galactic stars were identified and removed, and the satellite galaxies M32 and M110 were subtracted from the final set of images. The mean background "sky" level was measured 2.8° radius from the center of M31, and globally subtracted from the final set of images. For the flux calibration, we used the prescription given by Cutri et al. (2011), while using 7.871 Jy as the flux value for Vega (Brown et al. 2014; Jarrett et al. 2017). The uncertainty maps are composed and calculated from instrumental flat-field errors (1% of intensity value), Poisson errors and the sky background errors.

The 24 μm images are from the MIPS instrument on the *Spitzer Space Telescope* (Rieke et al. 2004, Werner et al. 2004,Engelbracht et al. 2007). We use the maps presented by Gordon et al. 2006. Unlike the 22 μm maps, the PSF of the 24 μm maps presents bright secondary Airy rings (Rieke et al. 2004, Kennicutt et al. 2007, Engelbracht et al. 2007, Temim et al. 2010, Aniano et al. 2011). These may present a problem when analyzing ISM features on the 24 μm maps at the highest resolutions. After carefully analyzing the shape of the PSF, we conclude that 90% of the flux of the source is contained within the first Airy ring.

We check how similar the 22 μm and 24 μm maps are, to evaulate whether the hybrid prescriptions would change when using different mid-IR tracers. The comparison shown in Fig. 3.1 demonstrates a tight correlation, implying that the two mid-IR maps match when convolved to the same resolutions. That is expected because the instruments' filters have a similar wavelength coverage (Wright et al. 2010; Jarrett et al. 2011). However, we find that the 22 μm data has 0.03 dex higher flux densities compared to 24 μm, with 0.05 dex scatter. A small fraction ($\approx$ 5% or less) of the pixels are brighter (≈ 0.1 dex brighter) in 24μm than in 22μm. This minor difference could be due to the different PSFs of the two instruments. We conclude that the hybrid SFR prescription would not change appreciably if we replace one mid-IR tracer with the other.

In the following sections, we will convolve the maps to larger spatial resolutions and use integrated intensities in apertures with a minimum radius of 13" to better sample the entire flux of compact sources (Kennicutt et al. 2007).

---

[4] We multiply the area of each pixel or aperture by a factor of 4 to correct the minor axis for the inclination. We estimate corrections following Eq. 1 in van den Bergh (1988).

Table 3.1 Instrument, wavelength coverage, effective wavelength, angular resolution, spatial resolution and size of pixel of datasets used.

Instrument Name	$\Delta\lambda$ (μm)	λ_{eff} (μm)	angular res. (arcsec)	spatial res. (pc)	original size of pixel (arcsec/pix)
PPaK IFU (Calar Alto)a	$0.37 - 0.7$	0.5	2.7	10	1
W4, 22 μm (*WISE*)b	$20 - 26$	22.1	11.9	45	4.4
MIPS 24 μm (*Spitzer*)c	$21.5 - 26.2$	24	6.4	24	2.4
FUV (*GALEX*)d	$0.135 - 0.175$	0.154	4.5	17	1.5
		Additional tracers:			
W3, 12 μm (*WISE*)b	$7 - 18$	11.6	6.6	23	2.2
PACS 70 μm e	$60 - 85$	71	5.7	20	2
PACS 160 μm e	$120 - 210$	160	11	40	4.2

SLIM survey; Kapala et al. (2015).
Jarrett et al. 2018; submitted.
Gordon et al. (2006).
Thilker et al. (2005).
Groves et al. (2012b).

3.2.2 Other IR tracers: WISE 12 μm, PACS 70 μm and PACS 160 μm data

In this chapter, we will test the SFR prescription as a function of the dust temperature and of the fraction of emission from the cold dust, which may indicate if our data originate from the dust dominantly heated by old stellar population instead of HII regions (Groves et al. 2012b; Ford et al. 2013). PACS 70 μm and PACS 160 μm maps (Poglitsch et al. 2010) are used to measure the 70 μm/160 μm ratio, which traces the dust temperature, and the 160 μm/TIR ratio, which indicates the fraction of emission from the cold dust. The reduction procedure is described in Groves et al. (2012b). The noise level of the PACS 70 μm (160 μm) maps is $7.5 \cdot 10^{-5}$ Jy arcsec^{-2} ($1.6 \cdot 10^{-3}$Jy arcsec^{-2}). We subtract the background using 10 apertures (R≈90”) outside the galaxy (at least ≈ 5 arcmin from the second ring in M31). We also use the WISE 12 μm map (W3 band), which is calibrated in a similar way as the WISE 22 μm map (described in Sec. 3.2.1).

3.2.3 GALEX FUV data

The FUV mosaic images were observed with *The Galaxy Evolution Explorer* (*GALEX*; Martin et al. 2005). Details of the observations and calibration are described in Thilker et al. (2005), Morrissey et al. (2007) and Thilker et al. (2007).

For the sky subtraction, we use 100 apertures (75”×75” in size) positioned around M31 (minimum of 5 arcmin from the second ring in M31). The mode of 100 aperture mean values is used as the background value, which is $\approx 1.3 \cdot 10^{-15}$ erg s^{-1} cm^{-2} arcsec^{-2} for the FUV images. The noise level of the FUV images is $\approx 2 \cdot 10^{-16}$ erg s^{-1} cm^{-2} arcsec^{-2}. Additionally, we correct the UV maps for MW foreground extinction using the Cardelli et al. (1989) extinction curve (CCM), assuming $\mathrm{R_V}$ =3.1 (Clayton et al. 2015) and using $\mathrm{E_{B-V}}$ =0.055 (Schlafly & Finkbeiner 2011). Peek & Schiminovich (2013) found that the foreground extinction of FUV should be 30% higher compared to the extinction derived by the CCM extinction curve. If we apply that correction, the extinction corrected FUV emission in M31 would increase by ≈10% (0.05 dex), and only have a minor effect on calibrating the SFR prescriptions. For the uncertainty maps, we follow the prescription described by Morrissey et al. (2007) and Thilker et al. (2005). The background sky uncertainty ($\approx 2 \cdot 10^{-17}$ erg s^{-1} cm^{-2} arcsec^{-2}) is added in quadrature to the instrumental uncertainty.

3.2.4 Optical Hα data

The optical IFU spectral data in this chapter are introduced in Sec. 2.2.1 (in Chap. 2), and were previously used by Kapala et al. (2015), Kapala et al. (2017) and Tomičić et al. (2017) as a part of the Survey of Lines in M31 (SLIM) project. The observation and calibration of the data and the derivation of Balmer emission lines are described in detail in Sec. 2.2.1, and in Kreckel et al. (2013), Kapala et al. (2015), Tomičić et al. (2017), and Tomičić et al. (2018).

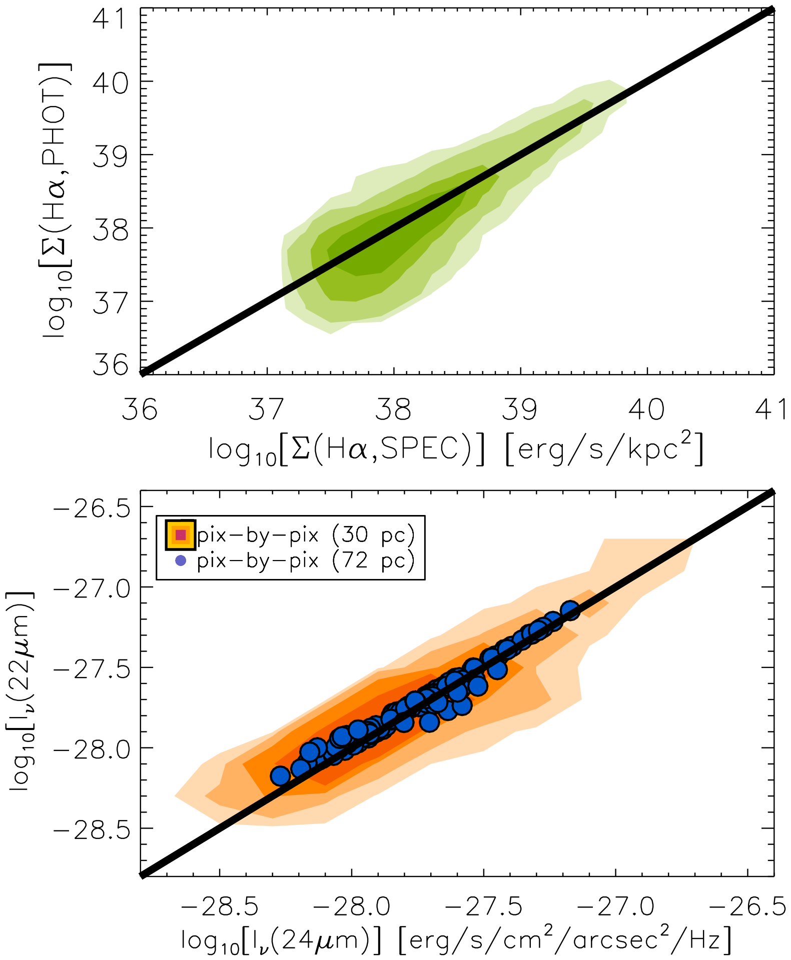

Fig. 3.1 *Top-* Pixel-by-pixel comparison between spectroscopic and photometric Hα surface brightness values (upper panel). The photometric narrowband *Hα+NII* images were taken from the Survey of the Local Group of Galaxies.
Bottom- Pixel-by-pixel comparison between the intensities of MIPS 24μm and WISE 22μm, at 25" (red contours) and 65" (blue filled circles) resolution. The 1-to-1 line is plotted in black. Generally, the data from the two instruments are equal except at lower fluxes. Some data points show slightly higher 24 μm values. The difference between the two images decreases with increasing pixel size. For details about the IR maps, see Sec. 3.2.1.

We needed to test if our Hα line fluxes are correct in order to use that emision line as a reliable SFR tracer. Therefore, we checked our flux calibration by comparing SDSS *r*-band images to bandpass matched images extracted from the IFU spectra. We estimate that our flux calibration is accurate within 0.06 dex scatter for the bright regions ($> 7 \times 10^{-18}$ erg s^{-1} cm^{-2} arcsec^{-2}) and is offset 0.11 dex with 0.08 dex scatter for the low-brightness regions ($< 7 \times 10^{-18}$ erg s^{-1} cm^{-2} arcsec^{-2}).

Additionally, in Fig. 3.1 we compared narrowband *Hα+NII* images from the Survey of the Local Group of Galaxies to the Hα+NII bandpass matched images extracted from the IFU spectra. While comparing these images, we assumed NII/Hα=0.4 ratio (as in Azimlu et al. 2011), although our spectral analysis indicates that ratios actually range from 0.2 to 0.6. The narrowband images agree within 0.1 dex scatter in the bright regions ($> 5 \times 10^{-16}$ erg^{-1}cm^{-2}arcsec^{-2}),

Table 3.2 Top: Resolutions and projected spatial sizes of the maps used. Bottom: distances of apertures used.

Maps		
Resolution (arcsec)	pixel size (pc)	pixel size (arcsec/pix)
≈ 6	7	2.4
11.7	13	4
25	30	10
65	72	20
Integrated	600-900	180-270

Apertures	
Radius in arcsec	projected radius in pc
13.5	50
27	100
55	200

with negligible scatter. The low-brightness regions ($< 5 \times 10^{-16}\,\mathrm{erg}^{-1}\mathrm{cm}^{-2}\mathrm{arcsec}^{-2}$) are offset by 0.07 dex with 0.15 dex scatter. These offsets are consistent with the quoted uncertainties from the literature (Massey et al. 2007; Azimlu et al. 2011).

3.2.5 Convolution & apertures

In this paper, we will show the impact of varying spatial scales on the SFR tracers and the SFR prescriptions. The calibration of the SFR prescriptions is done using two approaches.

The first compares pixels in the maps at matched angular resolution. We also test SFR prescriptions using integrated fields, i.e. treat an entire field (with a projected size of $\approx 0.6\,\mathrm{kpc} \times 0.9\,\mathrm{kpc}$) as one single aperture. When we change the resolution of the maps, we convolve and re-bin the maps using convolution kernels, pipeline, and procedures from Aniano et al. (2011). In the case of IFU data cubes, we convolve and re-bin the optical maps in each wavelength channel before applying spectral analysis on the resulting convolved data cubes. The integrated fields data from Fields 2 and 5 are not used in this chapter for calibrating the SFR prescriptions due to their relatively low surface brightness and correspondingly low signal to noise ratio of Hβ.

The second approach uses apertures with matched distances, applied to the maps at their native resolutions. We choose the positions of the apertures by eye, targeting regions with bright peaks in the SFR tracer maps and a few regions dominated by diffuse emission. The purpose of the apertures is to distinguish between star-forming and non-star-forming regions, and to be able to extract the diffuse emission outside all apertures. We test the SFR prescriptions with apertures that have distances of 13.5”, 27” and 55” (corresponding to $\approx 50\,\mathrm{pc}$, $\approx 100\,\mathrm{pc}$, $\approx 200\,\mathrm{pc}$ in physical scales, respectively). For apertures placed on the optical data cubes, we convolve the cubes to the native resolution of the IR instrument, integrate pixels at each wavelength channel within the aperture, and then apply spectral analysis on the resulting spectra. The PSF resolutions, pixel sizes, and aperture distances used for these measurements are tabulated in Table 3.2. The aperture positions are shown in Fig. 3.2.

3.2.6 Maps of SFR tracers

Figures 3.3, 3.4, 3.5, 3.6, 3.7, we show the M31's fields in all of the star formation tracers (Hα,corr, FUV, 22 μm and 24 μm). Additionally, in those figures we show observed $\Sigma_{\rm SFR}(\rm H\alpha)$, modeled $\Sigma_{\rm SFR}$ from Lewis et al. (2015) (see Sec. 3.3.3), $\rm A_V$, Hα,corr/$\rm f_\nu(FUV, corr)$ ratio maps, and the $\rm D_n4000$ break (estimated from the spectra and using the wavelength range as in Tab. 1 in Balogh et al. 1999).

The Hα,corr/$\rm f_\nu(FUV, corr)$ ratio and the $\rm D_n4000$ break are independent probes of the stellar age. The Hα,corr/$\rm f_\nu(FUV, corr)$ ratio (Leitherer et al. 1999; Whitmore et al. 2011; Sánchez-Gil et al. 2011) decreases with higher age of the clusters. However, a direct conversion between the Hα,corr/$\rm f_\nu(FUV, corr)$ ratio and the age is highly uncertain and dependent on assumptions of initial mass functions (IMFs), metallicities, and spatial scales. Similar to the Hα,corr/$\rm f_\nu(FUV, corr)$ ratio, the $\rm D_n4000$ break indicates a luminosity weighted age of stars, with higher values indicating older stellar populations. The $\rm D_n4000$ break is defined by Bruzual A. (1983) as a ratio of the fluxes in the stellar continuum at longer and shorter wavelengths from λ4000 Å.

Most of the bright HII regions, visible in the Hα maps, correspond to young stellar clusters with their emission dominated by O and B stars that ionize their surrounding gas. The maps show a good spatial correlation between the Hα emission, the Hα,corr/$\rm f_\nu(FUV, corr)$ ratio and the $\rm D_n4000$ break. We confirm that young stellar clusters lie in the centers of the bright HII regions using the PHAT catalog (Dalcanton et al. 2012) of young clusters from Fouesneau et al. (2014) and Johnson et al. (2016). HII regions show a diskrete and clumpy distribution throughout the fields. Between and around the HII regions, we observe diffuse Hα emission that corresponds to the diffuse ionized gas (DIG, Walterbos & Braun 1994, Haffner et al. 2009, Tomičić et al. 2017), and it can be seen up to 200 pc away from the HII regions. The mid-IR tracers show similar diffuse features.

Bright HII regions are well correlated with FUV and mid-IR emission. However, mid-IR and FUV maps reveal additional low-brightness features that are not correlated with Hα emission. Moreover, some regions have bright Hα emission and low intensity mid-IR emission, such as the bright northern HII region in Field 1. The FUV maps reveal a clumpy distribution around HII regions. Those FUV clumps do not show NUV emission, which excludes the possibility that it comes from less massive MW foreground stars. While mid-IR maps show a relatively smooth distribution, there are some mid-IR regions that are not seen on the Hα map. These spatial variations between different tracers could indicate different stages in the time evolution of the clusters (Whitmore et al. 2011; Sánchez-Gil et al. 2011). For example, the

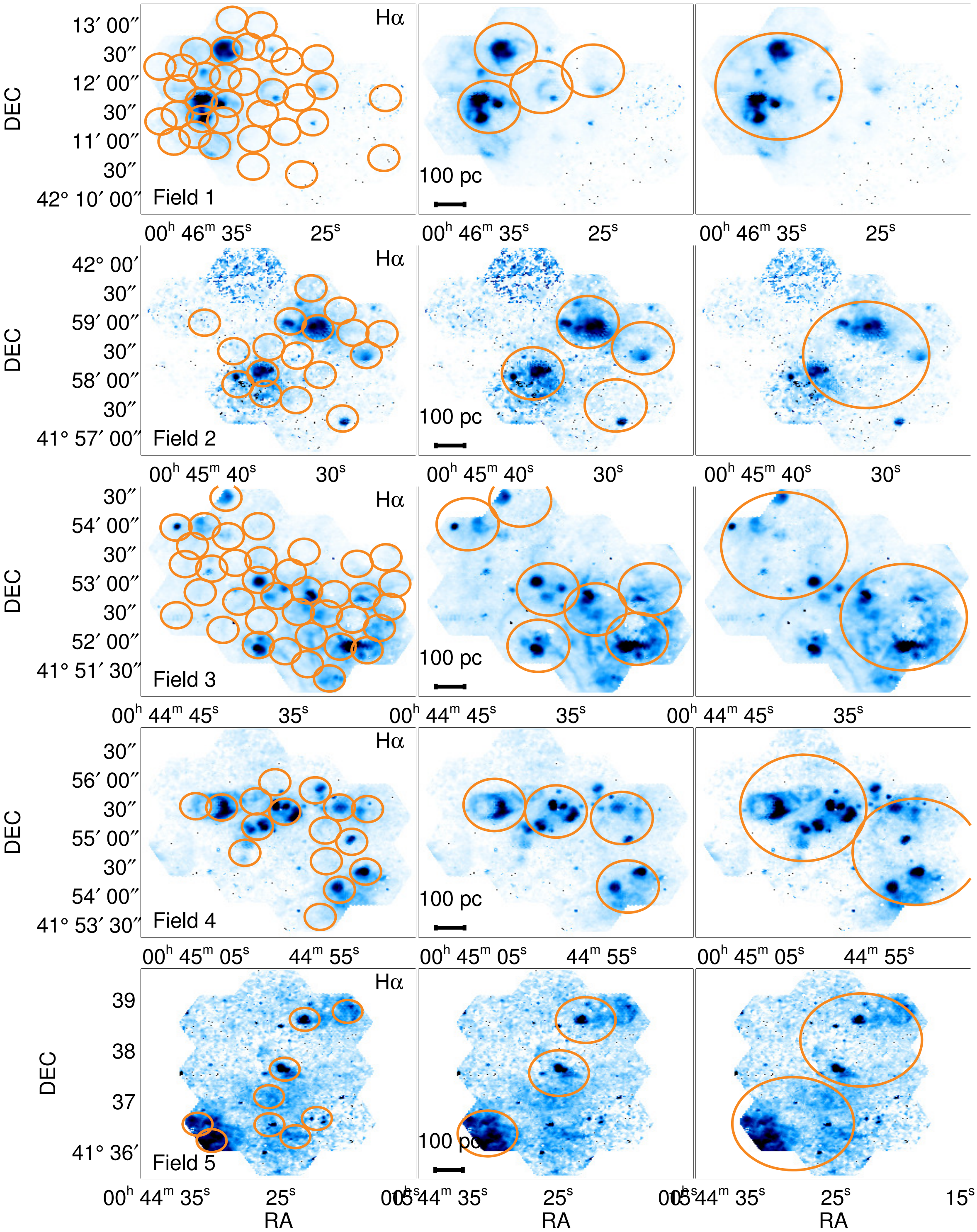
Hα
Field 1
Field 2
Field 3
Field 4
Field 5
100 pc
DEC
RA
13′ 00″
30″
12′ 00″
30″
11′ 00″
30″
42° 10′ 00″
00h 46m 35s
25s
42° 00′
30″
59′ 00″
30″
58′ 00″
30″
41° 57′ 00″
00h 45m 40s
30s
30″
54′ 00″
30″
53′ 00″
30″
52′ 00″
41° 51′ 30″
00h 44m 45s
35s
30″
56′ 00″
30″
55′ 00″
30″
54′ 00″
41° 53′ 30″
00h 45m 05s
44m 55s
39
38
37
41° 36′
00h 44m 35s
25s
15s

Fig. 3.2 Maps of the Hα tracer for Fields 1 to 5 (from top to bottom), with overploted apertures with distances of 13”(50 pc, left), 27”(100 pc, center), and 55”(200 pc, right). Fluxes in the apertures were calculated using the *IDL* software tool *aper* to extract pixel values without additional interpolation of pixel fluxes.

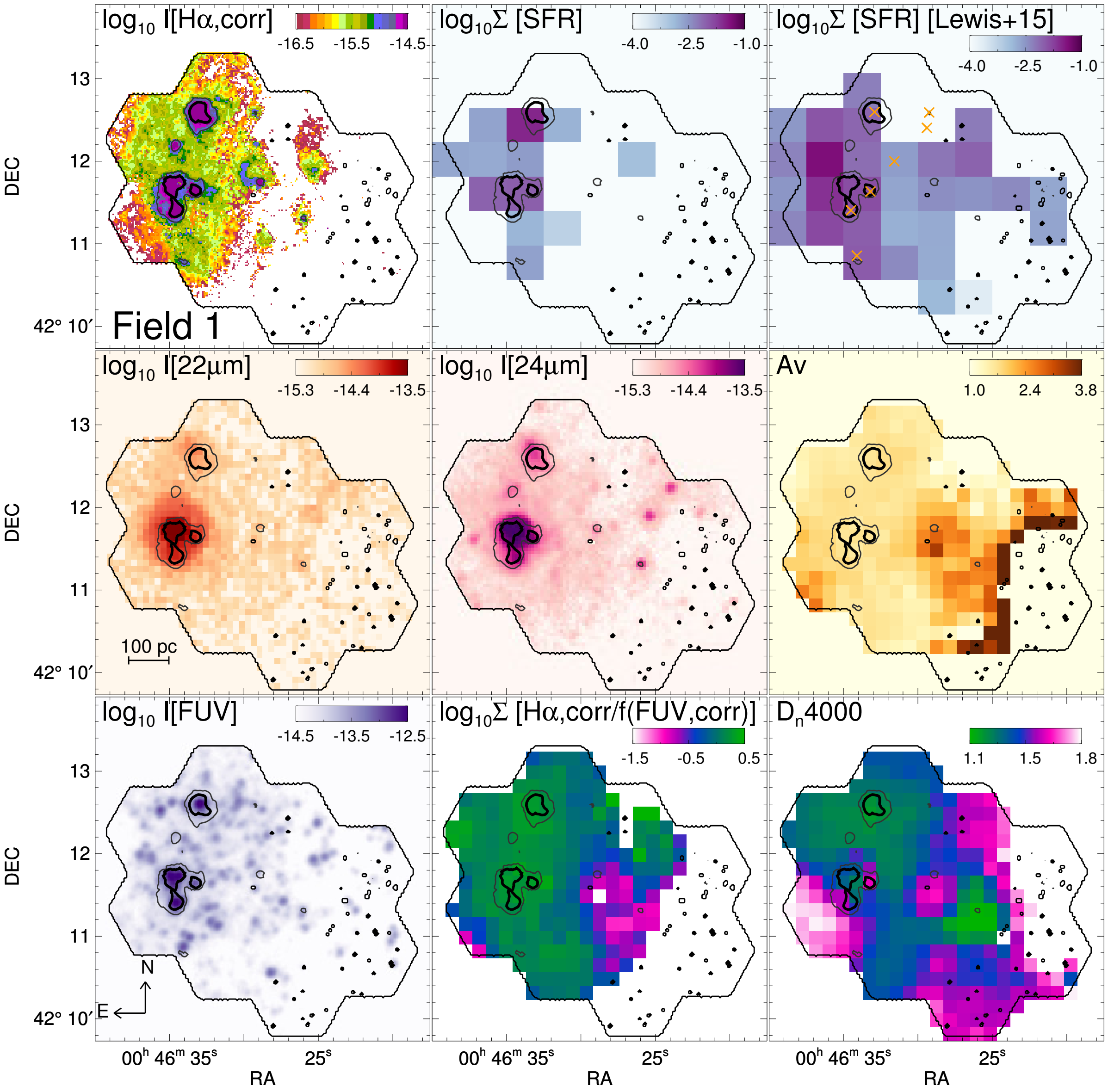

log$_{10}$ I[Hα,corr]
-16.5 -15.5 -14.5
log$_{10}$Σ [SFR]
-4.0 -2.5 -1.0
log$_{10}$Σ [SFR] [Lewis+15]
-4.0 -2.5 -1.0
log$_{10}$ I[22μm]
-15.3 -14.4 -13.5
log$_{10}$ I[24μm]
-15.3 -14.4 -13.5
Av
1.0 2.4 3.8
log$_{10}$ I[FUV]
-14.5 -13.5 -12.5
log$_{10}$Σ [Hα,corr/f(FUV,corr)]
-1.5 -0.5 0.5
D$_n$4000
1.1 1.5 1.8
Field 1
100 pc
N
E
DEC
13
12
11
42° 10′
00^h 46^m 35^s
25^s
RA

Fig. 3.3 Maps of Field 1 showing: $\Sigma(\mathrm{H}\alpha, corr)$ (at native resolution; top row left), $\Sigma_{\mathrm{SFR}}(\mathrm{H}\alpha, \mathrm{corr})$ from our spectra (pixel sizes of 23” or 100 pc; top row middle), Σ_{SFR} from the modeled star formation history by Lewis et al. (2015) (pixel sizes of 23” or 100 pc; top row right), $\Sigma(22\,\mu\mathrm{m})$ (at native resolution; middle row left), $\Sigma(24\,\mu\mathrm{m})$ (at native resolution; middle row middle), $\mathrm{A_V}$ (at Spire 360 μm resolution; middle row right), $\Sigma(\mathrm{FUV}\,\mu\mathrm{m})$ (at native resolution; bottom row left), the Hα,corr/f$_\nu$$(\mathrm{FUV}, \mathrm{corr})$ ratio (at Spire 360 μm resolution; bottom row middle), and the $\mathrm{D_n}4000$ break (at Spire 360 μm resolution and estimated from the spectra; bottom row right). Contours on all images correspond to observed Hα intensities of 3×10^{-16} (thin) and 10^{-15}(thick) $\mathrm{erg\,s^{-1}cm^{-2}\,arcsec^{-2}}$ at native resolution. discussion about the maps can be found in Sec. 3.2.6, and a comparison between $\Sigma_{\mathrm{SFR}}(\mathrm{H}\alpha, \mathrm{corr})$ and Σ_{SFR} from Lewis et al. (2015) in Sec. 3.3.3. We added positions of young stellar clusters identified by Fouesneau et al. (2014) as yellow crosses in upper right panel.

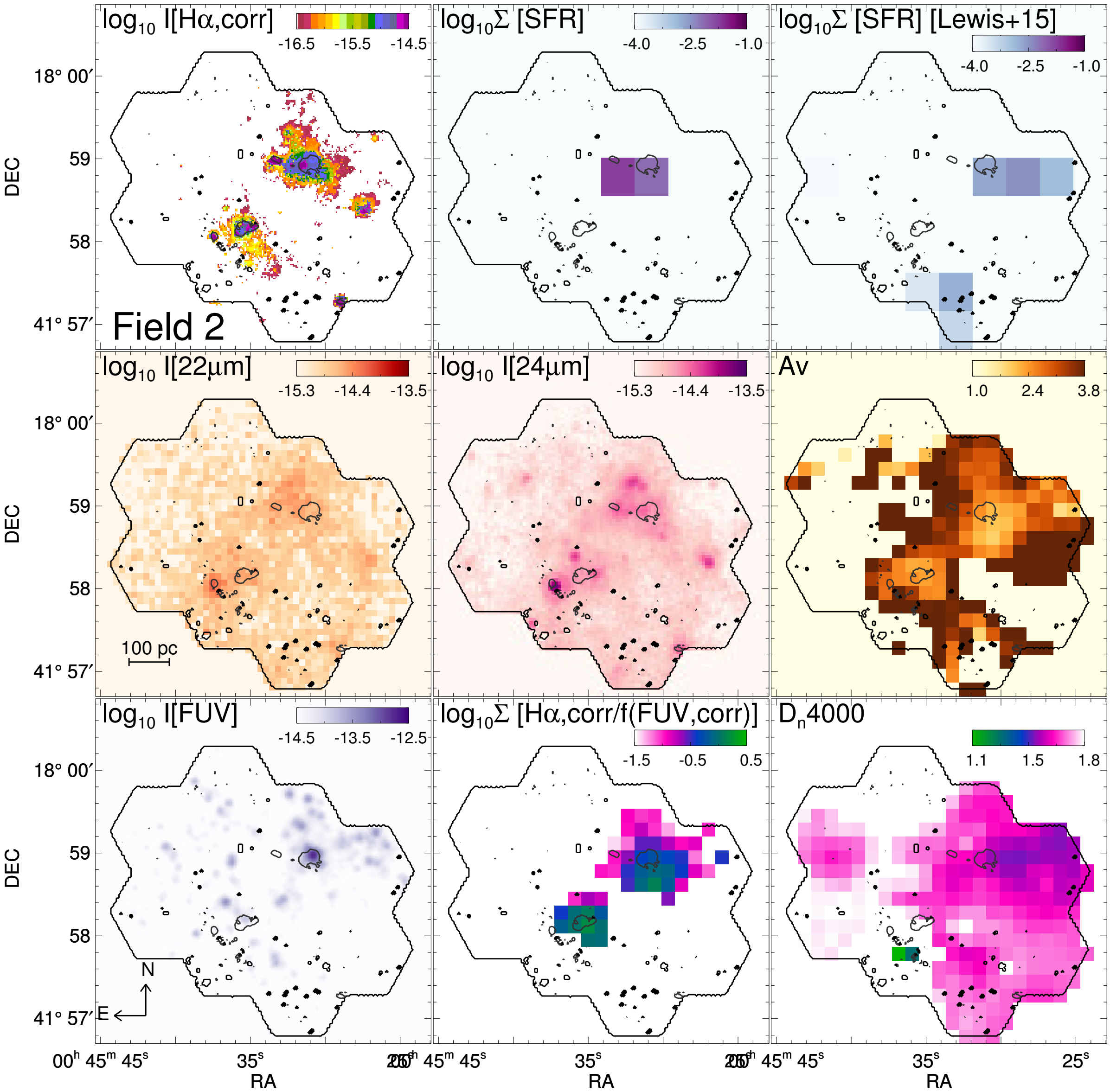
log$_{10}$ I[Hα,corr]
-16.5 -15.5 -14.5
log$_{10}$Σ [SFR]
-4.0 -2.5 -1.0
log$_{10}$Σ [SFR] [Lewis+15]
-4.0 -2.5 -1.0
Field 2
log$_{10}$ I[22μm]
-15.3 -14.4 -13.5
log$_{10}$ I[24μm]
-15.3 -14.4 -13.5
Av
1.0 2.4 3.8
100 pc
log$_{10}$ I[FUV]
-14.5 -13.5 -12.5
log$_{10}$Σ [Hα,corr/f(FUV,corr)]
-1.5 -0.5 0.5
D$_n$4000
1.1 1.5 1.8
N
E
18° 00′
59
58
41° 57′
DEC
00^h 45^m 45^s
35^s
25^s
RA

Fig. 3.4 Same as Fig. 3.3, but for Field 2.

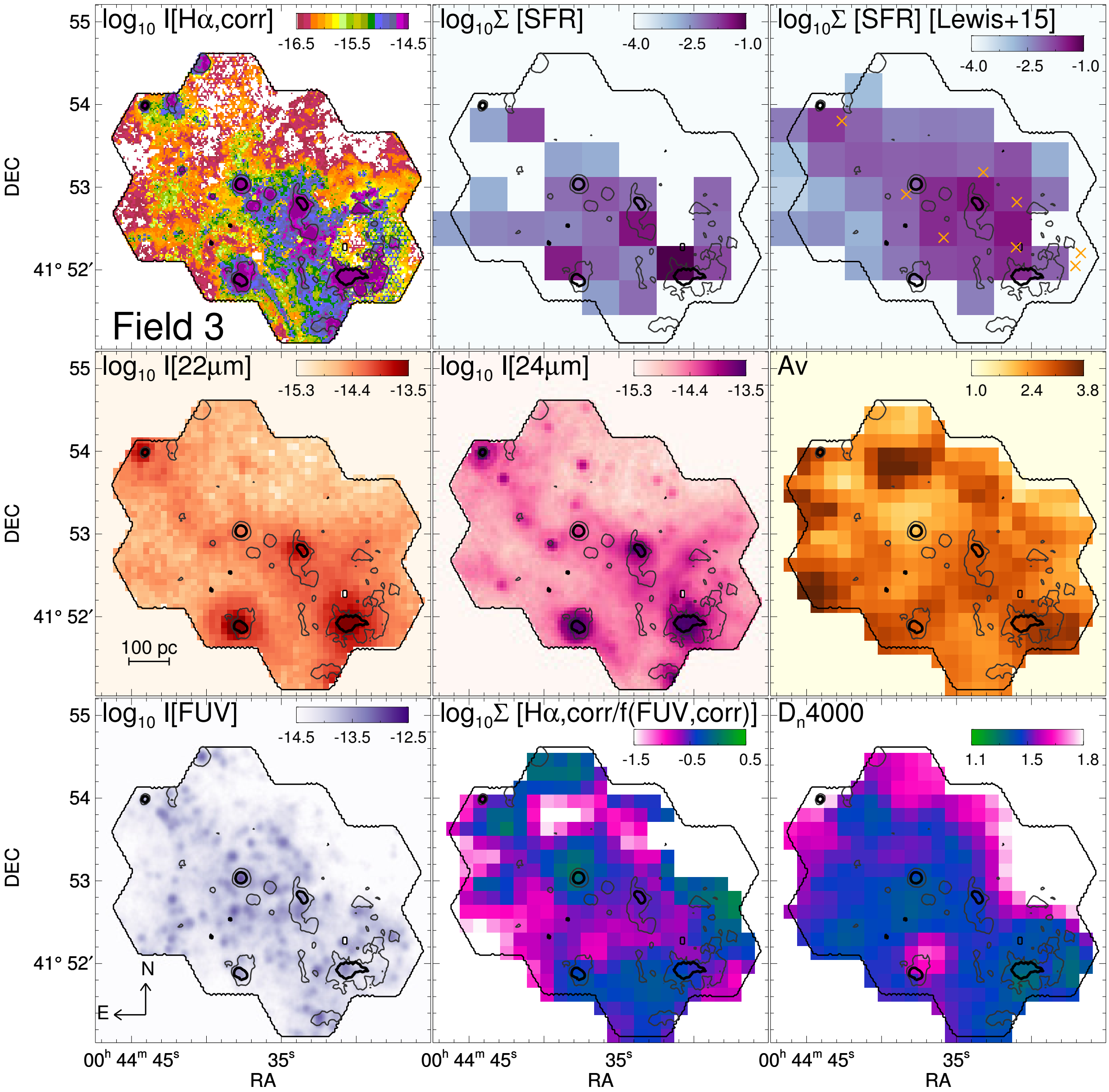

log$_{10}$ I[Hα,corr]
-16.5 -15.5 -14.5
Field 3
log$_{10}$Σ [SFR]
-4.0 -2.5 -1.0
log$_{10}$Σ [SFR] [Lewis+15]
-4.0 -2.5 -1.0
log$_{10}$ I[22μm]
-15.3 -14.4 -13.5
100 pc
log$_{10}$ I[24μm]
-15.3 -14.4 -13.5
Av
1.0 2.4 3.8
log$_{10}$ I[FUV]
-14.5 -13.5 -12.5
N
E
log$_{10}$Σ [Hα,corr/f(FUV,corr)]
-1.5 -0.5 0.5
D$_n$4000
1.1 1.5 1.8
DEC
55
54
53
41° 52′
RA
00^h 44^m 45^s
35^s

Fig. 3.5 Same as Fig. 3.3, but for Field 3.

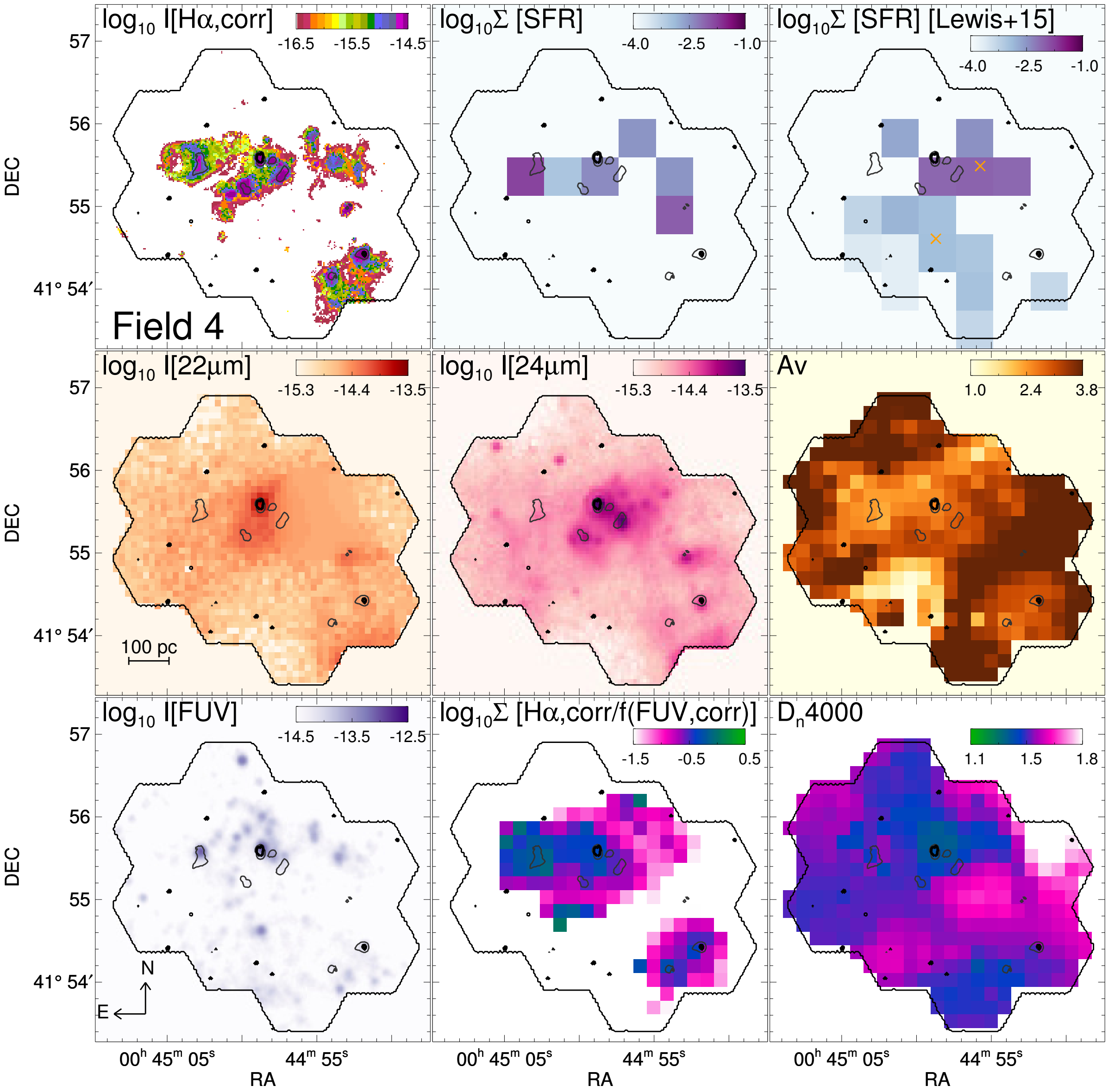
log$_{10}$ I[Hα,corr]
-16.5 -15.5 -14.5
log$_{10}$Σ [SFR]
-4.0 -2.5 -1.0
log$_{10}$Σ [SFR] [Lewis+15]
-4.0 -2.5 -1.0
Field 4
log$_{10}$ I[22μm]
-15.3 -14.4 -13.5
100 pc
log$_{10}$ I[24μm]
-15.3 -14.4 -13.5
Av
1.0 2.4 3.8
log$_{10}$ I[FUV]
-14.5 -13.5 -12.5
N
E
log$_{10}$Σ [Hα,corr/f(FUV,corr)]
-1.5 -0.5 0.5
D$_n$4000
1.1 1.5 1.8
DEC
57
56
55
41° 54′
00^h 45^m 05^s
44^m 55^s
RA

Fig. 3.6 Same as Fig. 3.3, but for Field 4.

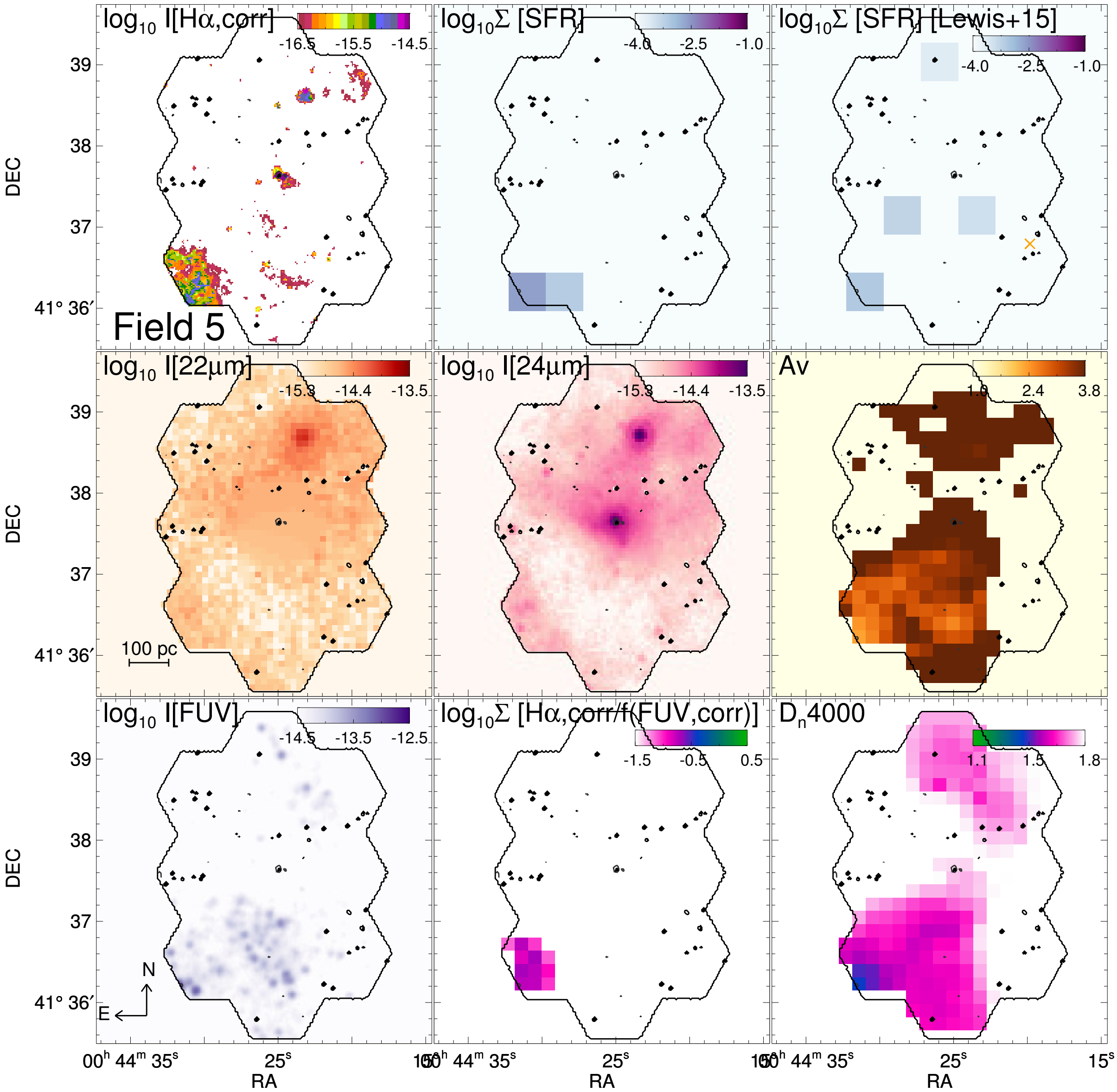
log$_{10}$ I[Hα,corr]
-16.5 -15.5 -14.5
Field 5
log$_{10}$Σ [SFR]
-4.0 -2.5 -1.0
log$_{10}$Σ [SFR] [Lewis+15]
-4.0 -2.5 -1.0
log$_{10}$ I[22μm]
-15.3 -14.4 -13.5
100 pc
log$_{10}$ I[24μm]
-15.3 -14.4 -13.5
Av
1.0 2.4 3.8
log$_{10}$ I[FUV]
-14.5 -13.5 -12.5
N
E
log$_{10}$Σ [Hα,corr/f(FUV,corr)]
-1.5 -0.5 0.5
D$_n$4000
1.1 1.5 1.8
DEC
39
38
37
41° 36′
RA
00^h 44^m 35^s
25^s
15^s

Fig. 3.7 Same as Fig. 3.3, but for Field 5.

presence of mid-IR emission without Hα may indicate a single embedded cluster within highly attenuated HII regions, while the reverse could be due to more evolved HII regions around OB associations. Lastly, FUV regions without mid-IR or Hα emission could point to evolved old stellar populations that do not ionize the gas or heat the dust around them.

3.3 Hα as our reference SFR tracer

One advantage of using IFU spectra is that we can separate the nebular emission lines from the underlying stellar continuum with proper estimation of the underlying absorption. Additionally, we can map the attenuation of the Hα line using the Balmer decrement. This combination allows us to spatially map the SFR at high physical resolution in M31, using extinction corrected Hα (Hα, corr) as our reference SFR tracer. In this chapter, we use this measure, $\Sigma_{\mathrm{SFR}}(\mathrm{H}\alpha, \mathrm{corr})$, as our fiducial SFR surface density.

3.3.1 Conversion from Hα and FUV to SFR

Hα, corr emisison serves as a proper estimate of the SFR if two major criteria are fulfilled. The first criterion is that the extinction corrected Hα, corr flux recovers all intrinsic Hα emission. The second important criterion is that the theoretical prescription for SFR estimation from Hα, corr flux is valid. The conversion from Hα, corr flux to SFR is well established under certain assumptions and widely used in the literature (for example in Kennicutt 1998, Kennicutt et al. 2003, Calzetti et al. 2005, Leroy et al. 2012, Murphy et al. 2011). It is derived under the assumptions that all ionizing radiation is absorbed, and that $\approx$45% of the ionized hydrogen atoms emit Hα photons during recombination (case B). It also assumes that the gas is purely ionized by young massive stars, and the stellar IMF is fully sampled. The duration of the star formation should also be taken into account. A constant star formation rate will lead to different Hα/FUV ratios and different mid-IR emission behavior compared to the case of a single aged starburst. In previous papers, the continuous star formation assumption held because of sampling large spatial scales (often the entire galactic disks) that encompasses multiple star-forming regions (Murphy et al. 2011). However, that assumption may be incorrect when observing smaller spatial scales (Faesi et al. 2014; Koepferl et al. 2017).

In this paper, we will adopt the Hα, corr-to-SFR conversion from Murphy et al. (2011) that uses the Starburst99[5] stellar population models:

$$\frac{\Sigma_{\mathrm{SFR}}(\mathrm{H}\alpha, \mathrm{corr})}{\mathrm{M}_{\odot}\mathrm{yr}^{-1}\mathrm{kpc}^{-2}} = 5.37 \times 10^{-42} \frac{\Sigma(\mathrm{H}\alpha, \mathrm{corr})}{\mathrm{erg\,s}^{-1}\mathrm{kpc}^{-2}} \tag{3.1}$$

This conversion assumes a constant star formation over 100 Myr, a Kroupa initial mass function (IMF; Kroupa 2001), solar metallicities, Case B recombination and a gas temperature of $\approx$

---

[5] http://www.stsci.edu/science/starburst99/docs/default.htm

10^4 K (for details see Murphy et al. 2011). If we assume that mostly the young, massive and short lived stars (<20 Myr) contribute significantly to the ionizing flux, then we can assume that this conversion factor is relatively independent of the previous star formation history and different time scales of star formation (Kennicutt 1998; Murphy et al. 2011).

To derive $\Sigma_{SFR}(FUV, corr)$ from $\Sigma(\mathrm{FUV, corr})$, we use the following prescription from Murphy et al. (2011):

$$\frac{\Sigma_{\mathrm{SFR}}(\mathrm{FUV, corr})}{\mathrm{M_{\odot} yr^{-1} kpc^{-2}}} = 4.42 \times 10^{-44} \frac{\Sigma(\mathrm{FUV, corr})}{\mathrm{erg\,s^{-1} kpc^{-2}}} \tag{3.2}$$

One caveat of this method is that the older stellar population may contribute to the FUV emission, and that this conversion is variable with different time scales (Kennicutt 1998; Murphy et al. 2011). The assumed timescale of star formation for this prescription is 100 Myr. However, this prescription may differ given the small spatial scales probed in M31 (Faesi et al. 2014).

In our previous paper, Tomičić et al. (2017), we found that the dust/gas distribution in M31 mostly follows the foreground screen models, and that the dust scale height is larger than the scale height of the DIG and HII regions for our studied fields. Therefore, in the following calculation, we will also assume a simple screen model of the dust/gas distribution, use the CCM extinction curve, the Balmer decrement of Hα/Hβ=2.86, and the selective extinction with R$_V$ =3.1 (Kreckel et al. 2013, Tomičić et al. 2017).

3.3.2 Effects of different extinction curves

We test and show in Fig. 3.8 the deviation in $\Sigma(\mathrm{H}\alpha, \mathrm{corr})$ when using different extinction curves. All histograms represent a comparison between $\Sigma(\mathrm{H}\alpha, \mathrm{corr})$ derived from different extinction curves (CCM, Calzetti et al. 2000, Fitzpatrick & Massa 2009) and our reference $\Sigma(\mathrm{H}\alpha, \mathrm{corr})$ calculated from the CCM extinction curve, R$_V$=3.1, and using the Hα/Hβ ratio. In all cases we assume R$_V$=3.1, due to the similarity in extinction curves and R$_V$ observed between the MW and M31 by Clayton et al. (2015). While different panels show different extinction curves, each individual histogram shows results using the ratio of different Balmer lines (Hα/Hβ, Hα/Hγ, Hβ/Hγ, and the ratio of all Balmer lines and Hδ line). For this test, we use pixels where AoN>5 for all considered Balmer lines.

For all extinction curves tested, $\Sigma(\mathrm{H}\alpha, \mathrm{corr})$ calculated from Hα/Hβ shows the smallest scatter and smallest offset from our reference $\Sigma(\mathrm{H}\alpha, \mathrm{corr})$ that is estimated using the CCM extinction curve. This is due to the higher S/N of the Hα and Hβ lines. The offset is only 0.1 dex from the reference $\Sigma(\mathrm{H}\alpha, \mathrm{corr})$, with a scatter of <0.1 dex. Higher scatter is seen in the histograms that use the line ratios with weaker Balmer lines (ratios with Hγ and Hδ lines). This is due to larger uncertainties and the small wavelength difference of those lines with Hβ, leading to higher systematic deviations in the line ratios and attenuation values. However, using

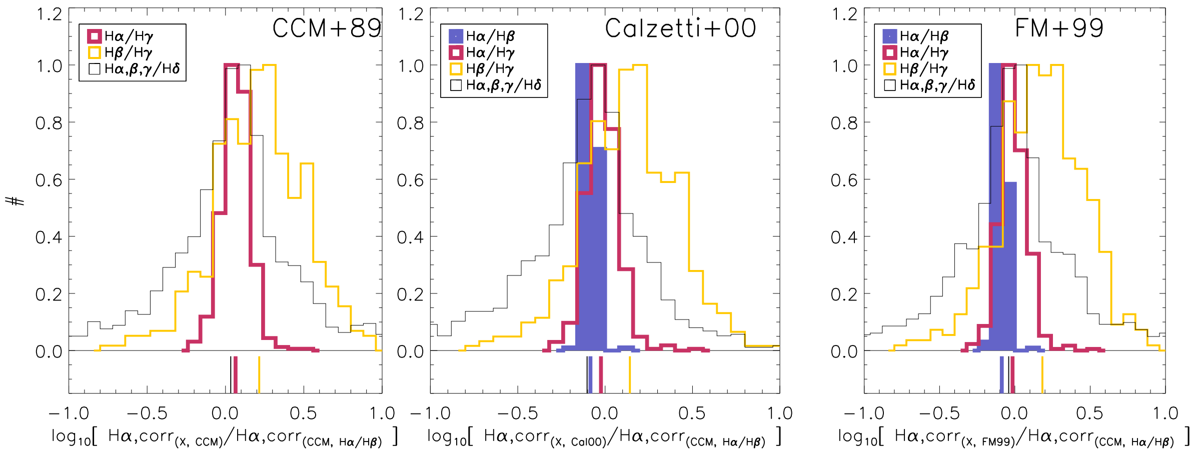

Fig. 3.8 Histograms of ratios between $\Sigma(\mathrm{H}\alpha, \mathrm{corr})$ derived from different extinction curves and different line ratios, and our reference $\Sigma(\mathrm{H}\alpha, \mathrm{corr})$ that uses the Cardelli et al. (1989) extinction curve (CCM), R_V=3.1, and the Hα/Hβ ratio. The purpose of this diagram is to see how much SFRs based on $\mathrm{H}\alpha, \mathrm{corr}$ deviate when we use different extinction curves or different Balmer line ratios. The extinction curves used within each panel are from: CCM (left panel), Calzetti et al. (2000) (middle panel) and Fitzpatrick & Massa (2009) (labeled as FM+99; right panel). We assume R_V=3.1 for all curves. Different histograms utilize different line ratios: Hα/Hβ (purple filled histogram), Hα/Hγ (thick red line), Hβ/Hγ (thin yellow line) and the line ratios with Hδ (thin black line). Median values of the corresponding distributions are presented as vertical lines below the histograms. If we use the Fitzpatrick & Massa (2009) or Calzetti et al. (2000) curve with Hα/Hβ, $\mathrm{H}\alpha, \mathrm{corr}$ would deviate by 0.1 dex and would have a small uncertainty. The $\Sigma(\mathrm{H}\alpha, \mathrm{corr})$ data derived from the other Balmer line ratios have more scatter due to the larger uncertainties in the line ratios and lines themselves. However, using Hα/Hγ instead of Hα/Hβ still gives an uncertainty of only $\approx$ 0.15dex. All data are from pixels with AoN>5 for all Balmer lines.

Hα/Hγ instead of Hα/Hβ ratios still gives an uncertainty of only ≈ 0.15 dex.

Our conclusion from these histograms is that the Hα/Hβ ratio is more reliable than other line ratios, and that using different extinction curves in M31 with this ratio would change derived $\Sigma_{SFR}(\mathrm{H}\alpha, \mathrm{corr})$ values by a maximum of 0.1 dex.

3.3.3 Comparison with SFRs derived from the PHAT survey

We compare our $\Sigma_{SFR}(\mathrm{H}\alpha, \mathrm{corr})$ values with those derived independently from resolved stellar photometry in M31. Lewis et al. (2015) and Lewis et al. (2017) modeled spatially resolved star formation histories (SFH), A_V, and extinction corrected FUV emission (from integrated SFH) using *Hubble Space Telescope* (HST) images of M31 from the PHAT survey. Their Σ_{SFR}(SFH) maps are derived by integrating the modeled SFH over the last 10 Myr in each pixel of their M31 map. Note that the most recent time bin available in their model is 4 Myr. To compensate for the lack of SFH on timescales shorter than 4 Myr, they estimated it by extrapolating from the time bin between 5 Myr and 6 Myr.

Examples of our $\Sigma_{SFR}(\mathrm{H}\alpha, \mathrm{corr})$ and the Σ_{SFR}(SFH) maps are shown in Fig. 3.3, 3.4, 3.5, 3.6, and 3.7. While there is good agreement overall, the limitations of such a comparison to Σ_{SFR}(SFH) is visible just north-east of the bright southern HII region in Field 1, where there is a peak in Σ_{SFR}(SFH) that is offset from both the Hα and mid-IR peaks. The FUV emission at the location of the peak in Σ_{SFR}(SFH) strongly suggests that here Σ_{SFR}(SFH) traces SF older than 5 Myr. Furthermore, areas outside the HII regions and with old stellar clusters (evident from the Hα,corr/f$_{\nu}(\mathrm{FUV}, \mathrm{corr})$ ratio and the spectral fit) have estimated Σ_{SFR}(SFH), while lacking Hα emission. We could not estimate $\Sigma_{SFR}(\mathrm{H}\alpha, \mathrm{corr})$ for those regions.

Fig. 3.9 shows a pixel-by-pixel comparison of the maps, where we re-bin our $\Sigma_{\mathrm{SFR}}(\mathrm{H}\alpha, \mathrm{corr})$ maps to spatially match the Σ_{SFR}(SFH) map, with pixel size of 23" ($\approx$ 70 pc). The data are color-coded by the Hα,corr/f$_{\nu}(\mathrm{FUV}, \mathrm{corr})$ ratio, with older clusters having lower values. Although, Σ_{SFR}(SFH) exhibits slightly higher ($\approx$ 0.2 dex) values than $\Sigma_{\mathrm{SFR}}(\mathrm{H}\alpha, \mathrm{corr})$, there is a large scatter (standard deviation of 0.5 dex and a variation of up to $\approx$1 dex). We do not find any correlation of the residuals with age. This comparison is robust, but the large scatter in the data could be due to: a) high uncertainties in the modeling of the recent SFH, b) uncertainty in the interpolation and estimation of the SFH in the last 4 Myr, and c) a gradual drop in Hα emission on time scales longer than 5 Myr.

3.3.4 Comparison by using molecular cloud masses

There is an additional evidence for the reliability of our reference SFR tracer. Viaene et al. (2018) found that the giant molecular clouds in M31 exhibit $\approx$0.5 dex lower SFRs then what is predicted by Milky Way studies of the dense molecular gas (Gao & Solomon 2004; Lada et al. 2012). In their study, Viaene et al. (2018) used the SFR map of M31 created by Ford et al. (2013), where the old stellar population contribution is subtracted. However, when we apply our hybrid SFR(FUV+24 μm) prescription derived from $\Sigma_{\mathrm{SFR}}(\mathrm{H}\alpha, \mathrm{corr})$ (see Tab. A.1 in the Appendix), the SFRs of those molecular clouds match better with the values predicted by Gao & Solomon (2004) than the SFRs used by Viaene et al. (2018). We show this on Fig. 3.10.

3.4 Calibration of the SFR prescriptions

In this section, we present the main results of our SFR calibrations. We compare $\Sigma_{SFR}(\mathrm{H}\alpha, \mathrm{corr})$ with Σ_{SFR} derived from different (monochromatic and hybrid) tracers. The comparisons are always shown with $\Sigma_{SFR}(\mathrm{H}\alpha, \mathrm{corr})$ on the x-axis, and Σ_{SFR} from other tracers on the y-axis. We also compare our SFR prescriptions with those of Calzetti et al. (2007) and Leroy et al. (2008). Hereafter, we will refer to Calzetti et al. (2005) and Calzetti et al. (2007) as C05 and C07, respectively. Their prescriptions are similar to those given in Kennicutt et al. (2003), Leroy et al. (2012) and Catalán-Torrecilla et al. (2015). Moreover, we evaluate the effects of varying

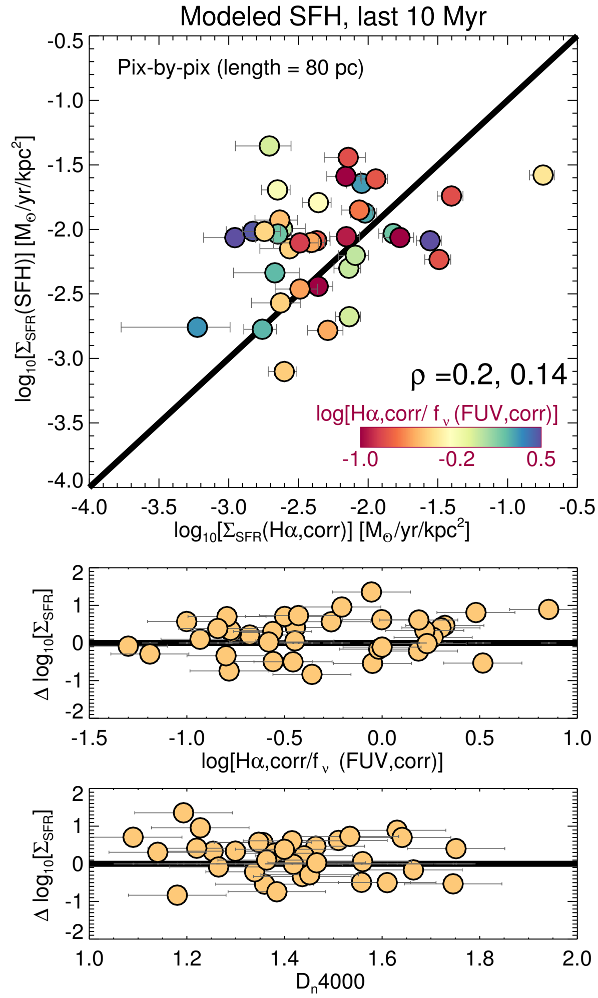

Fig. 3.9 Comparison between our reference $\Sigma_{SFR}(\mathrm{H}\alpha,\mathrm{corr})$ from spectral fitting and the $\Sigma_{SFR}(\mathrm{SFH})$ in M31 derived from the modeled star formation history (SFH) averaged over the last 10 Myr by Lewis et al. (2015). The pixel-by-pixel data points correspond to pixel sizes of 23" ($\approx$ 80 pc). The 1-to-1 relation lines are plotted as solid black lines, and we label the Spearman's correlation coefficient (ρ, left number) and the significance of its deviation from zero (right number). The data are color-coded by the Hα,corr/f$_\nu(\mathrm{FUV},\mathrm{corr})$ ratio. In the lower panels we show deviation of the data from the 1-to-1 relation as a function of the Hα,corr/f$_\nu(\mathrm{FUV},\mathrm{corr})$ ratio and the luminosity weighted $\mathrm{D_n}4000$ break. Lower Hα,corr/f$_\nu(\mathrm{FUV},\mathrm{corr})$ ratios and higher $\mathrm{D_n}4000$ break values indicate older stellar clusters (or populations).

the spatial resolution and subtracting the diffuse emission from non-star-forming regions on the SFR prescriptions.

The monochromatic and hybrid SFR prescriptions at different resolutions and aperture sizes are listed in Tab. A.1 and A.2 (in Appendix of this thesis). In Tab. A.2, we add the SFR prescription for $12\,\mu$m and $22\,\mu$m calculated by fitting lines between the logarithmic values of L(IR) and SFR(Hα,corr), instead of surface densities.

3.4.1 Monochromatic SFRs

The left panel of Fig. 3.11 shows the relation between $\Sigma_{\rm SFR}({\rm H}\alpha, {\rm corr})$ and monochromatic $\Sigma(22\mu{\rm m})$ at different pixel scales and apertures sizes. The dashed line indicate the monochromatic SFR prescriptions given by Calzetti et al. (2007) where they used apertures between 30 pc and 1.2 kpc in projected sizes. Here, we used units of surface densities to eliminate the dependency on spatial scales. Regardless of spatial scales, M31 data show an 0.2-0.5 dex offset from the Calzetti et al. (2007) prescription and a slope that is lower than 1.

On the right panel, we show a comparison between the L($22\mu{\rm m}$) and SFR(${\rm H}\alpha, {\rm corr}$). We use here the luminosity and SFR values in order to compare the data to the monochromatic SFR prescriptions from the literature, indicated by lines. The monochromatic SFR prescriptions from the literature are given by Catalán-Torrecilla et al. (2015), Davies et al. (2016), Brown et al. (2017), Jarrett et al. (2013), and Cluver et al. (2017). These prescriptions were derived from extragalactic surveys with scales larger than 1 kpc and employed spectroscopic measurements and extinction corrected Hα The exceptions are those from Jarrett et al. 2013 and Cluver et al. 2017, where they used integrated galactic values of mid-IR photometry and SFR measured from TIR. All these prescriptions are determined for SFR> $10^{-3}\,{\rm M}_{\odot}\,{\rm yr}^{-1}$ (gray shaded area on the figure), which is higher than the majority of our data (except for the integrated fields and the largest apertures). Therefore, we show only M31 data with larges scales. Combining largest apertures and the integrated fields, we observe that our data altogether has a single slope that is shallower than most of the monochromatic SFR prescriptions in the literature. These data also fall between relations from Catalán-Torrecilla et al. (2015), Cluver et al. (2017), and Brown et al. (2017).

Fig. 3.12 shows the residuals between $\Sigma_{\rm SFR}({\rm H}\alpha, {\rm corr})$ and $\Sigma_{\rm SFR}$(IR) as a function of $\Sigma_{\rm SFR}({\rm H}\alpha, {\rm corr})$ for different IR tracers. The IR tracers here are $22\,\mu$m, $70\,\mu$m, $160\,\mu$m and TIR. $\Sigma_{\rm SFR}$(IR) are derived from prescriptions given by Calzetti et al. (2007), Calzetti et al. (2010) and Calzetti (2013). The TIR values in this chapter are calculated using Eq. 5 in Dale et al. (2009), where we directly substitute the $22\,\mu$m for the $24\,\mu$m. We see that in M31 the $22\,\mu$m, $70\,\mu$m, and TIR calibrations all underpredict the SFR relative to the Hα by ≈ 0.5 dex and have a 0.5 dex scatter, while $160\,\mu$m tracer underpredicts the SFR relative to the Hα by 0.1 dex and have a 0.5 dex scatter. However, we note that the SFR($160\,\mu$m) prescription in

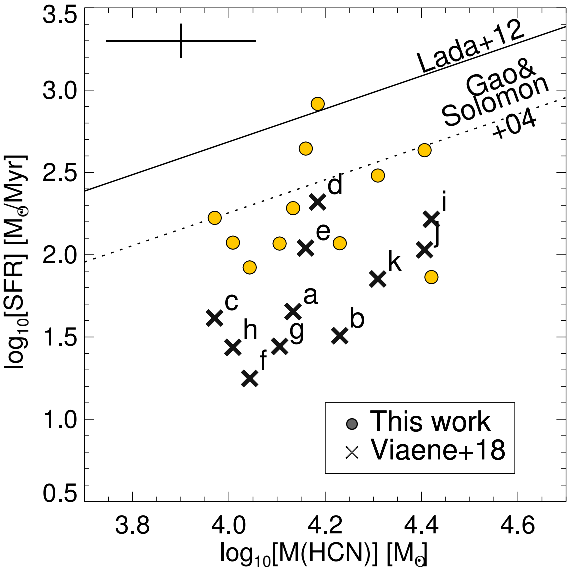

Fig. 3.10 The SFRs as a function of the dense molecular gas (HCN) masses of the giant molecular clouds in M31. The masses of the molecular clouds are derived by Brouillet et al. (2005). The data from Viaene et al. (2018) (x symbols) have SFRs estimated from the SFR map of M31, created by Ford et al. (2013). On the other hand, we estimated SFRs (circles) from the hybrid SFR(FUV+24μm) prescription from this paper (Appendix **??**). The SFR values of the clouds predicted by Gao & Solomon 2004 and Lada et al. (2012) are shown with dashed and solid lines, respectively. We show mean error bars of the data in upper left corner.

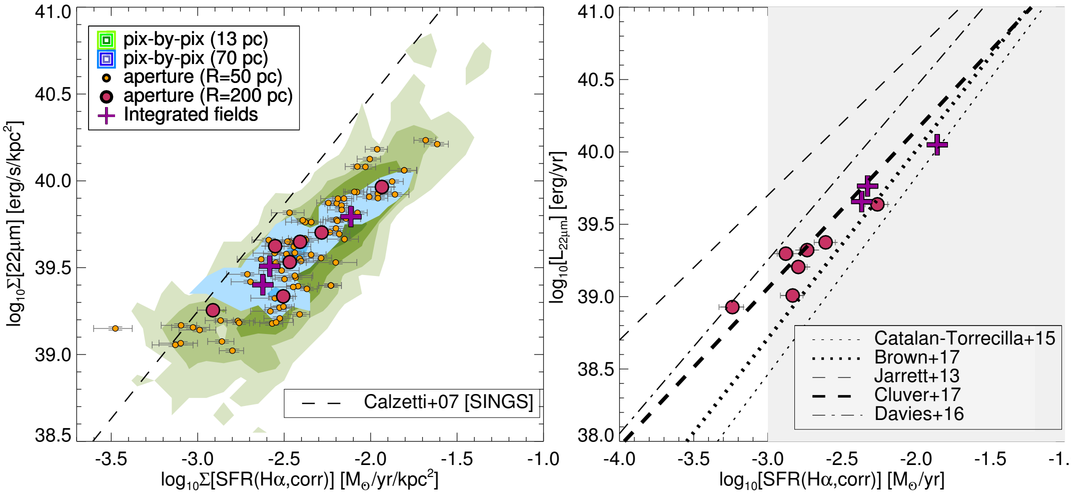

Fig. 3.11 On the left, we show $\Sigma(22\mu\mathrm{m})$ as a function of $\Sigma_{\mathrm{SFR}}(\mathrm{H}\alpha, \mathrm{corr})$, while on the right we show $\mathrm{L}(22\mu\mathrm{m})$ as a function of $\mathrm{SFR}_{\mathrm{SFR}}(\mathrm{H}\alpha, \mathrm{corr})$. The M31 data presented here probe different spatial scales. Circles mark apertures, contours pixel-by-pixel data points, and crosses the integrated fields. Lines indicate relations and monochromatic SFR prescriptions given by Calzetti et al. (2007, dashed line on the left panel), Catalán-Torrecilla et al. (2015, dotted line), Brown et al. (2017, thick dotted line), Jarrett et al. (2013, thin dashed line), Cluver et al. (2017, thick dashed line), and Davies et al. (2016, dash-dotted line). We indicate the range of SFRs covered by those papers with the shaded area.

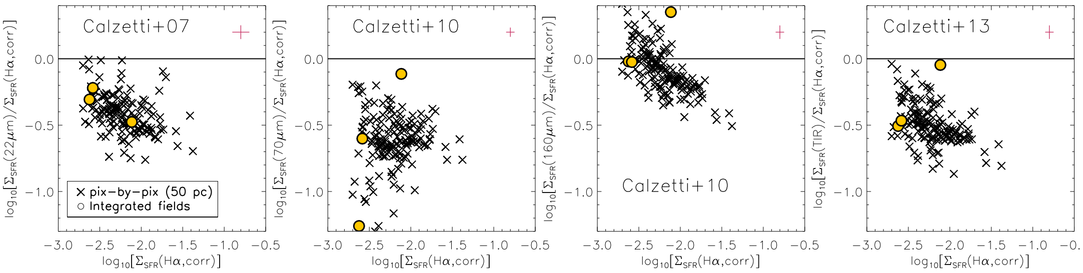

Fig. 3.12 The ratio of different wavelength monochromatic $\Sigma_{\rm SFR}$(IR) calibrations prescribed in the literature (Calzetti et al. 2007, 2010; Calzetti 2013) relative to the $\Sigma_{\rm SFR}(\rm H\alpha, corr)$ as a function of $\Sigma_{\rm SFR}(\rm H\alpha, corr)$. The tracers used here are the 22 μm, 70 μm, 160 μm and TIR (estimated using Eq. 5 in Dale et al. 2009). The data points show pixel-by-pixel comparison (crosses; with 50 pc pixel length) and integrated fields (yellow circles). The integrated field with a highest $\Sigma_{\rm SFR}(\rm H\alpha, corr)$ is Field 3, a field that is mostly covered with HII regions. We show a mean of the error bars in the upper right corner (red lines).

the literature has a large uncertainty due to 160 μm tracing the overall dust emission and it is dominated by the cold dust emission. Also, for the TIR we assume a SF timescale of 100 Myr.

3.4.2 The hybrid SFR prescriptions at smallest scales

We calibrate the SFR prescriptions for the hybrid tracers (Hα+IR and FUV+IR) by comparing them with the $\Sigma_{\rm SFR}(\rm H\alpha, corr)$ at the smallest spatial scales, without subtraction of the diffuse emission. The smallest pixel-by-pixels scales of ≈7 pc and the smallest aperture radius of ≈50 pc are comparable to the HII region sizes in M31 that are between 15 pc and 160 pc (Azimlu et al. 2011).

We calculate $\Sigma_{SFR}(\rm H\alpha + IR)$ and $\Sigma_{SFR}(\rm FUV + IR)$ as :

$$\Sigma_{\rm SFR}(\rm H\alpha + a_{IR}IR) = a \times [\Sigma(H\alpha_{observed}) + a_{IR}\Sigma(IR)], \tag{3.3}$$

$$\Sigma_{\rm SFR}(\rm FUV + b_{IR}IR) = b \times [\Sigma(FUV_{observed}) + b_{IR}\Sigma(IR)], \tag{3.4}$$

where mid-IR corresponds to 22 μm and 24 μm. The conversion factors *a* and *b* are 5.37×10^{-42} and 4.42×10^{-44}, respectively, given from Eq. 3.1 and 3.2. The single-valued calibration factors $\rm a_{IR}$ and $\rm b_{IR}$ are used to account for obscured emission of the tracers (Hα and FUV) and to recover extinction-corrected $\rm H\alpha, corr$ and FUV,corr. Those single-valued factors were measured by taking a median value of the calibration factors from individual data. We calculate the factors $\rm a_{IR}$ and $\rm b_{IR}$ for individual data as

$$a_{\rm IR} = \frac{\Sigma(H\alpha, \rm corr) - \Sigma(\rm H\alpha)}{\Sigma(\rm IR)}, \tag{3.5}$$

$$b_{\rm IR} = \frac{\Sigma(\rm FUV, corr) - \Sigma(FUV)}{\Sigma(\rm IR)}. \tag{3.6}$$

The calibration factor $a_{\rm IR}$ is independent of the $\rm H\alpha, corr$-SFR conversion factor because $a_{\rm IR}$ is derived directly from observable tracers (Hβ, Hα and IR). On the other hand, $b_{\rm IR}$ is sensitive to how we estimate SFRs, which depend on how we define the conversion factors *a* and *b*, and may differ with different assumptions taken in Sec. 3.3.1.

In Fig. 3.13, we compare $\Sigma_{\rm SFR}(\rm H\alpha, corr)$ with the hybrid $\Sigma_{\rm SFR}$ calculated from our prescription (left panels) and from the prescriptions given by C07 and Leroy et al. (2008) (right panels). The SFR(Hα+24 μm) and SFR(FUV+22 μm) are presented in the upper and lower panels, respectively. The figure shows apertures with R=13.5" ($\approx$50 pc), pixel-by-pixel comparison (pixels with 7 pc in length) and the integrated fields data. The residuals, presented below the main panels, show the difference between $\Sigma_{\rm SFR}(\rm H\alpha, corr)$ and the hybrid $\Sigma_{\rm SFR}$ values. For all the panels, we also show one-to-one lines and power-law fits [6] for the aperture data.

All the panels in Fig. 3.13 show a clear correlation between the hybrid Σ(SFR) and $\Sigma_{\rm SFR}(\rm H\alpha, corr)$. The scatter is usually between 0.3 and 0.5 dex. The right panels in Fig. 3.13 shows clear systematic differences between the SFR values that are derived from $\rm H\alpha, corr$ and the SFR values derived from the prescriptions given by C07 and Leroy et al. (2008). The diskrepancy between those values is around 0.5 dex, and may be up to 1 dex. Our calibration leads to the calibration factors $a_{24} \approx 0.2$ and $b_{22} \approx 22$, which are about 5-8 times larger than those given by C07 and Leroy et al. (2008) [7].

In Fig. 3.14 we present the residuals as a function of two physical quantities: $A_{\rm V}$ (derived from the Balmer lines) and 24 μm surface brightness. The residuals presented here are from the main panels of Fig. 3.13 for the hybrid Hα+24 μm prescriptions. Similarly, we show the results from this work on the left panels, and from using the C07 calibration on the right panels. Power-law fits are also included in the plots.

In the top panels, the residuals do not change with $A_{\rm V}$ for our prescription (left panel). However, the residuals anti-correlate with $A_{\rm V}$ when using the C07 prescription (right panel). This can be easily explained by the low value of $a_{24\,\mu\rm m}$ from C07. The Σ(24 μm) values are usually an order of magnitude higher than the observed Σ(Hα). When we multiply Σ(24 μm) by a small a_{24}, the observed Σ(Hα) dominates over Σ(24 μm). There is no clear trend in residuals with Σ(24 μm) for our data, but a small trend when using the C07 prescription.

We conclude that the SFR prescriptions at small spatial scales in M31 are different from those in the literature. The $\Sigma_{\rm SFR}(\rm H\alpha, corr)$ values are a factor of 3 ($\approx$0.5 dex) higher than the values obtained when using the prescriptions from the literature. Not only are the values different, but the scatter of the data is also large (0.3-0.5 dex).

---

[6] We useed the *IDL* tool mpfitexy for fitting (https://github.com/williamsmj/mpfitexy) including the estimated errors of the data.

[7] $a_{24} \approx 0.031$ in C07, $a_{24} \approx 0.05$ in C05 and $b_{24} \approx 3.8$ in Leroy et al. (2008).

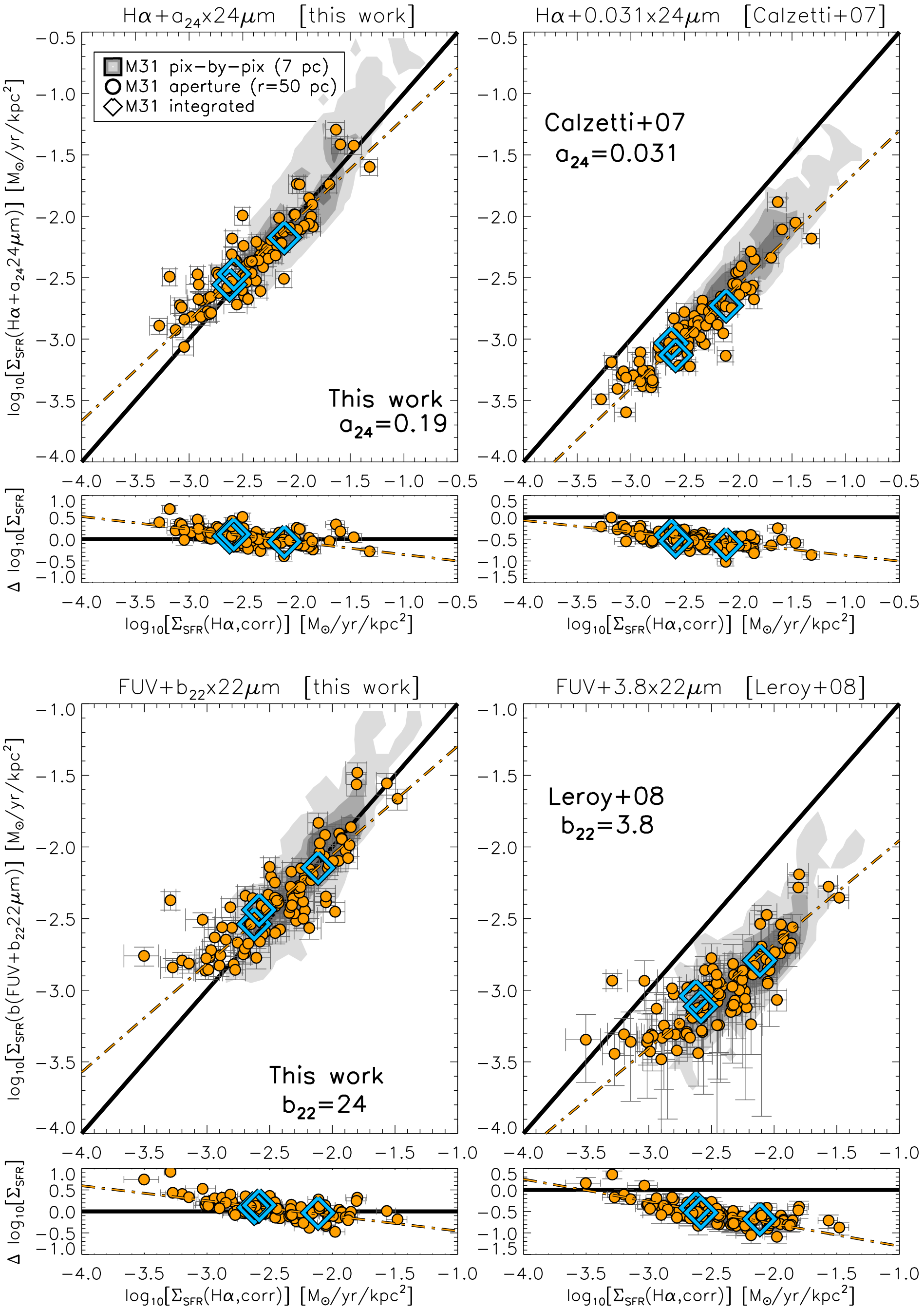

Fig. 3.13 Comparison between hybrid $\Sigma_{\rm SFR}$ prescriptions and $\Sigma_{\rm SFR}({\rm H}\alpha, {\rm corr})$, using the hybrid SFR prescriptions from this work (left panels) or the prescriptions given by Calzetti et al. (2007) and Leroy et al. (2008) (right panels). We use different tracers for the hybrid SFRs: Hα+24 μm (upper panels) and FUV+22 μm (bottom panels). For the hybrid SFR prescriptions, we use Hα, corr-SFR and FUV,corr-SFR (labeled as b on axis) conversions factors from relations in Eq. 3.1 and 3.2). Under each main panel, we plot residuals of the data from the above panel, where we calculate residuals as a hybrid SFR value subtracted from SFR(Hα, corr). The contours show pixel-by-pixel data (7 pc in length), the yellow circles R=50 pc apertures and the blue diamonds the integrated fields (each with a projected size of $\approx 0.6\,{\rm kpc} \times 0.9\,{\rm kpc}$). In all panels, we plot the 1-1 line (solid) that indicates an equivalence between the $\Sigma_{\rm SFR}$ values, and we add dashed line fits of the aperture data (fit of the data in logarithmic values). The prescriptions given by Calzetti et al. (2007) and Leroy et al. (2008) differ systematically from this work (seen as offsets between the data and the equivalence line on right panels).

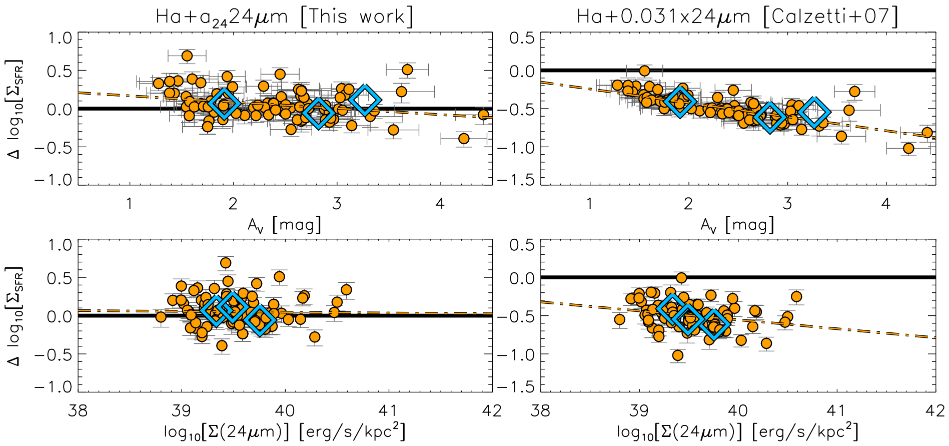

Fig. 3.14 We show here residuals between $\Sigma_{\rm SFR}({\rm H}\alpha, {\rm corr})$ and the hybrid Hα+24 μm values, as a function of physical quantities: $\rm A_V$ (upper panels) and 24 μm surface brightness (bottom panels). We show apertures with distances of 50 pc (circles) and integrated fields (diamonds). On the left, we show the behavior for the prescription from this work, while on the right panel we show the residuals for the C07 prescription ($\rm a_{24} = 0.031$). We add linear fits (dashed lines) of the data (in logarithmic) to the diagrams in order to better trace correlations between different quantities.

3.4.3 Effects of spatial scales and diffuse component subtraction

The prescriptions given in C07 and Leroy et al. (2008) are derived from apertures and maps with lower spatial resolutions (C07 applied apertures with distances ranging from 0.03 kpc to 1.26 kpc, while Leroy et al. 2008 probe spatial scales at 800 pc). They also included procedures to subtract diffuse emission from mid-IR cirrus and DIG. Thus, to properly compare the prescriptions we need to test how the prescriptions vary with changing spatial scales and with a subtraction of the diffuse emission.

We show the effects of varying spatial scales on the calibration factor $\rm a_{24}$ as a function of $\Sigma({\rm H}\alpha, {\rm corr})$, for the pixel-by-pixel based analyses in Fig. 3.15. The C07 value of $\rm a_{24} = 0.031$ is presented as the dashed line. The difference between the C07 factor and that from this work is around ≈0.7 dex at all spatial scales (maximum of 1 dex difference). Our $\rm a_{24}$ decreases from ≈0.22 at smallest scales to ≈0.17 for the field-integrated measurements, and $\rm b_{24}$ from ≈30 to ≈20 (see Tab. A.1). We also indicate the integrated fields data in Fig. 3.11, 3.12, 3.13 and 3.14 to show that, even at the same physical scales, the data in M31 consistently display an offset in the monochromatic and the hybrid SFR prescriptions from the values in the literature.

Fig. 3.16 shows how subtracting the diffuse emissions (DIG and mid-IR cirrus) affects the $\rm a_{24}$ values. We use 13.5” and 55” distances apertures, and measure the mid-IR cirrus and DIG brightness by taking the mode of all pixels outside all of the apertures in each M31 field respectively. The diffuse fraction of DIG and mid-IR cirrus in the apertures ranges from 5% (for apertures with high surface brightness) to 30%-60% (for apertures with low surface brightness). After the subtraction, we see no change in $\rm a_{24\,\mu m}$ for the high surface brightness (and high S/N)

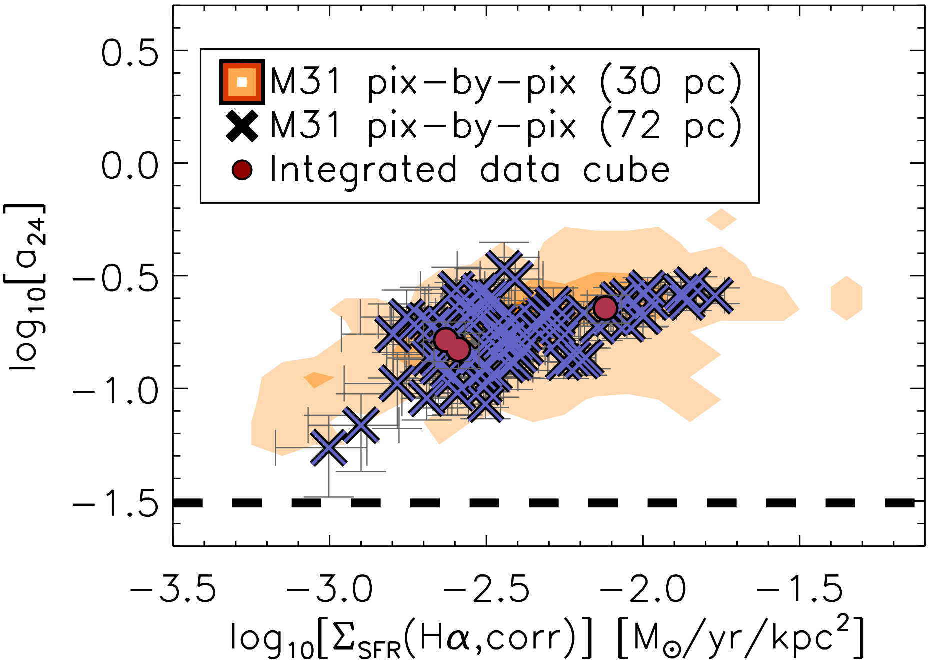

Fig. 3.15 The effect of varying spatial scales on the calibration factor $a_{24\,\mu m}$ as a function of $\Sigma(H\alpha, \mathrm{corr})$. The pixel-by-pixel data points shown in the panel are for pixels at 25" resolution (SPIRE 350 μm, contours), 65" resolution (blue X symbols) and the integrated fields (red circles). The data for apertures with different distances have similar values as the presented data. We indicate the $a_{24} = 0.031$ value from C07 with the dashed line.

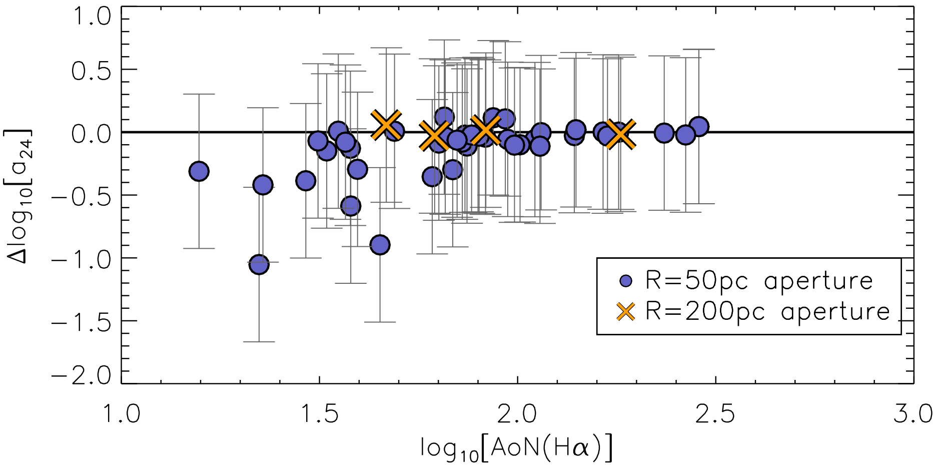

Fig. 3.16 Difference in the a_{24} values before and after subtracting the diffuse emission component (DIG and mid-IR cirrus) as a function of AoN(Hα). Apertures of 13.5" radius (circles) and 55" radius (X symbols) are presented. Unity is depicted with the solid line. Differences between the a_{24} values from C07 and this work are usually 1 dex as seen in Fig. 3.15. We conclude that subtracting diffuse emission cannot explain the difference between the SFR prescriptions. The biggest impact of the diffuse subtraction is seen for data of low AoN(Hα) or low surface brightness.

data. As expected, a stronger effect on a_{24} is seen for the low surface brightness data.

3.5 Effects of inclination and galactocentric distance on the SFR prescriptions

We compared the M31 data with other observed galaxies to examine how attenuation, galactic inclination and galactocentric distance affect the SFR prescriptions, and to put M31 in a context of other galaxies. We also discuss variations in the individually estimated $\mathrm{a}_{24\mu\mathrm{m}}$ factors as a function of SFRs, IR emission and the dust temperatures in M31 and nearby galaxies.

3.5.1 Effects of galactocentric distance and inclination

Fig. 3.17 show differences between the SFR values estimated from the Balmer emission lines, and the SFR values estimated from the C07 prescription (with $\mathrm{a}_{24\mu\mathrm{m}} = 0.031$), as a function of galactic inclination, galactocentric distance and observed attenuation. Each SFR value on these diagrams were derived using $\mathrm{a}_{24\mu\mathrm{m}}$ factors that are individually estimated for each data point. Thus the difference in the SFR values presented here indicates a difference between the estimated $\mathrm{a}_{24\mu\mathrm{m}}$ factors and the $\mathrm{a}_{24\mu\mathrm{m}} = 0.031$ prescribed by C07.

The data shown on the figure are from M31 (integrated fields and spaxels 50 pc in length), the SINGS galaxies (from C07), CALIFA[8] survey of galaxies from Catalán-Torrecilla et al. (2015), and NGC 628 and NGC 3627 observed by the MUSE[9] (Kreckel et al. 2018; McElroy in prep.). Here, the data from the SINGS galaxies come from the central regions (with a radius of the field of view between 0.5 and 2.5 kpc), pixel lengths of NGC 628 and NGC 3627 are 0.3 kpc and 0.8 kpc, and the data from the CALIFA survey are from the apertures (with 36” radius) covering entire or most of galaxies. The M31 spaxel data are binned to 50 pc from WISE resolution data, in order to show spatially independent spaxels. Additionally, we show the Spearman’s correlation coefficient and the significance of its deviation from zero. This coefficient is shown for all of the data (and with the integrated M31 fields), and for all of the data without M31, in order to show correlations among galaxies even without including M31 data. We also added a theoretical modeled diagram that show prediction of differences in the SFR prescriptions as a function attenuation, with different $\log_{10}(\mathrm{I}_{24\mu\mathrm{m}}/\mathrm{I}_{\mathrm{H}\alpha})$ ratios and different $\mathrm{a}_{24\mu\mathrm{m}}$ factors. In this diagram, a covered range in the $\mathrm{a}_{24\mu\mathrm{m}}$ factor is the same as the range observed by Leroy et al. (2012) in nearby galaxies (their Fig. 9).

The SFR prescription on Fig. 3.17 shows some correlation with galactocentric distance and a weak correlation with galactic inclination. Those correlations are still seen with ρ coefficient even if we exclude integrated M31 Fields. The scatter of the data in the case of inclinations is large, although the values of the Spearman’s correlation coefficient indicate some trends.

---

[8] The Calar Alto Legacy Integral Field Area Survey; Sánchez et al. (2012)

[9] The Multi Unit Spectroscopic Explorer; Laurent et al. (2006)

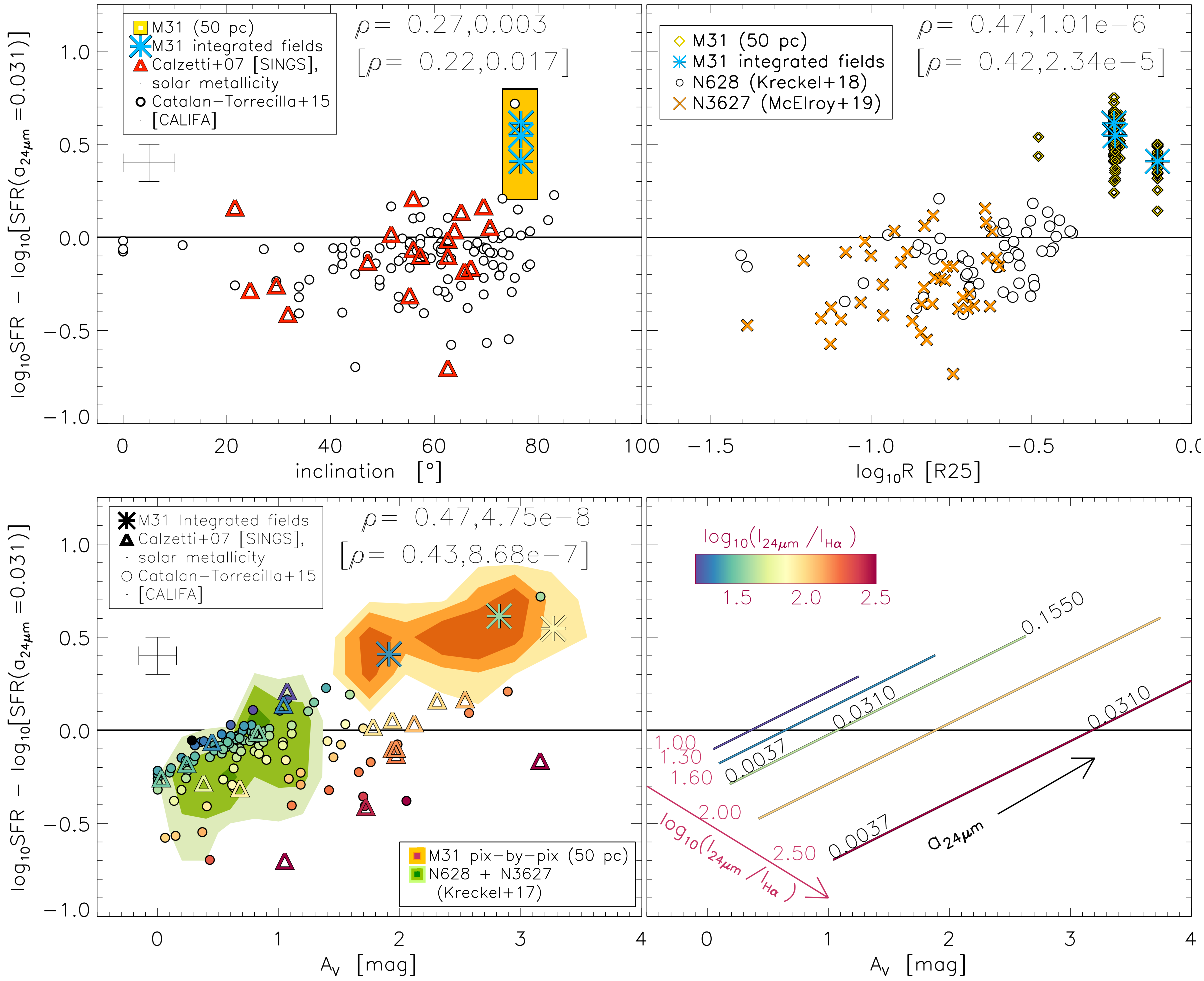

Fig. 3.17 Difference between SFR values estimated from the Balmer emission lines and SFR values from the hybrid SFR(Hα+a$_{24\mu\mathrm{m}}$24μm) prescription defined by C07, as a function of galactic inclination (upper left panel), galactocentric distance (upper right panel), attenuation (lower panels). Each SFR value on these diagrams were estimated without fixed a$_{24\mu\mathrm{m}}$ factor, thus the difference in the SFR values presented here indicate a difference between the estimated a$_{24\mu\mathrm{m}}$ factors and the factor prescribed by C07. The presented data are: M31 data (asterix for integrated fields, and the yellow contours or diamonds for the 50 pc size spaxels), SINGS sample of galaxies with metallicities similar to M31 (triangles; Calzetti et al. 2007), CALIFA survey of galaxies (circles; Catalán-Torrecilla et al. 2015), and NGC 628 and NGC 3627 (green contours in upper panel, and circles and crosses in upper right panel; Kreckel et al. 2018; McElroy in prep.). *Upper panels-* Difference between SFR values as a function of galactic inclination (estimated using Eq. 1 in van den Bergh 1988) and the galactocentric distance (in units of R$_{25}$). The estimated uncertainties are shown, as the Spearman's correlation coefficient (ρ, left number) and the significance of its deviation from zero (right number) for all the data (upper numbers), and the data without M31 (numbers in brackets). *Lower panels-* Difference between SFR values as a function of attenuation for observed data (left panel). The data are color-coded by the observed $\log_{10}(\mathrm{I}_{24\mu\mathrm{m}}/\mathrm{I}_{\mathrm{H}\alpha})$ ratio. On the lower right panel, we show theoretical behaviour of the data with different assumed $\log_{10}(\mathrm{I}_{24\mu\mathrm{m}}/\mathrm{I}_{\mathrm{H}\alpha})$ ratios and different a$_{24\mu\mathrm{m}}$ factors. The a$_{24\mu\mathrm{m}}$ covers a range observed by Leroy et al. (2012) (Fig. 9 in their paper). As above, we show uncertainties and Spearman's coefficients.

Most of the nearby galaxies have inclination lower than M31. A few galaxies with inclinations similar to M31 show in general slightly higher a_{IR} factors compared to other galaxies. On the other hand, we notice a slightly better correlation and stronger trend between the estimated a_{IR} factors and the galactocentric distance. Unfortunately, there is a lack of data with the galactocentric distances between the M31 data and central regions in nearby galaxies to clearly prove that the M31 follows this trend.

High inclination of M31 and large galactocentric distances of M31 data may be a source of their high attenuation values. We could see indication of this in the fact that the SFR prescription and its difference from the C07 prescription correlate with attenuation. Furthermore, the M31 data (integral or pixel-by-pixel) follow the trend seen in other nearby galaxies, and their observed $\log_{10}(\mathrm{I}_{24\mu\mathrm{m}}/\mathrm{I}_{\mathrm{H}\alpha})$ ratios follows the trends seen in the theoretical modeled diagram. The $\log_{10}(\mathrm{I}_{24\mu\mathrm{m}}/\mathrm{I}_{\mathrm{H}\alpha})$ ratio adds to the scatter in the SFR prescriptions for the same attenuation value. For example, data with a same a_{IR} factor exhibits higher attenuation values with an increasing $\log_{10}(\mathrm{I}_{24\mu\mathrm{m}}/\mathrm{I}_{\mathrm{H}\alpha})$ ratio.

3.5.2 Calibration factor as a function of various physical quantities

Fig. 3.18 presents a_{22}, estimated for each individual data point, as a function of physical quantities of observed $\Sigma(\mathrm{H}\alpha)$, $\Sigma(\mathrm{SFR})$, $\Sigma(22\,\mu\mathrm{m})$, $70\,\mu\mathrm{m}/160\,\mu\mathrm{m}$ ratio (tracing the dust temperature), and $160\,\mu\mathrm{m}/\mathrm{TIR}$ ratio (tracing a fraction of the cold dust emission within the TIR). Below each panel is a histogram of the data distribution for each corresponding physical quantity. We estimated Spearman's correlation coefficient (ρ) and the corresponding significance of its deviation from zero for the integrated M31 fields and SINGS data (upper numbers), and for the integrated M31 fields, SINGS and CALIFA data (numbers in brackets). The ρ factor that is estimated by combining the M31's integrated fields data and the SINGS data is more reliable because those data probe similar spatial scales, unlike when we combine them with the CALIFA data that may probe the entire galaxies.

The figure shows M31 data, the SINGS galaxies with metallicities comparable to M31 (used by C07 for their SFR calibrations), and the CALIFA survey galaxies (used by Catalán-Torrecilla et al. 2015). For the M31 data, we show integrated fields and the pixel-by-pixel comparison of the maps at $22\,\mu\mathrm{m}$ resolution. Here, we binned the pixels to a pixel length of 50 pc to have spatially independent pixel data. To estimate their a_{22} values for the SFR prescriptions, C07 apply apertures with R=13" to the SINGS galaxies (these aperture distances correspond to spatial scales ranging from 30 pc to 1.26 kpc) and subtract the diffuse mid-IR cirrus from the apertures. However, the data provided by C07 and shown in Fig. 3.18 represent the central regions in SINGS galaxies with a spatial length between 140 pc and 4 kpc. Without the diffuse subtraction, mid-IR surface brightness values for the C07 data points would yield slightly higher values. The PACS 70 μm and 160 μm of C07 are derived at galactic scales and taken from Dale et al. (2017). The data from the CALIFA survey are from the apertures (with

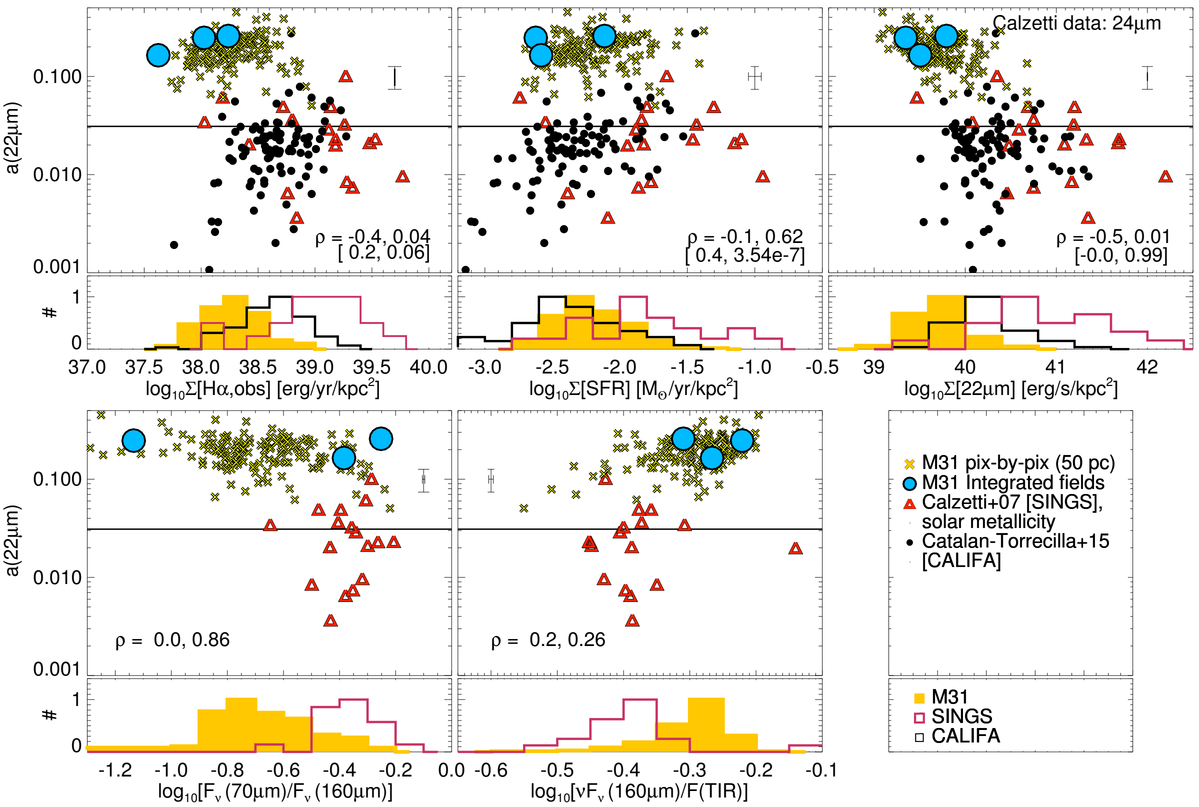

Fig. 3.18 In the diagrams, we show a_{22} values, estimated for each individual data point, as a function of observed $\Sigma(\mathrm{H}\alpha)$ (top left), $\Sigma(\mathrm{SFR})$ (top middle), $\Sigma(22\,\mu\mathrm{m})$ (top right), $70\,\mu\mathrm{m}/160\,\mu\mathrm{m}$ ratio (indicating the dust temperature; bottom left), and $160\,\mu\mathrm{m}/\mathrm{TIR}$ ratio (tracing a fraction of the cold dust emission within the TIR; bottom middle). Data points in upper panels are: M31 pixel-by-pixels data (spatially independent binned pixels 50 pc in length; yellow X symbols), integrated fields (blue circles), the data of the central regions in SINGS galaxies (spatial lengths of 140 pc-4 kpc) from C07 with metallicities comparable with M31 (red triangles; C07 and Dale et al. 2017), and the data from the CALIFA galaxies from Catalán-Torrecilla et al. (2015). A variation in the a_{22} factor indicates a behavior of the SFR prescription, with $a_{22} = 0.031$ from the C07 prescription indicated with the black solid line. The histograms bellow diagrams show the distribution of M31 data (filled yellow histograms), the SINGS galaxies data (red empty histograms) and CALIFA galaxies (black empty histograms) as a function of corresponding quantities on the x-axis in upper diagrams. The estimated uncertainties are shown, as the Spearman's correlation coefficient (ρ, left number) and the significance of its deviation from zero (right number) for the integrated M31 fields and SINGS data (upper numbers), and for the integrated M31 fields, SINGS and CALIFA data (numbers in brackets). In these diagrams and histograms, we see a slight trend in a_{22} with mid-IR emission, the dust temperature, and with $160\,\mu\mathrm{m}/\mathrm{TIR}$ ratio. For details, see the text.

36" radius) covering entire or most of galaxies.

The data and the histograms show that M31's fields exhibit an order of magnitude lower $\Sigma(\mathrm{H}\alpha, \mathrm{obs})$ and $\Sigma(\mathrm{IR})$ and a slightly lower $\Sigma(\mathrm{SFR})$ compared to the C07 data. We notice a slight trend (anti-correlation) between a_{IR} and $\Sigma(\mathrm{IR})$, $\Sigma(\mathrm{H}\alpha, \mathrm{obs})$, and slight correlation with the $160\,\mu\mathrm{m}/\mathrm{TIR}$ ratio. These trends are also seen in the ρ factors for the M31's integrated fields and the SINGS galaxies. Although, there is slight anti-correlation between $\mathrm{a_{IR}}$ and $70\,\mu\mathrm{m}/160\,\mu\mathrm{m}$ ratio (the dust temperature) when we compare pixel-by-pixel data in M31 and the SINGS data, this anti-correlation breaks for the integrated fields in M31. We explain this as an effect of HII regions emission dominating the emission within the integrated fields. The histograms also indicate that the pixel-by-pixel M31 data have lower $70\,\mu\mathrm{m}/160\,\mu\mathrm{m}$ ratios than the SINGS galaxies.

3.6 Discussion

We found in the M31 Fields that the monochromatic and hybrid SFR prescriptions, calibrated by using the extinction corrected $\Sigma_{\mathrm{SFR}}(\mathrm{H}\alpha, \mathrm{corr})$, differ from the standard prescriptions in the literature. The hybrid SFR prescription is calibrated by estimating the SFR prescription factors (a_{IR} and b_{IR}), which are multiplied with an un-attenuated IR emission and combined with an attenuated Hα or FUV emission to estimate total SFR. The M31 fields yield high a_{IR} and b_{IR} values, which are a factor of 5-8 higher compared to the prescriptions given in the literature (Calzetti et al., 2005, 2007; Leroy et al., 2008; Catalán-Torrecilla et al., 2015). In this section, we discuss what may cause this offset in the SFR prescriptions, and why the hybrid SFR prescriptions may not be universal, as assumed in the literature.

3.6.1 Galactocentric distance and inclination

In the literature, the hybrid SFR prescriptions are assumed to be universal, and that they trace 'local' attenuation. This 'local' attenuation of the light from star-forming regions is due to the hot dust, which is surrounding star-forming regions. Heated by the ionizing photons from the star-forming regions, this dust emits in near-IR. This is why the near-IR emission was associated with attenuated SFR tracers (FUV and Hα) and used for calibrating the SFR prescriptions. This model also assumes that there is no additional and more extended dust in galaxies. If this model is true, than there should be no variations in the SFR prescriptions as a function of attenuation, inclination or galactocentric distance.

However, when we compare the data between various galaxies and the data within the galaxies, we see that the SFR prescriptions change as a function of inclination, galactocentric distances and attenuation (Fig. 3.17). Similarly, some previous observations of nearby galaxies also indicate that the hybrid SFR prescriptions change with specific quantities or with galactocentric distance. For example, Pérez-González et al. (2006) compared their results for the spiral arms in M81 with M51 data in C05, and found an ≈ 0.2 dex offset in SFR(IR) values compared to the C05 results. They also observed lower $24\,\mu\mathrm{m}$/TIR ratios for their data compared to the prediction from C05 (Fig. 4 in Pérez-González et al. 2006), which indicates that the dust in the M81 data is cooler, similar to what we found in M31. Secondly, Catalán-Torrecilla et al. (2015) found a weak correlation between observed attenuation and the $\mathrm{a_{IR}}$ in their sample of

CALIFA galaxies, as do we in Fig. 3.17. Thirdly, Boquien et al. (2016) found that the b_{IR} factor increases from the centers toward the outskirts of disks in their sample of face-on galaxies (Fig. 4 in their paper). They concluded that b_{IR} factor and the SFR prescription change due to $\Sigma(M_{stellar})$ and Σ(sSFR), which decrease in values toward the outskirts of galaxies. However, we argue that $\Sigma(M_{stellar})$ and Σ(sSFR) alone can not explain variation in the SFR prescriptions, because we estimate $b_{IR} \approx 9 \pm 2$ values of our M31 fields when we apply their b_{IR}-Σ(sSFR) conversion. That is a higher value compared to the prescription from Boquien et al. (2016), but still lower than our prescription.

In Chap. 2, using the same M31 fields, we concluded that the vertical distribution of the dust and ionized gas changes as a function of galactocentric distance (as schematically represented in Fig. 2.16). If we assume that the dust is well mixed with the HI and H_2 gas (Holwerda et al. 2012; Hughes et al. 2014a), it can be argued that the vertical scale-hight of the dust increases with a galactocentric distance, as it does with the HI and H_2 (as seen for highly inclined M31 and other galaxies; Braun 1991; Olling 1996; Yim et al. 2014). On the other hand, the vertical scale height and intensity of the ionized gas (DIG and HII regions) are correlated with the number and brightness of star-formation activity, and decrease with a galactocentric distance (Dettmar 1990; Rand 1996; Oey et al. 2007; Bigiel et al. 2010). For example, Dettmar 1990 noticed that the vertical scale-hight of the DIG in an edge-on galaxy NGC 891 decreases with the galactocentric distance.

Therefore, we suggest that the SFR prescriptions should be used with a caution at large galactocentric distances and in galaxies with high inclinations. If the dust in HI dominated outskirts of galaxies is more extended extended along the line of sight and not spatially associated with star-forming regions, then it would not be heated by ionized photons that originate from the star-forming regions. This leads to higher attenuation that is not followed by higher mid-IR emission, and thus the a_{IR} and b_{IR} factors increase, changing the SFR prescriptions. High galactic inclination also adds a dust layer along the line of sight, which is not associated with star-forming regions, thus increasing attenuation. This may be a reason why on Fig. 3.17 we notice a variation in the SFR prescription as a function of galactocentric distance and inclination, which leads to its correlation with attenuation.

M31 is highly inclined galaxy, and M31 Fields used in this paper preside on galactocentric distances that are larger than the galaxies (KINGFISH, SINGS and CALIFA surveys, and NGC 3627, NGC 628) probed for calibration of the SFR prescriptions in the literature. This leads to higher attenuation for the same dust mass surface density compared to the nearby galaxies (see Chap. 2 and Tomičić et al. 2017), and higher a_{IR} and b_{IR} factors. Due to large galactocentric distances, M31 data also exhibits low surface brightness in mid-IR and observed Halpha (Fig. 3.18). Moreover, due to the additional, non-heated dust in a line of sight, component of a cold dust dominates the total IR emission in M31 Fields (Fig. 3.18). This is backed by the findings of Groves et al. (2012b), who found relatively cold dust in M31, and by Xu & Helou (1996) who found low $60\,\mu$m/$100\,\mu$m ratios in the M31 spiral arms. Xu & Helou (1996) concluded that the dust in M31 is cooler, more diffuse or lacking very small grains. By deriving a model of the dust heating in M31, Viaene et al. (2017) also concluded the most of the radiation heating the dust in the disk of M31 comes from an older stellar population (particularly in the bulge).

3.6.2 Spatial scales, age of the clusters and sampling initial mass function

As smaller spatial scales are probed, standard SFR prescriptions can break down due to three main issues: 1) SFR tracers that use reprocessed emission, such as Hα and IR, may arise from star formation outside the region probed (e.g., in other pixels; Boquien et al. 2016), 2) the simple assumption of continuous star formation over 10-100 Myr breaks down, with stochastic sampling of stellar ages (i.e. individual single aged clusters) being probed, and associated, 3) the initial mass function (IMF) is not sampled fully, with stochastic sampling of high mass stars, and thus changing the assumptions taken into account in Eq. 3.1. The topic of varying spatial scales and its possible effects on the SFR prescription has been previously discussed by Faesi et al. (2014). Faesi et al. (2014) observed star-forming regions in NGC 300 at 250 pc scales, and used STARBURST99 (Leitherer et al., 1999) modeling to infer the SFR. They assumed an instantaneous burst of star formation instead of the continuous star formation over 100 Myr used in C07 and Leroy et al. (2008). This results in SFRs that are 2-3 times ($\approx$0.3 dex) higher compared to the SFRs prescribed by C07 and Leroy et al. (2008). Faesi et al. (2014) argue that on these smaller spatial scales where we observe individual HII regions, the burst model is more appropriate compared to measurements done on larger spatial scales where averaging within the aperture would correspond to a more uniform SFH. Similarly, da Silva et al. 2014 and Krumholz et al. (2015) found in their SLUG[10] software that the stochastic fluctuations in star formation, can produce non-trivial errors at SFRs biases even $>$0.5 dex at the lowest SFRs.

Firstly, integrating the entire M31 fields (1-2 kpc in scales) should eliminate the issues of tracing the emission from another pixels and variation in the age of clusters, and integrated fields still show similar SFR prescriptions as at small scales. Secondly, calibrating the hybrid SFR(Hα+a$_{IR}$IR) prescriptions is independent from variation between FUV and Hα emission that is caused by age of the clusters. This is because this calibration avoids the conversion from Hα emission to FUV emission, and uses only mid-IR, Hα and Hβ emission. Finally, findings from da Silva et al. 2014 and Krumholz et al. (2015) do emphasize that a bias in the estimated SFR is mostly shown in regions with very low SFRs ($< 5\,\mathrm{M_\odot\,yr^{-1}}$). However, using apertures, integrated fields and larger spaxels in M31 Fields, we are probing a SFR range between -4 and -2 $\mathrm{M_\odot\,yr^{-1}}$, a range which SLUG simulations result with no bias for estimated SFR, but with a large 0.5 dex scatter (Fig. 6 in da Silva et al. 2014). Furthermore, we also probe in M31 Fields spatial scales comparable to the scales used in C07, Leroy et al. (2012) and Catalán-Torrecilla et al. (2015), and their prescriptions would suffer the same problems rose by da Silva et al.

---

[10] SLUG is a code that Stochastically Lights Up Galaxies, to simulate galaxies undergoing stochastic star formation.

2014 and Krumholz et al. (2015). Never the less, our SFR prescriptions still differ from the literature values, even when we use the same spatial resolutions. On the other hand, a scatter of SFR values within our fields (seen in Fig. 3.13) and a scatter of residuals between our SFRs and the SFRs by Lewis et al. (2015) (as seen in Fig. 3.9) do decrease with increasing spatial scales, as predicted by da Silva et al. 2014.

3.6.3 Effects of the diffuse emission components

Our result in M31 shows no change in the SFR prescriptions and a_{IR} when we subtract the diffuse emission, except in a case of the lowest surface brightness regions (Sec. 3.4.3). A possible caveat for our method of subtracting the diffuse emission is that we follow the procedure from C07. Unlike in C07, where they integrates areas outside the apertures and spiral arms to calculate the diffuse emission, we measure the diffuse emission inside the M31 fields that are still within the spiral arms. However, if our method of probing the diffuse emission within the spiral arms leads toward too bright diffuse emission, that would lead to even higher a_{IR} compared to the cases for not subtracting the diffuse emission.

On the other hand, the amount of the subtracted diffuse emission seem reasonable because we detect diffuse fractions of 5%-60%, which are the typical fractions observed in nearby galaxies (Leroy et al. 2012). Additionally, Leroy et al. (2012) measure and subtract the cirrus using the dust emissivity throughout their galaxies, and still find a SFR prescription that differs from ours.

3.6.4 Implications of the results

The first direct implication of our findings is that the traditional hybrid SFR prescriptions cannot be applied on M31, and that the previously estimated SFR values for M31 studies are unreliable using standard prescriptions. In Sec. 3.3.4, we indicated that the SFR values of the molecular clouds in M31 should have higher values than the values estimated by the prescriptions in the literature, and that those values match with what is predicted by the molecular cloud masses (Gao & Solomon 2004).

A broader implication of our findings is that standard SFR prescriptions are not universal, and should be used with caution at large galactocentric distances (with higher $a_{\rm IR}$ and $b_{\rm IR}$ in the outskirts of galaxies) and so in highly-inclined galaxies. Our results indicate that higher $a_{\rm IR}$ and $b_{\rm IR}$ factors should be applied to the outskirts of galaxies.

3.7 Summary

In this paper, we calibrate SFR prescriptions using different tracers and considering different spatial scales (between ≈10 pc and ≈0.9 kpc). We observe five 0.6 kpc×0.9 kpc fields in the spiral arms of M31. The tracers used here are: Hα (from IFU data), 22 μm (from WISE),

$24\,\mu$m (from SPITZER/MIPS) and FUV (GALEX). We also calibrated $12\,\mu$m, $70\,\mu$m, $160\,\mu$m and TIR SFR prescriptions. The reference SFR tracer uses the Balmer decrement to extinction correct Hα (Hα, corr), which we compare with the hybrid SFR tracers (Hα+IR or FIV+IR) and with other SFR prescriptions.

Our main results indicate the following:

- Our Σ_{SFR}(Hα,corr) matches relatively well with Σ(SFR) derived from independent procedures and from modeled star formation history of M31, modeled by Lewis et al. (2015). Similarly, SFRs of the molecular clouds in M31 estimated using our SFR prescription relatively match with the values predicted by Gao & Solomon (2004), unlike the SFRs values estimated by Viaene et al. (2018).
- At our smallest spatial scales (10 pc-50 pc), the hybrid SFR prescriptions give calibration factors (a$_{IR}$ and b$_{IR}$) that are systematically a factor of 5-8 times larger than the ones stated in the literature (Calzetti et al. 2007; Leroy et al. 2008; Catalán-Torrecilla et al. 2015). Thus the SFR(Hα, corr) values are higher than SFRs given by other prescriptions (0.5 dex).
- The SFR prescriptions do *not* change with spatial scales. Moreover, the prescription in our fields does not change when subtracting a diffuse component (the DIG and the mid-IR cirrus), except slightly for low surface brightness regions.
- Compared to the nearby galaxies used for calibrating the SFR prescriptions in the literature, the M31 fields have higher galactocentric distance, higher attenuation, high galactic inclination and shows an order of magnitude lower mid-IR and Hα surface brightness. The M31 fields also show a lower $70\,\mu\mathrm{m}/160\,\mu\mathrm{m}$ ratio and a higher $160\,\mu\mathrm{m}$/TIR ratio, which indicates that the fields probe colder dust.
- We noticed that the SFR prescriptions correlate with galactocentric distance, attenuation and galactic inclination, and that the M31 data lie in a continuation of these trends.

Our interpretation of the results is:

- We suggest that the SFR prescriptions across the galactic disks change with inclination and galactocentric distance due to variations in the relative dust/gas distribution. With a different dust/gas distribution in the outskirts of galaxies compared to the galactic centers, or in more inclined galaxies, the dust is more extended extended along the line of sight compared to the HII regions and the diffuse gas. This dust layer is not directly associated with star-forming regions which results in a lower mid-IR surface brightness (dominated by mid-IR cirrus emission), colder dust, and higher A$_{\mathrm{V}}$ of the Hα photons, and could explain the change we observe in the SFR prescriptions. This view is consistent with our conclusions of Chapter 2, and with recent results in Tomičić et al. (2017).

Chapter 4

"We are stardust brought to life, then empowered by the universe to figure itself out—and we have only just begun."

"Astrophysics for People in a Hurry"
by Neil deGrasse Tyson

NGC 2300, NGC 2276
c: Adam Block
Mount Lemmon
SkyCenter / UA

4. Multi-wavelength view of the interacting galaxy NGC 2276

This chapter will be published in a future refereed article (Tomičić 2019, in prep.), which is still in progress. This chapter also uses parts of the article Tomičić et al. (2018), for which I am the lead author, and where the parts of the articles have been adapted for this thesis.

Overview: In this chapter, we present observations of the interacting galaxy NGC 2276, to explore how a galactic interaction and external forces, such as tidal forces and ram pressure, affect the ISM in its disk. In Sec. 4.2, we present the IFU observations of NGC 2276 and the calibration of the data, mostly conducted by the author of this thesis. Results are presented in Sec. 4.3, where we derive the SFR, the galactic orientation and inclination, the BPT diagram, the diffuse gas fraction, and the metallicity gradient of NGC 2276. In Sec. 4.4, we present a summary and our conclusions.

4.1 Introduction

Star formation (SF) is a key process in the evolution of galaxies, affecting both their stellar populations and the properties of their interstellar medium (ISM). Yet the physical factors that set the efficiency at which galaxies convert gas into stars (star formation efficiency; SFE) and conditions that enhance or truncate the star formation rate (SFR) are not yet fully understood. Further uncertainty in estimating the SFE stems from systematic uncertainty in measuring the star formation rates (SFRs).

Utilizing the benefits of the integral field unit (IFU) spectroscopy, such as properly determining of the attenuation of the Balmer lines and accounting for the underlying stellar continuum, enables us to properly estimate the SFR in galaxies. Observations of nearby galaxies at sub-galactic or sub-kpc scales also enables us to probe the ISM in different environments (e.g., spiral arms, bulge, inter-arm regions) and to determine the physics that affect the ISM and SFR in galaxies.

Past and ongoing observations of interacting galaxies in clusters and groups has provided evidence that external dynamical forces, such as tidal forces and ram pressure, do affect the ISM and stellar distribution of the host galaxies, thus affecting their evolution and their SFR (Dressler 1980; Kennicutt et al. 1987; Kennicutt 1998; Cortese et al. 2007; Poggianti et al. 2017). As shown in Sec. 1.2.2, the SFR can be enhanced by galactic collisions and tidal gravitational forces (Kennicutt et al. 1987; Sivanandam et al. 2014; Renaud et al. 2014; Rodríguez-Baras et al. 2014; Moreno et al. 2015; Renaud et al. 2015; Saito et al. 2015), as seen in both the observations and the simulations of interacting galaxies in the groups. The tidal forces influence the stellar distribution, potentially causing asymmetries. Similarly, the ram pressure (RMP), an external force caused by a collision of the host galaxy with its surrounding inter-galactic medium (IGM), can strip the gas from the galaxy, thus quenching star formation (Abadi et al. 1999; Steinhauser et al. 2012; Kenney et al. 2015; Nehlig et al. 2016; Abramson et al. 2016; Bellhouse et al. 2017). Particularly, the quenching of SFR is seen in dwarf galaxies (Steinhauser et al. 2016). On the other hand, it can also locally compress gas and have the opposite effect, i.e. enhance the SFR of the galaxy (Gunn & Gott 1972; Bekki 2014; Sivanandam et al. 2014; Ebeling et al. 2014; Bournaud et al. 2015; Ruggiero & Lima Neto 2017; Ramos-Martínez et al. 2018; Vulcani et al. 2018), especially in more massive systems where the background potential helps inhibit gas stripping. The ram pressure is usually indicated by a bow-shock feature seen in the SFR tracers (Sivanandam et al. 2014; Lee et al. 2017; Gullieuszik et al. 2017), and by a tail of stripped gas in latter stages of interaction (Poggianti et al. 2017).

The interacting galaxy NGC 2276 is a star-forming spiral galaxy that is falling into the NGC 2300 group, and beginning to interact with its neighbouring galaxy NGC 2300, and with the surrounding IGM (Gruendl et al. 1993; Hummel & Beck 1995; Rasmussen et al. 2006; Wolter et al. 2015). Therefore, NGC 2276 is a good case study of galaxies that interact with their surroundings. It is also a good candidate to probe the effects of interactions on the ISM within its disk (Poggianti et al. 2017; Vulcani et al. 2018).

Previous observations of NGC 2276 found ample evidence of both tidal forces and ram pressure acting on the galaxy. The presence of tidal forces in NGC 2276 was invoked to explain the extended south-east arm in radio emission of NGC 2276 (Condon 1983), and truncation of the R-band continuum (Gruendl et al. 1993; Davis et al. 1997). Additional evidence for tidal forces includes a north-east extension in the I-band continuum of NGC 2300 (Forbes & Thomson 1992; Davis et al. 1997), and the enhanced magnetic fields (Hummel & Beck 1995). Enhanced X-ray emission outside NGC 2276, and the bow-shock feature on the western edge of NGC 2276's disk was attributed to ram pressure (Rasmussen et al. 2006) as similar features have been observed in galaxies with ongoing ram pressure (Iglesias-Paramo & Vilchez 1997; Sivanandam et al. 2014; Troncoso Iribarren et al. 2016; Poggianti et al. 2017; Vulcani et al. 2018). The explanation for high ram pressure acting on NGC 2276 is that it is caused by the unusually high density of the group's inter-galactic medium (Mulchaey et al. 1993). Simulations by Wolter et al. (2015) show that ram pressure alone could explain the morphology and the lack of some HI gas in NGC 2276.

In this chapter, we will present a multi-wavelength view of NGC 2276, and the calibration process of the raw IFU data of NGC 2276. We will provide further estimates of various quantities of the galaxy that were not established before. For example, we will present our estimation of NGC 2276's inclination, the SFR of the galaxy derived from the IFU, its stellar distribution, the source of excitation of ionized gas, the diffuse emission fractions, and the metallicity radial gradient at sub-kpc scales ($\approx 200\,pc$). Probing these quantities will show us if the galactic interaction does affects the ISM properties, and to which extent the interacting NGC 2276 differs from other normal star-forming galaxies.

4.2 Data

NGC 2276 is a star-forming, spiral galaxy with an ongoing interaction with its surrounding IGM and the neighboring galaxies in the NGC 2300 group (Gruendl et al. 1993). The NGC 2300 group is also known as HG 92 in the catalogue of Huchra & Geller (1982). The group has four members (Gruendl et al. 1993), of which NGC 2300 is an elliptical (early type) galaxy and the most massive, while NGC 2276 is the second most massive. The stellar mass of NGC 2276 is estimated to be $4.4 \times 10^{10}\,\mathrm{M}\odot$ and $7 \times 10^{10}\,\mathrm{M}\odot$ using B-band and K-band luminosities, respectively (Tully & Fisher 1988; Rasmussen et al. 2006).

The distance of the galaxy, estimated from redshifted nebular emission lines, is ≈ 35.5 Mpc (Gruendl et al. 1993). That distance leads to a spatial resolution of $\approx 170\,\mathrm{pc/arcsec}$. We estimate the projected distance between the centers of NGC 2276 and NGC 2300 to be ≈ 70 kpc. While previous papers (Gruendl et al. 1993; Hummel & Beck 1995; Rasmussen et al. 2006; Wolter et al. 2015) argue that NGC 2276 is in a phase after the first passage through the pericenter, they do not derive specific orbital characteristics for this system. Positions and further details about NGC 2276 and the NGC 2300 group are listed in Tab. 4.1.

4.2.1 Nebular emission line maps

Nebular line emission in galaxies indicate various physical and chemical attributes of the ISM in galaxies. Various recombination emission lines, notably the Hydrogen line emission, display the location and amount of star formation across the galactic disks. Forbidden emission lines ([OII], [OIII], [SII], [NeIV], etc.) and their ratios can be used to estimate the density (traced by e.g. the [SII]$\lambda 6731$/[SII]$\lambda 6717$ ratio) and temperature (traced by e.g. the [OIII]$\lambda 5007$/[OIII]$\lambda 4363$ ratio) of ionized gas (Dopita & Sutherland 2003). The diffuse gas emission, and therefore its fraction in the observed ISM, can be traced by the increase in the [SII]/Hα line ratio. Ratios of various emission lines indicate the gas-phase metallicity and the

Table 4.1 Global properties of NGC 2276.

Parameter	Value	Reference
RA	$07^{\mathrm{h}}27^{\mathrm{m}}13^{\mathrm{s}}609$	Peak in $^{12}\mathrm{CO}(J=1\rightarrow 0)$
DEC	$85^{\mathrm{d}}45^{\mathrm{m}}16^{\mathrm{s}}361$	Peak in $^{12}\mathrm{CO}(J=1\rightarrow 0)$
Systematic velocity $\left[\mathrm{km/s}\right]$	2416	From emission lines (this work).
Distance $\left[\mathrm{Mpc}\right]$	35.5±2.5	NED[a], Ackermann et al. (2012)
Scale $\left[\mathrm{pc/arcsec}\right]$	170±10	
Intergalactic medium density (IGM) $\left[\mathrm{g}\cdot\mathrm{cm}^{-3}\right]$	10^{-27}	Mulchaey et al. (1993); Rasmussen et al. (2006)
Projected distance from NGC 2300 $\left[\mathrm{kpc}\right]$	75±15	Rasmussen et al. (2006)
$\log \mathrm{M}_{\mathrm{stellar}}\left[\mathrm{M}_{\odot}\right]$ of NGC 2300	11.3	From K-band, and from 3.4 μm and 4.6 μm (WISE) (using Querejeta et al. 2015)
Line of sight velocity relative to IGM $\left[\mathrm{km/s}\right]$	≈300	Rasmussen et al. (2006)
Inclination	$\approx 20^{\circ} \pm 10^{\circ}$	From radial velocities and radial stellar profile
R_{25} $\left[\mathrm{kpc}\right]$	$67'' = 11.6\,\mathrm{kpc}$	HyperLeda[b]
$\log \mathrm{M}_{\mathrm{stellar}}\left[\mathrm{M}_{\odot}\right]$	10.7±0.2	From 3.4 μm and 4.6 μm (WISE) (using Querejeta et al. 2015), from this work
$\log \mathrm{M}_{\mathrm{H}_2}\left[\mathrm{M}_{\odot}\right]$	9.8±0.05	From $^{12}\mathrm{CO}(\mathrm{J}=1\rightarrow 0)$ estimated in this work
$\log \mathrm{M}_{\mathrm{HI}}\left[\mathrm{M}_{\odot}\right]$	9.8	Rasmussen et al. (2006)
$\mathrm{M}_{\mathrm{HI}}/\mathrm{M}_{\mathrm{stellar}}$	0.13	From this work
$\log \mathrm{L}_{\mathrm{IR}}\left[\mathrm{L}_{\odot}\right]$	10.75 ± 0.05	From IRAS; Sanders et al. (2003)
$\mathrm{SFR}(\mathrm{H}\alpha,\mathrm{corr})\left[\mathrm{M}_{\odot}/\mathrm{yr}\right]$	17±5	From the integrated spectra (this work)
$\mathrm{SFR}(\mathrm{FUV}+22\,\mu\mathrm{m})\left[\mathrm{M}_{\odot}/\mathrm{yr}\right]$	≈ 10	From FUV and 22 μm maps (this work)
$\mathrm{SFR}\left[\mathrm{M}_{\odot}/\mathrm{yr}\right]$	$5-19$	Literature (Wolter et al. 2015, Kennicutt 1983).

[a] `https://ned.ipac.caltech.edu/`

[b] `http://leda.univ-lyon1.fr/`

excitation mechanism of the ionized gas in galaxies. Therefore, in the following section, we will use various nebular emission line maps of NGC 2276 to determine the attenuation, SFR surface density, gas-phase metallicity, diffuse gas fraction, and excitation mechanism across its disk (see Sec. 4.3.1, 4.3.4, 4.3.5 and 4.3.6).

4.2.2 Calibration of optical IFU observations

To obtain maps of the nebular emission lines of NGC 2276, we observed the galaxy with the integral field unit (IFU) PMAS (Roth et al. 2005) in PPaK mode (Kelz et al. 2006) on the Calar Alto 3.5 m telescope in Spain (PI: S. Meidt; project no. F15-3.5-040). Details about the PPaK fibers bundle and CCD can be found in Sec. 2.2.1. We observed NGC 2276 with a mosaic of 6 pointings ($\approx 75''$ in diameter) to cover the entire galaxy. Each pointing was observed with a dither pattern (three dither positions shifted by $\Delta\mathrm{Dec} = -5.''22$, $\Delta\mathrm{Dec} = -4.''84$ and $\Delta\mathrm{RA} = -5.''22$, $\Delta\mathrm{RA} = +4.''84$), in order to fill in gaps between the fibers. The pointings were observed with 600 s exposures, and in the V500 grating. For flux calibration, we observed the standard star G191-B2B (Oke 1990). For the wavelength calibration, we obtained calibration continuum lamp images (used for positioning of the spectra), He+HgCd arc lamp images (used for wavelengths calibration) and twilight flats (used for accurate flat fielding).

The calibration of the raw data of NGC 2276 was done using the P3D software package (Sandin et al. 2010), written with the IDL tools[1], following the established IFU data calibration procedures[2] (Zanichelli et al. 2005; Blanc et al. 2009; Sandin et al. 2010; Mármol-Queraltó et al. 2011). We performed bias and flat field (from twilight images) corrections. Observations are cleaned of cosmic rays following the L.A. Cosmic technique (van Dokkum, 2001) as adapted within P3D. We verified that the cosmic ray removal algorithm implemented in P3D robustly cleans up the images and the corresponding noise maps. We created a master trace mask for determination of the positions of all spectra on the CCD, while adapting a modified optimal extraction method of the fitted Gaussian (Horne 1986) that simultaneously fits all the line profiles. The dispersion mask for the wavelength calibration is created using the He+HgCd arc lamp images. The data were absolute flux calibrated using a spectral response function calculated by comparing the observed spectrum of the standard star G191-B2B with its spectrum from the Oke (1990) catalog. The sky-subtracted stellar spectrum is derived from the sum of fibers containing flux from the standard star, and the spectrum is corrected for atmospheric extinction. The sky spectrum was derived from the PPaK sky fibers which lie outside the galaxy, and which were observed at the same time as the science pointings on NGC 2276. These sky spectra were subtracted from the spectra of corresponding pointings. An example of the P3D window during the calibration process of NGC 2276 raw data is shown in Fig. 4.1.

Astrometry for each pointing was corrected by comparing the positions of compact *R* band

---

[1] The IDL tools are explained on https://p3d.sourceforge.io/index.php?page=about

[2] http://ifs.wikidot.com/reducing-fibreoutline

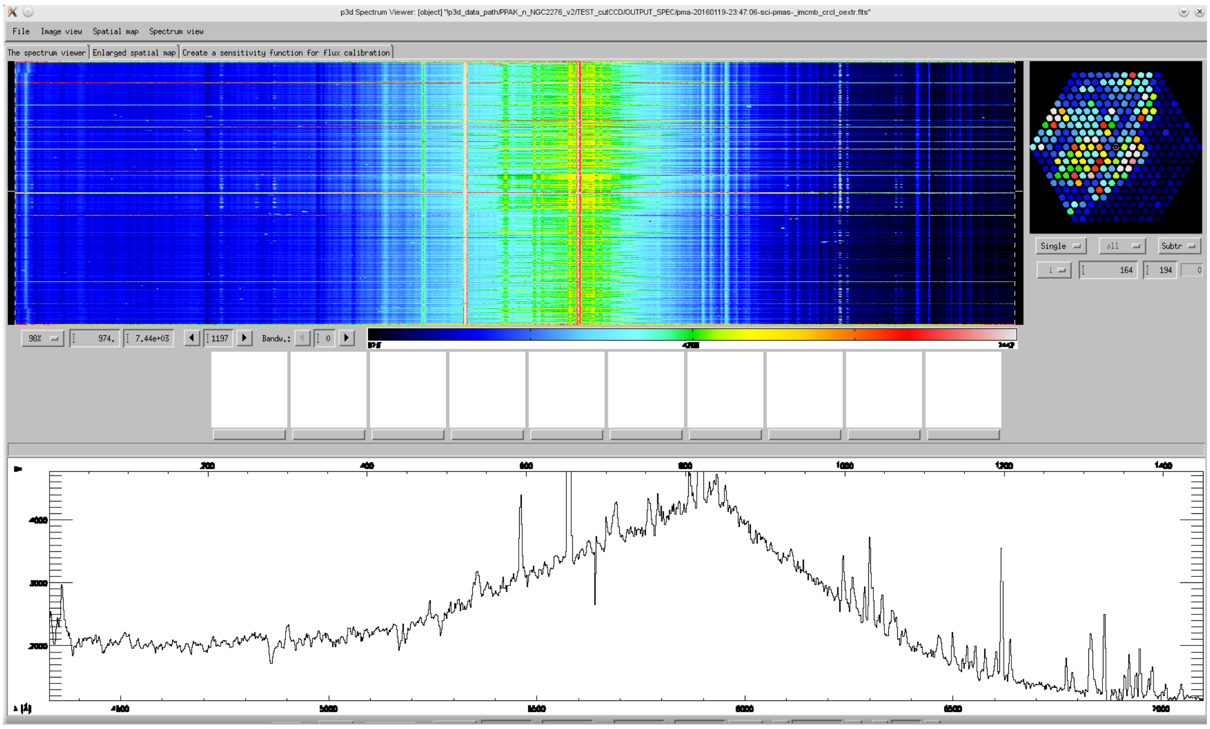
p3d Spectrum Viewer: [object] "!p3d_data_path/PPAK_n_NGC2276_v2/TEST_cutCCD/OUTPUT_SPEC/pma-20160119-23:47:06-sci-pmas-_imcmb_crcl_oextr.fits"
File
Image view
Spatial map
Spectrum view
The spectrum viewer
Enlarged spatial map
Create a sensitivity function for flux calibration
Single
All
Subtr
164
194
0
98%
974.
7.44e+03
1197
Bandw.:
0
200
400
600
800
1000
1200
1400
4000
3000
2000
λ [Å]
4500
5000
5500
6000
6500
7000

Fig. 4.1 This is an example of the P3D software package window, during the calibration of the raw NGC 2276 data. We present here the south-west pointing on NGC 2276. The data are not yet flux calibrated and the sky is not subtracted. In the upper left frame is the CCD detector image, with each bright line indicating light coming from an individual optical fiber. In the upper right panel is a spatial representation of light from the optical science fibers (except the sky and calibration fibers) placed on the south-west side of NGC 2276. In the lower panel is a raw spectrum from one fiber. Throughout the spectrum, the following features could be seen: the sky continuum (the bulge in the middle of the continuum), bright sky emission lines (mostly in the center and right), and the rest of the spectrum (galactic stellar continuum and nebular emission lines).

and Hα regions from PanSTARRS[3] images and our IFU images (at which we applied the PanSTARRS filter response functions). This was used to update the central position of the IFU pointings. In addition, we checked the astrometry by comparing the *R*- and *G*-band of the *Hubble Space Telescope* (HST) images with our data, by applying the HST response functions for the corresponding bands to our observed spectra. We used the *R* band images from the La Palma observatory (NED[4]) for absolute flux calibration.

The final step was to combine the now flux-calibrated and sky-subtracted RSS spectra for all pointings into a single 3D spectral data cube. We combined each of the spectra onto a grid of 1 arcsec^2 spatial pixels (spaxels) using a Delaunay linear triangulation (Delaunay, 1934) individually for each wavelength. The angular size of 1 arcsec for each spaxel corresponds to $\approx$ 170 pc for NGC 2276. The final datacube was Nyquist-sampled with $\approx$3 spaxels across the instrumental point spread function. Errors from the data and sky contribution (calculated by

---

[3] https://panstarrs.stsci.edu/

[4] `https://ned.ipac.caltech.edu/`

P3D) were propagated through the entire calibration process.

4.2.3 IFU spectral analysis

The reduced spectra have a spectral resolution of R=1000 and cover 3700-7010 Å. We analyzed the reduced spectra and extracted the emission lines using the GANDALF software package (Sarzi et al. 2006). The analysis process of the spectra closely follows the method described in Sec. 2.2.1.2. During the process, the spectra were corrected for foreground Galactic extinction, assuming the Cardelli extinction curve (Cardelli et al. 1989) and $\mathrm{E_{B-V}} = 0.088\,\mathrm{mag}$ (based on Schlegel et al. 1998 and Schlafly & Finkbeiner 2011). The angular resolution of the final data and the nebular emission line maps is 2.7" ($\approx 450\,\mathrm{pc}$). For the extinction correction of the Hα line, we assumed the foreground screen model for the dust/gas distribution, applied the Cardelli et al. (1989) extinction curve, assumed Hα/Hβ=2.86 (case B recombination at a gas temperature of $\approx 10^4\,\mathrm{K}$) and a selective extinction R$_V$ =3.1. These assumptions were also used for the M31 data in the previous chapters (Chaps. 2 and 3). Fig. 4.2 shows the observed $\Sigma_{\mathrm{H\alpha,obs}}$, extinction corrected H$\alpha$ ($\Sigma_{\mathrm{H\alpha,corr}}$), and measured attenuation (A$_\mathrm{V}$) maps of NGC 2276.

4.2.4 UV images

FUV continuum emission is radiated from the young stars (mostly the spectral type OB) and thus used as a SFR tracer (Kennicutt 1998; Calzetti et al. 2000; Leroy et al. 2012). Unlike the Hydrogen line emission that decreases rapidly after 5 Myr in the case of a single star-forming burst, the FUV continuum emission decreases slowly and may lasts up to 100 Myr (see Fig. 1 in Leroy et al. 2012 and Fig. 6 in Genzel et al. 2010). Therefore, assuming an instantaneous burst of star formation and a specific stellar initial mass function, the ratio of extinction corrected FUV and Hα emission maps indicates the age of stellar clusters (Sánchez-Gil et al. 2011). Assuming a different star-forming history, such as a continuous star formation within an observed region (equivalent to probing a large galactic scales), alters the FUV/Hα ratio. In this work, we use a FUV map of NGC 2276 as one of the SFR tracer maps (Sec. 4.3.1), and the FUV/Hα ratio map as a robust indicator of the age of the stellar clusters across the disk of NGC 2276 (Sec. 5.3.2).

We retrieved the FUV image of NGC 2276 (seen in Fig. 4.3) from the public AIS survey[5] (Bianchi et al. 2014). The FUV mosaic images were observed with GALEX (The Galaxy Evolution Explorer; Martin et al. 2005), and details of the observations and calibration are described in Thilker et al. (2005), Morrissey et al. (2007), and Thilker et al. (2007). The background FUV emission was subtracted from the galaxy using the mean value of 10 apertures outside NGC 2276. The correction for the foreground Milky Way extinction was implemented applying the extinction curve from Cardelli et al. (1989) and $\mathrm{E_{B-V}} = 0.088$.

---

[5] `http://galex.stsci.edu/GR6/?page=tilelist&survey=ais`

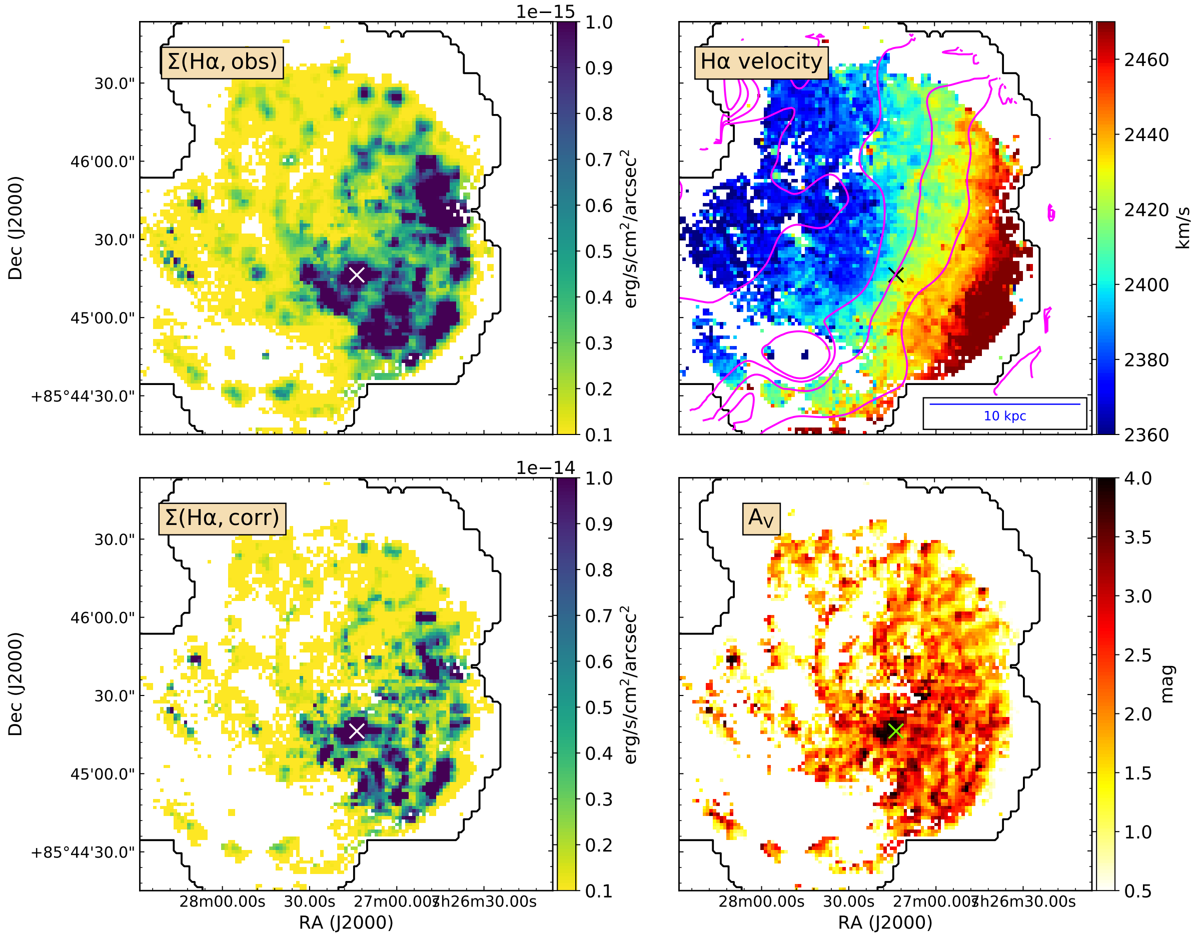
Σ(Hα, obs)
Hα velocity
Σ(Hα, corr)
A$_V$
1e−15
1e−14
erg/s/cm²/arcsec²
km/s
mag
10 kpc
Dec (J2000)
RA (J2000)
30.0"
46'00.0"
45'00.0"
+85°44'30.0"
28m00.00s
30.00s
27m00.00s
7h26m30.00s
0.1
0.2
0.3
0.4
0.5
0.6
0.7
0.8
0.9
1.0
2360
2380
2400
2420
2440
2460
0.5
1.0
1.5
2.0
2.5
3.0
3.5
4.0

Fig. 4.2 The observed Hα surface brightness ($\Sigma_{\mathrm{H}\alpha,\mathrm{obs}}$; upper left), the gas velocity estimated from the Hα line (upper right), the extinction corrected Hα surface brightness ($\Sigma_{\mathrm{H}\alpha,\mathrm{corr}}$; bottom left), and the A_V (bottom right) maps of NGC 2276. The contours indicate the field of view that is observed by the optical IFU observations. The isovelocity (thin, magenta) contours are overplotted in steps of 20 km/s on the velocity profile map.

4.2.5 IR and stellar distribution

In this work, we use near-IR tracers (3.4 μm, 4.6 μm, and 22 μm) to probe the spatial distribution of both old stars (dominating the 3.4 μm and 4.6 μm emission) and hot dust around the star-forming regions (dominating the 22 μm emission) in NGC 2276 and its companion NGC 2300.

These near-IR emission maps were retrieved from the Wide Field Infrared Survey Explorer (WISE; Wright et al. 2010). The mean background emission was calculated from the mean value of 10 apertures outside the galaxies, and subtracted from NGC 2276 and NGC 2300. For the flux calibration of the 22 μm emission, we used the prescription given by Cutri et al. (2011), while using a flux value of 7.871 Jy for Vega (Brown et al. 2014; Jarrett et al. 2017). The 3.4 μm and 22 μm emission maps are shown in Fig. 4.3.

We estimated the stellar surface density distribution $\Sigma(\mathrm{M}_{\mathrm{stellar}})$ of NGC 2276 and NGC 2300

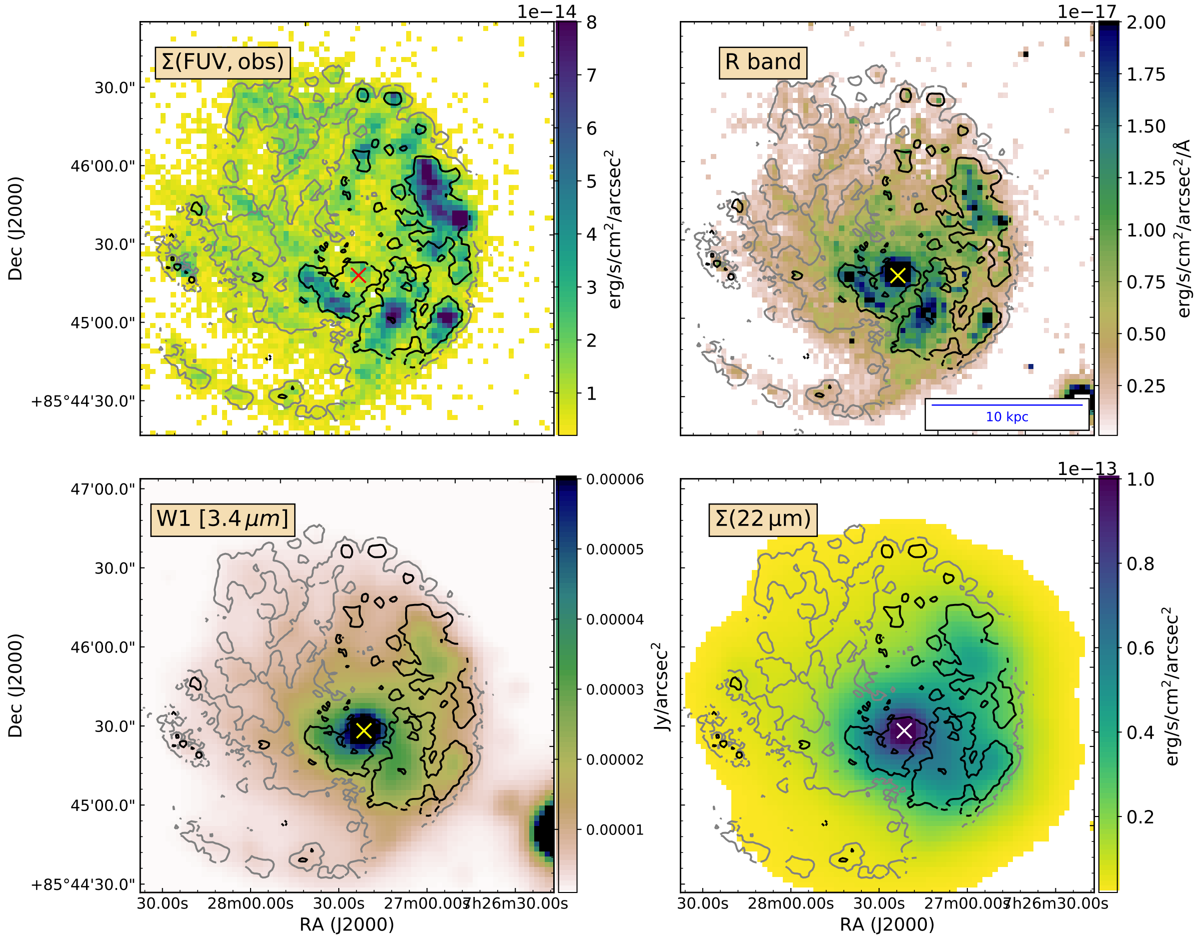
Σ(FUV, obs)
1e−14
8
7
6
5
4
3
2
1
erg/s/cm²/arcsec²
R band
1e−17
2.00
1.75
1.50
1.25
1.00
0.75
0.50
0.25
erg/s/cm²/arcsec²/Å
10 kpc
W1 [3.4 μm]
0.00006
0.00005
0.00004
0.00003
0.00002
0.00001
Jy/arcsec²
Σ(22 μm)
1e−13
1.0
0.8
0.6
0.4
0.2
erg/s/cm²/arcsec²
Dec (J2000)
47'00.0"
30.0"
46'00.0"
30.0"
45'00.0"
+85°44'30.0"
RA (J2000)
30.00s
28m00.00s
30.00s
27m00.00s
7h26m30.00s

Fig. 4.3 Maps of the star formation and stellar light tracers of NGC 2276: the FUV (upper left), the *R* band continuum (retrieved from NED[6]; upper right), the WISE images at 3.4 μm (bottom left) and the 22 μm (bottom right). The contours indicate the $\Sigma(\mathrm{H}\alpha, \mathrm{obs})$ emission at $1 \times 10^{-16}\,\mathrm{erg\,s^{-1}\,cm^{-2}arcsec^{-2}}$ (gray) and $6 \times 10^{-16}\,\mathrm{erg\,s^{-1}\,cm^{-2}arcsec^{-2}}$ (black). The galactic center is marked with an 'x', and estimated from the molecular $^{12}\mathrm{CO}(J = 1 \rightarrow 0)$ line map (Sec. 5.2).

from the WISE images at 3.4 μm and 4.6 μm following Eq. 8 in Querejeta et al. (2015). The emission from 4.6 μm was used to correct the stellar continuum emission in the near-IR (3.4 μm) for a contribution from hot dust, traced also in the 4.6 μm. The resulting $\Sigma(\mathrm{M_{stellar}})$ map is shown in Fig. 4.4, which shows an asymmetric stellar distribution. This can be explained as an effect of the gravitational tidal force exerted by NGC 2300 on NGC 2276's disk. For the details about tidal forces affecting the stellar distribution, see Sec. 5.3.2. From these tracers, we estimated NGC 2276's stellar mass to be $\approx 5 \times 10^{10}\,\mathrm{M}\odot$ (Tab. 4.1).

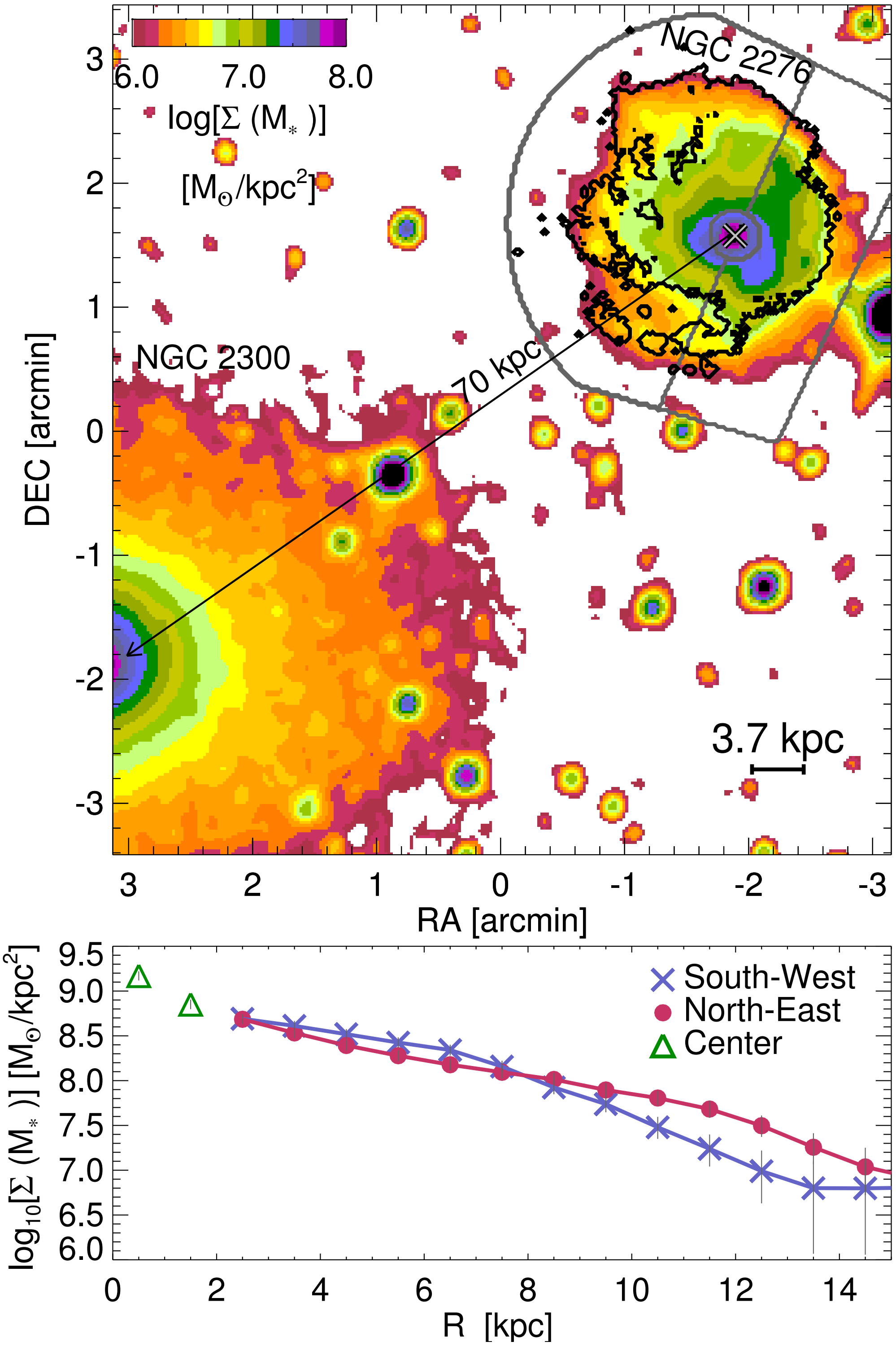

Fig. 4.4 $\Sigma(\mathrm{M_{stellar}})$ of NGC 2276 and NGC 2300 derived from WISE images. NGC 2276's stellar mass distribution is asymmetric and has a shorter scale-length on the south-west side compared to the north-east side. We attribute this to tidal forces exerted by NGC 2300. The black contour on NGC 2276 shows the observed Hα emission. The projected distance between the galaxies is marked. We show below a radial profile of $\Sigma(\mathrm{M_{stellar}})$ for the south-west (crosses), central (triangles), and north-east (circles) sides of NGC 2276 that are marked on the upper map.

4.3 Results

4.3.1 SFR and the star formation tracers

NGC 2276's maps of various SF tracers are presented in Fig. 4.2 and 4.3. Fig. 4.2 shows the observed Hα surface brightness ($\Sigma_{\mathrm{H}\alpha,\mathrm{obs}}$) map, extinction corrected Hα surface brightness ($\Sigma_{\mathrm{H}\alpha,\mathrm{corr}}$) map (details about how it is derived can be found in Sec. 5.2), and Balmer line attenuation $\mathrm{A_V}$. Fig. 4.3 shows the maps of FUV (from GALEX), 3.4 μm and 22 μm (from WISE) emission, and the *R* band continuum image (retrieved from NED[7]).

All SF tracers follow the distribution of the HII regions, and show an asymmetry around the galactic center, with their emission being more pronounced on the western side of the disk. The galactic center does not show bright FUV emission, but exhibits high $\mathrm{A_V}$ and bright near-IR and Hα emission. This indicates that the FUV light is absorbed by the high amount of dust present in the galactic center.

We estimated the total SFR of the galaxy to be $17 \pm 5\,\mathrm{M_\odot\,yr^{-1}}$ using the total Balmer lines fluxes from the galaxy, and $\mathrm{SFR} \approx 10\,\mathrm{M_\odot\,yr^{-1}}$ using the combination of the total FUV and $22\,\mu$m fluxes with the SFR prescription from Leroy et al. (2008). Previous papers report the SFR to be between 5-19.4 $\mathrm{M_\odot}\,yr^{-1}$ (Wolter et al. 2015; Kennicutt 1983), consistent with our derived values. Thus, for its stellar mass, NGC 2276 has an SFR too high to be on the main sequence (expected SFR≈5-6 $\mathrm{M_\odot}\,yr^{-1}$; Elbaz et al. 2007). However, NGC 2276's total IR emission is $\approx 5.6 \times 10^{10}\,\mathrm{L_\odot}$, which is not bright enough to be classified as an ultra-luminous infrared galaxy (LIRG, ULIRG; Soifer et al. 1987; Sanders et al. 1988a,b; Saintonge et al. 2011; Martinez-Badenes et al. 2012).

4.3.2 Gas velocity

In nearby disk galaxies, the gas velocity fields show a typical 'spider' profile (van der Kruit & Allen 1978; Walter et al. 2008) due to regular galactic rotation with a constant velocity (Puche et al. 1990; Martinsson et al. 2013; García-Lorenzo et al. 2015). However, Gruendl et al. (1993) found that NGC 2276's Hα velocity field shows a 'half-moon' profile of the disk, which deviates from the 'spider' profile seen in other galaxies.

The Hα velocity profile of NGC 2276, derived from the PMAS/PPaK observation in this work, is shown with colors and isovelocity contours in Fig. 4.2. The new observations also show a 'half-moon' profile of the disk, thus confirming the results from Gruendl et al. (1993). Most notably, the largest deviation from a regular rotation profile is seen on the north-west and the south-east sides, and in the outskirts of the disk. On the other hand, the central region of the galaxy exhibits a regular rotation profile.

---

[7] https://ned.ipac.caltech.edu/

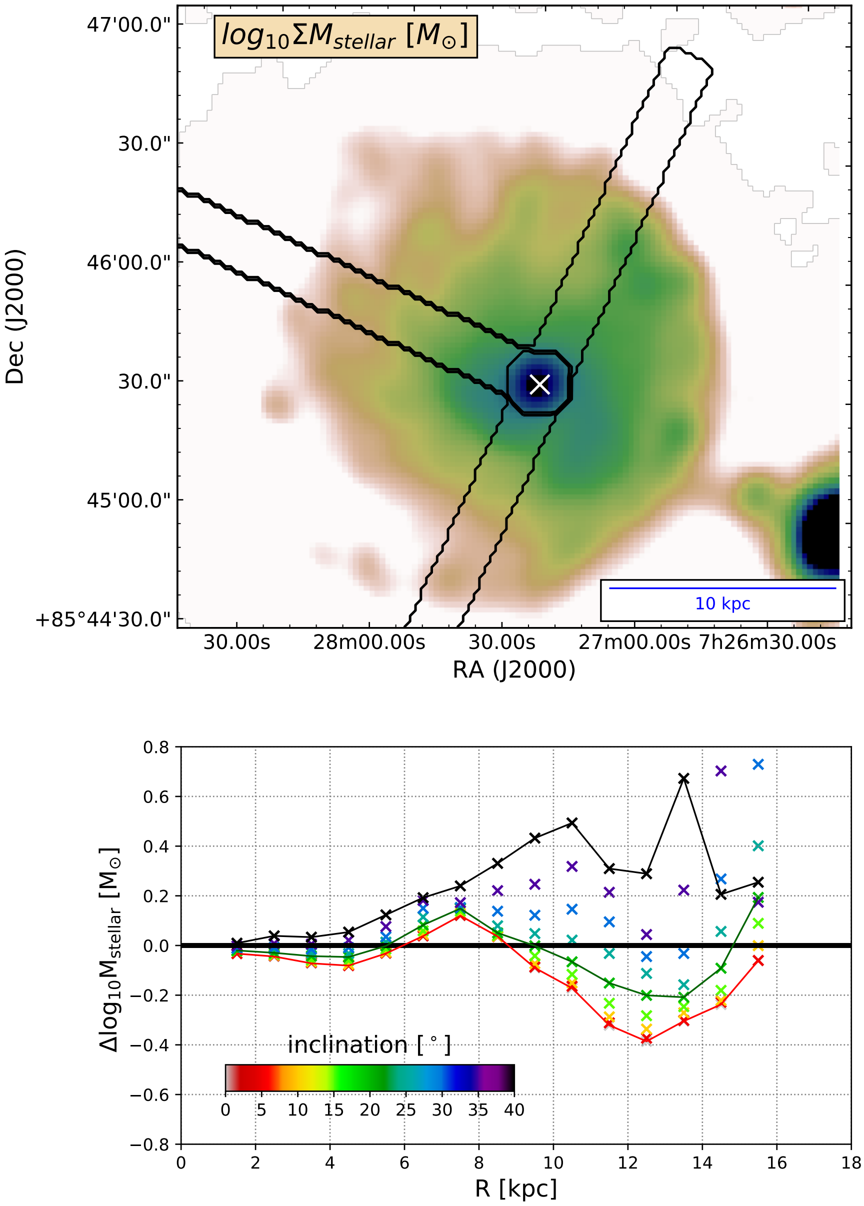

Fig. 4.5 NGC 2276's galactic inclination is determined by comparing the stellar mass surface densities $\Sigma(\mathrm{M_{stellar}})$ along the major and minor kinematic axes. *Top*- $\Sigma(\mathrm{M_{stellar}})$ image of NGC 2276, overplotted with slits along the major (north-east) and minor (north-west and south-east) axes. *Bottom*- Difference between the $\Sigma(\mathrm{M_{stellar}})$, from major and minor axes (y-axis), as a function of galactocentric distance (x-axis), for different assumed inclinations (color-coded). Here, the $\Sigma(\mathrm{M_{stellar}})$ at each distance is estimated from the WISE images at 3.4 μm and 4.6 μm (Sec. 4.2.5). The solid lines are highlighting the cases for an assumed inclination of $0°$ (red), $20°$ (green) and $40°$ (blue).

4.3.3 Inclination

The galactic inclination of NGC 2276 was previously estimated by comparing the major and minor axis seen on the *B* or K_s band images. From those images, it was estimated that the galactic inclination ranges between 20° (from the NED[8] and Gruendl et al. 1993) and 40° (K_s from 2MASS[9]). However, due to asymmetries found in both the stellar distribution (Sec. 5.3.2) and nebular emission from the ionized gas, estimating the orientation of NGC 2276's disk from the *B* or *K* bands alone is not reliable.

For this reason, we used the stellar distribution, obtained from the WISE 3.4 μm and 4.6 μm maps, to properly derive NGC 2276's orientation. We estimated the position angle of the kinematic major axis from the NGC 2276's Hα velocity field (Sec. 4.3.2). The resulting kinematic major axis is towards the north-east direction with a position angle (PA) $\approx 55°$ from the North. To estimate the inclination, we tested how the stellar mass distribution differs across the major and minor axis for different assumed inclinations (see Fig. 4.5). On the WISE images, we applied a slit (see Fig. 4.5) from the north-west to the south-east direction, across the entire disk (following the minor axis), and a slit in the north-east direction (following the major axis). The major axis in the south-west side of the disk is avoided due to the strong tidal and ram pressure effects seen in both the stellar and gas distributions (for details see Sec. 5.3.2). The smallest difference in the stellar masses across the minor and major axes occurs when the assumed inclination is $\approx 20°$ (Fig. 4.5).

4.3.4 BPT diagram

The Baldwin, Phillips & Telervich diagram (BPT) diagram, named after the authors of Baldwin et al. (1981), uses the bright nebular emission lines in order to determine the excitation mechanism of the bright nebular lines (Kewley et al. 2001, 2006; Kauffmann et al. 2003; Dopita et al. 2016). The most commonly used lines are Hβ, [OIII]$\lambda 5008$, [OI]$\lambda 6300$, [NII]$\lambda 6584$, Hα, and [SII]$\lambda 6717, 6731$. The excitation mechanisms investigated by the BPT diagram are from normal star-forming regions, excitation by photo-ionization from AGNs and shock-wave heating from LINERS, and a composite (a mixture of the previous mechanisms).

The BPT map and diagram for NGC 2276 are shown in Fig. 4.6. The parts of the diagram are labeled (SFR, AGN, and composite) corresponding to the excitation mechanisms. The lines between those regimes are defined by Kewley et al. (2001) and Kauffmann et al. (2003), and summarised by Eq. 1 and 4 in Kewley et al. (2006). Surprisingly, almost all of the line emission from NGC 2276 originates from normal star-forming regions. This implies that we can use Eq. 3.1 for converting $\mathrm{H}\alpha, \mathrm{corr}$ to SFR in NGC 2276 (described in detail in Sec. 3.3).

---

[8] https://ned.ipac.caltech.edu/.

[9] Retrieved from the NED

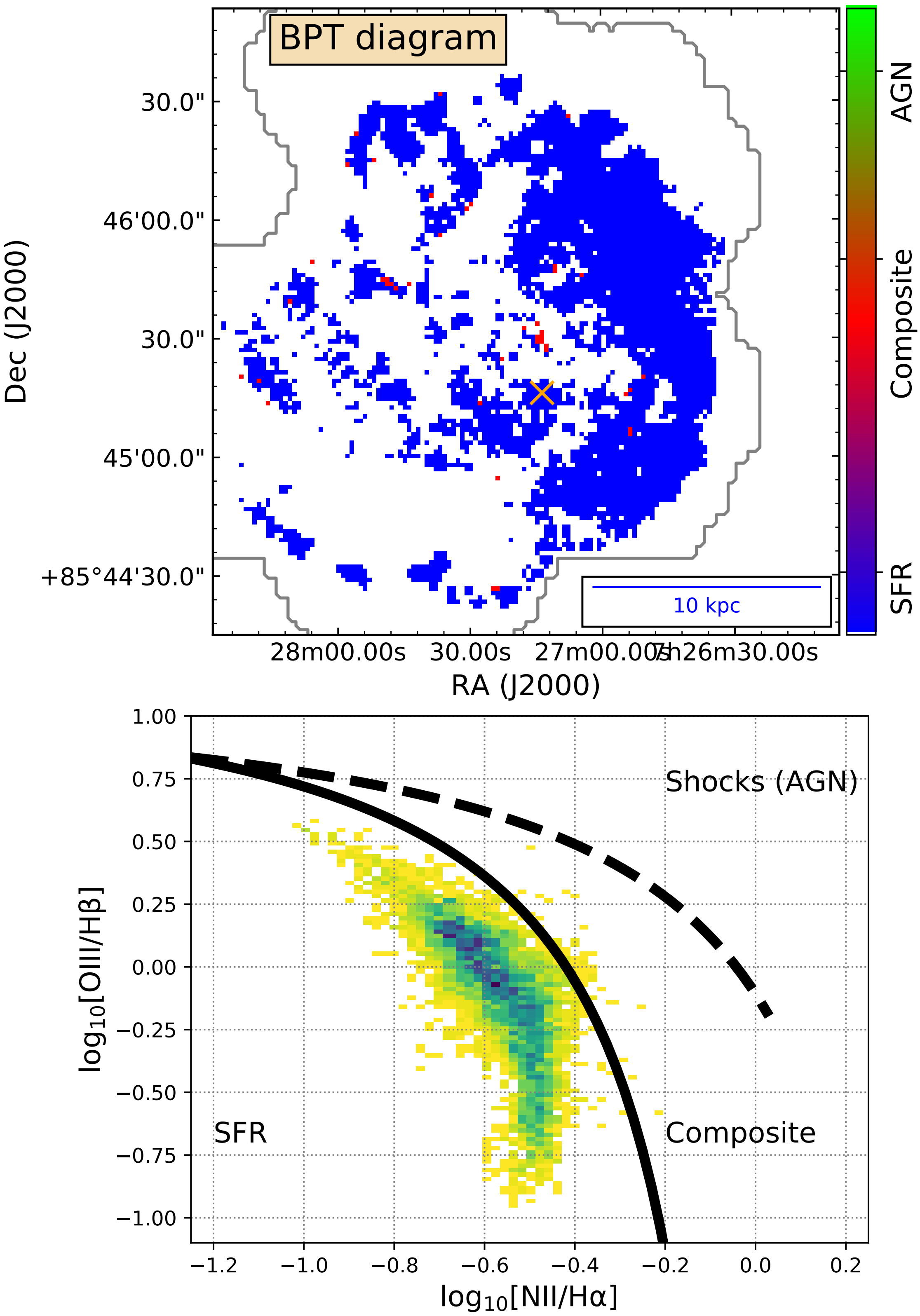

Fig. 4.6 The BPT map (top panel) and BPT diagram (Baldwin et al. 1981; bottom panel) for NGC 2276. The dashed and solid lines (Kewley et al. 2006) separate the areas into three excitation mechanism (SFR, shock-heated or AGN, and a composite).

4.3.5 The diffuse gas fraction

Observed gas line emission from galaxies is composed of a large fraction (up to 60%) arising from the diffuse ionized gas (DIG) and IR cirrus (Haffner et al. 2009; Leroy et al. 2012), thus introducing uncertainties and biases in estimating the SFR and gas-phase metallicities. For example, Sanders et al. (2017) found that the DIG emission in galaxies may bias gas-phase metallicity estimates by more than 0.3 dex due to different ISM characteristics and line ratios (Erroz-Ferrer et al. 2019). To properly estimate the gradient of the gas-phase metallicity across NGC 2276, we only use the data with a low fraction of DIG. Therefore, we estimate the fraction of the diffuse gas across the disk of NGC 2276 by tracing the [SII]λ6717/Hα ratio and adopting the method described by Blanc et al. (2009, Sec. 8 in their work).

As we showed in Sec. 2.4.2.2, a higher [SII]$\lambda 6717, 6731$/Hα ratio indicates the presence of DIG, that is more spatially extended than the HI regions (Reynolds 1984; Blanc et al. 2009; Haffner et al. 2009; Tomičić et al. 2017). NGC 2276's map of the [SII]λ6717/Hα ratio (hereafter [SII]/Hα ratio; see Fig. 4.7) exhibits low (< 0.2) [SII]/Hα ratios in the galactic center, the bright Hα regions, and the metal-rich areas. The outskirts and the metal-poor regions have higher (up to 0.5) [SII]/Hα ratios. The estimation of the gas-phase metallicity is described in Sec. 4.3.6.

As expected, there is a clear correlation between Hα,corr brightness and the [SII]/Hα ratio (Fig. 4.7). This correlation is due to the DIG emission dominating in areas with fainter HII regions, as already seen for M31 in the previous chapters and in the literature (Minter & Balser 1998; Haffner et al. 2009; Blanc et al. 2009). In Fig. 4.7, two thick lines represent the empirical fit that was derived for NGC 5194 (hereafter M51) by Blanc et al. (2009) (their Fig. 9), and the theoretical fit for the ISM with solar metallicity, derived from Eq. 8 and 9, respectively, in Blanc et al. (2009). The following equations, corresponding to Eq. 8 and 9 in Blanc et al. (2009), describe the observed [SII]/Hα ratio as a function of metallicity (Z), the diffuse gas emission fraction ($\mathrm{C_{DIG}}$), and $\mathrm{H\alpha, corr}$:

$$\mathrm{[SII]H\alpha}\Big|_{\mathrm{obs}} = \mathrm{Z'}\left[(1-\mathrm{C_{DIG}})\cdot\frac{\mathrm{[SII]}}{\mathrm{H\alpha}}\Big|_{\mathrm{HII}} + \mathrm{C_{DIG}}\cdot\frac{\mathrm{[SII]}}{\mathrm{H\alpha}}\Big|_{\mathrm{DIG}}\right], \tag{4.1}$$

$$\mathrm{C_{DIG}} = \frac{\mathrm{I_0^{DIG}}}{\mathrm{I(H\alpha, corr)}}, \tag{4.2}$$

where the metallicity is evaluated as a fraction of solar ($\mathrm{Z_\odot}$) metallicity ($\mathrm{Z'} = \mathrm{Z/Z_\odot}$), and $\mathrm{I_0^{DIG}}$ represents the $\mathrm{I(H\alpha, corr)}$ at which the DIG emission completely dominates ($\mathrm{C_{DIG}} = 1$). It was found that the HII regions within the Milky Way exhibit line ratios of [SII]/Hα=0.11, while the typical DIG regions show ratios of [SII]/Hα=0.34 (Madsen et al. 2006). Similar to Blanc et al. (2009), we take those ratios as the cases when the emission from the HII or DIG regions completely dominate the flux, corresponding to the cases of $\mathrm{C_{DIG}} = 0$ and $\mathrm{C_{DIG}} = 1$, respectively. In the case of M51, $\mathrm{I_0^{DIG}}$ was found to be equal to $\approx 2.5 \times 10^{-15}\,\mathrm{erg\,s^{-1}\,cm^{-2}\,arcsec^{-2}}$. Blanc

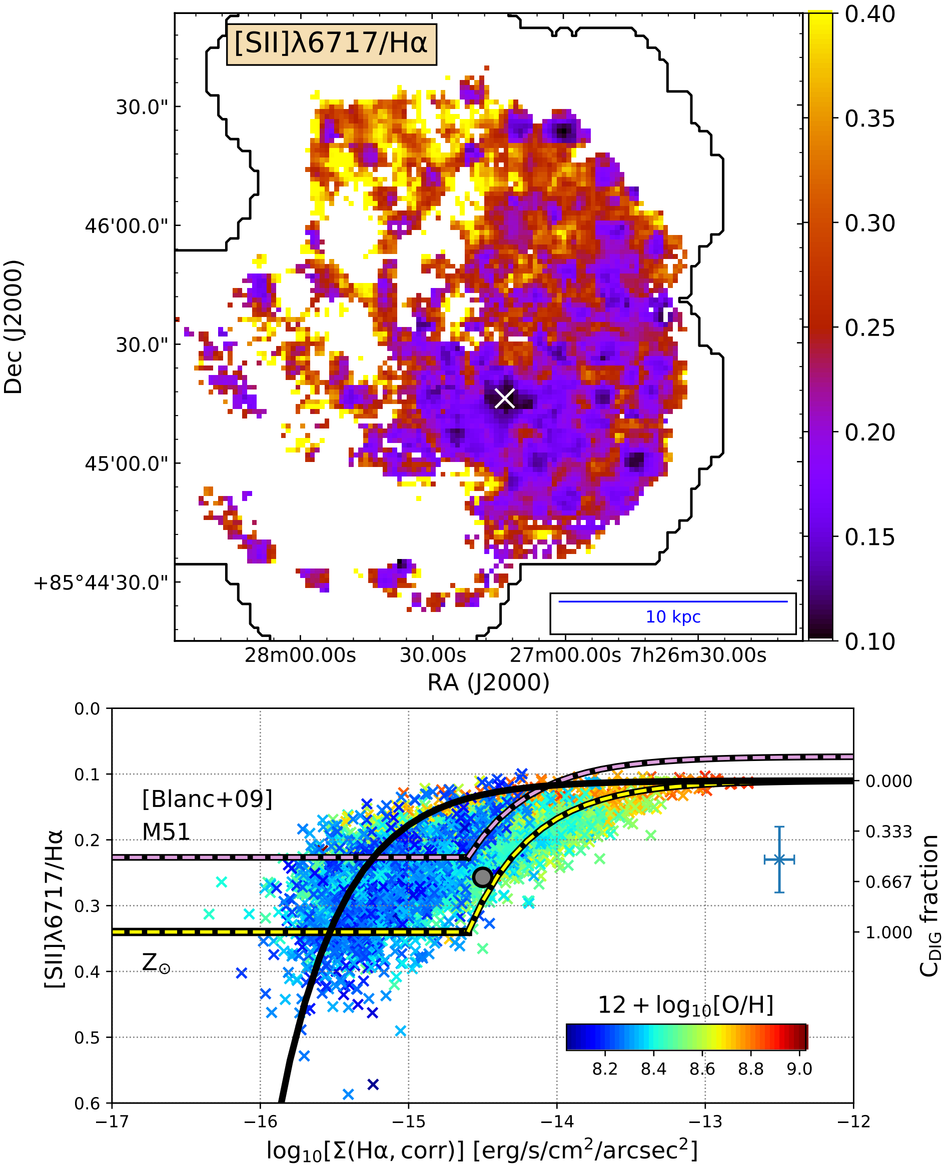

Fig. 4.7 Map of the [SII]$\lambda 6717, 6731$/Hα ratio (top panel), and the pixel-by-pixel [SII]$\lambda 6717, 6731$/Hα ratio as a function of $\Sigma_{\mathrm{H}\alpha,\mathrm{corr}}$ (bottom panel) in NGC 2276, colored by the nebular metallicity. The dashed overplotted lines show the theoretical and emphirical models described by Eq. 8 and 9 in Blanc et al. (2009). The upper (pink, dashed) line gives the empirical fit to data from the galaxy M 51, while the lower (light green, dashed) line is the theoretical line for the case of nebular gas with solar metallicity. The black line is the fit of the NGC 2276 data. The corresponding fractions of the diffuse gas emission C_{DIG} are labeled on the right y-axis (see the text for details). The estimated mean of the data uncertainties are indicated by the error bar on the right, and the mean NGC 2276 value with a large, gray circle.

et al. (2009) also assumed M51's metallicity to be sub-solar ($\approx 0.6\,\mathrm{Z}_{\odot}$), which lowers the [SII]/Hα ratio (represented by a pink dashed line in Fig. 4.7) compared to the ISM data with solar metallicity (represented by a light-green dashed line in Fig. 4.7). However, these fitted lines should be taken with caution, as they were derived specifically for M51, and may introduce biases when applied to other galaxies. Another caveat of comparing M51 with NGC 2276 is that Blanc et al. (2009) probed only the central $4 \times 4\,\mathrm{kpc}^2$ area (with galactocentric distance $< 0.3\,\mathrm{R}_{25}$) and the brightest regions, which have $\mathrm{I}(\mathrm{H}\alpha) > 10^{-15}\,\mathrm{erg\,s^{-1}\,cm^{-2}\,arcsec^{-2}}$.

While calculating the fit for the NGC 2276 data, to estimate the $\mathrm{C_{DIG}}$ fraction, we used the data within the entire range of metallicities. The slope of the theoretical fitted line assumes the diffuse emission fraction to behave as $\mathrm{C_{DIG}} \sim \mathrm{I}(\mathrm{H}\alpha, \mathrm{corr})^{-1}$. However, the observed NGC 2276 data show a large scatter, which does not allow for a clear fit to the data. Therefore, a large portion of our data show higher [SII]/Hα ratios than what our overall fitting line predicts. The data with Hα,corr between 10^{-15} and $10^{-14}\,\mathrm{erg\,s^{-1}\,cm^{-2}\,arcsec^{-2}}$ show a slope that is shallower than the fits from this work and from Blanc et al. (2009). The slope of these data approximately corresponds to a diffuse emission fraction that behaves as $\mathrm{C_{DIG}} \sim \mathrm{I}(\mathrm{H}\alpha, \mathrm{corr})^{-0.55}$. We conclude that predicting the exact $\mathrm{C_{DIG}}$ fraction from our data is difficult due to the large scatter, large variations in metallicities, and large uncertainties in the line ratio.

The fitted $\mathrm{I}_0^{\mathrm{DIG}}$ for NGC 2276 corresponds to $\approx 3 \times 10^{-16}\,\mathrm{erg\,s^{-1}\,cm^{-2}\,arcsec^{-2}}$, which is lower than in M51. NGC 2276's regions with brighter Hα, which also show higher metallicities, match well with the theoretical lines for solar metallicity from Blanc et al. (2009). On the other hand, data with lower metallicities match well with the fitted line for the M51 data. The mean NGC 2276 value lies between these two fits, which corresponds to the model with a metallicity that is slightly lower than the solar value.

To determine a proper radial behaviour of the gas-phase metallicity in NGC 2276 (Sec. 4.3.6), we will use only the data with a low DIG fraction. Because we find our fit on Fig. 4.7 not very reliable, we will not use $\mathrm{I}_0^{\mathrm{DIG}}$ to determine which data to omit from the estimation of the metallicity gradient and use instead the [SII]/H$\alpha \leq 0.2$ criterion that corresponds to $\leq 30\%$ of the DIG fraction.

4.3.6 Metallicities

NGC 2276's nebular (gas-phase) metallicity is estimated using Eq. 3 from Dopita et al. (2016), with the [NII]λ6584/[SII]λ6717, 6731 and [NII]λ6584/Hα line ratios. The metallicity prescription from Dopita et al. (2016) is independent from internal attenuation as it uses emission lines that are close in wavelengths, and independent from gas pressure and the ionization parameter (corresponding to the pressure of the ionization photons). Using other nebular metallicity prescriptions, which use Hβ/[OIII]λ5008 and [SII]λ6717, 6731/Hα ratios, may introduce certain biases in the metallicity values. The Hβ/[OIII]λ5008 ratio may be elevated above what could be explained by the ionization parameter (Kewley et al. 2013; Masters et al. 2014; Shapley et al.

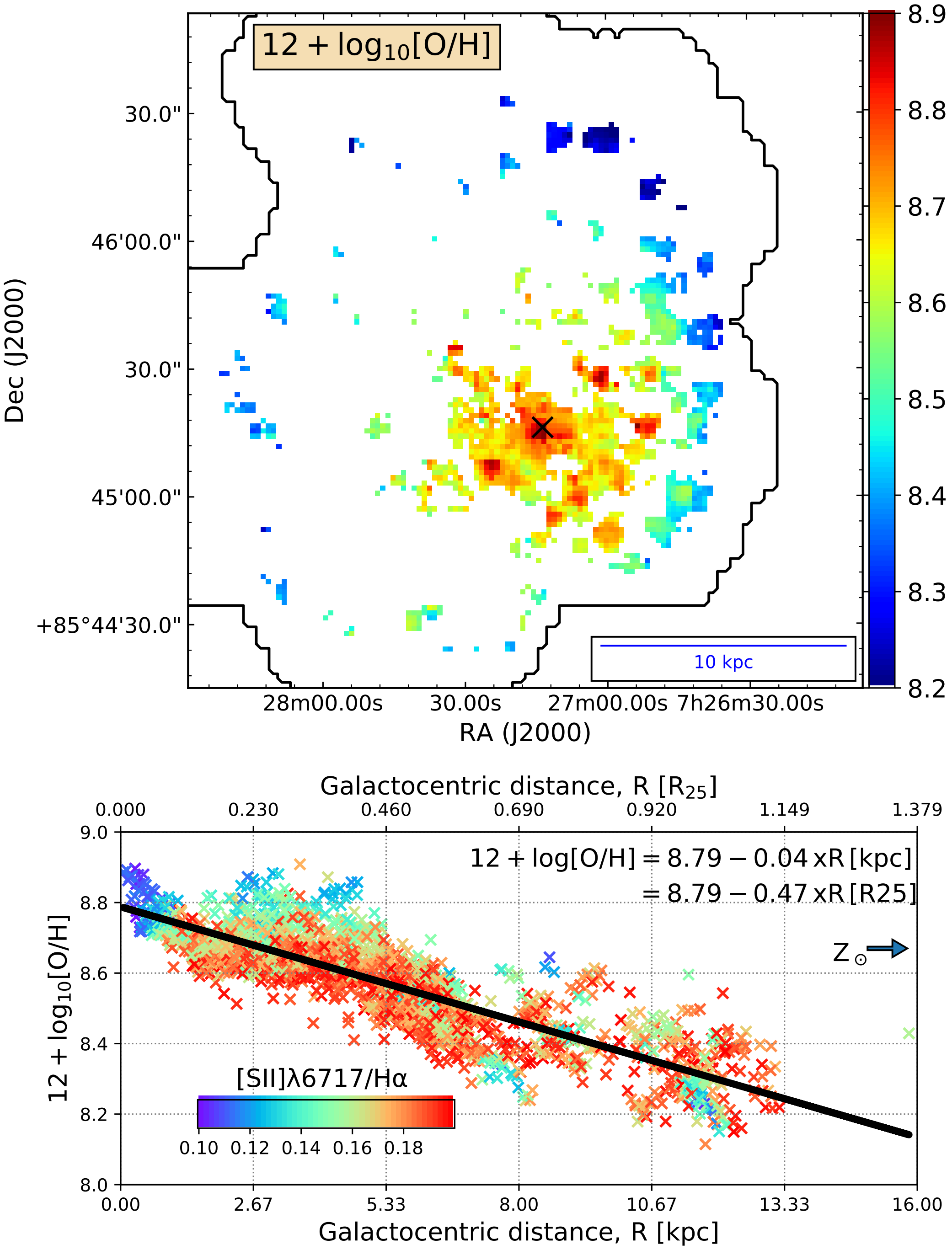

Fig. 4.8 The nebular (gas-phase) metallicity map of NGC 2276 (top), and the pixel-by-pixel metallicity values as a function of deprojected galactocentric distance (in kpc and R_{25} units; bottom), which are colored by the [SII]/Hα ratio. Here, we excluded data with [SII]/Hα >0.2 ($C_{DIG} > 0.35$). The metallicity is estimated using Eq. 3 in Dopita et al. (2016). The metallicity radial gradient is estimated by fitting the pixel-by-pixel data (black line). The fitted parameters are listed on the top of the panel, and a solar metallicity $Z_{\odot}$ value marked with the arrow ($12 + \log_{10}[\mathrm{O/H}]_{\odot} = 8.69$; Allende Prieto et al. 2001).

2015) and [SII]$\lambda 6717, 6731$/Hα may be decreased due to increased interstellar gas pressure.

Fig. 4.8 presents the spatial distribution of the measured metallicity, and the pixel-by-pixel metallicity values as a function of deprojected galactocentric distance, colored by the [SII]/Hα ratio. Here, we show and use only the pixels that have [SII]/Hα ≤ 0.2, which is a proxi for pixels with $\leq 30\%$ of DIG emission fraction ($\mathrm{C_{DIG}} < 0.35$). This is similar to the criteria used by Erroz-Ferrer et al. (2019).

The NGC 2276 data indicate an increase in nebular metallicity from 8.2 (at $\mathrm{R_{25}}$) to 8.9 (in the galactic center). As expected, data at the same galactocentric distance but with a lower [SII]/Hα ratio has a lower metallicity (Fig. 4 in Dopita et al. 2016). Most of the data points have metallicities lower than the solar value ($12 + \log_{10}[\mathrm{O/H}]_{\odot} = 8.69$; Allende Prieto et al. 2001). The calculated slope of the metallicity gradient is -0.04 $\mathrm{dex\,kpc^{-1}}$ or -0.47 $\mathrm{dex\,R_{25}^{-1}}$, with an offset of $\approx$8.8. This slope is slightly steeper than those determined for NGC 2997 (with a slope of -0.03 $\mathrm{dex\,kpc^{-1}}$ or -0.42 $\mathrm{dex\,R_{25}^{-1}}$; Ho et al. 2018) and M51 (-0.02 $\mathrm{dex\,kpc^{-1}}$ or -0.3 $\mathrm{dex\,R_{25}^{-1}}$; Bresolin et al. 2004).

4.4 Summary

In this chapter, we observed some properties of an interacting galaxy, NGC 2276, to investigate how external interaction with the surrounding IGM and a companion galaxy affects the ISM properties within the disk of the host galaxy. We explored properties such as gas velocity, metallicity gradient, excitation mechanism of the ionized gas, and the fraction of the diffuse gas emission.

Similar to Fig. 1 in Gruendl et al. (1993), we derived the velocity profile of the Balmer lines which deviates from the typical ‘spider’ profile expected for a spiral disk galaxy. NGC 2276’s velocity profile shows a ‘half moon’ feature, which Gruendl et al. (1993) explain as an effect of both the ram pressure and the tidal forces. Similar features in the velocity profiles are observed in interacting and ram pressured galaxies, such as JO201 and P11695 from the GASP survey (Bellhouse et al. 2017; Gullieuszik et al. 2017; Vulcani et al. 2018).

The BPT diagram of the NGC 2276 data indicates that all of the line emission in the disk is consistent with the ionization via the radiation from HII regions. This is a surprising result as we were expecting the emission on the western edge to show signatures of shocks due to ram pressure effects, as it was found for the IGM outside NGC 2276’s disk (Rasmussen et al. 2006). Therefore we were expecting that data to be situated in the part of the BPT diagram designated for the composite, LINER, or AGN excitation mechanism. Although, not all of the ram pressured galaxies in the GASP survey show clear shock excitation features (e.g., P11695 in Vulcani et al. 2018), some partly show those features in the outskirts of their disks (e.g., JO36, JO201 and JO204; Bellhouse et al. 2017; Fritz et al. 2017; Gullieuszik et al. 2017). Another example of clear signatures of shocks in the ISM is found between the interacting members of the Stephan’s quintet (Iglesias-Páramo et al. 2012). However, the outskirts of the disks of Stephan's quintet members exhibit values in the composite region (e.g., NGC 7318; Rodríguez-Baras et al. 2014).

The derived fraction of diffuse gas emission in NGC 2276 is uncertain due to the large scatter of the data, uncertainties in the line ratio, and a large variations in the nebular metallicities.

NGC 2276's disk does not have an unusual range, slope, or distribution of nebular metallicity. The metallicity range, where we used the Dopita et al. (2016) calibration, is similar to the ranges seen in other spiral galaxies (Ho et al. 2018) and in galaxies from the GASP survey (Poggianti et al. 2017; Gullieuszik et al. 2017; Vulcani et al. 2018). The $-0.4\,\mathrm{dex\,kpc^{-1}}$ slope of the radial gradient in metallicity is similar to the slope observed in a survey of 130 spiral galaxies by Pilyugin et al. (2014), in their Fig. 6.

The interacting galaxy NGC 2276 shows an unusual asymmetric distribution of various SFR tracers, and of the stellar distribution. It also has an enhanced SFR, estimated to be between 5-19.4 $\mathrm{M_{\odot}}$/yr (in this work and in Wolter et al. 2015; Kennicutt 1983), which is higher than what is typical for main sequence galaxies of NGC 2276's stellar mass (expected SFR$\approx$5-6 $\mathrm{M_{\odot}}$/yr; Elbaz et al. 2007).

While the origin of NGC2276's exceptional star formation activity is undoubtedly linked to its interaction with NGC 2300 and the surrounding IGM, the exact nature and mechanism that stimulates the star formation remains debated, largely because NGC 2276's molecular gas distribution had not been studied. The first hypothesis is that the asymmetry and enhancement of the SFR is caused by an accumulation of the cold molecular gas on the western side of the galaxy, with the star formation efficiency of the molecular gas not being enhanced. The second hypothesis is that this asymmetry is due to changes in the ISM properties and variations in the star formation efficiency across the disk, caused by the external forces (the tidal forces and the ram pressure). In the following chapter (Chap. 5), we probe the distribution of the bulk of the molecular gas in NGC 2276 to investigate the variation of the star formation efficiency across the NGC 2276 disk and discuss the sources of its variation.

Chapter 5

"Change is the essential process of all existence."

Spock, first officer on USS Enterprise NCC-1701
"Let That Be Your Last Battlefield"; Star Trek: The Original Series

5. Large variation in SFE in interacting galaxy NGC 2276

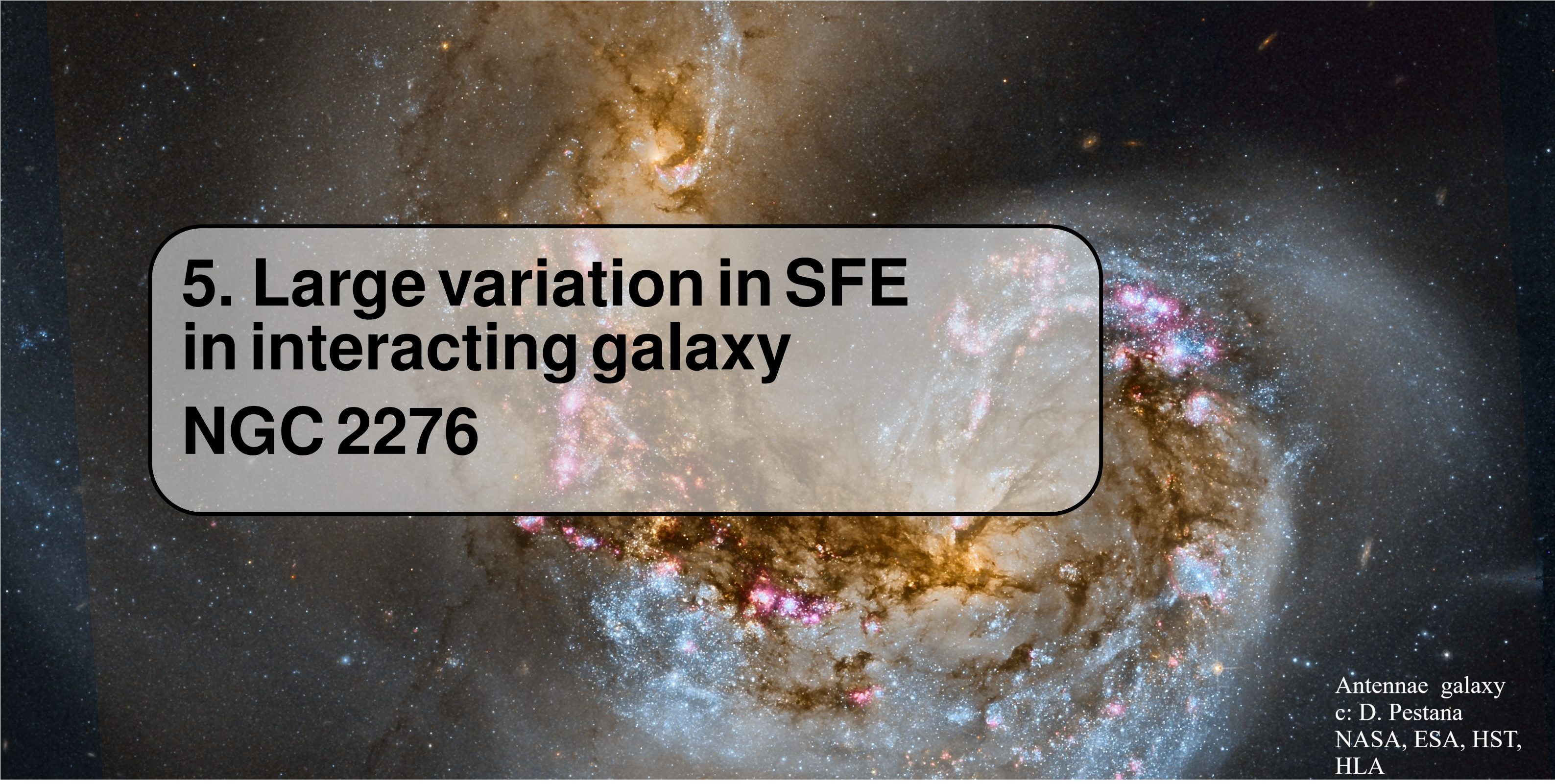

Antennae galaxy
c: D. Pestana
NASA, ESA, HST,
HLA

This chapter is published in a refereed article "Two Orders of Magnitude Variation in the Star Formation Efficiency Across the Pre-Merger Galaxy NGC 2276", Tomičić et al. (2018), for which I am the lead author and which has been adapted for this thesis.

Overview: Following Chap. 4, in this chapter, we present observations of the bulk of the molecular gas (Sec. 5.2) in an interacting galaxy, NGC 2276, to explore how a galactic interaction and external forces, such as tidal force and ram pressure (Sec. 5.3.2), affect the star formation efficiency within the disk. The variation of the star formation efficiency across the disk is shown in Sec. 5.3.1 and discussed in Sec. 5.4.

5.1 Introduction

The star formation rate (SFR) and the bulk molecular gas (H_2) correlate well in nearby galaxies, both at local scales (e.g.,, Bigiel et al. 2008; Leroy et al. 2013) and global scales (e.g., Kennicutt 1998). The ratio between the H_2 mass and SFR yields the depletion time of the H_2, i.e. the time needed to deplete the molecular gas reservoir assuming that the current SFR is constant, $\tau_{\rm depl} = {\rm M_{H_2}/SFR}$. The depletion time is universally proportional to the star formation efficiency (SFE) as $\tau_{\rm depl} = 1/{\rm SFE}$. A characteristic $\tau_{\rm depl}$ of 1-2 Gyr is observed for local normal star-forming disk galaxies on the main-sequence (Saintonge et al. 2011; Leroy et al. 2013). Surveys of nearby galaxies show a scatter in $\tau_{\rm depl}$ of ~ 0.3 dex at galactic and sub-galactic scales (Saintonge et al. 2011; Leroy et al. 2013). However, local interacting starburst galaxies (Klaas et al. 2010; Nehlig et al. 2016; Saito et al. 2016) and ultra-luminous infrared galaxies (LIRGs, ULIRGS; Saintonge et al. 2011; Martinez-Badenes et al. 2012) exhibit a lower systematic $\tau_{\rm depl}$ of 0.05-0.8 Gyr.

Investigations into the physics that drive variations in $\tau_{\rm depl}$ among and within galaxies are still ongoing. Stellar feedback and molecular cloud evolution have each been put forward to explain these variations, but there is increasing evidence that internal and external galactic dynamics also affect $\tau_{\rm depl}$. An example of internal dynamical processes is gravitational torque caused by galactic stellar structures, which has been observed to modify the $\tau_{\rm depl}$ in the spiral arms of M51 (Meidt et al. 2013). Observations and numerical simulations indicate that external dynamical processes such as gravitation can also produce compressive and disruptive tides within galaxy gas disks during galaxy-galaxy interactions, leading to a broader distribution of $\tau_{\rm depl}$ (Renaud et al. 2014,Bournaud et al. 2015). Studies of $\tau_{\rm depl}$ in galaxies at various stages of interaction indicate that the tidal gravitational forces *change* $\tau_{\rm depl}$ up to 0.4 dex (Martinez-Badenes et al., 2012; Nehlig et al., 2016; Lee et al., 2017). In the case of the ram pressure, Nehlig et al. (2016) observed that ram pressure can decrease $\tau_{\rm depl}$, but not as effectively as the tidal effects. Within starburst-like interacting galaxies, $\tau_{\rm depl}$ can vary by up to 1 dex (Saito et al. 2016; Pereira-Santaella et al. 2016). Renaud (in prep., priv. comm.) also conclude from their simulations of interacting galaxies that tidal forces generally decrease $\tau_{\rm depl}$ and increase its variation within galaxies. Contrary, Moreno et al. (2015) concluded from their simulated colliding galaxies that the SFE increases by 1 dex in the galactic centers, while drops in their disks (Fig. 6 in their work). The aforementioned studies only address moderate to late stages of galaxy interactions, where the galaxies are already colliding or interacting at small separation from each other.

Following Chap. 4, here we study the interacting spiral galaxy NGC 2276 to investigate how its interaction with the companion galaxy NGC 2300 and surrounding intergalactic medium (IGM) affects the star formation and the star formation efficiency across NGC 2276's disk. Previous papers (Gruendl et al. 1993; Hummel & Beck 1995; Rasmussen et al. 2006; Wolter et al. 2015) argue that the enhanced and asymmetric SF in NGC 2276 may be caused by tidal forces or ram pressure. Tidal forces could be sufficient to trigger SF despite the large projected separation ($\approx$ 75 kpc) to neighbor NGC 2300, as Scudder et al. (2012) show in their simulations that SFR may be enhanced by 0.3-0.6 dex at large separations (up to 70 kpc) between merging galaxies.

Despite its exceptional SFR, the distribution of NGC 2276's molecular gas reservoir has not previously been mapped at high spatial resolution. Spatial variations in $\tau_{\rm depl}$ could indicate if tidal forces and/or ram pressure have an impact on the ISM physics and $\tau_{\rm depl}$ as such in NGC 2276. This chapter presents observations of H_2 gas (as traced by CO emission) at sub-kpc scales and spatially resolved measurements of $\tau_{\rm depl}$ in NGC 2276 for the first time. Additionally, we correct our IFU measurements of Hα emission from the star-forming regions for internal extinction caused by dust, an important step that has not been applied to previous studies of SF in NGC 2276, using narrowband imaging.

5.2 Data

To estimate the SFR surface density $\Sigma_{\rm SFR}$(Hα,corr) in NGC 2276, we use extinction-corrected Hα surface brightness Σ(Hα,corr). The data calibration, analysis of the spectra, and derivation of the nebular emission lines of the galaxy are described in previous chapter (Sec. 4.2.2 and 4.2.3).

Based on the BPT diagrams (see Sec. 4.3.4) of the emission lines, we find that most of the Hα emission arises from star-forming regions and not from shocks. To convert Σ(Hα,corr) to $\Sigma_{\rm SFR}$(Hα,corr), we use the SFR prescription from Murphy et al. (2011, Eq. 1 and 2), that are used as Eq. 3.1 in Sec. 3.3. The resulting map of $\Sigma_{\rm SFR}$(Hα,corr) in NGC 2276 is shown in Fig. 5.1.

To estimate the mass surface density of the H$_2$ ($\Sigma_{\rm H_2}$), we mapped the $^{12}{\rm CO}(J = 1 \rightarrow 0)$ emission from NGC 2276 with the NOEMA interferometer at Plateau de Bure (NOrthern Extended Millimeter Array; project ID: w14cg001) and the IRAM 30m telescope (project ID: 246-14). The NOEMA observations consisted of a 19-point hexagonal mosaic (with a field of view 2.2' in diameter) centered on RA(J2000) $07^{\rm h}27^{\rm m}14^{\rm s}.55$ and Dec.(J2000) $+85^{\rm d}45^{\rm m}16^{\rm s}.3$. The 30m observations covered a 3×3 arcminute field centered on the same position. Both targeted the $^{12}{\rm CO}({\rm J} = 1 \rightarrow 0)$ emission assuming a systemic LSR velocity of 2425 km/s. The final combined (NOEMA+30m) cube has an angular resolution of 2.5"×2.1", a channel width of 5 km/s, and 1σ sensitivity of 60 mK per channel. For the analysis in this paper, we use a version of the cube that has been smoothed to 2.7" resolution using a Gaussian convolution kernel. The sensitivity of this cube is 50 mK per 5 km/s channel. More details will be presented in Hughes (in prep.).

For the $\Sigma_{\rm H_2}$, we assumed the Galactic value X$_{\rm CO}$=$2 \times 10^{20}{\rm cm}^{-2}\ ({\rm K \cdot km/s})^{-1}$ (Bolatto et al. 2013) of the conversion factor. We show $\Sigma_{\rm H_2}$ map of NGC 2276 in Fig. 5.1. We use this conversion factor as the NGC 2276's nebular metallicity, estimated from the [NII]/[SII] and [NII]/Hα ratios and using Eq. 3 in Dopita et al. (2016), is similar to the solar value (log[O/H]+12 ranges between 8.4 and 8.9). However, in Fig. 5.3 we also present the NGC 2276 data for the case of a spatially varying X$_{\rm CO}$ factor taking into account local variation in metallicity. In Fig. 5.2, we show a map of a difference in the estimated $\Sigma_{\rm H_2}$ due to metallicity variation, and a diagram that show how it varies as a function of metallicity. As expected, the difference in decrease with increasing metallicity, which increase toward the galactic center.

5.3 Results

5.3.1 The depletion time

The $\Sigma({\rm H_2})$ distribution is consistent with a fairly normal disk while the prominent asymmetry toward the western edge of the disk is seen in $\Sigma_{\rm SFR}$(Hα,corr) (Fig. 5.1). The resulting $\tau_{\rm depl}$

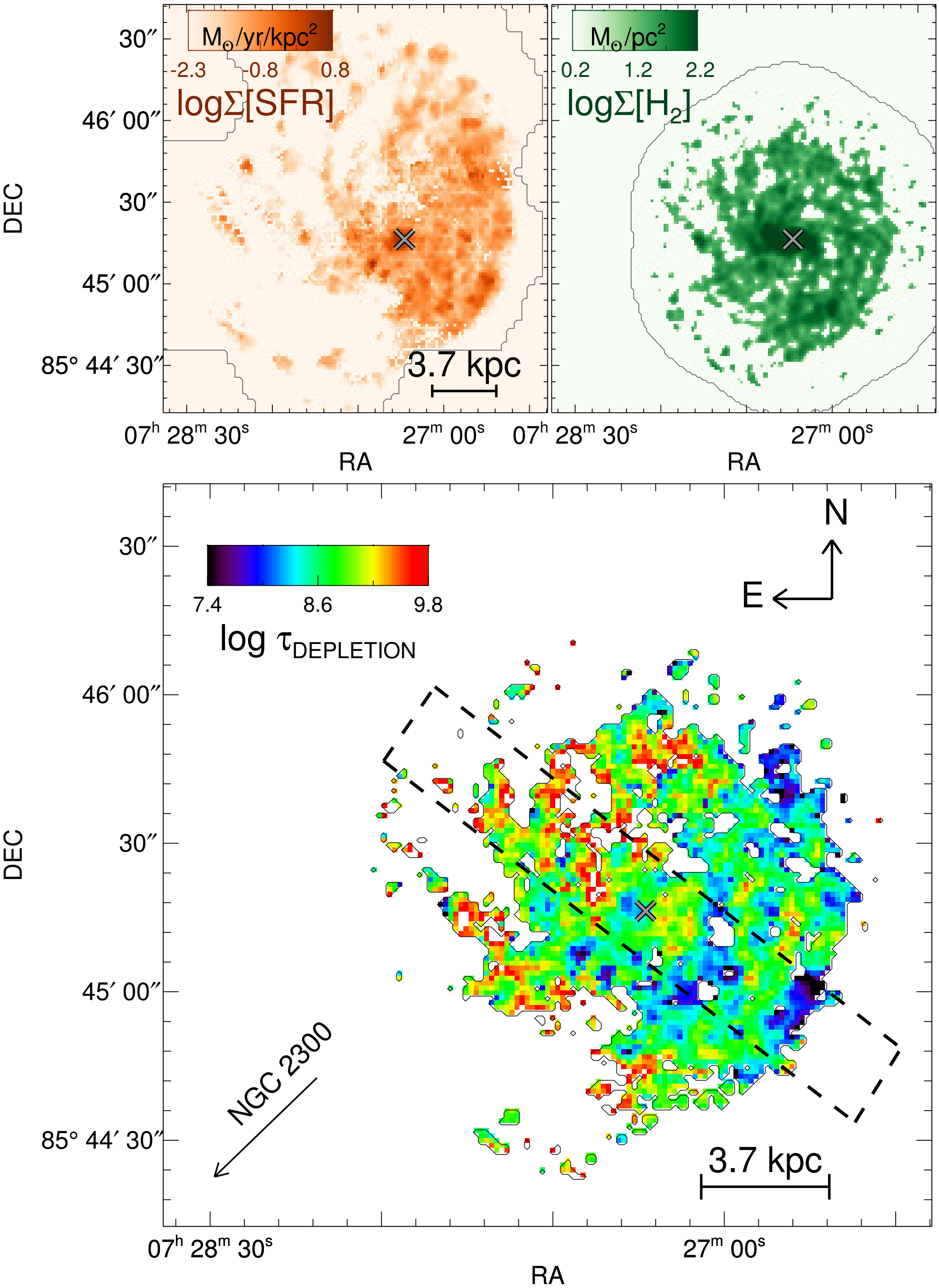
M$_\odot$/yr/kpc^2
-2.3 -0.8 0.8
logΣ[SFR]
M$_\odot$/pc^2
0.2 1.2 2.2
logΣ[H$_2$]
30″
46′ 00″
30″
45′ 00″
85° 44′ 30″
DEC
3.7 kpc
07^h 28^m 30^s
27^m 00^s
RA
7.4 8.6 9.8
log $\tau_{DEPLETION}$
N
E
NGC 2300

Fig. 5.1 Distribution of $\Sigma_{\rm SFR}$(Hα,corr) (upper left), $\Sigma_{\rm H_2}$ (upper right), and the depletion time $\tau_{\rm depl}$ (= $\Sigma_{H_2}/\Sigma_{SFR}$; bottom) across the disk of NGC 2276. We indicate the areas observed in each tracers. In the panel showing the $\tau_{\rm depl}$, we show the slit used to extract the data for the Kennicutt-Schmidt diagram in Fig. 5.3 by a dashed rectangle. The slit orientation was chosen to encompass the largest range in $\tau_{\rm depl}$ values. Annotations indicate the direction towards the neighbor elliptical galaxy NGC 2300 and NGC 2276's center (X symbol).

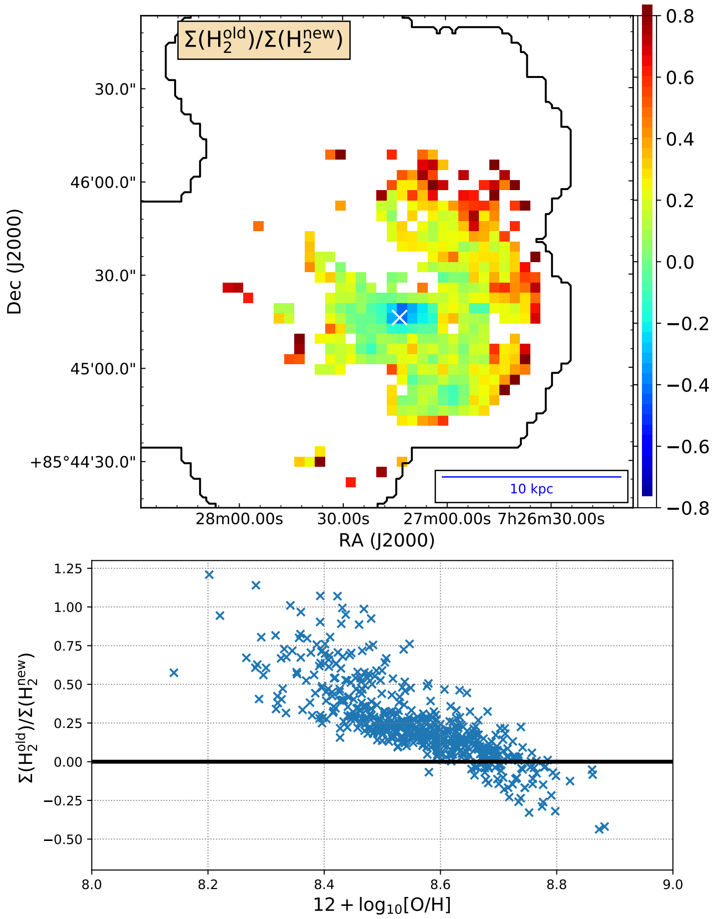

Fig. 5.2 A map (upper panel) of the difference in the estimated $\Sigma_{\mathrm{H_2}}$, after and before taking into account the local variation in nebular metallicity. This variation as a function of metallicity is presented in lower panel.

distribution is shown in Fig. 5.1. The standard deviation of τ_{depl} values is 0.52 dex. The highest observed $\tau_{\mathrm{depl}}(\mathrm{H_2})$ value is 9 Gyr, and it gradually decreases to 0.1 Gyr across the disk, from north-east (NE) to south-west (SW). The lowest τ_{depl} values (10 Myr-100 Myr) are found along the western edge of the disk. The mean galactic τ_{depl} value is 0.55 Gyr. From the integrated spectra, we estimate NGC 2276's galactic SFR to be $\approx$17$\pm$5 $\mathrm{M_\odot}$/yr.

To demonstrate the amplitude of the variation in τ_{depl} in NGC 2276, we plot the pixel-by-pixel data on the Kennicutt-Schmidt diagram (Fig. 5.3). On the left panel we show NGC 2276 data from the 20$''$ wide slit oriented in NE-SW direction (that follows the τ_{depl} gradient), and other panels present NGC 2276 data from the entire disk. The right panel shows NGC 2276 data from the entire disk where we used a variable $\mathrm{X_{CO}}$ factor corrected for local variation in metallicity (Narayanan et al. 2012). The contours show the data from the HERACLES survey of nearby galaxies (Leroy et al. 2013), and X symbol represents the NGC 2276's mean galactic value. The HERACLES survey examines $\sim$1 kpc regions in 30 galaxies. We added sub-galactic regions from the mid-stage merger VV 114 (Saito et al. 2015), luminous merger remnant NGC 1614 (Saito et al. 2016), and Antennae (Klaas et al. 2010) (middle and right panels). The NGC 2276 data from the slit show a decrease in $\tau_{\rm depl}$ from 3 Gyr to 10 Myr from NE toward SW, while the center exhibits a $\tau_{\rm depl}$ of about 0.4 Gyr. The $\tau_{\rm depl}$ values in the disk show ≈0.5 dex larger range when a single $X_{\rm CO}$ factor is used compared to one that takes metallicity variation into account.

5.3.2 Tidal forces and ram pressure

Galactic-scale tidal forces are responsible for features such as stellar streams, disk thickening and asymmetries in stellar disks. We derived $\Sigma(\rm M_{stellar})$ map of NGC 2276 and NGC 2300 from WISE images at 3.4 μm and 4.6 μm following Eq. 8 in Querejeta et al. (2015), as described in Sec. 4.2.5. The $\Sigma(\rm M_{stellar})$ map, shown in Fig. 4.4, confirms that the stellar distribution in NGC 2276 is strongly asymmetric, and shows a steeper drop on the SW side compared to the NE side. While other external (e.g., minor mergers, gas accretion) or internal (asymmetries in the dark matter halo) mechanisms cannot be ruled out as the origin of these features (Laine et al. 2014), we propose (as previous authors have done) that the asymmetric $\Sigma(\rm M_{stellar})$ in NGC 2276 is due to tidal forces.

To compare NGC 2276 to other galaxies, we quantify the tidal strength of the interaction Q experienced by NGC 2276 following Eq. 1 in Argudo-Fernández et al. (2015), i.e.

$$Q = \log_{10}\left[\frac{M_{comp}}{M_{2276}}\left(\frac{D_{25}}{r}\right)^{3}\right] , \tag{5.1}$$

where $\log(\rm M_{comp}/M_{\odot}) = 10^{11.3}$ and $\log(\rm M_{2276}/M_{\odot}) = 10^{10.7}$ are the stellar masses of NGC 2300 and NGC 2276, respectively; D_{25} is the B-band optical diameter of NGC 2276, and $r = 75$ kpc is the projected separation between NGC 2300 and NGC 2276. For NGC 2276, we find $Q = -0.9$, which is significantly higher than the typical value for isolated galaxies ($Q = -5.2 \pm 0.8$) and on the high end of isolated galaxy pairs ($Q = -2.3 \pm 1.2$, Argudo-Fernández et al. 2015).

As well as galactic-scale tides, our new observations also show evidences for ram pressure affecting NGC 2276. First, the scale-length of the ionized gas on the SW side of NGC 2276's disk is significantly shorter (up to 1-2 kpc) than the scale-length of the stellar emission (see Hα contour in Fig. 4.4, in Sec. 4.2.5). In contrast, the ionized gas follows well the stellar distribution on the NE side. This feature cannot be explained by tidal forces alone, and may be a signature of ram pressure stripping of the interstellar gas. Secondly, we observe an increase in the Hα,corr/f$_\nu$(FUV,corr) ratio along the western rim of NGC 2276's disk (see Fig. 5.4). The calibration of the FUV data is described in Sec. 4.2.4. The Hα,corr/f$_\nu$(FUV,corr) ratio robustly indicates the age of stellar clusters (Sánchez-Gil et al. 2011), showing that the westernmost regions are dominated by the youngest clusters. We link this most recent SF on the western edge of the disk to ram pressure (as similarly observed in the Large Magellanic Cloud by Piatti et al. 2018).

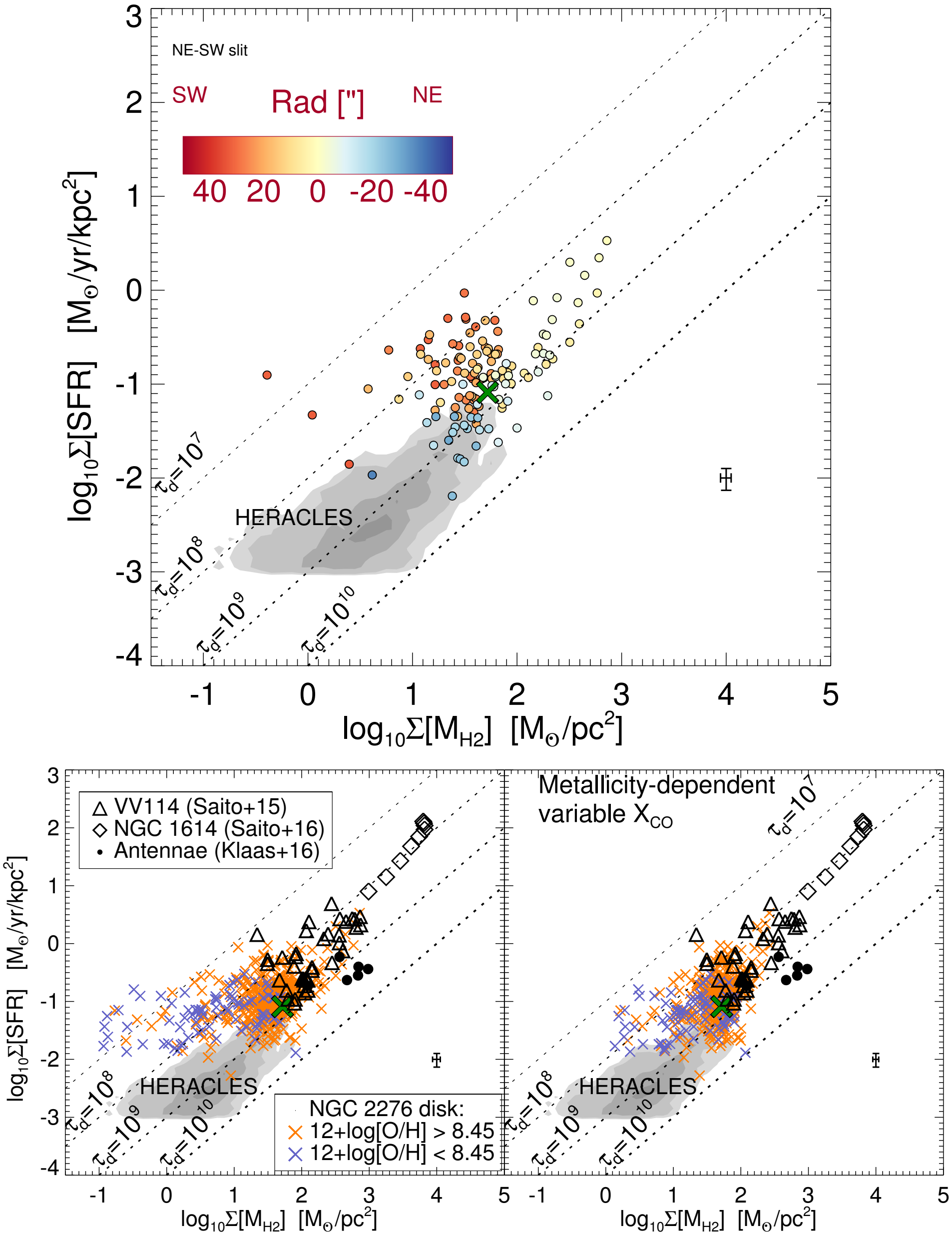

Fig. 5.3 Large variation in the $\tau_{\rm depl}$ is seen across different regions of NGC 2276's disk, and presented in the $\Sigma_{\rm SFR}$(Hα,corr) vs. $\Sigma_{\rm H_2}$ diagram (Kennicutt-Schmidt diagram). The upper panel shows NGC 2276 data from the 20" wide slit (shown in the bottom panel in Fig. 5.1), which are color-coded from north-east (blue) toward south-west (red). The bottom left and right panels present data from NGC 2276's entire disk (orange crosses for metallicities $12 + \log_{10}[{\rm O/H}] > 8.45$, and blue crosses for metallicities $12 + \log_{10}[{\rm O/H}] < 8.45$), the mid-stage merger VV 114 (Saito et al. 2015), the luminous merger remnant NGC 1614 (Saito et al. 2016), and the Antennae (Klaas et al. 2010). While we used constant $X_{\rm CO}$=$2\times10^{20}{\rm cm}^{-2}({\rm K\cdot km/s})^{-1}$ for NGC 2276 data in the upper and bottom left panels, on the bottom right panel we applied an $X_{\rm CO}$ factor that takes into account the spatial variation in nebular metallicity (Narayanan et al. 2012). The contours present the data from the HERACLES survey of nearby galaxies at sub-galactic scales (Leroy et al. 2013), and the green X symbol is the mean galactic value for NGC 2276 ($\langle\tau_{depl}\rangle$=0.55 Gyr). The pixels from the NGC 2276 maps are binned to sizes of 2.7" ($\approx$ 450 pc) to show spatially independent data. Typical uncertainties are shown in the right corner. The dashed lines indicate $\tau_{\rm depl}$ of constant values.

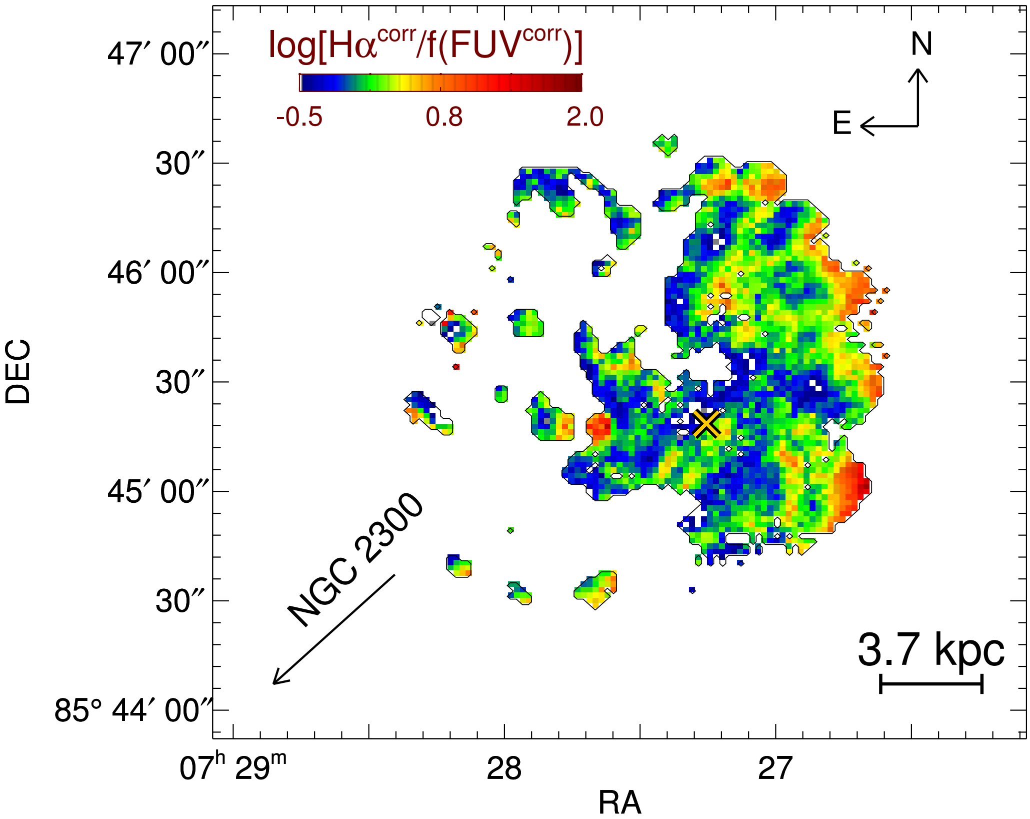

Fig. 5.4 Hα,corr/f$_\nu$(FUV,corr) ratio map, with lower ratios robustly indicating older clusters (Sánchez-Gil et al. 2011). Shown data have S/N>5 in both Balmer lines and FUV emission. The mean uncertainty of the data shown is ≈ 0.3 dex. We attribute the increase in the ratio on the western edge of the disk to ram pressure triggering recent star formation.

5.4 Discussion and summary

For the first time, a spatially resolved measurements of the H$_2$ and $\tau_{\rm depl}$ in NGC 2276 could be seen. On galactic scales, the mean $\tau_{\rm depl}$ of NGC 2276 is 0.55 Gyr, which is lower than the 1-2 Gyr found in surveys of nearby galaxies (COLD GASS, HERACLES; Saintonge et al. 2011; Leroy et al. 2013). Despite the low value, the mean galactic $\tau_{\rm depl}$ of NGC 2276 is still within the scatter of $\tau_{\rm depl}$ seen in nearby galaxies (see Fig. 5.3 or Fig. 14 in Leroy et al. 2013). NGC 2276 exhibits $\Sigma_{\rm SFR}$(Hα,corr) and $\Sigma_{\rm H_2}$ values that are higher than in the HERACLES survey, and lower values than in the galaxies at the coalescence phase (Saito et al. 2015, 2016). On the other hand, I observe a large variation in $\tau_{\rm depl}$ at sub-galactic scales in NGC 2276.

On a pixel-to-pixel scale (pixels ≈ 450 pc in size) in a 20" wide NE-SW slit, $\tau_{\rm depl}$ ranges from 10 Myr to 3 Gyr. This is almost *2 orders of magnitude variation* in $\tau_{\rm depl}$ within a single disk. Furthermore, my results reveal a *gradual decrease* in $\tau_{\rm depl}$ across the disk in the NE-SW direction.

This is a factor of ≈30 larger variation at sub-galactic scales compared to other nearby galaxies. For individual galaxies in the HERACLES survey, sub-galactic regions show a typical of ≈0.5 dex (Fig. 18 and 19 in Leroy et al. 2013). However, $\tau_{\rm depl}$ scatter in NGC 2276 decrease by 0.5 dex when we use variable metallicity-dependent $\rm X_{CO}$ factor, which indicates that sub-galactic variation in $\tau_{\rm depl}$ may be affected by a different metallicity prescriptions or when using a single $\rm X_{CO}$ factor. The NGC 2276's variation in the $\tau_{\rm depl}$ is comparable only with the merging starburst LIRGs observed by Pereira-Santaella et al. (2016) and Saito et al. (2016), although their mean galactic values exhibit lower $\tau_{\rm depl}$ than NGC 2276. The mid-stage merging galaxy VV114 (Saito et al. 2016) covers a similar range in parameters ($\Sigma_{\rm SFR}({\rm H}\alpha, {\rm corr})$ and $\Sigma_{\rm H_2}$) as NGC 2276 on the Kennicutt-Schmidt diagram and shows almost 2 dex variation in $\tau_{\rm depl}$. Renaud (in prep.) find a 1-3 dex difference in $\tau_{\rm depl}$ between regions in their simulations of the Antennae during early phases of interaction. However, the observed variation in $\tau_{\rm depl}$ is only 0.5 dex in late-phase merging LIRGs such as the Antennae (Klaas et al. 2010) and NGC $4567/8$ (Nehlig et al. 2016).

Based on the clear asymmetric distribution of the stellar disk, we tentatively attribute the large-scale gradient in $\tau_{\rm depl}$ as to tidal forces acting on NGC 2276. The tidal forces act on the entire disk, and likely cause a gradual 1-1.5 dex decrease of $\tau_{\rm depl}$ between the two sides of the disk. The ram pressure further disturbs the morphology of the gas disk, and particularly compresses gas on its western edge, which has younger stellar clusters and 1 dex lower $\tau_{\rm depl}$ compared to the rest of the disk.

NGC 2276 shows that galaxies in the pre-coalescence phase of interaction may already exhibit large variations in $\tau_{\rm depl}$ at sub-galactic scales, while still showing a typical $\tau_{\rm depl}$ value for the galaxy-wide average. Our observations demonstrate clearly that a galaxy-galaxy interaction significantly modifies the star formation efficiency of molecular gas locally, that the effect is distributed throughout the galactic disk and not just at the galaxy center, and that these changes occur well before coalescence.

Chapter 6

“There is no science in this world like physics. Nothing comes close to the precision with which physics enables you to understand the world around you. It’s the laws of physics that allow us to say exactly what time the sun is going to rise. What time the eclipse is going to begin. What time the eclipse is going to end.”

by Neil deGrasse Tyson

6. Conclusions & Future Perspective

NGC 4565
c: Christoph Kaltseis,
CEDIC, NASA

6.1 Summary

The interstellar medium (ISM) is an important component of galaxies, which regulates star formation, morphology, and evolution of galaxies. Measuring the spatial distribution and the rate of star formation (SFR) in galaxies helps us to understand the driving forces behind star formation and galactic evolution.

For a long time, estimation of the SFR in nearby galaxies was hindered by probing too large spatial scales (Kennicutt 1998), by the inability to properly measure the attenuation of light from star-forming regions (Calzetti et al. 2005), improper subtraction of the diffuse and non-star-forming emission (Leroy et al. 2012), and by not accounting for underlying absorption lines in stellar spectra (Blanc et al. 2009). Recently, the ISM in nearby galaxies has been observed at smaller scales by instruments and facilities with better angular resolutions (Leroy et al. 2012). Attenuation measurements are factored in the calibration of hybrid SFR prescriptions that combine SFR tracers such as attenuated emission in ultraviolet and optical with un-attenuated infrared emission (Calzetti et al. 2010). However, recent advancement in optical integral field unit (IFU) technology have greatly improved our ability to address the issues with attenuation and underlying absorption features (Sánchez 2006; Blanc et al. 2009). Specifically, this enables us to properly determine the attenuation of the Balmer lines and thus to properly estimate the SFR in galaxies.

The main goal of this thesis is to use optical IFU observations of nearby galaxies to determine the Balmer line attenuation, in order to properly estimate the resulting SFR and star formation efficiency (SFE) at sub-kpc scales (from 10 pc to kpc). We primarily use observations of the ionized gas in the Andromeda galaxy (M31) and the nearby interacting galaxy NGC 2276 from the PMAS/PPaK optical IFU on the 3.5m telescope at the Calar Alto Observatory (Spain). Those observations are combined with other tracers (ultra-violet, infra-red and (sub-)mm images) to probe the distribution of other components of the ISM (such as dust and molecular gas). The reason behind probing the ISM and SFR in M31 is to trace high spatial resolutions (down to $\approx$10 pc), while in NGC 2276 we test how the early phase galactic interaction affects its disk.

6.1.1 The dust/gas geometry in nearby galaxies

Combining dust mass surface density maps with Balmer line attenuation maps allows for an estimation of the 3-dimensional distribution of the dust relative to the young massive stars and ionized gas. In chapter 2, we found that our data for M31 most closely follows the foreground screen model of the dust/gas geometry, which differs from the geometry derived for nearby galaxies. This dust/gas geometry does not change when varying the spatial resolution (from 100 pc to $\approx 1 - 2$ kpc). Our hypothesis for the origin of the difference in the gas/dust distributions between M31 and these other nearby galaxies is that the vertical distribution of the dust, star-forming regions, and the diffuse ionized gas changes with galactocentric distance and with inclination. Thus the vertical geometry of those ISM components in central regions of nearby galaxies, which were observed before, differs markedly from the regions probed in the outskirts of the M31 disk.

6.1.2 SFR prescriptions at small scales

Following our measurement of attenuation, in chapter 3, we use the extinction corrected Balmer line as a reference SFR tracer, in combination with ultra-violet (UV) and infrared (IR) images, to calibrate hybrid SFR prescriptions at sub-galactic scales. M31's proximity enables us to distinguish the star formation regions from the rest of the disk and to test the SFR prescriptions as a function of different spatial scales (from 50 pc to 1 kpc). Our results suggest the hybrid SFR prescriptions that are different from the current prescriptions in the literature, that leads to a 0.7 dex higher SFRs than when we apply the prescriptions from the literature. Our results indicate that the hybrid SFR prescriptions do not change with spatial scales or with the subtraction of a diffuse component. These results imply that the hybrid SFR prescriptions used for the SFR measurements of nearby galaxies are not universal. As hypothised in the previous chapter, a comparison with other galaxies indicates that both the inclination and the galactocentric radius may alter the SFR prescriptions due to varying dust/gas distribution. This is in agreement with other studies in the literature that also noticed that the SFR prescriptions are not universal (Catalán-Torrecilla et al. 2015; Boquien et al. 2016) and that they vary with galactocentric distances, attenuation, and specific SFR (=SFR/$\mathrm{M}_{\mathrm{stellar}}$).

6.1.3 Effects of galactic interactions on ISM and galaxy

In chapter 4, we observe the interacting galaxy NGC 2276, which is at an early phase of interaction, in order to investigate if the interaction affects its star formation and its ISM. The IFU observations probe NGC 2276 at sub-galactic spatial scales ($\approx$0.5 kpc). We probed its SFR, gas-phase metallicity, stellar distribution, diffuse gas fractions, and the source of ionization of its gas. Our results show an elevated and asymmetric SFR, a metallicity gradient consistent with other disk galaxies, asymmetric stellar distribution, and that star formation is the dominant source of ionization. The asymmetric stellar distribution is likely caused by the gravitational tides exerted on NGC 2276 from its neighbour NGC 2300. The following chapter discusses the source of the elevated and asymmetric SFR.

6.1.4 Effects of galactic interactions on the SF efficiency

Recent simulations of interacting galaxies indicate that the SFE may be affected by the turbulence generated by tidal forces. To test this hypothesis, in chapter 5, we estimate the SFE of NGC 2276, introduced in the previous chapter. By combining the SFR of NGC 2276 at sub-galactic scales ($\approx$0.5 kpc) with CO(1-0) data, observed by the IRAM facilities, we find more than two orders of magnitude of variation in the SFE of the molecular gas. This unusually large variation in SFE at sub-kpc scales is much higher than the variation seen by the HERACLES survey of galaxies, despite NGC 2276's mean galactic SFE value being within the HERACLES scatter. We speculate that this large variation in SFE is caused by tidal forces exerted from the neighboring galaxy NGC 2300, and, to some effect, by ram pressure affecting the ISM in NGC 2276.

6.2 Concluding remarks

6.2.1 Effects of our results on star formation estimation in nearby galaxies

Past observations of nearby galaxies have resulted in similar SFR prescriptions because they mostly probed similar galactocentric distances, and they have taken the mean values from their SFR calibration factors that usually show large scatter (up to ≈0.5 dex; Calzetti et al. 2007). However, recent studies by Catalán-Torrecilla et al. (2015) and Boquien et al. (2016) noticed trends in values of the SFR calibration factors as a function of attenuation, specific SFRs, and galactocentric distances. Nevertheless, their data uses mean galactic values (in the case of Catalán-Torrecilla et al. 2015) or they are restricted to the central regions of galaxies (in the case of Boquien et al. 2016) at much lower galactocentric distances ($< 0.3\,\mathrm{R}_{25}$) than the M31 fields ($> 0.4\,\mathrm{R}_{25}$). Despite a clear variation in the dust/gas distribution and the SFR prescriptions with respect to galactocentric distances and inclinations, we cannot establish if those trends are generally common to disk galaxies, if the dust/gas distribution is the main driver of changes in SFR prescriptions, or if M31 is just a peculiar galaxy that desplaying an unusual behaviour. Furthermore, it is possible that the variation in the dust/gas distribution increases the scatter in sub-galactic and mean galactic SFR values of nearby galaxies, thus affecting the estimation of the SF laws and the comparison between galaxies.

We hypothesize that if nearby galaxies are observed toward the outskirts of their disks, the SFR prescriptions would change. In that case, applying the traditional and established hybrid SFR prescriptions from the literature (Kennicutt 1998; Calzetti et al. 2007; Leroy et al. 2012), which combine UV/optical and IR tracers, would underestimate SFRs toward the outskirts of galaxies by up to 0.5 dex. The low gas density regions in the HI dominated outskirts of galaxies (Bigiel et al. 2008) may exhibit higher SFRs than what was estimated in the literature, thus changing our view of the SF law and the SFE of the ISM in those regions. Future observations of more galaxies and especially their outskirts are required to indicate how much the dust/gas geometry varies across the disks, and how much it changes the hybrid SFR prescriptions.

Our examination of M31 further shows that dust/gas distribution and SFR prescriptions do *not* change with varying spatial scales (from 50 pc to 1-2 kpc). This indicates that even the observations of nearby galaxies at ≈kpc scales are still likely to properly probe the dust/gas distribution and thus SFRs prescriptions. Nevertheless, more observations of nearby galaxies at sub-kpc scales are needed to confirm these results.

6.2.2 Varying star formation and star formation efficiency at sub-galactic scales

The more than two order of magnitude variation across the entire disk of NGC 2276 implies that tidal forces and ram pressure may significantly affect the ISM and the star formation process in the entire disk of interacting galaxies, already at early stages of the interaction. Furthermore, we noticed that the galaxies at later phase of interaction, such as the highly luminous IR galaxies (LIRGs and ULIRGs) and mergers, show high SFE values and a narrower variation in SFE at sub-galactic scales (Saito et al. 2015, 2016).

NGC 2276 displays an increase in SFR and SFE in both its galactic center and disk, and an asymmetrically distributed star formation. This is in a contrast to the findings of Barrera-Ballesteros et al. (2015) and Ellison et al. (2018), where they observed that the SFR in most galaxy mergers at latter phases of interactions can be widespread, but statistically centrally located. However, recent observations of galaxies experiencing ram pressure in the GASP survey show many galaxies with asymmetric star formation that does not follow their stellar distribution (Fritz et al. 2017; George et al. 2018; Vulcani et al. 2018). Additionally, the simulations of interacting galaxies by Moreno et al. (2015) indicate an increase in SFE in the galactic center while a decrease is expected in the rest of the disk.

With these results in mind, we hypothesize that at the early phase of interactions, the external galactic forces increase star formation and its efficiency to form stars across the entire galactic disks, while in the later phases both the star formation and star formation efficiency in disks (but not in the centers) are quenched. This would complement both the observations of centrally enhanced SFR in the observed mergers by Barrera-Ballesteros et al. (2015) and Ellison et al. (2018), and decreasing variation in SFE in ULIRGS and LIRGS observed by Saito et al. (2015), and Saito et al. (2016).

6.3 Future perspective

The main results in this work show deviations from what was previously found in nearby galaxies. However, our results were obtained using only two galaxies, and it is unclear if they tell us an universal story about the ISM in nearby galaxies, if our observed galaxies are peculiar and very different from other galaxies. On one hand, the data in the outskirts of M31's disk shows a different dust/gas geometry, and a different SFR prescriptions for that – as we argue – is caused by variation of the dust/gas geometry. Unfortunately, there is no data, in the literature, probing galactocentric distances between the M 31 data and the more central regions observed in other nearby galaxies that would allow a robust test for the trends seen between the dust/gas geometry and the SFR prescriptions. On other hand, NGC 2276 shows a large variations in SFE at sub-kpc scales. Furthermore, when we compare NGC 2276 with other galaxies, we noticed that the galaxies at different phases of interactions show different variations in the sub-galactic SFE.

6.3.1 What affects SFR prescriptions in nearby galaxies?

In the future, it would be worth investigating how the vertical dust/gas distribution and the SFR prescription in galaxies varies as a function of: 1) galactocentric distance, 2) inclination, 3) spatial scale, 4) diffuse emission fraction (using multiple nebular lines), 5) specific SFR (estimated from near-IR emission), 5) age of stellar clusters (using the UV/Hα ratio and the stellar D$_n$4000 break), and 6) galactic structures (such as bars, arm and inter-arm regions, and outskirts). This would lead to a better understanding of what is driving the scatter and variations in observed attenuations and estimated SFR values within and between observed galaxies. This could affect our interpretation of the SF law, and would test our hypothesis that the variation in the vertical dust/gas distribution with galactocentric distance can have a pronounced effect on attenuation and SFR estimates.

To correct the emission of nebular lines for attenuation in order to properly calibrate the SFR prescriptions, observations of the full disks of nearby galaxies with IFU instruments are needed. There are now several IFU instruments (e.g. MUSE, PPaK/PMAS, SAMI, etc.) that can accomplish this, and as even observations without seeing restrictions (with angular resolutions of at about 2”-5”) would probe sub-kpc spatial scales in very nearby galaxies. The number (e.g. 10) of required galaxies should be large enough for a minimal statistical sample to account for different features (bars, rings, spiral arms) and inclinations, and small enough to allow for observing their entire disks. To calibrate the widely used SFR prescriptions, the IFU observations could be combined with publicly available UV and IR images from the GALEX, WISE and Spitzer space telescopes.

For example, there are three surveys that offer a good opportunity to achieve these goals. First is the KINGFISH survey (Kennicutt et al. 2011) that has publicly available IR images, thus offering the opportunity to estimate the dust mass surface density in each galaxy. Until now, mostly the central regions ($< 0.3\,\mathrm{R}_{25}$) of galaxies were observed with optical IFU. Expanding the IFU observations toward the outskirts (up to R_{25}) of those galaxies would enable the estimation of the dust/gas geometry across entire galactic disks. This will also pave the way toward testing the link between the SFR prescriptions, the dust/gas geometry and galactic features. The second possible survey could be the PHANGS survey (an ALMA and VLT/MUSE IFU survey of nearby galaxies; Kreckel et al. 2018), whose data is becoming public, and which probes the ISM in nearby galaxies at small ($\approx 50 - 100$ pc) scales. Some of the galaxies from the PHANGS survey are part of the KINGFISH survey. The third survey may be the SDSS-V Local Volume Mapper (LVM), which will be initiated in the near future. Its goal is to map the entire disks of the Milky Way and galaxies in the Local Group (including M31, M33, Magellanic clouds) with an IFU instrument, achieving good spatial resolutions (e.g., ≈ 50 pc in M31).

6.3.2 Variations in SFE at different phases of interactions

In the future, it would be worth investigating the behaviour of SFE in a sample of a few well selected galaxies, probing the properties of their ISM at sub-kpc scales for different phases of galactic interactions. Observations of SFE at different phases of interactions would inform observational and theoretical astronomers, and help them understand how external, dynamical processes affect the ISM, SFR, and SFE in galaxies during the various stages of galactic interactions. This could also lead to a better understanding of the evolutionary path of disk galaxies and star formation within them to finding a link between the normal star-forming galaxies and the LIRGs and ULIRGs.

In order to test how external forces modulate the SFE, this sample of galaxies would include a few galaxies experiencing ram pressure only, and some being in galaxy groups or in clusters. In order to derive the SFE of the molecular gas (bulk and/or dense), IFU observations of those galaxies should be combined with data from (sub-)mm facilities such as ALMA or IRAM.

There are two potential surveys at both the optical IFU and (Sub-)mm data that offer access to a wide range of interacting galaxies, at different phases of interaction, and with different type of interactions (ram pressure vs. tidal forces). One is the GOALS survey (Great Observatories All-sky LIRG Survey; Armus et al. 2009) that contains public (sub-)mm data of massive star-burst galaxies, at different phases of interactions. The Second is the GASP survey (Gas Stripping Phenomena in galaxies with MUSE; Poggianti et al. 2017), that offers both IFU (MUSE) and (sub-)mm (ALMA, IRAM, etc.), which contains observations of galaxies in different interacting environments (interacting with nearby galaxies in groups and clusters, or gas being stripped by the ram pressure).

Another way to continue research in this direction is to investigate the star-forming properties of the dense molecular gas, as it is not well established how the dense phase of the molecular gas evolves during galaxy interaction. For example, our NOEMA project (PI. Tomicic N.; IRAM project ID: S18BO) for observing the dense molecular gas tracers in NGC 2276 is currently ongoing. These observations will allow us to investigate if the dense gas SFE in NGC 2276 shows similar variations as the SFE of the bulk of the molecular gas, and how such variations in SFE relate to the dense gas fraction.

APPENDIX: SFR PRESCRIPTIONS

Here we present the SFR prescriptions derived in Chap. 3, which show results at different spatial scales, and different tracers (monochromatic and hybrid). The results for Hα, FUV, 22 μm and 24 μm are listed in Tab. A.1.

We also added the monochromatic calibration for 12 μm, 70 μm, 160 μm and TIR tracers in Tab. A.2. TIR values in this work are calculated using Formula 5 in Dale et al. (2009). If we were to use the TIR prescription from Galametz et al. (2013), the TIR values would be ≈10% lower. For TIR, we used 22 μm instead of 24 μm tracer. As seen on Fig. 3.12, SFR prescriptions from 70 μm and TIR differ from those prescribed by Calzetti et al. (2010); Calzetti (2013). The prescription for 160 μm from Calzetti et al. (2010) match with our prescription. However, the prescription for that tracer is uncertain due to the fact that the 160 μm trace cold dust, and not the hot dust around the star forming regions.

There is a disagreement between the log(SFR)-log(IR) correlation derived in this work and prescribed by Cluver et al. (2017). Here, IR indicates L(12 μm) or L(22 μm). We investigate the shift in the intercept of the log(SFR)-log(IR) correlation in the case where we fixed the slope of the power-law fit through the data. Here we assume the slopes to have values stated in Cluver et al. (2017). We list results for the intercept in that case in lower part of Tab. A.2. We find that the intercept for 22 μm matches with prescription given by Cluver et al. (2017). On the other hand, the intercept for 12 μm data show lower values (by ≈0.7 dex) then the intercept in Cluver et al. (2017).

If we apply the fit given by Cluver et al. (2017) to M31 data, SFR(12 μm) values would be by a factor of 3 higher (0.5 dex) than the SFR(Hα, corr), regardless of the aperture sizes. Cluver et al. (2017) argue that the 12 μm do have the components of PAH (Polycyclic aromatic hydrocarbon) emission and continuum emission from the hot dust, that the PAH emission contributes only ≈30% and that the SFR(12 μm) prescription is robust. However, we argue that the 12 mum and 22 mum tracers in M31 could be less reliable because it could be affected by metallicity, dust composition, chemistry and the dust distribution more than in other galaxies. M31 data show ratios of Σ(12 μm)/Σ(22 μm) to be $\approx\, 3 \pm 1$. On the contrary, Cluver et al. (2017) fount similar luminosity values of $\nu \mathrm{L}_\nu$(12 μm) and $\nu \mathrm{L}_\nu$(22 μm) (see Fig. 4 in their paper). That ratio is lowest in the bright HII regions (≈1), and increases outside them. Similarly, weak anti-correlation between the 12 μm/22 μm ratios and the 70 μm/160 μm ratios was found in our fields. Soifer & Neugebauer (1991) and Sanders et al. (2003) found that the 12 μm/25 μm ratios in nearby galaxies strongly anti-correlate with 60 mum/100 μm ratio and with IR surface brightness. They argue that it is the cause of destruction of small grains in bright mid-IR emission regions.

Table A.1 SFR prescriptions derived from various observed tracers (left column) at different resolution. We give prescriptions for the case of pixel-by-pixel comparison of star formation tracers maps (middle column), and the case of the apertures with different radii (right column). In all examples, we *did not* remove the diffuse emission from apertures or pixels (for those cases see Sec. 3.4.3). In the square brackets, we put the scatter of the calibration factors. Units of star formation tracers used in this table are in surface brightness (units of $\mathrm{erg\,s^{-1}\,kpc^{-2}}$), which were derived by multiplying the observed fluxes of the SFR tracers (units in $erg\,s^{-1}\,cm^{-2}\,arcsec^{-2}$) with number 5.1×10^{54}. Fluxes of mid-IR (FUV) are in units of νF_ν (λF_λ), where ν (λ) is effective frequency (wavelength), and F_ν (F_λ) a flux density from the maps of tracers. $\mathrm{H\alpha,corr}$-SFR and FUV,corr-SFR conversion factors $a_{\mathrm{H\alpha,corr}}$ and $b_{\mathrm{FUV,corr}}$ are stated in the formula 3.1 and 3.2. Other prescriptions give values $a_{24} \approx 0.031 \pm 0.006$ (Calzetti et al. 2007), $a_{24} \approx 0.05$ (Calzetti et al. 2005), and $b_{22} \approx 3.9$ (Leroy et al. 2012).

SF Tracer	pixel-by-pixel (native IR resolution)	apertures (R≈50 pc)
$\Sigma_{\mathrm{SFR}}(24\mu\mathrm{m}) = a\times\Sigma_{24\,\mu\mathrm{m}}$	$a = 1.8 \pm 0.9 \times 10^{-42}$	$a = 1.4 \pm 0.8 \times 10^{-42}$
$\Sigma_{\mathrm{SFR}}(22\mu\mathrm{m}) = a\times\Sigma_{22\,\mu\mathrm{m}}$	$a = 1.5 \pm 0.9 \times 10^{-42}$	$a = 1.2 \pm 0.6 \times 10^{-42}$
$\Sigma_{\mathrm{SFR}}(\mathrm{H}\alpha+24\mu\mathrm{m}) = a_{\mathrm{H\alpha,corr}} \cdot (\Sigma_{\mathrm{H\alpha}} + a_{24} \times \Sigma_{24\,\mu\mathrm{m}})$	$a_{24} = 0.24 \pm 0.14$	$a_{24} = 0.19 \pm 0.14$
$\Sigma_{\mathrm{SFR}}(\mathrm{H}\alpha+22\mu\mathrm{m}) = a_{\mathrm{H\alpha,corr}} \cdot (\Sigma_{\mathrm{H\alpha}} + a_{22} \times \Sigma_{22\,\mu\mathrm{m}})$	$a_{22} = 0.21 \pm 0.12$	$a_{22} = 0.17 \pm 0.1$
$\Sigma_{\mathrm{SFR}}(\mathrm{FUV}+24\mu\mathrm{m}) = b_{\mathrm{FUV,corr}} \cdot (\Sigma_{\mathrm{FUV}} + b_{24} \times \Sigma_{24\,\mu\mathrm{m}})$	$b_{24} = 33 \pm 21$	$b_{24} = 27 \pm 19$
$\Sigma_{\mathrm{SFR}}(\mathrm{FUV}+22\mu\mathrm{m}) = b_{\mathrm{FUV,corr}} \cdot (\Sigma_{\mathrm{FUV}} + b_{22} \times \Sigma_{22\,\mu\mathrm{m}})$	$b_{22} = 28 \pm 17$	$b_{22} = 24 \pm 13$

SF Tracer	pixel-by-pixel (25” resolution)	apertures (R≈100 pc)
$\Sigma_{\mathrm{SFR}}(24\mu\mathrm{m}) = a\times\Sigma_{24\,\mu\mathrm{m}}$	$a = 1.3 \pm 0.5 \times 10^{-42}$	$a = 1.3 \pm 0.5 \times 10^{-42}$
$\Sigma_{\mathrm{SFR}}(22\mu\mathrm{m}) = a\times\Sigma_{22\,\mu\mathrm{m}}$	$a = 1.2 \pm 0.6 \times 10^{-42}$	$a = 1.1 \pm 0.5 \times 10^{-42}$
$\Sigma_{\mathrm{SFR}}(\mathrm{H}\alpha+24\mu\mathrm{m}) = a_{\mathrm{H\alpha,corr}} \cdot (\Sigma_{\mathrm{H\alpha}} + a_{24} \times \Sigma_{24\,\mu\mathrm{m}})$	$a_{24} = 0.18 \pm 0.08$	$a_{24} = 0.22 \pm 0.08$
$\Sigma_{\mathrm{SFR}}(\mathrm{H}\alpha+22\mu\mathrm{m}) = a_{\mathrm{H\alpha,corr}} \cdot (\Sigma_{\mathrm{H\alpha}} + a_{22} \times \Sigma_{22\,\mu\mathrm{m}})$	$a_{22} = 0.180.1$	$a_{22} = 0.17 \pm 0.09$
$\Sigma_{\mathrm{SFR}}(\mathrm{FUV}+24\mu\mathrm{m}) = b_{\mathrm{FUV,corr}} \cdot (\Sigma_{\mathrm{FUV}} + b_{24} \times \Sigma_{24\,\mu\mathrm{m}})$	$b_{24} = 33 \pm 21$	$b_{24} = 25 \pm 12$

$\Sigma_{\rm SFR}$(FUV+22μm)= b$_{\rm FUV,corr}\cdot(\Sigma_{\rm FUV}$+b$_{22}\times\Sigma_{22\,\mu{\rm m}})$	b$_{22}=24\pm14$	b$_{22}=21\pm11$

SF Tracer	pixel-by-pixel (65” resolution)	apertures (R≈200 pc)
$\Sigma_{\rm SFR}$(24μm)= a$\times\Sigma_{24\,\mu{\rm m}}$	a$=1.2\pm0.3\times10^{-42}$	a$=1.1\pm0.3\times10^{-42}$
$\Sigma_{\rm SFR}$(22μm)= a$\times\Sigma_{22\,\mu{\rm m}}$	a$=1.1\pm0.3\times10^{-42}$	a$=1\pm0.3\times10^{-42}$
$\Sigma_{\rm SFR}$(Hα+24μm)= a$_{\rm H\alpha,corr}\cdot(\Sigma_{\rm H\alpha}$+a$_{24}\times\Sigma_{24\,\mu{\rm m}})$	a$_{24}=0.19\pm0.06$	a$_{24}=0.16\pm0.05$
$\Sigma_{\rm SFR}$(Hα+22μm)= a$_{\rm H\alpha,corr}\cdot(\Sigma_{\rm H\alpha}$+a$_{22}\times\Sigma_{22\,\mu{\rm m}})$	a$_{22}=0.16\pm0.05$	a$_{22}=0.13\pm0.05$
$\Sigma_{\rm SFR}$(FUV+24μm)= b$_{\rm FUV,corr}\cdot(\Sigma_{\rm FUV}$+b$_{24}\times\Sigma_{24\,\mu{\rm m}})$	b$_{24}=25\pm8$	b$_{24}=23\pm6$
$\Sigma_{\rm SFR}$(FUV+22μm)= b$_{\rm FUV,corr}\cdot(\Sigma_{\rm FUV}$+b$_{22}\times\Sigma_{22\,\mu{\rm m}})$	b$_{22}=22\pm7$	b$_{22}=20\pm6$

SF Tracer	Integrated field
$\Sigma_{\rm SFR}$(Hα+24μm)= a$_{\rm H\alpha,corr}\cdot(\Sigma_{\rm H\alpha}$+a$_{24}\times\Sigma_{24\,\mu{\rm m}})$	a$_{24}=0.17\pm0.04$
$\Sigma_{\rm SFR}$(Hα+22μm)= a$_{\rm H\alpha,corr}\cdot(\Sigma_{\rm H\alpha}$+a$_{22}\times\Sigma_{22\,\mu{\rm m}})$	a$_{22}=0.15\pm0.04$
$\Sigma_{\rm SFR}$(FUV+24μm)= b$_{\rm FUV,corr}\cdot(\Sigma_{\rm FUV}$+b$_{24}\times\Sigma_{24\,\mu{\rm m}})$	b$_{24}=20\pm6$
$\Sigma_{\rm SFR}$(FUV+22μm)= b$_{\rm FUV,corr}\cdot(\Sigma_{\rm FUV}$+b$_{22}\times\Sigma_{22\,\mu{\rm m}})$	b$_{22}=19\pm5$

Table A.2 SFR prescriptions derived from for 12 μm, 22 μm, 70 μm, 160 μm and TIR tracers (left column) for different apertures (radii of 50 pc, 100 pc and 200 pc). In lower part of the table, we fixed the slope of log(SFR)-log(IR) relations at the value calibrated by Cluver et al. (2017). In that case, Cluver et al. (2017) prescribe the intercept to be -8 (-7.8) for the 22 μm (12 μm) tracer. In all examples, we *did not* remove the diffuse emission from apertures. In the square brackets, we put the scatter of the calibration factors. Units of star formation tracers used in this table are in surface brightness (units of $\mathrm{erg\,s^{-1}\,kpc^{-2}}$), which were derived by multiplying the observed fluxes of the SFR tracers (units in $erg\,s^{-1}\,cm^{-2}\,arcsec^{-2}$) with number 5.1×10^{54}. Fluxes of IR are in units of νF_ν (λF_λ), where ν (λ) is effective frequency (wavelength).

R=50 pc	R=100 pc	R=200 pc	
log_{10}[SFR(22μm)]= a$\times log_{10}[\frac{L_{22\,\mu\mathrm{m}}}{L_\odot}]$+b	a= 0.3±0.1, b= -5.3	a= 0.5±0.2, b= -6.3	a= 1.1±0.2, b= -9.1
log_{10}[SFR(12μm)]= a$\times log_{10}[\frac{L_{12\,\mu\mathrm{m}}}{L_\odot}]$+b	a= 0.9±0.1, b= -8.3	a= 0.9±0.2, b= -8.4	a= 1.2±0.5, b= -10.1
Σ_{SFR}(12μm)= a$\times\Sigma_{12\,\mu\mathrm{m}}$	a=$4.7 \pm 2.8 \times 10^{-43}$	a=$4.1 \pm 1.8 \times 10^{-43}$	a=$3.6 \pm 1.7 \times 10^{-43}$
Σ_{SFR}(70μm)= a$\times\Sigma_{70\,\mu\mathrm{m}}$	a=$4.8 \pm 4.3 \times 10^{-43}$	a=$3.7 \pm 1.9 times 10^{-43}$	a=$3.5 \pm 1.9 \times 10^{-43}$
Σ_{SFR}(160μm)= a$\times\Sigma_{160\,\mu\mathrm{m}}$	a=$1.8 \pm 0.9 \times 10^{-43}$	a=$1.6 \pm 0.7 \times 10^{-43}$	a=$1.4 \pm 0.6 \times 10^{-43}$
Σ_{SFR}(TIR)= a$\times\Sigma_{\mathrm{TIR}\,\mu\mathrm{m}}$	a=$9.3 \pm 4.8 \times 10^{-44}$	a=$8 \pm 3 \times 10^{-44}$	a=$7 \pm 3 \times 10^{-44}$
Σ_{SFR}=$a_{\mathrm{H}\alpha,\mathrm{corr}} \cdot (\Sigma_{\mathrm{H}\alpha}+a_{12} \times \Sigma_{12\,\mu\mathrm{m}})$	$a_{12} = 0.04 \pm 0.03$	$a_{12} = 0.04 \pm 0.02$	$a_{12} = 0.04 \pm 0.02$
Σ_{SFR}=$a_{\mathrm{H}\alpha,\mathrm{corr}} \cdot (\Sigma_{\mathrm{H}\alpha}+a_{70} \times \Sigma_{70\,\mu\mathrm{m}})$	$a_{70} = 0.07 \pm 0.07$	$a_{70} = 0.06 \pm 0.03$	$a_{70} = 0.06 \pm 0.07$
Σ_{SFR}=$a_{\mathrm{H}\alpha,\mathrm{corr}} \cdot (\Sigma_{\mathrm{H}\alpha}+a_{160} \times \Sigma_{160\,\mu\mathrm{m}})$	$a_{160} = 0.03 \pm 0.02$	$a_{160} = 0.03 \pm 0.01$	$a_{160} = 0.02 \pm 0.01$
Σ_{SFR}=$a_{\mathrm{H}\alpha,\mathrm{corr}} \cdot (\Sigma_{\mathrm{H}\alpha}+a_{\mathrm{TIR}} \times \Sigma_{\mathrm{TIR}})$	$a_{\mathrm{TIR}} = 0.013 \pm 0.008$	$a_{\mathrm{TIR}} = 0.012 \pm 0.005$	$a_{\mathrm{TIR}} = 0.011 \pm 0.004$
Fixed slope (Cluver et al. 2017):			
log_{10}[SFR(22μm)]= 0.92$\times log_{10}[\frac{L_{22\,\mu\mathrm{m}}}{L_\odot}]$+b	b=-7.9 ± 0.4	b=-7.9 ± 0.3	b=-7.8 ± 0.1
log_{10}[SFR(12μm)]= 0.89$\times log_{10}[\frac{L_{12\,\mu\mathrm{m}}}{L_\odot}]$+b	b=-8.3 ± 0.2	b=-8.3 ± 0.2	b=-8.3 ± 0.2

PUBLICATIONS OF NEVEN TOMIČIĆ USED IN THIS THESIS

1st AUTHOR PUBLICATION

1. **Tomičić N.**, Kreckel K., Groves B., Schinnerer E., Sandstrom K., Kapala M., Blanc G. A., Leroy A. 2017, ApJ, 844, 155T;
   "Attenuation modified by DIG and dust as seen in M31"

   [Chap. 2 in this PhD Thesis]
2. **Tomičić N.**, Hughes A., Kreckel K, Renaud F., Pety J., Schinnerer E., Saito T., Querejeta M., Faesi C. M., Garcia-Burillo S. 2018, ApJL, 869, L38;
   "Two Orders of Magnitude Variation in the Star Formation Efficiency Across the Pre-Merger Galaxy NGC 2276"

   [Chap. 3 in this PhD Thesis]
3. **Tomičić N.**, Ho I-T., Kreckel K., Schinnerer E., Leroy A., Groves B., Sandstrom K., Blanc G.A., Jarrett T., Thilker D., Kapala M., and McElroy R. 2019, ApJ, 873, 1;
   "Calibrating star-formation rate prescriptions at different scales (10 pc to 1 kpc) in M31"

   [Chap. 4 and 5 in this PhD Thesis]

2nd & 3rd AUTHOR PUBLICATIONS

1. Smolčić V., Miettinen O., **Tomičić N.** et al. 2018, A&A, 597, A4;
   "(Sub)millimetre interferometric imaging of a sample of COSMOS/AzTEC submillimetre galaxies. III. Environments"

OTHER PUBLICATIONS

1. Bigiel F., Leroy, A. K., Jiménez-Donaire M. J., ... incl. **Tomičić N.** et al. 2016, ApJL, 822, 2 ;
   “The EMPIRE Survey: Systematic Variations in the Dense Gas Fraction and Star Formation Efficiency from Full-disk Mapping of M51”

2. Jiménez-Donaire M. J., Bigiel F.,Leroy A. K., ... incl. **Tomičić N.** et al. 2017, MNRAS, 466, 49J ;
   “Optical Depth Estimates and Effective Critical Densities of Dense Gas Tracers in the Inner Parts of Nearby Galaxy Discs”

3. Jiménez-Donaire M. J., Cormier D., Bigiel F., ... incl.**Tomičić N.** et al. 2017, ApJL, 836L, 29J ;
   “^{13}CO/C^{18}O gradients across the disks of nearby spiral galaxies”

REFERENCES

Abadi, M. G., Moore, B., & Bower, R. G. 1999, MNRAS, 308, 947

Abbott, B. P., Abbott, R., Abbott, T. D., et al. 2016, Physical Review X, 6, 041015

Abramson, A., Kenney, J., Crowl, H., & Tal, T. 2016, AJ, 152, 32

Ackermann, M., Ajello, M., Allafort, A., et al. 2012, ApJ, 755, 164

Allende Prieto, C., Lambert, D. L., & Asplund, M. 2001, ApJ, 556, L63

Allington-Smith, J., & Content, R. 1998, PASP, 110, 1216

Allington-Smith, J. R., Content, R., Haynes, R., & Lewis, I. J. 1997, in , Vol. 2871, Optical Telescopes of Today and Tomorrow, ed. A. L. Ardeberg, 1284–1294

Alton, P. B., Xilouris, E. M., Misiriotis, A., Dasyra, K. M., & Dumke, M. 2004, A&A, 425, 109

Aniano, G., Draine, B. T., Gordon, K. D., & Sandstrom, K. 2011, Publications of the Astronomical Society of the Pacific, 123, 1218

Aniano, G., Draine, B. T., Calzetti, D., et al. 2012, ApJ, 756, 138

Argudo-Fernández, M., Verley, S., Bergond, G., et al. 2015, A&A, 578, A110

Armus, L., Mazzarella, J. M., Evans, A. S., et al. 2009, PASP, 121, 559

Ascasibar, Y., Guidi, G., Casado, J., Scannapieco, C., & Díaz, A. I. 2016, arXiv e-prints, arXiv:1602.08474

Azimlu, M., Marciniak, R., & Barmby, P. 2011, AJ, 142, 139

Bacon, R., Adam, G., Baranne, A., et al. 1995, A&AS, 113, 347

Baldwin, J. A., Phillips, M. M., & Terlevich, R. 1981, PASP, 93, 5

Balogh, M. L., Morris, S. L., Yee, H. K. C., Carlberg, R. G., & Ellingson, E. 1999, ApJ, 527, 54

Barden, S. C., & Wade, R. A. 1988, in Astronomical Society of the Pacific Conference Series, Vol. 3, Fiber Optics in Astronomy, ed. S. C. Barden, 113–124

Barnard, E. E. 1907, ApJ, 25, doi:10.1086/141434

Barnes, J. E., Wood, K., Hill, A. S., & Haffner, L. M. 2014, MNRAS, 440, 3027

—. 2015, MNRAS, 447, 559

Barrera-Ballesteros, J. K., Sánchez, S. F., García-Lorenzo, B., et al. 2015, A&A, 579, A45

Beckwith, S. V. W., Stiavelli, M., Koekemoer, A. M., et al. 2006, AJ, 132, 1729

Bekki, K. 2014, Monthly Notices of the Royal Astronomical Society, 438, 444

Bellhouse, C., Jaffé, Y. L., Hau, G. K. T., et al. 2017, ApJ, 844, 49

Bianchi, L., Conti, A., & Shiao, B. 2014, Advances in Space Research, 53, 900

Bigiel, F., & Blitz, L. 2012, ApJ, 756, 183

Bigiel, F., Leroy, A., Seibert, M., et al. 2010, ApJ, 720, L31

Bigiel, F., Leroy, A., Walter, F., et al. 2008, AJ, 136, 2846

Bigiel, F., Leroy, A. K., Jiménez-Donaire, M. J., et al. 2016, ApJ, 822, L26

Bishop, J., Mierkiewicz, E. J., Roesler, F. L., Gómez, J. F., & Morales, C. 2004, Journal of Geophysical Research (Space Physics), 109, A05307

Blanc, G. A., Heiderman, A., Gebhardt, K., Evans, II, N. J., & Adams, J. 2009, ApJ, 704, 842

Blanc, G. A., Weinzirl, T., Song, M., et al. 2013, AJ, 145, 138

Bocchio, M., Bianchi, S., Hunt, L. K., & Schneider, R. 2016, A&A, 586, A8

Bolatto, A. D., Wolfire, M., & Leroy, A. K. 2013, ARA&A, 51, 207

Bond, J. R., Szalay, A. S., & Turner, M. S. 1982, Phys. Rev. Lett., 48, 1636

Boquien, M., Calzetti, D., Aalto, S., et al. 2015, A&A, 578, A8

Boquien, M., Kennicutt, R., Calzetti, D., et al. 2016, A&A, 591, A6

Bournaud, F., Daddi, E., Weiß, A., et al. 2015, A&A, 575, A56

Braun, R. 1991, ApJ, 372, 54

Bresolin, F., Garnett, D. R., & Kennicutt, Jr., R. C. 2004, ApJ, 615, 228

Bromm, V., & Yoshida, N. 2011, Annual Review of Astronomy and Astrophysics, 49, 373

Brouillet, N., Muller, S., Herpin, F., Braine, J., & Jacq, T. 2005, A&A, 429, 153

Brown, M. J. I., Jarrett, T. H., & Cluver, M. E. 2014, PASA, 31, HASH

Brown, M. J. I., Moustakas, J., Kennicutt, R. C., et al. 2017, ApJ, 847, 136

Bruzual, G., & Charlot, S. 2003, MNRAS, 344, 1000

Bruzual A., G. 1983, ApJ, 273, 105

Bull, P., Akrami, Y., Adamek, J., et al. 2016, Physics of the Dark Universe, 12, 56

Bundy, K., Bershady, M. A., Law, D. R., et al. 2015, ApJ, 798, 7

Bush, S. J., Cox, T. J., Hayward, C. C., et al. 2010, ApJ, 713, 780

Calzetti, D. 2013, Star Formation Rate Indicators, ed. J. Falcón-Barroso & J. H. Knapen, 419

Calzetti, D., Armus, L., Bohlin, R. C., et al. 2000, ApJ, 533, 682

Calzetti, D., Kinney, A. L., & Storchi-Bergmann, T. 1994, ApJ, 429, 582

—. 1996, ApJ, 458, 132

Calzetti, D., Kennicutt, Jr., R. C., Bianchi, L., et al. 2005, ApJ, 633, 871

Calzetti, D., Kennicutt, R. C., Engelbracht, C. W., et al. 2007, ApJ, 666, 870

Calzetti, D., Wu, S.-Y., Hong, S., et al. 2010, ApJ, 714, 1256

Caplan, J., & Deharveng, L. 1986, A&A, 155, 297

Cappellari, M., & Emsellem, E. 2004, Publications of the Astronomical Society of the Pacific, 116, 138

Cardelli, J. A., Clayton, G. C., & Mathis, J. S. 1989, ApJ, 345, 245

Carilli, C., & Walter, F. 2013, Annual Review of Astronomy and Astrophysics, 51, 105

Catalán-Torrecilla, C., Gil de Paz, A., Castillo-Morales, A., et al. 2015, A&A, 584, A87

Chauke, P. 2014, diploma thesis, University of Cape Town, Private Bag X3, Rondebosch 7701, South Africa

Clayton, G. C., Gordon, K. D., Bianchi, L. C., et al. 2015, ApJ, 815, 14

Cluver, M. E., Jarrett, T. H., Dale, D. A., et al. 2017, The Astrophysical Journal, 850, 68

Collins, J. A., Rand, R. J., Duric, N., & Walterbos, R. A. M. 2000, ApJ, 536, 645

Condon, J. J. 1983, ApJS, 53, 459

—. 1992, ARA&A, 30, 575

Connaughton, V., Burns, E., Goldstein, A., et al. 2016, ApJ, 826, L6

Content, R. 1997, in , Vol. 2871, Optical Telescopes of Today and Tomorrow, ed. A. L. Ardeberg, 1295–1305

Cortese, L., Marcillac, D., Richard, J., et al. 2007, MNRAS, 376, 157

Corwin, Jr., H. G., Buta, R. J., & de Vaucouleurs, G. 1994, AJ, 108, 2128

Courteau, S., Widrow, L. M., McDonald, M., et al. 2011, ApJ, 739, 20

Croom, S. M., Lawrence, J. S., Bland-Hawthorn, J., et al. 2012, MNRAS, 421, 872

Cutri, R. M., Wright, E. L., Conrow, T., et al. 2011, Explanatory Supplement to the WISE Preliminary Data Release Products, Tech. rep.

da Silva, R. L., Fumagalli, M., & Krumholz, M. R. 2014, MNRAS, 444, 3275

Dalcanton, J. J., Williams, B. F., Lang, D., et al. 2012, The Astrophysical Journal Supplement Series, 200, 18

Dalcanton, J. J., Fouesneau, M., Hogg, D. W., et al. 2015, ApJ, 814, 3

Dale, D. A., Cohen, S. A., Johnson, L. C., et al. 2009, ApJ, 703, 517

Dale, D. A., Cook, D. O., Roussel, H., et al. 2017, ApJ, 837, 90

Dasyra, K. M., Xilouris, E. M., Misiriotis, A., & Kylafis, N. D. 2005, A&A, 437, 447

Davies, L. J. M., Driver, S. P., Robotham, A. S. G., et al. 2016, MNRAS, 461, 458

Davies, R. I., Agudo Berbel, A., Wiezorrek, E., et al. 2013, A&A, 558, A56

Davis, D. S., Keel, W. C., Mulchaey, J. S., & Henning, P. A. 1997, AJ, 114, 613

Davis, T. A., Young, L. M., Crocker, A. F., et al. 2014, MNRAS, 444, 3427

de Vaucouleurs, G., de Vaucouleurs, A., & Corwin, J. 1991, Third Reference Catalogue of Bright Galaxies. Volume I: Explanations and references. Volume II: Data for galaxies between 0^h and 12^h. Volume III: Data for galaxies between 12^h and 24^h.

Delaunay, B. 1934, Bulletin de l'Académie des Sciences de l'URSS, 6, 793

Dettmar, R. J. 1990, A&A, 232, L15

Dettmar, R. J., & Schulz, H. 1992, A&A, 254, L25

Dong, H., Li, Z., Wang, Q. D., et al. 2014, ApJ, 785, 136

Dopita, M. A., Kewley, L. J., Sutherland, R. S., & Nicholls, D. C. 2016, Ap&SS, 361, 61

Dopita, M. A., & Sutherland, R. S. 2003, Astrophysics of the diffuse universe

Draine, B. T. 2011a, ApJ, 732, 100

—. 2011b, ApJ, 732, 100

—. 2011c, Physics of the Interstellar and Intergalactic Medium

Draine, B. T., & Li, A. 2007, ApJ, 657, 810

Draine, B. T., Aniano, G., Krause, O., et al. 2014, ApJ, 780, 172

Dreher, J. W., & Welch, W. J. 1981, ApJ, 245, 857

Dressler, A. 1980, ApJ, 236, 351

Ebeling, H., Stephenson, L. N., & Edge, A. C. 2014, ApJ, 781, L40

Eisenhauer, F., Abuter, R., Bickert, K., et al. 2003, in , Vol. 4841, Instrument Design and Performance for Optical/Infrared Ground-based Telescopes, ed. M. Iye & A. F. M. Moorwood, 1548–1561

Elbaz, D., Daddi, E., Le Borgne, D., et al. 2007, A&A, 468, 33

Ellison, S. L., Sánchez, S. F., Ibarra-Medel, H., et al. 2018, MNRAS, 474, 2039

Engelbracht, C. W., Blaylock, M., Su, K. Y. L., et al. 2007, PASP, 119, 994

Erroz-Ferrer, S., Carollo, C. M., den Brok, M., et al. 2019, MNRAS, 200

Eufrasio, R. T., Dwek, E., Arendt, R. G., et al. 2014, ApJ, 795, 89

Faesi, C. M., Lada, C. J., Forbrich, J., Menten, K. M., & Bouy, H. 2014, The Astrophysical Journal, 789, 81

Falcón-Barroso, J., Sánchez-Blázquez, P., Vazdekis, A., et al. 2011, A&A, 532, A95

Fall, S. M., & Efstathiou, G. 1980, MNRAS, 193, 189

Ferguson, A. M. N., Wyse, R. F. G., Gallagher, J. S., I., & Hunter, D. A. 1996, AJ, 111, 2265

Ferguson, A. M. N., Wyse, R. F. G., Gallagher, J. S., & Hunter, D. A. 1998, ApJ, 506, L19

Ferrière, K. M. 2001, Reviews of Modern Physics, 73, 1031

Fitzpatrick, E. L. 1999, PASP, 111, 63

Fitzpatrick, E. L., & Massa, D. 2009, ApJ, 699, 1209

Forbes, D. A., & Thomson, R. C. 1992, MNRAS, 254, 723

Ford, G. P., Gear, W. K., Smith, M. W. L., et al. 2013, ApJ, 769, 55

Fouesneau, M., Johnson, L. C., Weisz, D. R., et al. 2014, ApJ, 786, 117

Fritz, J., Moretti, A., Gullieuszik, M., et al. 2017, ApJ, 848, 132

Fukui, Y., & Kawamura, A. 2010, Annual Review of Astronomy and Astrophysics, 48, 547

Galametz, M., Kennicutt, R. C., Albrecht, M., et al. 2012, MNRAS, 425, 763

Galametz, M., Kennicutt, R. C., Calzetti, D., et al. 2013, MNRAS, 431, 1956

Galbany, L., Mora, L., González-Gaitán, S., et al. 2017, MNRAS, 468, 628

Galliano, F., Galametz, M., & Jones, A. P. 2018, Annual Review of Astronomy and Astrophysics, 56, 673

Gao, Y., & Solomon, P. M. 2004, The Astrophysical Journal, 606, 271

García-Burillo, S., Combes, F., & Neri, R. 1999, A&A, 343, 740

García-Lorenzo, B., Márquez, I., Barrera-Ballesteros, J. K., et al. 2015, A&A, 573, A59

Geehan, J. J., Fardal, M. A., Babul, A., & Guhathakurta, P. 2006, MNRAS, 366, 996

Genzel, R., Tacconi, L. J., Gracia-Carpio, J., et al. 2010, MNRAS, 407, 2091

Genzel, R., Tacconi, L. J., Lutz, D., et al. 2015, ApJ, 800, 20

George, K., Poggianti, B. M., Gullieuszik, M., et al. 2018, MNRAS, 479, 4126

Giavalisco, M., Ferguson, H. C., Koekemoer, A. M., et al. 2004, The Astrophysical Journal, 600, L93

Gordon, K. D., Clayton, G. C., Misselt, K. A., Landolt, A. U., & Wolff, M. J. 2003, ApJ, 594, 279

Gordon, K. D., Bailin, J., Engelbracht, C. W., et al. 2006, ApJ, 638, L87

Greenawalt, B., Walterbos, R. A. M., Thilker, D., & Hoopes, C. G. 1998, ApJ, 506, 135

Griffin, M. J., Abergel, A., Abreu, A., et al. 2010, A&A, 518, L3

Groves, B., Krause, O., Sandstrom, K., et al. 2012a, MNRAS, 426, 892

—. 2012b, MNRAS, 426, 892

Groves, B. A., & Allen, M. G. 2010, , 15, 614

Gruendl, R. A., Vogel, S. N., Davis, D. S., & Mulchaey, J. S. 1993, ApJ, 413, L81

Gullieuszik, M., Poggianti, B. M., Moretti, A., et al. 2017, ApJ, 846, 27

Gunn, J. E., & Gott, III, J. R. 1972, ApJ, 176, 1

Haffner, L. M., Reynolds, R. J., Tufte, S. L., et al. 2003, The Astrophysical Journal Supplement Series, 149, 405

Haffner, L. M., Dettmar, R. J., Beckman, J. E., et al. 2009, Reviews of Modern Physics, 81, 969

Hamajima, K., & Tosa, M. 1975, Publications of the Astronomical Society of Japan, 27, 561

Hao, C.-N., Kennicutt, R. C., Johnson, B. D., et al. 2011, ApJ, 741, 124

Hartwick, F. D. A. 1971, ApJ, 163, 431

Heald, G. H., Rand, R. J., Benjamin, R. A., & Bershady, M. A. 2006, ApJ, 647, 1018

Henderson, A. P. 1979, A&A, 75, 311

Herrera-Camus, R., Bolatto, A. D., Wolfire, M. G., et al. 2015, ApJ, 800, 1

Heyer, M. H., Corbelli, E., Schneider, S. E., & Young, J. S. 2004, ApJ, 602, 723

Ho, I.-T., Meidt, S. E., Kudritzki, R.-P., et al. 2018, A&A, 618, A64

Holwerda, B. W., & Keel, W. C. 2013, A&A, 556, A42

Holwerda, B. W., Bianchi, S., Böker, T., et al. 2012, A&A, 541, L5

Hony, S., Gouliermis, D. A., Galliano, F., et al. 2015, MNRAS, 448, 1847

Horne, K. 1986, Publications of the Astronomical Society of the Pacific, 98, 609

Howk, J. C. 2012, in EAS Publications Series, Vol. 56, EAS Publications Series, ed. M. A. de Avillez, 291–298

Huchra, J. P., & Geller, M. J. 1982, ApJ, 257, 423

Hughes, A. in prep.

Hughes, T. M., Baes, M., Fritz, J., et al. 2014a, A&A, 565, A4

—. 2014b, A&A, 565, A4

Hummel, E., & Beck, R. 1995, A&A, 303, 691

Iglesias-Páramo, J., López-Martín, L., Vílchez, J. M., Petropoulou, V., & Sulentic, J. W. 2012, A&A, 539, A127

Iglesias-Paramo, J., & Vilchez, J. M. 1997, ApJ, 479, 190

Issa, I. A. 1981, Astronomische Nachrichten, 302, 251
Jarrett, T. H., Cohen, M., Masci, F., et al. 2011, ApJ, 735, 112
Jarrett, T. H., Masci, F., Tsai, C. W., et al. 2012, AJ, 144, 68
—. 2013, AJ, 145, 6
Jarrett, T. H., Cluver, M. E., Magoulas, C., et al. 2017, ApJ, 836, 182
Jeans, J. H. 1902, Philosophical Transactions of the Royal Society of London Series A, 199, 1
Johnson, L. C., Seth, A. C., Dalcanton, J. J., et al. 2016, VizieR Online Data Catalog, 182
Kapala, M. J., Sandstrom, K., Groves, B., et al. 2015, ApJ, 798, 24
Kapala, M. J., Groves, B., Sandstrom, K., et al. 2017, ApJ, 842, 128
Kauffmann, G., Heckman, T. M., Tremonti, C., et al. 2003, MNRAS, 346, 1055
Kelz, A., Verheijen, M. A. W., Roth, M. M., et al. 2006, PASP, 118, 129
Kenney, J. D. P., Abramson, A., & Bravo-Alfaro, H. 2015, The Astronomical Journal, 150, 59
Kennicutt, Robert C., J., Keel, W. C., van der Hulst, J. M., Hummel, E., & Roettiger, K. A. 1987, AJ, 93, 1011
Kennicutt, R. C., & Evans, N. J. 2012, Annual Review of Astronomy and Astrophysics, 50, 531
Kennicutt, R. C., & Evans, N. J. 2012, Annual Review of Astronomy and Astrophysics, 50, 531
Kennicutt, R. C., Calzetti, D., Aniano, G., et al. 2011, Publications of the Astronomical Society of the Pacific, 123, 1347
Kennicutt, Jr., R. C. 1983, ApJ, 272, 54
—. 1998, ApJ, 498, 541
Kennicutt, Jr., R. C., Armus, L., Bendo, G., et al. 2003, PASP, 115, 928
Kennicutt, Jr., R. C., Calzetti, D., Walter, F., et al. 2007, ApJ, 671, 333
Kenworthy, M. A., Parry, I. R., & Taylor, K. 1998, in Society of Photo-Optical Instrumentation Engineers (SPIE) Conference Series, Vol. 3355, Optical Astronomical Instrumentation, ed. S. D'Odorico, 926–931
Kewley, L. J., Dopita, M. A., Sutherland, R. S., Heisler, C. A., & Trevena, J. 2001, ApJ, 556, 121
Kewley, L. J., Groves, B., Kauffmann, G., & Heckman, T. 2006, MNRAS, 372, 961
Kewley, L. J., Maier, C., Yabe, K., et al. 2013, ApJ, 774, L10
Kitchin, C. R. 2013, Astrophysical Techniques
Klaas, U., Nielbock, M., Haas, M., Krause, O., & Schreiber, J. 2010, A&A, 518, L44
Koepferl, C. M., Robitaille, T. P., & Dale, J. E. 2017, ApJ, 849, 2
Kong, X., Charlot, S., Brinchmann, J., & Fall, S. M. 2004, MNRAS, 349, 769
Koyama, H., & Ostriker, E. C. 2009, ApJ, 693, 1346
Kravtsov, A. V., & Borgani, S. 2012, Annual Review of Astronomy and Astrophysics, 50, 353
Kreckel, K., Groves, B., Schinnerer, E., et al. 2013, ApJ, 771, 62
Kreckel, K., Armus, L., Groves, B., et al. 2014, ApJ, 790, 26

Kreckel, K., Faesi, C., Kruijssen, J. M. D., et al. 2018, ApJ, 863, L21

Kroupa, P. 2001, MNRAS, 322, 231

Krumholz, M. R., Dekel, A., & McKee, C. F. 2012, ApJ, 745, 69

Krumholz, M. R., Fumagalli, M., da Silva, R. L., Rendahl, T., & Parra, J. 2015, MNRAS, 452, 1447

Krumholz, M. R., & McKee, C. F. 2005, ApJ, 630, 250

Lada, C. J., Forbrich, J., Lombardi, M., & Alves, J. F. 2012, ApJ, 745, 190

Lada, C. J., Lombardi, M., & Alves, J. F. 2010, ApJ, 724, 687

Laine, S., Knapen, J. H., Muñoz-Mateos, J.-C., et al. 2014, MNRAS, 444, 3015

Larson, R. B. 1981, MNRAS, 194, 809

Laurent, F., Henault, F., Renault, E., Bacon, R., & Dubois, J. 2006, Publications of the Astronomical Society of the Pacific, 118, 1564

Lee, B., Chung, A., Tonnesen, S., et al. 2017, MNRAS, 466, 1382

Leitherer, C., Schaerer, D., Goldader, J. D., et al. 1999, ApJS, 123, 3

Lequeux, J. 2005, The Interstellar Medium, doi:10.1007/b137959

Leroy, A. K., Walter, F., Brinks, E., et al. 2008, AJ, 136, 2782

Leroy, A. K., Bigiel, F., de Blok, W. J. G., et al. 2012, AJ, 144, 3

Leroy, A. K., Walter, F., Sandstrom, K., et al. 2013, AJ, 146, 19

Lewis, A. R., Dolphin, A. E., Dalcanton, J. J., et al. 2015, ApJ, 805, 183

Lewis, A. R., Simones, J. E., Johnson, B. D., et al. 2017, ApJ, 834, 70

Li, Y., Mac Low, M.-M., & Klessen, R. S. 2006, ApJ, 639, 879

Liddle, A. R. 1999, An introduction to modern cosmology

Liu, G., Calzetti, D., Hong, S., et al. 2013, ApJ, 778, L41

Liu et al., D. e. a. 2019, in prep.

Looney, L. W., Geis, N., Genzel, R., et al. 1999, in Bulletin of the American Astronomical Society, Vol. 31, American Astronomical Society Meeting Abstracts #193, 663

Madau, P., & Dickinson, M. 2014, Annual Review of Astronomy and Astrophysics, 52, 415

Madore, B. F. 1977, MNRAS, 178, 1

Madsen, G. J., Reynolds, R. J., & Haffner, L. M. 2006, ApJ, 652, 401

Mármol-Queraltó, E., Sánchez, S. F., Marino, R. A., et al. 2011, A&A, 534, A8

Martin, D. C., Fanson, J., Schiminovich, D., et al. 2005, ApJ, 619, L1

Martinez-Badenes, V., Lisenfeld, U., Espada, D., et al. 2012, A&A, 540, A96

Martinsson, T. P. K., Verheijen, M. A. W., Westfall, K. B., et al. 2013, A&A, 557, A130

Massey, P., McNeill, R. T., Olsen, K. A. G., et al. 2007, AJ, 134, 2474

Masters, D., McCarthy, P., Siana, B., et al. 2014, ApJ, 785, 153

Matthews, L. D., & Wood, K. 2003, ApJ, 593, 721

McElroy, R. in prep.

McKee, C. F., & Ostriker, E. C. 2007, Annual Review of Astronomy and Astrophysics, 45, 565

Meidt, S. E., Schinnerer, E., García-Burillo, S., et al. 2013, ApJ, 779, 45

Miller, J. S. 1974, Annual Review of Astronomy and Astrophysics, 12, 331

Minter, A., & Balser, D. S. 1998, Turbulent Heating in the Galactic Diffuse Ionized Gas, ed. D. Breitschwerdt, M. J. Freyberg, & J. Truemper, 543–546

Misiriotis, A., Xilouris, E. M., Papamastorakis, J., Boumis, P., & Goudis, C. D. 2006, A&A, 459, 113

Mo, H., van den Bosch, F. C., & White, S. 2010, Galaxy Formation and Evolution

Moreno, J., Torrey, P., Ellison, S. L., et al. 2015, MNRAS, 448, 1107

Morrissey, P., Conrow, T., Barlow, T. A., et al. 2007, ApJS, 173, 682

Mulchaey, J. S., Davis, D. S., Mushotzky, R. F., & Burstein, D. 1993, ApJ, 404, L9

Murphy, E. J., Condon, J. J., Schinnerer, E., et al. 2011, ApJ, 737, 67

Narayanan, D., Krumholz, M. R., Ostriker, E. C., & Hernquist, L. 2012, MNRAS, 421, 3127

Nehlig, F., Vollmer, B., & Braine, J. 2016, A&A, 587, A108

Neugebauer, G., Habing, H. J., van Duinen, R., et al. 1984, ApJ, 278, L1

Nossal, S., Roesler, F. L., Bishop, J., et al. 2001, Journal of Geophysical Research, 106, 5605

O'Brien, J. C., Freeman, K. C., & van der Kruit, P. C. 2010, A&A, 515, A63

Oey, M. S., Meurer, G. R., Yelda, S., et al. 2007, ApJ, 661, 801

Oke, J. B. 1990, AJ, 99, 1621

Olling, R. P. 1996, AJ, 112, 457

Osterbrock, D. E. 1974, Astrophysics of gaseous nebulae

Osterbrock, D. E., & Martel, A. 1992, Publications of the Astronomical Society of the Pacific, 104, 76

Peebles, P. J. E. 1982, ApJ, 263, L1

Peek, J. E. G., & Schiminovich, D. 2013, ApJ, 771, 68

Penzias, A. A., & Wilson, R. W. 1965, ApJ, 142, 419

Pereira-Santaella, M., Colina, L., García-Burillo, S., et al. 2016, A&A, 587, A44

Pérez-González, P. G., Kennicutt, Jr., R. C., Gordon, K. D., et al. 2006, ApJ, 648, 987

Perlmutter, S., & Schmidt, B. P. 2003, Measuring Cosmology with Supernovae, ed. K. Weiler, 195–217

Pety, J., Schinnerer, E., Leroy, A. K., et al. 2013, ApJ, 779, 43

Piatti, A. E., Cole, A. A., & Emptage, B. 2018, MNRAS, 473, 105

Pilbratt, G. L., Riedinger, J. R., Passvogel, T., et al. 2010, A&A, 518, L1

Pilyugin, L. S., Grebel, E. K., & Kniazev, A. Y. 2014, AJ, 147, 131

Planck Collaboration, Ade, P. A. R., Aghanim, N., et al. 2014, A&A, 571, A16

—. 2016, A&A, 586, A132

Poggianti, B. M., Moretti, A., Gullieuszik, M., et al. 2017, ApJ, 844, 48

Poglitsch, A., Waelkens, C., Geis, N., et al. 2010, A&A, 518, doi:10.1051/0004-6361/201014535

Popescu, C. C., Tuffs, R. J., Dopita, M. A., et al. 2011, A&A, 527, A109

Popping, G., Somerville, R. S., & Trager, S. C. 2014, Monthly Notices of the Royal Astronomical Society, 442, 2398

Puche, D., Carignan, C., & Bosma, A. 1990, AJ, 100, 1468

Querejeta, M., Meidt, S. E., Schinnerer, E., et al. 2015, ApJS, 219, 5

Ramos-Martínez, M., Gómez, G. C., & Pérez-Villegas, Á. 2018, MNRAS, 476, 3781

Rand, R. J. 1996, ApJ, 462, 712

—. 1998, ApJ, 501, 137

Rand, R. J. 2005, in Astronomical Society of the Pacific Conference Series, Vol. 331, Extra-Planar Gas, ed. R. Braun, 163

Rasmussen, J., Ponman, T. J., & Mulchaey, J. S. 2006, MNRAS, 370, 453

Reach, W. T. 1997, in Astronomical Society of the Pacific Conference Series, Vol. 124, Diffuse Infrared Radiation and the IRTS, ed. H. Okuda, T. Matsumoto, & T. Rollig, 33

Regan, M. W., Thornley, M. D., Vogel, S. N., et al. 2006, ApJ, 652, 1112

Renaud, F., Bournaud, F., & Duc, P.-A. 2015, Monthly Notices of the Royal Astronomical Society, 446, 2038

Renaud, F., Bournaud, F., Kraljic, K., & Duc, P.-A. 2014, MNRAS, 442, L33

Renaud, F. e. a. in prep.

Reynolds, R. J. 1971, in Bulletin of the American Astronomical Society, Vol. 3, 17

Reynolds, R. J. 1984, ApJ, 282, 191

Reynolds, R. J. 1990, in IAU Symposium, Vol. 139, The Galactic and Extragalactic Background Radiation, ed. S. Bowyer & C. Leinert, 157

Reynolds, R. J., & Cox, D. P. 1992, ApJ, 400, L33

Rieke, G. H., Alonso-Herrero, A., Weiner, B. J., et al. 2009, ApJ, 692, 556

Rieke, G. H., Young, E. T., Engelbracht, C. W., et al. 2004, ApJS, 154, 25

Robert C. Kennicutt, J. 1998, The Astrophysical Journal, 498, 541

Robertson, B. E., Ellis, R. S., Furlanetto, S. R., & Dunlop, J. S. 2015, The Astrophysical Journal, 802, L19

Rodríguez-Baras, M., Rosales-Ortega, F. F., Díaz, A. I., Sánchez, S. F., & Pasquali, A. 2014, MNRAS, 442, 495

Rosales-Ortega, F. F., Kennicutt, R. C., Sánchez, S. F., et al. 2010, MNRAS, 405, 735

Roth, M. M., Kelz, A., Fechner, T., et al. 2005, Publications of the Astronomical Society of the Pacific, 117, 620

Ruggiero, R., & Lima Neto, G. B. 2017, Monthly Notices of the Royal Astronomical Society, 468, 4107

Rupen, M. P. 1991, AJ, 102, 48

Saintonge, A., Kauffmann, G., Wang, J., et al. 2011, MNRAS, 415, 61

Saito, T., Iono, D., Yun, M. S., et al. 2015, ApJ, 803, 60

Saito, T., Iono, D., Xu, C. K., et al. 2016, PASJ, 68, 20

Salim, D. M., Federrath, C., & Kewley, L. J. 2015, ApJ, 806, L36

Salim, S., Rich, R. M., Charlot, S., et al. 2007, ApJS, 173, 267

Sánchez, S. F. 2006, Astronomische Nachrichten, 327, 850

Sánchez, S. F., Kennicutt, R. C., Gil de Paz, A., et al. 2012, A&A, 538, A8

Sánchez-Blázquez, P., Peletier, R. F., Jiménez- Vicente, J., et al. 2006, MNRAS, 371, 703

Sánchez-Gil, M. C., Jones, D. H., Pérez, E., et al. 2011, MNRAS, 415, 753

Sancisi, R., & Allen, R. J. 1979, A&A, 74, 73

Sanders, D. B., Mazzarella, J. M., Kim, D.-C., Surace, J. A., & Soifer, B. T. 2003, AJ, 126, 1607

Sanders, D. B., Soifer, B. T., Elias, J. H., et al. 1988a, ApJ, 325, 74

Sanders, D. B., Soifer, B. T., Elias, J. H., Neugebauer, G., & Matthews, K. 1988b, ApJ, 328, L35

Sanders, N. E., Caldwell, N., McDowell, J., & Harding, P. 2012, ApJ, 758, 133

Sanders, R. L., Shapley, A. E., Zhang, K., & Yan, R. 2017, ApJ, 850, 136

Sandin, C., Becker, T., Roth, M. M., et al. 2010, A&A, 515, A35

Sanduleak, N. 1969, AJ, 74, 47

Sarzi, M., Falcón-Barroso, J., Davies, R. L., et al. 2006, MNRAS, 366, 1151

Sazhin, M. V. 1978, Soviet Ast., 22, 36

Schinnerer, E., Meidt, S. E., Pety, J., et al. 2013, ApJ, 779, 42

Schlafly, E. F., & Finkbeiner, D. P. 2011, ApJ, 737, 103

Schlegel, D. J., Finkbeiner, D. P., & Davis, M. 1998, ApJ, 500, 525

Schmidt, M. 1959, ApJ, 129, 243

Schmitt, H. R., Calzetti, D., Armus, L., et al. 2006, ApJ, 643, 173

Schramm, D. N., & Turner, M. S. 1998, Reviews of Modern Physics, 70, 303

Schruba, A., Leroy, A. K., Walter, F., et al. 2011, AJ, 142, 37

Schultz, G. V., & Wiemer, W. 1975, A&A, 43, 133

Scoville, N., Aussel, H., Brusa, M., et al. 2007, The Astrophysical Journal Supplement Series, 172, 1

Scoville, N., Sheth, K., Aussel, H., et al. 2016, ApJ, 820, 83

Scoville, N., Lee, N., Vanden Bout, P., et al. 2017, ApJ, 837, 150

Scoville, N. Z., & Solomon, P. M. 1975, ApJ, 199, L105

Scoville, N. Z., Thakkar, D., Carlstrom, J. E., & Sargent, A. I. 1993, ApJ, 404, L59

Scudder, J. M., Ellison, S. L., Torrey, P., Patton, D. R., & Mendel, J. T. 2012, MNRAS, 426, 549

Shapley, A. E. 2011, Annual Review of Astronomy and Astrophysics, 49, 525

Shapley, A. E., Reddy, N. A., Kriek, M., et al. 2015, ApJ, 801, 88

Sharples, R., Bender, R., Bennett, R., et al. 2006, New Astronomy Reviews, 50, 370

Sivanandam, S., Rieke, M. J., & Rieke, G. H. 2014, ApJ, 796, 89

Slanger, T. G., Huestis, D. L., Cosby, P. C., & Osterbrock, D. E. 2000, J. Chem. Phys., 113, 8514

Smolčić, V., Miettinen, O., Tomičić, N., et al. 2017, A&A, 597, A4

Soifer, B. T., & Neugebauer, G. 1991, AJ, 101, 354
Soifer, B. T., Sanders, D. B., Madore, B. F., et al. 1987, ApJ, 320, 238
Stanek, K. Z., & Garnavich, P. M. 1998, ApJ, 503, L131
Steinacker, J., Baes, M., & Gordon, K. D. 2013, Annual Review of Astronomy and Astrophysics, 51, 63
Steinhauser, D., Haider, M., Kapferer, W., & Schindler, S. 2012, A&A, 544, A54
Steinhauser, D., Schindler, S., & Springel, V. 2016, A&A, 591, A51
Strömgren, B. 1939, ApJ, 89, 526
Tabatabaei, F. S., & Berkhuijsen, E. M. 2010, A&A, 517, A77
Tacconi, L. J., Genzel, R., Saintonge, A., et al. 2018, ApJ, 853, 179
Tasker, E. J., & Bryan, G. L. 2006, ApJ, 641, 878
Temim, T., Slane, P., Reynolds, S. P., Raymond, J. C., & Borkowski, K. J. 2010, ApJ, 710, 309
Tempel, E., Tuvikene, T., Tamm, A., & Tenjes, P. 2011, A&A, 526, A155
Thilker, D. A., Hoopes, C. G., Bianchi, L., et al. 2005, ApJ, 619, L67
Thilker, D. A., Boissier, S., Bianchi, L., et al. 2007, ApJS, 173, 572
Tielens, A. 2008, Annual Review of Astronomy and Astrophysics, 46, 289
Tielens, A. G. G. M. 2005, The Physics and Chemistry of the Interstellar Medium (Cambridge University Press), doi:10.1017/CBO9780511819056
Tomičić, N., Ho, I.-T., Kreckel, K., et al. 2019, The Astrophysical Journal, 873, 3
Tomičić, N., Kreckel, K., Groves, B., et al. 2017, ApJ, 844, 155
Tomičić, N., Hughes, A., Kreckel, K., et al. 2018, ApJ, 869, L38
Tomičić, N. e. a. 2019, in prep.
Toomre, A., & Toomre, J. 1972, ApJ, 178, 623
Tremonti, C. A., Heckman, T. M., Kauffmann, G., et al. 2004, ApJ, 613, 898
Troncoso Iribarren, P., Padilla, N., Contreras, S., et al. 2016, Galaxies, 4
Tully, R. B., & Fisher, J. R. 1988, Catalog of Nearby Galaxies, 224
Tyler, K., Quillen, A. C., LaPage, A., & Rieke, G. H. 2004, ApJ, 610, 213
van den Bergh, S. 1957, ZAp, 43, 236
—. 1988, PASP, 100, 344
van den Bosch, F. C., Abel, T., Croft, R. A. C., Hernquist, L., & White, S. D. M. 2002, ApJ, 576, 21
van der Hulst, J. M., Kennicutt, R. C., Crane, P. C., & Rots, A. H. 1988, A&A, 195, 38
van der Kruit, P. C., & Allen, R. J. 1978, ARA&A, 16, 103
van Dokkum, P. G. 2001, Publications of the Astronomical Society of the Pacific, 113, 1420
Velusamy, T., & Langer, W. D. 2014, A&A, 572, A45
Verheijen, M. A. W., Bershady, M. A., Andersen, D. R., et al. 2004, Astronomische Nachrichten, 325, 151
Verley, S., Relaño, M., Kramer, C., et al. 2010, A&A, 518, L68
Verstappen, J., Fritz, J., Baes, M., et al. 2013, A&A, 556, A54

Viaene, S., Forbrich, J., & Fritz, J. 2018, MNRAS, 475, 5550

Viaene, S., Baes, M., Tamm, A., et al. 2017, A&A, 599, A64

Vulcani, B., Poggianti, B. M., Moretti, A., et al. 2018, ApJ, 852, 94

Vutisalchavakul, N., Evans, II, N. J., & Heyer, M. 2016, ApJ, 831, 73

Wada, K., & Norman, C. A. 2007, ApJ, 660, 276

Walcher, C. J., Wisotzki, L., Bekeraité, S., et al. 2014, A&A, 569, A1

Wall, W. 2018, A History of Optical Telescopes in Astronomy, doi:10.1007/978-3-319-99088-0

Walter, F., Brinks, E., de Blok, W. J. G., et al. 2008, AJ, 136, 2563

Walterbos, R. A. M., & Braun, R. 1994, ApJ, 431, 156

Wang, J., Heckman, T. M., & Lehnert, M. D. 1999, ApJ, 515, 97

Weiss, R., & Block, B. 1965, J. Geophys. Res., 70, 5615

Weitzel, L., Krabbe, A., Kroker, H., et al. 1996, Astronomy and Astrophysics Supplement Series, 119, 531

Werner, M. W., Gallagher, D. B., & Irace, W. R. 2004, Advances in Space Research, 34, 600

White, S. D. M., & Rees, M. J. 1978, MNRAS, 183, 341

Whitmore, B. C., Chandar, R., Kim, H., et al. 2011, ApJ, 729, 78

Williams, B. F. 2003, AJ, 126, 1312

Williams, R. E., Blacker, B., Dickinson, M., et al. 1996, AJ, 112, 1335

Witt, A. N., Thronson, Harley A., J., & Capuano, John M., J. 1992, ApJ, 393, 611

Wolter, A., Esposito, P., Mapelli, M., Pizzolato, F., & Ripamonti, E. 2015, MNRAS, 448, 781

Wong, T., & Blitz, L. 2002, ApJ, 569, 157

Wright, E. L., Eisenhardt, P. R. M., Mainzer, A. K., et al. 2010, AJ, 140, 1868

Wu, J., II, N. J. E., Gao, Y., et al. 2005, The Astrophysical Journal Letters, 635, L173

Wynn-Williams, C. G. 1982, Annual Review of Astronomy and Astrophysics, 20, 587

Xu, C., & Helou, G. 1996, ApJ, 456, 152

Yasui, K., Nishiyama, S., Yoshikawa, T., et al. 2015, Publications of the Astronomical Society of Japan, 67, 123

Yeh, S. C. C., & Matzner, C. D. 2012, The Astrophysical Journal, 757, 108

Yim, K., Wong, T., Xue, R., et al. 2014, AJ, 148, 127

York, D. G., Adelman, J., Anderson, John E., J., et al. 2000, AJ, 120, 1579

Zanichelli, A., Garilli, B., Scodeggio, M., et al. 2005, PASP, 117, 1271

Zschaechner, L. K., & Rand, R. J. 2015, ApJ, 808, 153

Zurita, A., & Bresolin, F. 2012, MNRAS, 427, 1463

LIST OF ACRONYMS AND ABBREVIATIONS

Λ **CDM**	Cold Dark Matter cosmological model with a cosmological constant
2MASS	Two Micron All Sky Survey
AGN	Active Galactic Nucleus
ALMA	Atacama Large Millimeter/submillimeter Array
BPT	Baldwin, Phillips and Telervich diagram, Baldwin et al. (1981)
C05	Calzetti et al. (2005)
C07	Calzetti et al. (2007)
CALIFA	Calar Alto Legacy Integral Field Area Survey
CCD	Charge-Coupled Device
CO	Molecular CO Gas
COLD GASS	CO Legacy Database for GASS
COSMOS	Cosmic Evolution Survey
CR	Cosmic Rays
DIG	Diffuse Ionised Gas
DSS	Digitized Sky Survey
ESA	European Space agency
ESO	European South Observatory
FUV	Far-Ultraviolet
GALEX	Galaxy Evolution Explorer

GASP	GAs Stripping Phenomena in galaxies with MUSE
GASS	The GALEX Arecibo SDSS Survey
GMC	Giant Molecular Cloud
GOALS	Great Observatories All-sky LIRG Survey
GOODS	Great Observatories Origins Deep Survey
HI	Neutral Atomic Hydrogen Gas
HII	Ionised Atomic Hydrogen Gas
H$_2$	Molecular Hydrogen Gas
H$\alpha, H\beta, H\gamma, H\delta$	Ionised Hydrogen gas, Balmer emission line series
HCN	Molecular HCN Gas
HDF	Hubble Deep Field
HERACLES	HERA CO-Line Extragalactic Survey
HST	Hubble Space Telescope
HUDF	Hubble Ultradeep Field
IDL	Interactive Data Language
IFS	Integral Field Spectrometry
IFU	Integral Field Unit
IMF	Initial Mass Function
IR	Infrared
IRAM	Institut de Radioastronomie Millimétrique
IRAS	Infrared Astronomical Satellite
ISM	Interstellar Medium
K13	Kreckel et al. (2013)
KINGFISH	Key Insights on Nearby Galaxies: a Far-Infrared Survey with Herschel
KMOS	K-band Multi Object Spectrograph
KPNO	Kitt Peak National Observatory
LINER	Low-Ionization Nuclear Emission line Region

LIRG	Luminous Infrared Galaxy
LVM	Local Volume Mapper, SDSS-V survey
M31	Andromeda Galaxy
MaNGA	Mapping Nearby Galaxies at APO
MUSE	Multi Unit Spectroscopic Explorer, ESO
NAOJ	National Astronomical Observatory of Japan
NASA	National Aeronautics and Space Administration
NED	NASA/IPAC Extragalactic Database
NOEMA	NOrthern Extended Millimeter Array, IRAM
NRAO	National Radio Astronomy Observatory
Pα	Ionised Hydrogen gas, Paschen α emission line
PA	Position Angle
PHANGS	Physics at High Angular Resolution in Nearby Galaxies
PHAT	Panchromatic Hubble Andromeda Treasury
PINGS	PPAK IFS Nearby Galaxies Survey
PMAS	Potsdam Multi-Aperture Spektrophotometer at the Calar Alto Observatory in Spain
PPaK	IFU fiber bundle at the Calar Alto Observatory in Spain
pPXF	Penalized Pixel-Fitting code
SDSS	Sloan Digital Sky Survey
SF	Star Formation
SFE	Star Formation Efficincy
SFH	Star Formation History
SFR	Star Formation Rate
SED	Spectral of Energy Distribution
SINGS	Spitzer Infrared Nearby Galaxies Survey
SINFONI	SINgle Faint Object Near-IR Investigation
SLIM	Survey of Lines in M31

SN	Supernova
SOFIA	Stratospheric Observatory for Infrared Astronomy
sSFR	Specific Star Formation Rate
SSP	Simple Stellar Population
THINGS	The HI Nearby Galaxy Survey
TIR	Total Infrared
ULIRG	Ultra Luminous Infrared Galaxy
UV	Ultraviolet
VENGA	VIRUS-P Exploration of Nearby Galaxies survey
VIRUS-P	Visible Integral field Replicable Unit Spectrograph Prototype
VLA	Very Large Array
WFC	Wide Field Camera, HST
WIM	Warm Ionised Gas. Synonym for the DIG.
WISE	Wide-field Infrared Survey Explorer

ACKNOWLEDGEMENTS / ZAHVALE

There is a large number of people to whom I wish to express my sincere gratitude and to thank for contributing to this thesis. This thesis is not only a product of my work, but also a product of feedback, hard work, and advices from my colleagues (supervisor, collaborators, researchers, and PhD students) at my research institute and elsewhere. Furthermore, this thesis would not exist without the people from my past and present (family, friends, and former professors).

First and foremost, I would like to thank my supervisor Dr. Eva Schinnerer, for mentoring me through my PhD studies, and for her guidance regarding scientific research and life. Her knowledge in astronomy, and her useful and abundant feedback in our written work was and will always be of great importance to me. I wish you great successes in research in the future.

Secondly, I wish to express my gratitude to Drs. Kathryn Kreckel and I-Ting Ho, who advised me during our scientific research, and worked closely with me during my PhD studies. I am grateful for their consultations, their calming effect on me when I was nervous, and their wise approach to writing papers. Thirdly, I would like to thank the other members of my research group, both current and former, for their support and encouragement in many aspects of life and research, and for contributing to this thesis. These PhD students and post-doctoral researchers are: Emer Brady, Christopher Faesi, Philipp Lang, Sarah Leslie, Daizhong Liu, Rebecca McElroy, Miguel Querejeta, Ismael Pessa, Toshiki Saito, Francesco Santoro, Kazimierz Sliwa, and Sharon (Meidt) van der Wel.

I wish to acknowledge the help with the English language and the proofreading of this thesis provided by Vincent Carpenter, Christopher Faesi, Micah Klettke, Kathryn Kreckel, Jacob Isbell, Sarah Leslie, Toshiki Saito, Eva Schinnerer, and Steffi Yen. I am also grateful for the help with the German language provided by Miriam Keppler, Philipp Lang, Manuel Riener, Eva Schinnerer, and Matthias Samland. Special thanks to my mum and Prof. Snježana Novković Mahmet, a professor of the English language at my high school, for teaching me English and for breaking my significant unwillingness to learn it during my teenage years.

I would like to express my appreciation to the researchers, IT personnel, and other employees at the Max Planck Institute for Astronomy (MPIA) in Heidelberg for all the technical, logistical, and scientific support, as well as all the advice that they provided during my time in Heidelberg. Particular thanks should also go to Christian Fendt and employees of the International Max Planck Research School in Heidelberg (IMPRS-HD) for providing me the opportunity to work with and to meet other PhD students in astrophysics, and for the fun retreats. To my collaborators near and far, I express my sincere gratitude for the assistance given while writing our scientific papers and observing, as well as the astrophysical discussions. These collaborators, outside my current group at MPIA, are: Guillermo A. Blanc, Santiago Garcia-Burillo, Brent Groves, Annie Hughes, Simon Glover, Karl Gordon, Thomas Jarrett, María Jesús

Jiménez-Donaire, Maria Kapala, Adam Leroy, Alexia Lewis, Mark Norris, Miguel Querejeta, Eric Pellegrini, Jérôme Pety, Daniel Rahner, Allesandro Raza, Florent Renaud, Karin Sandstrom, Andreas Schruba, David Thilker, Sharon (Meidt) van der Wel.

Over the last few years, I have learned that there is a lot more fun to scientific research than just looking at beautiful images of galaxies. What I will remember the most from my time at MPIA are the friends with whom I spent many fun and happy moments during my PhD studies. As I write these last words, reflecting on my time in Heidelberg, my gaze falls onto some important objects on my desk.
30 cm model of the USS Discovery (NCC-1031) from Star Trek: 35 euros.
The large dragon & castle model: 55 euros.
A photograph of my adopted wolf friend Pyrro Adelfo (Greek for “Amber brother”) M2075, who I made regular donations to, at the New York Wolf Conservation Center: a lot of money.
However, the time I spent with my friends and PhD students in Heidelberg: **PRICELESS**.
For their names not to be forgotten, I am writing them here for the future generations at MPIA.

First and foremost, I would like to thank to all former and current members of my awesome office 225 because they made me happy to come to the office every day. I traveled with them, drank with them, dined with them, and enjoyed life with them. We also supported and encouraged each other. They are:
Aida Ahmadi (Ziad negarane zendegi nabash! Va man hamchenan royaye baghlavaye khanegie to ra dar sar daram.), Mayte Alfaro (Tu máquina de café me convirtió en un verdadero adicto al café. Estuvo buenísimo nuestro viaje a Dinamarca!), Fabrizio Arrigoni Battaia (Il tuo sorriso non può essere più ampio.), Salvatore Cielo (Grazie per la scrivania, me ne sto prendendo cura!), Miriam Keppler (Ich werde Sie die ”Working Bee” unseres Büros nennen. Stellen Sie sich meine strengen Blicke vor, wann immer Sie Ihr ”Mittagessen” nehmen, wenn ich fort bin.), Gabriel-Dominique Marleau (Je suis toujours fascin´ par vos compétences linguistiques.), Camilla Penzo (Tu lavori troppo, come Miriam), Ismael Pessa (Te deseo gran éxito y espero que disfrutes trabajar en el grupo de Eva tanto como yo lo hice.), Manuel Riener (Ich freue mich über die gegenseitige Vereinbarung der Nachspeisen aus Österreich und K & K. Ich bin dankbar für deine Witze und Lachen.), Matthias Samland (いつかあなたが日本に行き、コーディングの達人になることを願っています。もうあなたがいなくて寂しいです。), Daniele Sorini (Mi ricordo il tuo essere nerd, e conservo ancora il ricordo delle tue lezioni sulla cultura del caffè, le tue feste e i giochi col Feuerzangenbowle.), and Shiwei Wu (I do not want to say anything in Chinese, so that I avoid embarrassing myself, unlike last time.).
Also, unforgettable times at our office are due to regular visits from people from other offices and institutes, such as Micah Klettke (I was really happy when you found the job position at MPIA because it meant you could come to our office every day.), Anahí Caldú Primo (Tu sonrisa ilumina la oficina, incluso cuando en Alemania está nublado.), and Steffi Yen (You and

your simple drawings put a smile on my face. You also make the gloomy Sundays we spend working at MPIA more cheerful. Our office would not be as awesome without you.).

I am grateful for the other close friends I made at MPIA. We spent a lot of fun times in office 216 B, at the cinemas, at IMPRS dinners, at barbecues, at the Dungeons & Dragons game nights, and on our regular trips to various castles. They inspire me to enjoy my life and have made writing this thesis easier: Branislav Avramov (Thank you for the fun moments on our trips to the castles.), Vincent Carpenter (I will miss your imagination and your wit.), Alexander Hygate (I will miss your British wit, your posh British language, and your 'love' of citrus fruits.), Jacob Isbell (I will miss your jokes, and Leafy, who rocks.), Giancarlo Mattia (I will miss our short but useful gym times.), Riccardo Nanni (My Celtic brother from Italy and fellow fantasy/history/Star Trek nerd, see you soon in Italy!), Sabina Puerckhauer (I am grateful for the fun days/evenings with you, and all of our wonderful trips.), Christos Vourellis (Thank you for the sofa and time spent in your office. I will miss your laugh and 'down to earth' approach with life.), Yulong Zhuang (You are the Space Dragon of our institute, master of magic, and painter of your magnificent pyramids. I will miss your quirkiness.).

In addition to the friends mentioned above, I will also miss many other PhD students and post-docs, former and current, who made me love coming to the institute. They influenced me and made me love my work even at dark moments. I discussed science, drank at Mirendela and Science coffee, partied (thanks Tobi and Sven), barbecued (thanks Matthias and Tobi), hiked, sweated in saunas, and so much more with them. The names of those students include: Theodoros Anagnos, Francisco Aros, Branislav Avramov, Asmita Bhandare, Arianna Musso Barcucci, Ivana Barišić, Tobias Buck, Hans Baehr, Felix Bosco, Miguel Botran, Sven Buder, Camille Bergez-Casalou, Priscilla Chauke, Josha van Houdt, Anna-Christina Eilers, Paul Heeren, Hector Hiss, Sebastian Bustamante Jaramillo, Vikas Joshi, Melanie Kaasinen, Diana Kossakowska, Mikhail Kovalev, Sarah Leslie, Gigi Leung, Johanna Coronado Martinez, Matteo Mazzarini, Irina Smirnova-Pinchukova, Marcelo Tala Pinto, Daniel Rahner, Sepideh Sadegi, Paula Sarkis, Maximilian Sasserath, Martin Schlecker, and many others.
The post-docs, former students, and the group leaders are: Chiara Battistini, Paolo Bianchini, Faustine Cantalloube, Ludmila Carone, Roxana Chira, Alyssa Drake, Christopher Faesi, Emanuele Paolo Farina, Carl Ferkinhoff, Diane Feuillet, Morgan Fouesneau, Andy Gallagher, Iskren Georgiev, Felipe Goicovic, Thales Gutcke, Robert Harris, Jonathan Henshaw, Nikolay Kacharov, Sara Rezaei Khoshbakht, Taisiya Kopytova, Alessandra Mastrobuono-Battisti, María J. Jiménez-Donaire Chiara Mazzucchelli, Rebecca McElroy, Rosalie McGurk, Allison Merritt, Dániel Molnár, Miguel Querejeta, Wu Po-Feng, Gabriele Rodeghiero, Michael Rugel, Kalyan Kumar Radhakrishnan Santhakumari, Dmitry Semenov, Richard Teague, Sassa Tsatsi, Valera Vasilev, and Peter Zeidler. I will miss you all!

I also wish to express deep gratitude towards the people that provided me feedback on our published papers, the grants, and the facilities, which provided scientific data and observation

time:
First and foremost, I thank all the referees of the journals in which we published our papers. Their constructive comments greatly improved our papers and this thesis. I also thank Mónica Relaño, Rebecca McElroy and Sharon Meidt for constructive comments on the papers. I wish to kindly thank Alexia Lewis, who shared the maps of modeled FUV emission and star formation history in the Andromeda galaxy.

Neven Tomičić and Kathryn Kreckel acknowledge grants SCHI 536/8-2 and KR 4598/1-2 from the DFG Priority Program 1573. This work is also based on observations collected at the Centro Astronómico Hispano-Alemán (CAHA), operated jointly by the Max-Planck Institut für Astronomie and the Instituto de Astrofísica de Andalucía (CSIC). Furthermore, this work is based on observations carried out under project number w14cg001 with the IRAM NOEMA Interferometer and 30m telescope. IRAM is supported by INSU/CNRS (France), MPG (Germany) and IGN (Spain).

It is also based on observations made with Herschel. Herschel is an ESA space observatory with science instruments provided by European-led Principal Investigator consortia and with important participation from NASA. PACS has been developed by a consortium of institutes led by MPE (Germany) and including UVIE (Austria); KU Leuven, CSL, IMEC (Belgium); CEA, LAM (France); MPIA (Germany); INAFIFSI/OAA/OAP/OAT, LENS, SISSA (Italy); and IAC (Spain). This development has been supported by the funding agencies BMVIT (Austria), ESA-PRODEX (Belgium), CEA/CNES (France), DLR (Germany), ASI/INAF (Italy), and CICYT/MCYT (Spain). SPIRE has been developed by a consortium of institutes led by Cardiff University (UK) and including Univ. Lethbridge (Canada); NAOC (China); CEA, LAM (France); IFSI, Univ. Padua (Italy); IAC (Spain); Stockholm Observatory (Sweden); Imperial College London, RAL, UCL-MSSL, UKATC, Univ. Sussex (UK); and Caltech, JPL, NHSC, Univ. Colorado (USA). This development has been supported by national funding agencies: CSA (Canada); NAOC (China); CEA, CNES, CNRS (France); ASI (Italy); MCINN (Spain); SNSB (Sweden); STFC (UK); and NASA (USA). Based on observations made with the NASA Galaxy Evolution Explorer. GALEX is operated for NASA by the California Institute of Technology under NASA contract NAS5-98034. This publication makes use of data products from the Wide-field Infrared Survey Explorer (Wright et al., 2010), which is a joint project of the University of California, Los Angeles, and the Jet Propulsion Laboratory/California Institute of Technology, funded by the National Aeronautics and Space Administration. This work is also based on observations made with the NASA Galaxy Evolution Explorer (GALEX). GALEX is operated for NASA by the California Institute of Technology under NASA contract NAS5-98034.

Last but not least, I would especially like to thank my parents, Marina Štemberger-Tomičić and Milan Tomičić, for their continuous support and encouragement through my life. Also, I would like to thank Dr. Krešimir Pavlovski (PMF, Zagreb) and my Master Thesis supervisor

Dr. Vernesa Smolčić (PMF, Zagreb) for teaching and motivating me to carry out research in astrophysics, and for helping me in the first steps of my career. I want to thank my close friends in Zagreb, especially Marin Šako and Krešimir Tisanić, with whom I regularly skyped during my time in Heidelberg. I would also like to personally thank my professors in primary school (e.g., Ankica Benček, Josip Matijević, and Andreja Pehar), music school (Dea Detiček), high school V. Gymnasium (e.g., Romana Halapir Franković, Ana-Marija Kukuruzović, Snježana Novković Mahmet, Milena Ćulav Markičević, and Svjetlana Vorel), and the Department of Physics at the Faculty of Science (PMF) in Zagreb (e.g., Matko Milin, Tamara Nikšić, Nikola Poljak, Zoran Rukelj, and Selma Supek). They made me love astronomy, physics, biology, history, mathematics, and music. Their lessons changed my critical thinking skills, and pushed my view of the world towards new horizons. Without my parents and mentors, I would not be who and where I am today, and this PhD thesis would not exist.
Thank you!

Na kraju, htio bih se posebno zahvaliti mojim roditeljima, Marini Štemberger-Tomičić i Milanu Tomičiću, za njihovu stalnu podršku i ohrabrivanje tijekom cijelog mog života. Uz to, htio bih se zahvaliti Dr. Krešimiru Pavlovskom (PMF, Zagreb) i mojoj mentorici diplomskog rada Dr. Vernesi Smolčić (PMF, Zagreb) što su me podučavali i motivirali da nastavim sa znanstvenim zvanjem u astrofizici, i sto su mi pomogli u prvim koracima moje karijere. Htio bih se zahvaliti mojim bliskim prijateljima u Zagrebu, posebno Marinu Šaki i Krešimiru Tisaniću, sa kojima sam regularno skypao za vrijeme mog boravka u Heidelbergu. Osobno bih zahvalio mojim profesorima u osnovnoj školi (npr. Ankici Benček, Josipu Matijeviću, i Andreji Pehar), muzičkoj školi (Dei Detiček), V. Gimnaziji (npr. Romani Halapir Franković, Ana-Mariji Kukuruzović, Snježani Novković Mahmet, Mileni Ćulav Markičević, i Svjetlani Vorel), i u Fizičkom zavodu Prirodoslovno-Matematičog Fakulteta (PMF) u Zagrebu (npr. Matku Milinu, Tamari Nikšić, Nikoli Poljaku, Zoranu Rukelji, i Selmi Supek). Oni su me naveli da zavolim astronomiju, fiziku, biologiju, povijest, matematiku, i muziku. Njihive lekcije su promijenili moje kritično razmisljanje, te pomicalo moj pogled na svijet prema novim horizontima. Bez mojih roditelja i mentora, danas ne bih bio tko jesam i gdje jesam, te ovaj doktorski rad ne bi postojao.
Hvala vam!

Place:
Max-Planck Institut für Astronomie (MPIA),
Heidelberg, Baden-Württemberg,
Germany, The European Union

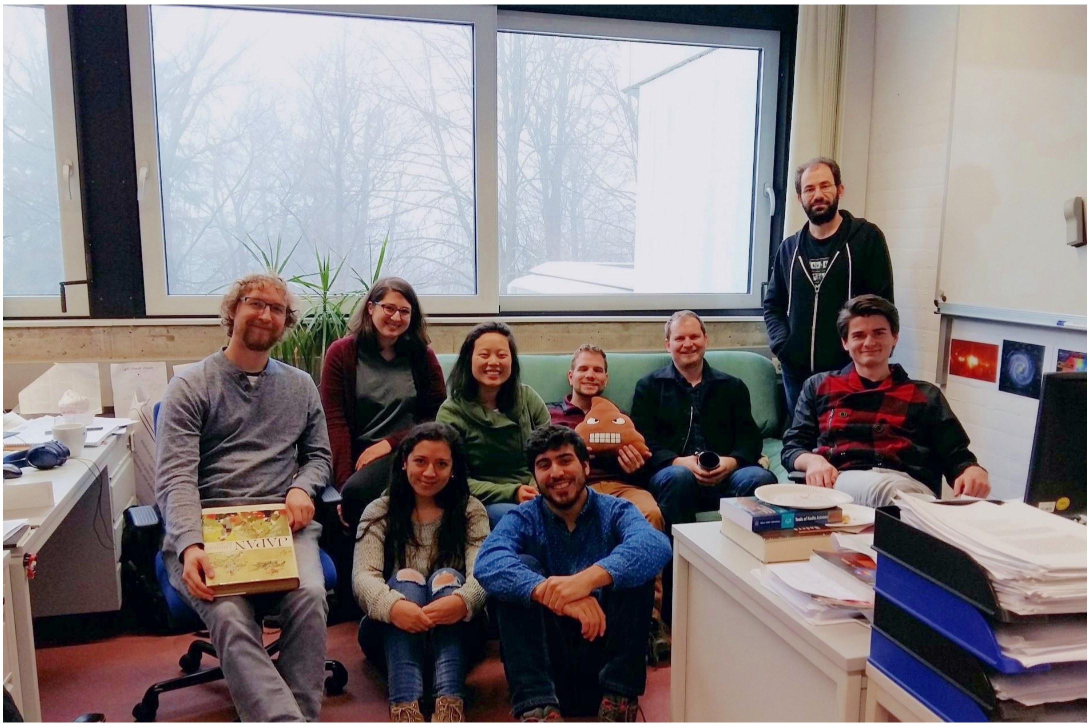Date: March of 2019 **Neven Tomičić**